Polarization Spectroscopy of High Order Harmonic Generation in Semiconductors

Shatha Kaassamani

Thèse de doctorat

NNT: 2020UPASP091

université PARIS-SACLAY

Polarization Spectroscopy of High Order Harmonic Generation in Semiconductors

Thèse de doctorat de l'université Paris-Saclay

École doctorale n° 572, Ondes et Matière (EDOM)
Spécialité de doctorat: Optique et Photonique
Unité de recherche: Université Paris-Saclay, CEA, CNRS, LIDYL, 91191, Gif-sur-Yvette, France
Référent: Faculté des sciences d'Orsay

Thèse présentée et soutenue à Paris-Saclay, le 10 Décembre 2020, par

Shatha KAASSAMANI

Composition du jury:

Annie KLISNICK Directrice de recherche Institut des Sciences Moléculaires d'Orsay (ISMO) - France	Présidente
Caterina VOZZI Directrice de recherche (HDR) Institute for Photonics and Nanotechnologies (IFN), CNR - Italie	Rapportrice & Examinatrice
Marcelo CIAPPINA Professeur associé Guangdong Technion – Israel Institute of Technology - Chine	Rapporteur & Examinateur
Milutin KOVACEV Professeur Institute for Quantum Optics, Leibniz University Hannover - Allemange	Examinateur
Eric CONSTANT Directeur de recherche Institut Lumière Matière (ILM), Université Claude Bernard Lyon 1 - France	Examinateur
Stefan HAESSLER Chargé de recherche Laboratoire d'Optique Appliquée (LOA), Institut Polytechnique de Paris - France	Examinateur
Hamed MERDJI Directeur de recherche LIDYL CEA Saclay - France	Directeur de thèse
David GAUTHIER Chargé de recherche LIDYL CEA Saclay - France	Co-encadrant

Contents

Acknowlegements

I would like to take the chance here to express how grateful I am for this whole journey, and for all the people who have contributed to make this piece of work enjoyable, meaningful and successful.

Special thanks go to Caterina Vozzi, Marcelo Ciappina, Annie Klisnick, Milutin Kovacev, Eric Constant and Stefan Haessler for accepting the invitation to be a part of my thesis committee, and for their insightful comments, discussions and questions. It was a great honor and pleasure to have such distinguished jury members. I was excitedly looking forward to meet them in person at my thesis defense, yet due to the restrictions imposed by the coronavirus pandemic, my thesis defense had to be done through videoconference. Nevertheless, it was still a one of a kind experience.

Reflecting back to the beginning of the journey almost four years ago, I cannot but truly thank my thesis director Hamed Merdji first for giving me the opportunity to join his group, and second for all his help and mentorship throughout these years. I had the privilege to be a part of the LIDYL laboratory and to be surrounded by distinguished researchers. I also thank Hamed for always trying to establish a nice and friendly environment in the group, which have made these years pass very pleasantly and smoothly. A special thank you to my thesis co-director Willem Boutu for being available at all times and for his assistance and contribution to this work. I believe that the work wouldn't have been possible without his full commitment and dedication to the lab.

The journey was enriching and fruitful having had the opportunity to collaborate with external researchers and theoreticians. I am grateful for all the constructive discussions with our collaborators Nicolas Tancogne-Dejean and Thierry Auguste, which have enlightened my understandings to the strong field physics in general, and the high harmonic generation (HHG) process in particular. It was also a pleasure to work in Marc Hanna's group at Institut d'Optique Graduate School (IOGS) during two beamtimes during my PhD. I thank him for his warm welcome and assistance during my stay.

The experimental work wouldn't have been achieved without the help of Marc Billon who assisted in the all the electronic connections, Sylvain Foucquart and André Fillon who helped in producing the mechanical components, and Georges Vigneron, the friendliest general and laser security director, who was always attentive about working in safe conditions. I sincerely thank them for their assistance, sense of humor and energetic spirit, which have been a special part of the LIDYL. Indeed, a nice greeting, joke or smile from them have made nice moments during tough days. Thanks also to Sylvie Jubera our IT technician, and the LIDYL secretaries Caroline Lebe and Véronique Gereczy.

A big and a very special thank you to David Gauthier, who I consider myself very lucky to have worked with since the beginning of my thesis and even before during my 6 months internship in the group. I thank him infinitely for his guidance and support, and I appreciate the patience he had to transmit his knowledge and experience; I have indeed learned a lot from him. His encouragement and trust to my experimental work, made me gain confidence in dealing with optical setups, lasers and alignments, and allowed me to grow as the young researcher I am today. Maybe chance made us colleagues, but the daily time spent together, our talks, laughter, complaints and "les petits accidents de travaille" made us friends. To my colleague Dominik Franz, who continuously showed support and appreciation to our joint work, I truly thank him for all his assistance, and for always proposing his help. I was lucky to work with him and share memorable scientific conferences, and I also thank him for being such a great friend and colleague.

I am so thankful to have worked with friendly and supportive colleagues, Maria Kholodtsova, Rana Nicolas, Joana Duarte, Viktoria Nefedova and Sven Froehlich who made their best to welcome me since my arrival and integrate me in the group. I will always remember our coffee breaks, barbeques and social events which have brought spirit to our lab and team work. We have created great memories and memorable moments which I will cherish forever. And to my friends here in Paris Wassim, Bilal, Howaida, Rasha, Luca, Cassiano, Nour, Mohannad, Walid and Malik, a million times thank you for all the great moments spent together. Your presence have supported me and have added a special taste to my stay.

Last but not least, to my family: my parents, sister and brother, I owe and dedicate this success. I thank them, from the bottom of my heart, for their unconditional love, continuous support and sacrifice throughout these four years particularly, which have made me survive living abroad and away from them. They are my backbone, my source of strength and joy and I am forever grateful to have them in my life.

French summary

L'objectif de cette thèse est d'étudier la génération d'harmoniques d'ordre élevé (HHG) dans différents semi-conducteurs ainsi que dans le graphène, un matériau bidimensionnel. La génération d'harmoniques d'ordre élevé est un processus hautement non-linéaire qui a lieu lors de l'interaction entre un laser focalisé à de forts éclairements ($10^{13} - 10^{14}\,\mathrm{W/cm^2}$) et un milieu. La HHG dans les gaz, découverte à la fin des années 80s, est aujourd'hui bien connue et s'est avérée être une source efficace de rayonnement extrême ultraviolet cohérent. En 2010, la génération d'harmonique d'ordre élevé dans un cristal de ZnO (oxyde de zinc) a été observée pour la première fois. Les dynamiques électroniques ultrarapides dans le champ très intenses génère un rayonnement aux fréquences harmoniques du fondamental. Nous concentrons nos études sur les effets des propriétés de symétrie du cristal et celles du laser sur le processus de génération d'harmonique, notamment l'intensité, l'ellipticité et la polarisation du laser. Du fait de la forte absorption du rayonnement par le cristal, l'émission HHG mesurée provient uniquement d'une épaisseur restreinte sur la face arrière du cristal. Cependant, le laser accumule des effets linéaires et non linéaires pendant sa propagation dans le cristal épais. Nous surlignons l'importance de ces effets, notamment l'effet Kerr, sur les caractéristiques du rayonnement HHG.
Le processus de générations d'harmonique d'ordre élevé dans les cristaux peut être compris dans l'espace réciproque par le modèle suivant: dans une première étape, (1) la très haute intensité du champ laser permet à l'électron de passer par effet tunnel de la bande de valence à la bande de conduction où (2) il accélère dans le champ électrique, ce qui entraîne un courant, appelé courant intrabande, qui contribue à l'émission harmonique. Ensuite (3) l'électron peut se recombiner avec un trou dans la bande de valence (processus interbande), émettant des photons de haute énergie. Ces deux mécanismes sont responsables de la génération d'harmoniques. La structure des bandes électroniques du cristal, et notamment leur courbure, jouent un rôle très important dans ces processus pour déterminer l'efficacité de la HHG. Pour cela, nous choisissons d'étudier la HHG dans différents matériaux: graphène, oxyde de zinc (ZnO), silicium (Si), arséniure de gallium (GaAs) et oxyde de magnésium (MgO).
Le graphène, un semi-conducteur bidimensionnel, est caractérisé par des propriétés particulières. Intéressant pour la HHG, sa structure de bande est conique autour du gap d'énergie minimum (qui est nul pour du graphène pur) et non conique loin de ce minimum. Nous employons un laser infrarouge délivrant des impulsions de quelques nanojoules à une longueur d'onde de 2,1 μm avec une durée d'impulsion de 80 fs. Le rayonnement HHG est étudié spatialement et spectralement. Nous

détectons les ordres harmoniques 3 et 5 (H3 et H5, 700 et 420 nm respectivement) d'échantillons constitués de trois couches de graphène déposés sur quartz. Les efficacités de générations des harmoniques 3 et 5 montrent une dépendance isotrope avec la polarisation du laser. Ces résultats sont validés par des simulations théorique (TDDFT: Time Dependent Density Functional Theory) qui montrent également que la génération des harmoniques d'ordres plus élevés devient anisotrope. Cependant, deux limitations expérimentales empêchent la détection de ces ordres harmoniques d'intérêt: la première est l'endommagement très rapide (quelques secondes) de nos échantillons lors de l'interaction du laser et du graphène, même à très faible éclairement ($\sim$ 0.04 TW/cm^2), et la deuxième est la présence d'une émission de fluorescence très large bande. L'endommagement des échantillons est favorisé par l'oxydation du graphène lors de l'interaction. Par conséquent, nous présentons un dispositif afin d'isoler le graphène dans un environnement sous azote, qui nous a permis d'augmenter le temps de dommage du graphène (i.e. le temps de décroissance du signal harmonique) jusqu'à $\sim$ 3 minutes. Néanmoins, cela n'a pas entrainé de diminution significative du signal de fluorescence. Finalement, nous détectons, pour la première fois, la génération d'harmoniques d'ordres 3 et 5 dans un échantillon de graphène non déposé sur un substrat.

Une grande partie de ce travail de thèse est consacré à l'étude de la HHG dans différents cristaux afin d'étudier leurs dépendances en fonction des propriétés structurelles et optiques (linéaires et non linéaires) du cristal. Les harmoniques H3 (700 nm), H5 (420 nm) et H7 (300 nm) du rayonnement laser à 2,1 μm, générées par un cristal de ZnO (0001) montrent une dépendance isotrope avec la polarisation du laser, alors que celles générées dans du silicium (Si (100)) montrent une dépendance anisotrope, en particulier une symétrie quadruple, ce qui reflète la structure cubique du silicium. En comparant les efficacités de génération d'harmonique dans des cristaux de silicium de différentes épaisseurs (2 et 300 μm), nous observons que le rayonnement émis est plus intense dans le cristal le plus épais. La caractérisation spatiale du mode des harmoniques dans le champ proche démontre la présence d'un effet d'autofocalisation du faisceau laser incident. Ces effets de propagation ont des conséquences plus délétères lors de l'utilisation de lasers de plus haute énergie. Avec un laser OPCPA (1,55 μm et 3,1 μm) de nos collaborateurs de l'IOGS (Palaiseau), nous mesurons une diminution du signal harmonique dans le cristal plus épais. Ce comportement est attribué aux effets non linéaires, notamment à l'absorption non linéaire à ces longueurs d'ondes: 2PA (absorption de deux photons) à 1,55 μm, et 3PA (absorption de trois photons) à 3,1 μm. De la même façon, nous étudions l'effet d'autofocalisation dans des cristaux de GaAs. L'autofocalisation du faisceau laser incident est plus importante quand la polarisation du laser est alignée avec l'axe ΓK du cristal, contrairement à la direction ΓX. Ces effets non linéaires ont été observés également dans un cristal de MgO, à la fois dans les domaines spatial et temporel. Pour la caractérisation temporelle, nous utilisons un FROG (Frequency Resolved Optical Gating) fait maison afin de caractériser les impulsions du laser en sortie du cristal générateur. Un effet d'auto-compression temporel des impulsions laser dans le cristal de génération a été observé, avec une diminution de 40 fs à $\sim$ 20 fs.

La spectroscopie de polarisation du rayonnement harmonique dans un cristal de

GaAs (100) est ensuite étudiée en fonction de l'éclairement du laser. Les ordres 3, 5 et 7 du laser de 2,1 μm de longueur d'onde dévoilent une dépendance anisotrope avec la polarisation, et plus particulièrement une dépendance quadruple. En effet, GaAs présente une structure atomique de type zinc-blende. De façon surprenante, la dépendance de l'efficacité de génération de H3 et H5 avec la polarisation changent lorsque l'éclairement augmente, contrairement à la dépendance de H7. Ces résultats sont validés par une étude similaire effectuée avec une géométrie en réflexion avec le laser OPCPA du LIDYL (2,4 μm). En effet, cette géométrie permet d'écarter les effets non linéaires précédemment mentionnés. En plus, les simulations théoriques TDDFT montrent des résultats similaires, ce qui confirme que ces changements de dépendances de polarisation proviennent du processus fondamental de la HHG dans GaAs, dans lequel les électrons explorent des parties différentes de la structure de bande du cristal en fonction de leur énergie et de l'éclairement. La spectroscopie de polarisation de la HHG dans les cristaux offre donc une technique fondamentale pour explorer la structure de bandes électroniques des matériaux.

Pour de nombreuses applications, il est intéressant d'étendre la génération d'harmonique vers des ordres plus élevés, c'est-à-dire dans le domaine de l'extrême ultraviolet (EUV). Pour cela, nous étudions ensuite la HHG dans un cristal de MgO avec un setup de génération sous-vide, ce qui permet la détection dans l'EUV. En comparant la génération d'harmoniques dans le visible aux comportements dans l'EUV, nous trouvons que les harmoniques de plus courtes longueurs d'onde dépendent fortement de la polarisation du laser. Suivant l'orientation relative du cristal et de la direction de polarisation, il est même possible d'éteindre l'émission harmonique. Nous profitons de cette dépendance pour proposer une nouvelle méthode de génération d'impulsions attoseconde isolées; technique que nous appelons une porte d'anisotropie ("Anisotropy Gating" en anglais). La technique repose sur une mise en forme du laser de telle sorte que la polarisation quasi-linéaire du champ électrique tourne pendant la durée de l'impulsion. Il est alors possible d'aligner la polarisation d'un unique demi-cycle optique avec l'axe du cristal pour lequel la génération est plus efficace. Nous présentons dans cette thèse des résultats préliminaires de cette méthode montrant notamment un élargissement des harmoniques mesurées par rapport à celles obtenues avec une impulsion non mises en forme.

Un des grands avantages de la HHG dans les cristaux par rapport aux gaz est la capacité de structurer facilement le milieu de génération pour manipuler le champ électromagnétique incident ou le rayonnement harmonique. Par exemple, on peut structurer le cristal pour confiner spatialement le champ électromagnétique du laser. Ce confinement entraine une exaltation locale du champ qui résulte en un accroissement de l'efficacité de la génération d'harmonique. Dans ce travail, nous avons créé sur la face arrière d'un cristal de ZnO des cônes tronqués (4 μm de diamètre à la base, 2 μm de diamètre au sommet, 6 μm de hauteur) par la technique FIB (Focused Ion Beam). En employant un laser délivrant des impulsions nanojoules ($\sim$ 9 nJ par impulsion, 20 MHz), nous trouvons que le signal des ordres élevés (dont les énergies de photon sont supérieures à l'énergie de la bande interdite) générés par ces microcônes sont plus intenses de deux ordres de grandeur par rapport à ceux issus du ZnO non structuré. Le flux de photons est alors suffisamment important pour permettre

les premières applications, ce qui en fait une source de rayonnement cohérent ultrabref ultracompacte. Nous l'utilisons pour une première démonstration à l'imagerie sans lentille (CDI - Imagerie Diffractive Cohérente). Nous utilisons l'harmonique d'ordre 5 (420 nm) généré par un cône de ZnO pour faire l'image d'un échantillon micrométrique. Dans une seconde partie, nous façonnons les propriétés spatiales des faisceaux harmoniques pour induire un moment angulaire orbital (OAM - Orbital Angular Momentum) de deux façons différentes. La première consiste à manipuler le cristal de génération lui-même. Pour cela, nous gravons des objets de phase en spirale, à savoir des zones de Fresnel en spirales binaires et non binaires, sur la surface de sortie du cristal. Les harmoniques générées sont diffractées par ces objets de phase, qui combinent la focalisation du faisceau d'harmonique et en même temps introduisent un mode OAM. La caractérisation spatiale du mode du rayonnement harmonique au niveau du foyer de la zone de Fresnel montre une distribution d'intensité annulaire, due à la présence d'un OAM non nulle, mesuré en outre par interférométrie. Dans la deuxième façon, nous introduisons un ordre OAM l_f sur le laser de génération, et nous prouvons la conservation du moment angulaire lors de la HHG dans les cristaux, avec un OAM des harmoniques $l_q = q \times l_f$.
Les résultats obtenus dans cette thèse valident la génération d'harmoniques d'ordre élevé dans des cristaux, non seulement comme une source compacte et efficace de rayonnements EUV, mais aussi comme une technique intrinsèque de spectroscopie nouvelle pour étudier les propriétés structurelles et optiques du milieu de génération.

Chapter 1

Introduction

In recent days, research is accelerating towards understanding the fundamentals of ultrafast proccesses, hence the growing need for coherent ultrashort radiation both in space and time domains. By ultrashort is meant going down to the EUV/X-ray wavelength range and to the attosecond timescale, which are the scales required to resolve and probe an atom or even an electron in motion (figure 1.1). Such coherent sources have been provided by the huge facilities that are synchrotrons since decades, and free-electron lasers (FELs) more recently. Lately, an outstanding achievement of X-ray radiation provided by the FELs is the record of X-ray molecular movies which provides an access to study the electron motion with sub-angstrom resolution and track its dynamics at the femtosecond timescale [1, 2]. Other achievements of vacuum UV radiation include TR-ARPES Time Resolved and Angle Resolved Photoelectron Spectroscopy to map the band structure of materials over their first Brillouin zone [3]. In biology, X-rays from synchrotrons and free-electron lasers have found vast applications particularly in imaging biological specimens through the Coherent X-ray Diffraction Imaging technique (CXDI) [4]. CXDI is a *lensless* micropscopy technique that relies on illuminating micrometer and nanometer sized samples with coherent X-ray light, collecting their diffraction pattern and then reconstructing their image by an algorithm. This technique, based on synchrotron and FEL X-rays, has been implemented to image bacteria [5], viruses [6, 7, 8, 9], human cells [10, 11], chromosomes [12] and many other biological species with resolutions ranging between 30 nm [5] to 6 Å [8]. However, only few synchrotrons and FEL facilities are available worldwide and researchers can have limited access due to the huge user demands and the nontrivial access procedures. Another alternative source of coherent XUV radiation, yet much more compact, is High Harmonic Generation (HHG) in gases that has paved its way as a tabletop coherent attosecond light source in the x-ray spectral region since more than 30 years. HHG in gases is a highly nonlinear phenomenon resulting from the interaction of intense laser pulses with a gas. It was first observed in 1987 and 1988 from intense ultraviolet and near-infrared (1.064 μm) laser beams, respectively [13, 14]. With the advances in laser technology and the recent developments in near and mid-infrared laser systems generation down to the water window (couple of nanometers in wavelength) has been demostrated [15]. A remarkable and exciting recent achievement is the observation of High Harmonic Generation in crystals. It was first observed in 2010, in the group of Prof. David Reis at the PULSE Institute and SLAC laboratory

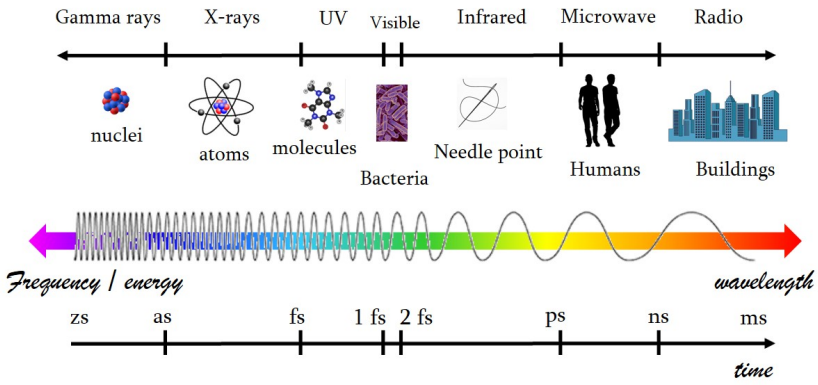

Figure 1.1: The characteristics of the electromagnetic spectrum in the time, frequency and wavelength ranges.

in Stanford. Harmonics up to 9.5 eV in photon energy were generated by focusing a mid-IR laser onto a zinc oxide crystal [16]. While 10^{14} W/cm^2 are the typical intensities required for HHG in gases, HHG in crystals was achieved by much lower laser intensities $\sim 10^{11} - 10^{12}$ W/cm^2. This suggests employing lasers of moderate field amplitudes and thus avoiding big and expensive amplifiers to reach the strong field regime, consequently developing HHG beamlines more compact and easier to handle than the current ones, which are based on gas phase HHG. Since then extensive research has been carried out to understand the underlying fundamental physical mechanism driving HHG in solids, mainly in semiconductors. HHG in crystals has been investigated in a number of semiconductor crystals, including wide, narrow and indirect band gap materials, 2D materials, such as graphene and molybdenum disulfide, ferromagnetic and topological materials [17, 18, 19]. Interestingly, the generation efficiency exhibits strong dependence on the laser parameters, such as the polarization and intensity, as well as on the structural and optical properties of the generation medium. The harmonic efficiency is anisotropic with respect to the angle between the laser polarization and the crystal axis. For instance, for semiconductors with a cubic crystal stucture such as magnesium oxide, the harmonic yield is maximum when the polarization is aligned along one of the main crystal axis and by every 90° rotation of the crystal [20]. Besides, the solid-state nature of the generation medium offers additional degrees of freedom to tailor the crystal at the source of the emission in order to meet certain requirements. For example, Sivis et al. [21] and Franz et al. [22] have patterned nanostructured cones to confine and enhance the driving optical electric field of relatively low amplitudes, consequently increasing the high order harmonic yields. Plasmonic effects, particularly surface plasmon-polaritons, have also been used to enhance the driving laser field and the harmonic yield [23, 24]. In the near future, HHG in crystals has the potential to become a novel semiconductor-based attosecond source, and could lead to the developement of compact, integrated and electrically gatable optoelectronic devices operating at petahertz frequencies.

Thesis outline

The goal of this thesis is to investigate high harmonic generation (HHG) in different semiconductor crystals with special emphasis on microscopic and macroscopic effects upon laser-crystal interaction. The thesis reports on the fundamental aspects of solid-state HHG which are related to the generation medium of choice, its optical and structural properties, and the chosen laser parameters such as the wavelength, intensity and polarization state. The dependence of the generation efficiency on the laser polarization is investigated and employed as a spectroscopy technique to map the band structure of the generation medium, and as an optically gatable technique for the generation of XUV-attosecond radiation.

The manuscript is organized in the following manner: After a general introduction and a motivation behind High Harmonic Generation in crystals, Chapter 2 presents theoretical basics and explanation of the HHG mechanism in crystals by drawing a comparison to HHG in gases. It also highlights the critical role of nonlinear propagation effects on the fundamental laser and as a result on the generated harmonics. Moreover, an overview of the recent research and findings in HHG in crystals are summarized.
The studies and results of the thesis are reported in three main parts:

- Chapter 3 reports on HHG in graphene, an unconventional 2D material that possesses extraordinary properties. Although some experimental limitations, related to the generation of incoherent fluorescence and the fast permanent damage of the sample, couldn't be avoided, visible harmonics are generated from graphene, and their dependences on the laser intensity and polarization are studied [25]. In addition, the generation of visible harmonics from freestanding graphene is reported for the first time.

- Chapter 4 represents the main part of this thesis. Different semiconductors, including zinc oxide (ZnO), silicon (Si), gallium arsenide (GaAs) and magnesium oxide (MgO), are studied as the generation media. The correlation between the characteristics of each crystal and the driving laser parameters is studied. Since the laser propagates in the medium before generation, nonlinear propagation effects play a significant role and should be carefully treated. On the one hand, nonlinear propagation effects can affect the pure HHG microscopic response, but on the other hand one can make use of the nonlinear effects to control the laser properties spatially and temporally. Finally, a new polarization-based gating approach, the *Anisotropy Gating* technique, is introduced, in which a rotating linear polarization within the pulse is combined with the anisotropic dependence of vacuum harmonics generated in MgO to generate isolated attosecond pulses.

- Chapter 5 explores one of the great advantages of HHG in crystals, particularly, the possibility to shape the generation medium to enhance the electric field and spatially manipulate the harmonics. First, single ZnO nanostructured cones are patterned on the exit surface of the crystal, and the enhancement of the high harmonic generation efficiency in these nanostructures as

compared to the bulk is investigated [22]. Second, orbital angular momentum is introduced into the harmonic beams in two ways; by patterning spiral zone plates (SZPs) which create focused harmonic beams carrying orbital angular momentum, and by transfering the OAM from the fundamental laser to the harmonics [26]. Finally, a first demonstration of the CDI technique, *Coherent Diffraction Imaging* technique, based on solid-state generated coherent harmonics permits the imaging of a micrometer sized structure.

Lastly, Chapter 6 summarizes an overall conclusion of the results achieved, with future perspectives for which the work of this thesis sets a basis.

Chapter 2

High Harmonic Generation in Crystals: Theory and Overview

In this chapter, high harmonic generation (HHG) in gases is firstly introduced in section 2.1 as a basis to explain HHG process in solids in section 2.2. The characteristics of both HHG mechanisms are emphasized in each section. In section 2.3, two different experimental geometries of HHG in solids are described. A major effect presented by one of these geometries is pointed out in section 2.4. Finally, in section 2.5, an overview of the various studies of HHG in solids, since it's first observation in 2010, is summarized. The research reported in this section tackles different studies which assist in the fundamental physical undertanding of the HHG process in solids.

2.1 High Harmonic Generation (HHG) in Atomic Gases

2.1.1 Brief Theory

HHG in gases has been well studied over the past 30 years and the process is thoroughly understood. It can mostly be described by a semi-classical picture, well-known as the three step model [27]. The model states that upon the interaction of an intense laser field ($\geq 10^{14}\,\mathrm{TW/cm^2}$) with a gas atom, usually a noble gas, close to the maximum of the peak pulse the atomic potential is deformed in a way that permits the electron to (1) tunnel to the continuum. It then (2) accelerates within the laser field in the continuum. Finally, when the laser field reverses direction the electron accelerates backwards and returns to the vicinity of it's parent ion, where it can (3) recombine to the core, releasing its gained energy by the emission of a burst of light i.e. a broadband XUV radiation. This is illustrated in figure 2.1. This process is repeated every half cycle of the laser pulse. Due to the coherence of the HHG process, the successive bursts of XUV radiation interfere which results in a train of attosecond pulses in the time domain and a frequency-comb spectrum in the spectral domain which is the HHG spectrum.

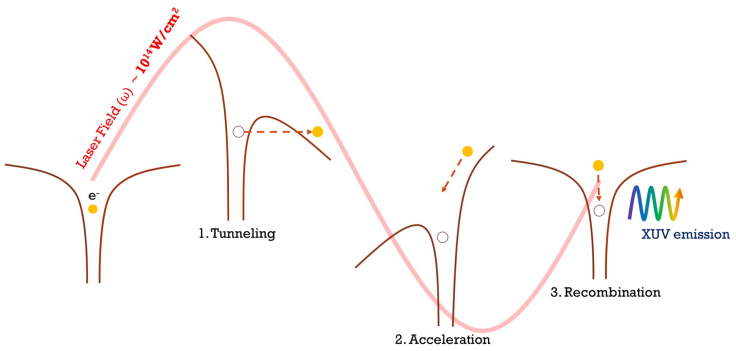

Figure 2.1: The three step model of HHG in atomic gas.

2.1.2 Atomic HHG in the Strong-Field Regime

Perturbative Regime

In general, when a weak electric field interacts with a medium, regardless of whether it is a gas, liquid or solid, it induces a polarization $\overrightarrow{P}$ in the medium, such that:

$$\overrightarrow{P} = \epsilon_0 \sum_n \overleftrightarrow{\chi}^{(n)} \overrightarrow{E}^n \tag{2.1}$$

where the tensor $\overleftrightarrow{\chi}^{(1)}$ is the linear electric susceptibility of the medium, and for $n \geq 2$, $\overleftrightarrow{\chi}^{(n)}$ is the nonlinear electric susceptibility of order n. For an isotropic medium such as atomic gas, the susceptibility is scalar. However, in other materials such as crystals, the response of the medium to the electric field may not be identical along all directions. Such materials are known to be anisotropic, and their three-dimensional nonlinear response is quantified in the tensorial elements of the nonlinear susceptibility $\overleftrightarrow{\chi}^{(n)}$. The polarization (equation 2.1) is a result of the perturbative response of the medium to the electric field, which gives rise to the emission of harmonics by a multiphoton process. For instance, the n^{th} harmonic order is emitted when an electron absorbs n photons of frequency ω, gets promoted to a virtual excited state, and by recombining back it emits a photon at a frequency $n\omega$. In this case, the intensity of the n^{th} harmonic, S_n, scales perturbatively with the driving laser intensity I:

$$S_n \propto I^n \tag{2.2}$$

Strong-Field Nonperturbative Regime

High harmonic generation is a highly nonlinear nonperturbative process that usually starts by the tunneling of the electron wavepacket. Tunnel ionization takes place when a highly intense electric field interacts with an atom or a solid. The strong laser field can distort the potential and increase the electron's probability to tunnel through the barrier. To mathematically determine the strong-field nonperturbative

regime, Leonid Keldysh introduced in 1965 the so-called Keldysh parameter γ [28]. In case of gas atoms, the Keldysh parameter γ is given by:

$$\gamma = \frac{\omega\sqrt{2mI_p}}{eE_0} \tag{2.3}$$

where ω and E_0 are the angular frequency and the amplitude of the laser field, respectively, I_p is the ionization potential of the atom, m and e are the electronic mass and charge, respectively. Tunnel ionization occurs when $\gamma < 1$. Therefore high electric field amplitudes or intensities are required to reach this regime. In this case, the n^{th} harmonic yield, S_n, scales as:

$$S_n \propto I^q \tag{2.4}$$

where q is an arbitrary power. Experimentally, q can be extracted by measuring the harmonic yield versus laser intensity and hence verifying the regime in which each harmonic is generated.

2.1.3 Characteristics of HHG in Atomic Gases

Phase matching

Phase matching is a very important requirement of HHG in gas atoms. The up-conversion from the fundamental field to the harmonics is achieved because the generated bursts of XUV radiation travel *in phase* with respect to each other and with respect to the fundamental electric field, i.e. they travel at the same phase velocity. This leads to a coherent build up of the harmonic radiation. In gases, phase matching is achieved by a compromise between the gas pressure, laser intensity and laser focus position. To achieve the proper phase matching conditions in a strong focusing geometry, the laser focus is placed well before the gas-jet. For an optimized coherence of high order harmonics, P. Salières et al. [29] had their focus placed at $\sim 3\,\text{mm}$ before the generating medium. Later, it was demonstrated by Hergott et al. [30] and P. Rudawski et al. [31] that a loose focusing geometry (2.5 m - 5 m focal length) is also recommended to achieve phase-matched harmonics and to enhance the harmonic efficiency. For longer wavelength drivers, higher gas pressure is needed to meet the phase-matching requirement [32].

Conversion Efficiency

The conversion efficiency of the generated harmonics is defined as the ratio of the harmonic yield to the laser intensity. The conversion efficiency depends on the laser parameters and the generating medium properties, including the laser wavelength, electric field amplitude and atom's ionization potential [33]. It is optimized by an interplay between the gas pressure, gas medium length and the laser focus position [30]. The conversion efficiency of the generation process from gas atoms is low. For instance, from Ti:sapphire laser pulses (800 nm in wavelength), neon gas records a conversion efficiency 5×10^{-7} at the 59^{th} harmonic [34], while the conversion efficiencies achieved in argon and xenon gas are $1.5 - 5 \times 10^{-5}$ [35, 31] and 4×10^{-5} [36, 30], respectively.

Odd and even harmonics

Due to the symmetry of the HHG process which occurs every half cycle of the laser field, only odd harmonics are generated. In order to generate even harmonics the symmetry of the process has to be broken. This can be achieved by two-color mixing experiments [37, 38, 39]. By simultaneously ionizing helium atoms with the fundamental driving field ω and its second harmonic wave 2ω, I. J. Kim et al. [38] generated even harmonics from helium, with a high conversion efficiency of the 38^{th} harmonic (21.6 nm) $\sim 5 \times 10^{-5}$.

Cutoff

A typical high harmonic generation spectrum consists of perturbative low order harmonics whose signal decreases as the harmonic order increases, followed by a plateau with constant signal over several frequencies. The last or highest harmonic order of the plateau is defined as the cutoff (figure 2.2). The cutoff energy is

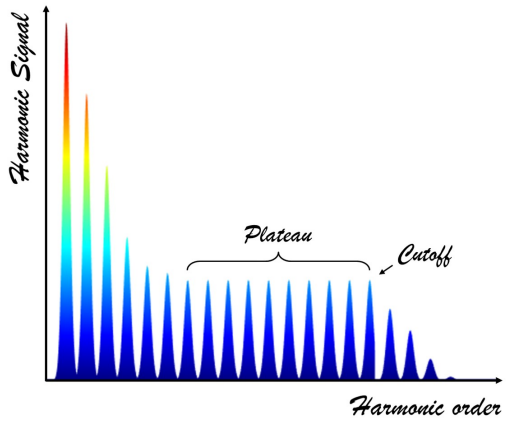

Figure 2.2: A typical harmonic spectrum, showing low order harmonics, the plateau and the cutoff harmonic.

calculated by the following equation [15]:

$$E_{cutoff} = I_p + 3.17U_p \tag{2.5}$$

where I_p is the atom's ionization potential, U_p is the ponderomotive energy which is the energy required to free an electron from its bound state and quiver the system. It is directly proportional to the square of the laser electric field amplitude E_0, by $U_p = \frac{e^2 E_0^2}{4m\omega^2}$. In the case of atomic gas HHG, the cutoff scales linearly with the square of the laser field and wavelength.

Polarization and ellipticity dependence

Atomic gas being isotropic, high harmonic generation efficiency exhibits no dependence on the direction of the linear polarization of the driving field. However, there's

a strong dependence on the laser ellipticity. The efficiency of low order harmonics decreases slowly as the ellipticity of the driving field increases, but for high order harmonics the decrease in the harmonic efficiency is steeper [40, 41]. At a relatively low ellipticity (the exact value depends on the gas and the harmonic order), the HHG is even turned off. This is because during the acceleration step, an electron in the elliptically polarized laser field is not driven back towards its parent ion. This prevents the recombination step, and hence no emission takes place.

2.2 High Harmonic Generation in Crystals

2.2.1 Introduction

High harmonic generation in solids occurs when an intense laser in the middle or near infrared range interacts with a solid crystal. An analogy to HHG in gases, specifically the three step model, can be drawn here to explain the process. Due to the high intensity of the laser field, the electron initially in the ground state in the valence band (1) tunnels to the conduction band. (2) It then oscillates and accelerates with the laser field in the conduction band, undergoing what is known as intraband oscillations which give rise to an intraband current $\vec{j}(t)$. Finally, at a certain moment within the laser pulse the electron can (3) recombine with a hole in the valence band; this transition is referred to as interband transition causing an interband polarization. This three step description is illustrated in figure 2.3.

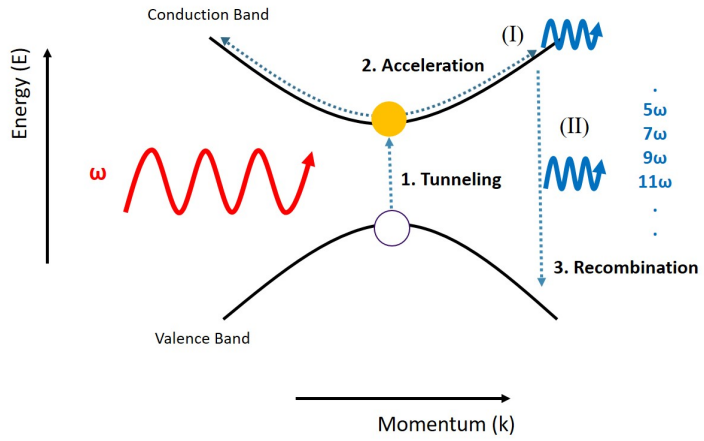

Figure 2.3: Three step description of HHG in solids in momentum space.

Hence there are two main mechanisms contributing to high harmonic generation in solids namely:

- ***Intraband Dynamics*** (I): which correspond to the oscillations and acceleration of the electron with the laser field in the conduction band. As a result a current is generated referred to as intraband current. The frequency at which

these oscillations take place is known as the Bloch frequency. It is given by:

$$\omega_B = \frac{eE_0 a}{\hbar} \tag{2.6}$$

where a is the lattice constant, e is the elementary charge and E_0 is the electric field strength.

- ***Interband Dynamics*** (II): At certain moment within the laser pulse the electron can recombine with a hole in the valence band at a sub-optical cycle timing. This transition is accompanied by high harmonic emission.

Although the band gap (E_g) of semiconductors is the region of forbidden electronic states, harmonics whose energies are lower than E_g can be generated and are referred to as below band gap harmonics. Below band gap harmonics are generated by multiphoton absorption, when an electron is excited to a virtual state within the band gap by absorbing n photons such that the harmonic energy $n\hbar\omega < E_g$. In addition, they scale perturbatively with the laser field. On the other hand, above band gap harmonics are generated by either intraband or interband dynamics or by both, and scale nonperturbatively. The contribution of both dynamics to the HHG emission is still under debate and further investigation in the solid-state HHG community. It is noteworthy to mention an important difference between both mechanisms; intraband emission results in a chirp-free harmonic radiation, while interband emission emerges with a natural chirp that is dependent on the laser properties [42, 17], the latter having a similar characteristic as attosecond pulses generated from gas atoms. This is because intraband current is only dependent on the band structure curvatures and, in the time domain, it is generated at any time within the laser pulse, while interband emissions take place at different times within half a cycle of the laser pulse [42].

2.2.2 Theoretical Description

2.2.2.1 The Strong-Field Regime in Solids

In solid HHG, the perturbative and nonperturbative regimes of laser-matter interaction are also determined by the the corresponding Keldysh parameter γ. For a laser field, of an amplitude E_0 and angular frequency ω, interacting with a crystal of band gap E_g, the Keldysh parameter is calculated as:

$$\gamma = \frac{\omega\sqrt{m^* E_g}}{eE_0} \tag{2.7}$$

where m^* is the effective mass of the electron. Similar to gas HHG, the strong-field nonperturbative regime is achieved when $\gamma < 1$ [43]. In the intraband picture, Ghimire et al. [43] introduced a new parameter that determines the Bloch oscillation limits during half a cycle of the laser field. It is called β, and defined as the ratio of the Bloch frequency to twice the driving laser frequency:

$$\beta = \frac{\omega_B}{2\omega} \tag{2.8}$$

In the case, when $\beta > 1$ full Bloch oscillations take place, which means that the electron is expected to traverse the entire Brillouin zone within half a cycle of the laser field. For lower electric field strengths, i.e. when $\beta < 1$, the electron explores partially the Brillouin zone.

2.2.2.2 The Acceleration Theorem

When an intense laser described by an electric field $\overrightarrow{E}(t)$ is focused onto the sample, the electron initially in the valence band, tunnels to the conduction band and is therefore subject to a Lorentz force $\overrightarrow{F}(t) = e\overrightarrow{E}(t)$. The acceleration theorem (i.e. Newton's second law of motion) states that the electron accelerates in the condution band and its equation of motion reads the following:

$$\frac{d\overrightarrow{k}}{dt} = e\overrightarrow{E}(t) \tag{2.9}$$

where $k(t)$ is the electron's momentum at time t. By integrating both sides of equation 2.9 from time t_0, the birth time of the electron wavepacket from it's ground state, until a certain time $t > t_0$ we obtain the following:

$$k(t) - k(t_0) = e\int_{t_0}^{t} \mathrm{E(t')}\,\mathrm{d}t' \tag{2.10}$$

Considering an electric field defined by $\overrightarrow{E}(t) = E_0\cos(\omega t)$, equation 2.10 can then be written as:

$$k(t) - k(t_0) = \frac{eE_0}{\omega}\sin(\omega t) \tag{2.11}$$

Tunnel ionization, the first step in the HHG process, occurs mainly at the minimum band gap, i.e. at the Γ point where the electron's momentum is zero in most semiconductors, hence $k(t_0)$=0. Therefore from equation 2.11, the evolution of the electron wavepacket at any time t can be expressed as:

$$k(t) = \frac{eE_0}{\omega}\sin(\omega t) \tag{2.12}$$

This means that the maximum momentum the electron can aquire is given by:

$$k_{max} = \frac{eE_0}{\omega} \tag{2.13}$$

Equation 2.13 can be rewritten as a wavenumber ($\Rightarrow k_{max} = \frac{eE_0}{\omega\hbar}$) and in units of $\frac{\pi}{a}$, to express the maximum excursion of the electron in the conduction band in the first Brillouin zone. For example, let's consider a driving laser field of wavelength $\lambda = 2.1\ \mu$m which corresponds to an angular frequency $\omega = \frac{2\pi c}{\lambda}$. The interaction of this electric field of an amplitude $E_0 = 1.4\,V/\mathring{A}$ with a semiconductor crystal, results in a maximum momentum (equation 2.13) acquired by the electron $k_{max} = 0.37\pi/a$. This means that the electron wavepacket can explore 37% of the Brillouin zone.

2.2.2.3 Intraband Current and Interband Polarization

The acceleration theorem discussed in section 2.2.2.2 is a good estimate to derive the trajectories of the electron wavepacket in the Brillouin zone, and therefore realize how far it explores the conduction band and the possible regions of recombinations [44]. However, for a realistic description of the HHG mechanism, intraband and interband processes have to be addressed. The acceleration of the electron in the conduction band generates a current, the intraband current, which we denote by $\overrightarrow{j}_{\text{intra}}(\text{t})$. It is expressed as the integral of the group velocity over all possible states:

$$\overrightarrow{j}_{intra}(t) = \int_k n_k v_k \, \mathrm{d}^3k \tag{2.14}$$

where k is the momentum in reciprocal space, n_k is the electron density, and v_k is the group velocity. In solids, the group velocity, the velocity at which the electron wavpacket travels in the Brillouin zone, corresponds to the slope of the bands in the band structure at a particular momentum k and it is given by:

$$v_k = \frac{1}{\hbar}\frac{\partial \epsilon(k)}{\partial k} \tag{2.15}$$

The electron can recombine at a certain moment within the laser pulse, with the hole in the valence band. This transition induces an interband polarization $\overrightarrow{P}(t)$ [45]. As a result a current is generated which we denote by $\overrightarrow{j}_{inter}(t)$. It is calculated as:

$$\overrightarrow{j}_{inter}(t) = \frac{\mathrm{d}}{\mathrm{d}t}\int_k \overrightarrow{P}(k,t) \, \mathrm{d}^3k \tag{2.16}$$

Therefore, the total current generated during the process is the sum of the intraband current and the interband polarization $\overrightarrow{j}_{total}(t) = \overrightarrow{j}_{intra}(t) + \overrightarrow{j}_{inter}(t)$. The HHG spectrum can be obtained by the Fourier transform of the total current $\overrightarrow{j}_{total}(t)$ to the spectral domain:

$$HHG(\omega) = |\mathcal{FT}(\overrightarrow{j}_{total}(t))|^2 \tag{2.17}$$

2.2.3 Characteristics of HHG in Crystals

We highlight here the characteristics of solid HHG, emphasizing its advantagous aspects as compared to atomic HHG, and pointing it's major limitations.

Conversion efficiency: Below and above band gap harmonics

The higher density of atoms in a solid permits a higher conversion efficiency from the generating laser as compared to the atomic gas case. Ghimire et al. [46] derived theoretically the conversion efficiency of high order harmonics generated from solids including propagation effects. The conversion efficiency scales as the square of the carrier density and with the square of the wavelength. For a modest carrier density $\mathrm{N} = 10^{19}\,\mathrm{cm}^{-3}$, the calculated conversion efficiency in a 500 μm thick ZnO crystal ionized by a 3.25 μm, showed a decrease with the increase of the harmonic order,

where the efficiency reaches 10^{-15} for the 25^{th} harmonic (figure 2.4 (a)). In solid-state HHG, two main limitations hinders higher conversion efficiencies. On the one hand, below band gap harmonics which originate from each atomic site in the crystal, propagate towards the exit surface, however their efficiency is limited by the phase mismatch between the harmonic wave and the fundamental field. This is pictured in figure2.4 (b) reported by Ghimire et al. [46], which shows strong modulations in the conversion efficiencies of below band gap harmonics (H5 and H7) along the crystal thickness. The efficiency is highest when the harmonic emissions are phase-matched. In addition, it is reported that the rapid phase mismatch takes place on a scale of the coherence length of the harmonic. On the other hand, above band gap harmonics are limited by their re-absorption by the crystal itself. Despite the fact that above band gap harmonics can be generated everywhere in the crystal, the signal detected arises from only a thin layer at the output surface of the crystal, about one absorption length thick (in the order of few tens of nanometers).

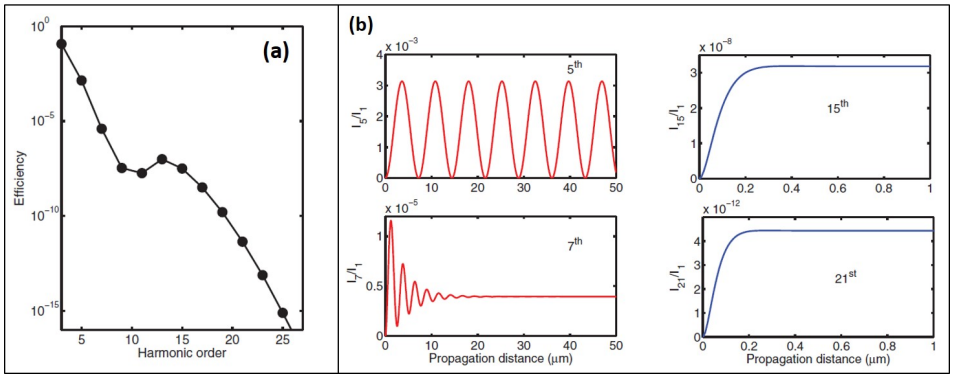

Figure 2.4: Calculated conversion efficiencies of high order harmonics of the 3.25 μm driving laser beam, generated from a 500 μm thick ZnO crystal, assuming a modest carrier density N = 10^{19} cm^{-3} [46].

Odd and even harmonics

In the case of HHG from solids, odd harmonics are generated not only because of the symmetry of the generation process, but the symmetry of the crystal also plays a role. Only odd harmonics are generated in centrosymmetric crystals i.e. crystals with an inversion symmetry such as silicon (Si). Even harmonics emerge as a result of broken inversion symmetry which is the case of noncentrosymmetric crystals like gallium arsenide (GaAs) [47] and quartz [48], or due to surface and interface effects [49].

Polarization and ellipticity dependence

A very interesting property of HHG in solids is the dependence of the generation efficiency on the linear polarization of the driving field, unlike HHG in atomic gases. The laser polarization drives the electron dynamics after tunneling to the conduction band. This can be viewed in the real-space or momentum space picture. The

direction in which the electron wavepacket travels is determined by the polarization of the laser field, and its maximum excursion along this direction is determined by the amplitude of the field. Therefore, in the momentum space picture the electron wavepacket is strongly influenced by the bands of the band structure which determines its group velocity. The harmonic generation efficiency can be controlled and optimized by rotating the crystal in the plane of the polarization of the field. Such orientation dependences can reveal information about the crystal structure, reflect the symmetry of the Brillouin Zone [44], and consequently give insight into the generation process. The polarization dependence of each harmonic can be different, in particular, high order harmonics emitted in the XUV, are expected to show stronger dependence on the laser polarization than low order harmonics [20]. Some studies regarding this aspect will be presented in section 2.5. Odd harmonics emerge with a polarization parallel to the polarization of the driving laser field, while even harmonics have been observed with a polarization state perpendicular to that of the driver [48, 18]. While in gas atoms no harmonics are generated from a circularly polarized field, in solids, high harmonics from an elliptically or circularly polarized field can be generated with a lower efficiency as compared to a linearly polarized field [20].

Cutoff and Wavelength Dependence

A typical harmonic spectrum of HHG from solids is similar to the one of HHG from gases, except that multiple plateaus are expected due to the complex band structure of crystals. The HHG spectrum, as shown on the right of figure 2.5, is composed of perturbative low order harmonics whose signal decrease as the harmonic order increases, followed by two plateaus, the first at a higher signal than the second, each one extending up to a cutoff harmonic energy. In the interband picture, the first cutoff is defined as the maximum band gap between the valence band and the first conduction band (CB1). When the laser field is strong enough to drive the electron to the edge of the Brillouin zone, the electron can tunnel to the second conduction band (CB2), as shown on the left of figure 2.5. The HHG process involving the second conduction band gives rise to a second plateau that extends to a second cutoff, which is the maximum band gap energy between the valence band and the second conduction band [50]. In solid HHG, the cutoff of intraband or interband mechanisms scales linearly with the laser field strength [16, 51, 52]; as the electric field increases, the harmonic efficiency and the cutoff increase. In the intraband picture, numerical calculations have confirmed that the intraband cutoff scales linearly with the laser wavelength [42, 50], while other calculations have shown that the intraband cutoff is independent of the laser wavelength and only the interband cutoff scales linearly with the laser wavelength [53, 51]. According to X. Liu et al. [51], from an interband picture, intraband mechanims dominate for harmonics generated below the band gap, but interband mechanisms dominate in the plateau and cutoff region. In terms of the generation efficiency, as the wavelength increases, the interband yield decreases exponentially while the intraband yield exhibits a more complex dependence, and increases for long wavelengths [54]. Measurements of the HHG yields from ZnO, in the wavelength range 2-4 μm by Z. Wang et al.

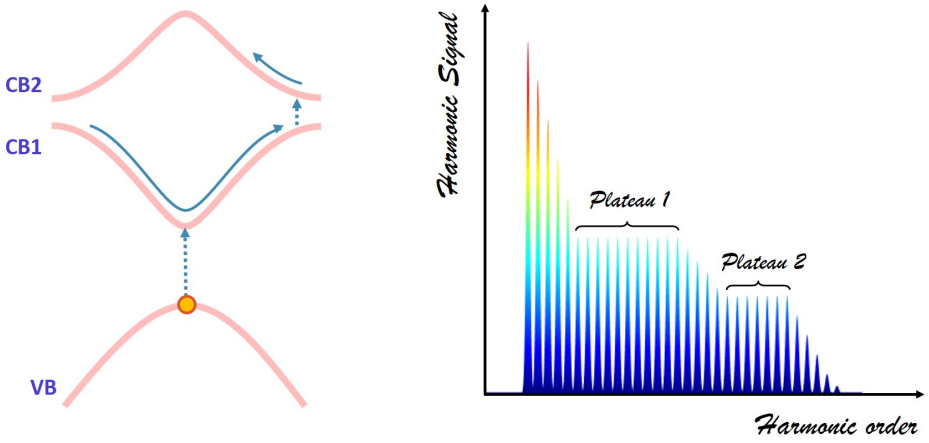

Figure 2.5: Left: Schematic representation of the band structure of a crystal, including a valence band (VB) and two conduction bands (CB1 and CB2). Right: High harmonic generation (HHG) spectrum extending to double plateaus. Note that the dotted arrows represent tunneling of the electron, while the solid arrows represent the oscillations of the electron in the conduction bands.

[55], showed that the dominant interband HHG efficiency decreases and scales as $\lambda^{-11.4\pm2.9}$, faster than the intraband yield and stronger than the case of gas atoms ($\lambda^{-(5-6)}$) [56, 57]. X. Liu et al. [51] and G. Vampa et al. [45] have proposed to use the dependence of the cutoff on the laser wavelength to experimentally differentiate the intraband and interband mechanisms.

Damage Threshold

A major limitation in HHG in solids is the damage of the generation medium at very high laser intensities. Each crystal possesses a damage threshold beyond which the laser intensity ablates matter around its focus position and causes local permanent damage. Therefore experimentally we are limited to a maximum value of the laser intensity. Usually, wide band gap materials like MgO [20] and sapphire [58] can tolerate higher laser intensities than narrow band gap semiconductors such as ZnSe [59] and graphene [60]. It is also recommended to employ long wavelength drivers for narrow band gap semiconductors, to avoid, most importantly, nonlinear absorption such as two-photon and three-photon absorption.

2.3 Experimental Geometries: HHG in Transmission and Reflection

High harmonic generation in crystals can occur either in transmission or in reflection geometry. In transmission geometry, the laser is focused at normal incidence to the exit surface of the crystal. This is because the absorption of above band gap nonperturbative high order harmonics plays a fundamental role. Although

they are generated at different layers along the laser propagation, due to their re-absorption by the crystal only those generated within one absorption depth (few tens of nanometers) close to the exit surface are collected. In this configuration, the laser propagates in the crystal before generating the detected harmonic radiation. The fundamental laser field defocuses and diverges from the exit surface along with the harmonic radiation as shown in figure 2.6(a). In reflection geometry, the laser is

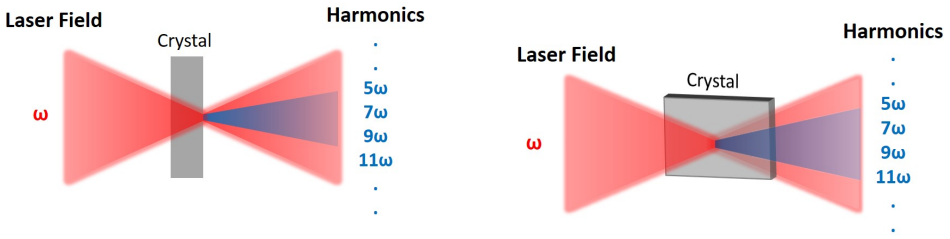

(a) THHG (b) RHHG

Figure 2.6: Experimental sketch of high harmonic generation in solids in (a) transmission geometry (THHG) and in (b) reflection geometry (RHHG)

focused at a given angle of incidence to the entrance face of the crystal and reflects back at the angle of reflection. The harmonics co-reflecting with the driving laser are therefore collected in reflection (figure 2.6(b)). Both configurations have their advantages and disadvantages. In the transmission geometry, during the propagation of the laser in the crystal, the laser field accumulates linear and nonlinear propopagation effects before generating harmonics. Propagation effects can come into play and can drastically affect the generation process for crystals with high nonlinearity [47]. Linear propagation effects include linear absorption and refraction, whereas, nonlinear propagation effects include nonlinear absorption such as two-photon absorption (TPA), self-phase modulation (SPM), and self-focusing. More details will be discussed in the next section (section 2.4). One disadvantage that HHG in reflection presents is when the absorption length is larger than the harmonic wavelength; in this case forward emission becomes significant [61]. However, the advantage of the reflection geometry is that the measurements and results are free from linear and nonlinear propagation effects and reflect a purely microscopic response of the generation process. XUV harmonics generated in reflection has been reported [61] and proved as a suitable configuration for coherent phase-matched harmonics.

2.4 Propagation Effects in the Generation Medium

In the example discussed in section 2.2.2.2, we considered the ionization of the electron by calculating the electric field amplitude in vacuum. However, in HHG in crystals one has to consider the electric field amplitude in matter. At the interface between air and a medium, the transmitted power of a laser beam inside the crystal can be estimated by calculating the Fresnel transmission coefficient, i.e. the power transmission coefficient. At normal incidence, the Fresnel transmission equation is

given by:

$$T_f = \frac{4n}{(1+n)^2} \tag{2.18}$$

Note that each material is characterized by its own optical properties, which means that the linear index of refraction n differs from one material to the other and for different laser wavelengths. For instance, at a wavelength of 2.1 μm, gallium arsenide has a refractive index $n_{GaAs} = 3.3$, while zinc oxide has a refractive index $n_{ZnO} = 1.92$ [62]. In addition, when the laser propagates in the medium it might be absorbed. When the absorption is uniform, the output intensity I_{output} is described by the Beer-Lambert law which is given by $I_{output} = I_0 e^{-\alpha z}$, where α and z are the linear absorption coefficient and the propagation distance of the fundamental field in the medium, respectively, and I_0 is the input intensity. Both transmission and absorption determine the output intensity exiting the medium, which differs from one crystal to the other. Consider, for example, the propagation of a laser beam, at a central wavelength $\lambda = 2.1$ μm, in a gallium arsenide (GaAs) crystal. The linear absorption in GaAs is negligible at this wavelength. Following the example in section 2.2.2.2, the effective electic field amplitude is calculated as $E_{matter} = t\,E_0$, where $t = \sqrt{T_f/n}$ [63]. The maximum wavevector is then $k_{max} = 0.17\pi/a$, which means that the electron wavepacket would traverse 17% of the Brillouin zone of GaAs rather than 37%. Moreover, the nonlinear properties of the medium play a very important role, especially at high electric field strengths and for materials with high nonlinearity. As a result, nonlinear effects such as the Kerr effect ($\chi^{(3)}$ process) can be induced, which strongly determines the propagation of the laser beam in the generation medium and consequently its effective intensity in the sample. The Kerr effect could take place both in the space domain and in the time domain; these are known as the self-focusing effect and the self-phase modulation (SPM) effect, respectively. Discussions and analysis of nonlinear propagation effects will be elaborated in Chapter 4.

2.5 Overview of HHG in Solids

The first experimental generation and detection of high harmonics in solids was in a 200 μm thick zinc oxide (ZnO) crystal [16]. Afterwards, extensive experimental studies of high harmonic generation have been reported in a number of crystals including wide band gap semiconductors such as krypton and argon polycrystalline solids [64], MgO [20, 61], quartz [48] and sapphire [58], and lower band gap semiconductors including zinc oxide [16, 65, 66], gallium selenide [67], zinc selenide [59], gallium arsenide [47] and silicon [68, 61]. Interestingly, 2D materials such as graphene [69, 60] and monolayer of molybdenum disulfide (MoS_2) [18] have also generated efficient high harmonics. HHG in $BaTiO_3$, a ferroelectric semiconductor, was also explored [70]. In addition, theoretical studies have further investigated HHG in other unconventional crystals including insulating 2D materials like hexagonal boron notride (h-BN) [71], ferromagnetic materials such as iron (Fe) monolayers [19], and topological insulators like Bi_2Se_3 [72]. Figure 2.7 summarizes the different

crystals experimentally investigated as the high harmonic generation media, showing the cutoff for a given photon energy of the driving laser field. The circles' sizes illustrate the direct band gap energy of each semiconductor crystal.

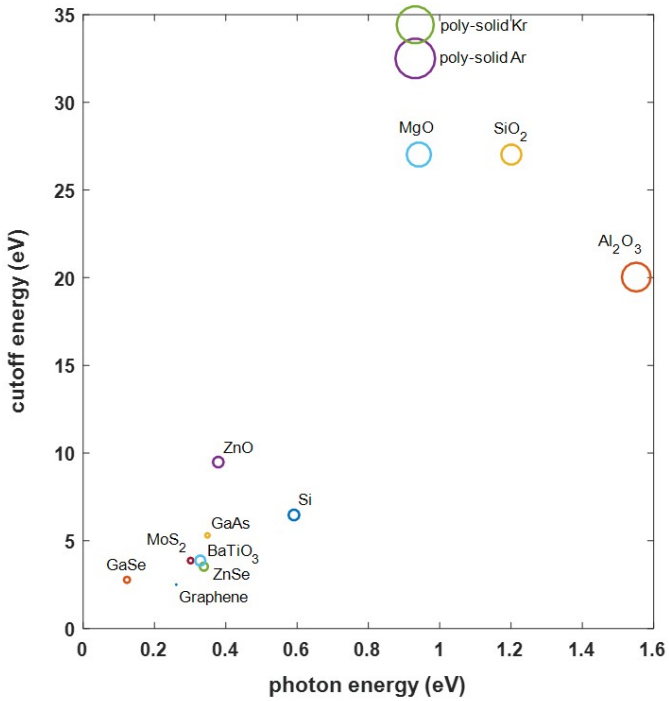

Figure 2.7: HHG studies synthesis. *Inspired by [17].*

2.5.1 Polarization Dependent HHG

A distinguished feature of solid state HHG is the strong dependence of the generation process on the angle between the linear laser polarization and the crystal axis. By rotating the crystal in the plane of the laser polarization, the generation efficiency varies. High harmonic generation in solids depends strongly on the crystal structure. Through polarization measurements, one can extract fundamental physical knowledge about the generation medium properties and the generation process by itself.

- H. Kim et al. [58] reported on the anisotropic polarization dependence of high order harmonics generated from sapphire. A 6-fold symmetry and a 4-fold symmetry was associated with the polarization dependences of the harmonics from C-plane and A-plane sapphire, respectively.
- S. Han et al. [73] extracted the higher order nonlinear susceptibilities of the generation medium (sapphire) through the high harmonic generation yield in the multiphoton absorption regime.

Moreover, polarization measurements provide a mean to probe the electron trajectory during the HHG process [74, 53, 75] and imprint the crystal and band structure of the solid. For example,

- Lanin et al. [59] generated harmonics from a zinc selenide (ZnSe) crystal, having a zinc blende structure. A general 6-fold symmetry of the polarization dependence of the harmonics was measured, consistent with the zinc blende crystal structure of ZnSe. However, each harmonic revealed a different dependence on the laser polarization and at different laser intensities, which reflects the electron wavepacket trajectories in the conduction band and hence reflects the band structure of ZnSe (figure 2.8 (c)).

- You et al. [20] studied the dependence of low and high order harmonics generated from MgO on the laser polarization. The polarization measurements of the harmonics revealed a fourfold symmetry due to the cubic crystal structure of MgO. The study concluded that high order harmonics, XUV harmonics, show a stronger dependence, than low order harmonics (visible harmonics) on the laser polarization (figure 2.8 (a-b)). Indeed, high order harmonics originate from higher energy regions of the conduction band, and therefore the process is more sensitive to the anisotropic nature of the high energy bands.

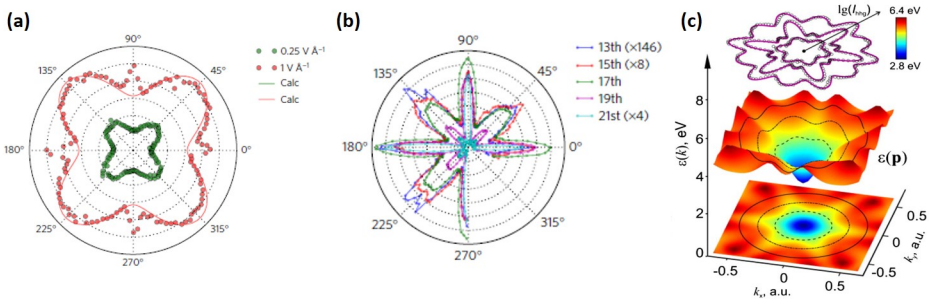

Figure 2.8: (a) Polarization measurements of the third harmonic and (b) higher order harmonics generated from MgO [20]. (c) Polarization measurements of harmonic 9 generated from ZnSe at different laser intensities accompanied by a direct mapping to its conduction band [59].

2.5.2 Ellipticity Dependent HHG

The ellipticity of the driving laser field is also an interesting variable in solid-state HHG. Contradicting results have been reported concerning the high harmonic generation yield as a function of the ellipticity.

- Y. S. You et al. [20] generated high harmonics from an elliptically polarized laser field. When the linear polarization is aligned along the crystal axis connecting Mg-O sites, the generation yield was maximum then decreases as the ellipticity of the driver increases to $\epsilon \pm 0.4$. Surprisingly, the yield increases as the ellipticity increases to 1, i.e. circularly polarized state. This

is explained from a real space trajectory picture: for an ellipticity $\epsilon \pm 0.4$ the traveling electron does not encounter any lattice sites, however, the circular polarization drives the electron to collide to oxygen atomic sites.

- N. Yoshikawa et al. [69] investigated the generation of harmonics from monolayer of graphene and reported on the enhanced high order harmonic yields, particularly, of the 7^{th} and 9^{th} harmonics, from an elliptically polarized 4.7 μm laser. A contradicting study by Taucer et al. [60], showed that the harmonic generation efficiency from graphene decreases gradually with the laser ellipticity, reaching zero above an ellipticity of 0.5.

- N. Klemke et al. [76] also reported on a decrease of the efficiency of UV-VIS harmonics generated from silicon and quartz with the increase of the driver ellipticity, however the harmonic signal does not disappear when the driver is circularly polarized. Although the harmonic efficiency is lower than that obtained with a linear polarization, they measured circularly polarized harmonics from both crystals when the HHG process is driven by a circular or elliptical polarization.

2.5.3 Nonlinear Propagation Effects

Propagation effects are of great importance when investigating HHG in transmission geometry. These effects have to be handled with care especially when considering materials possessing high degree of linear and nonlinear properties.

- Xia et al. [47] have reported on the harmonic generation from GaAs samples having different thicknesses. The study revealed a drastic change in the polarization dependences of the generated harmonics from thicker crystals and attributed this change to the nonlinear propagation effects, particularly the nonlinear absorption along the different crystal axes (figure 2.9(a)). Moreover, the study showed that the harmonics generated in transmission are spectrally broader than those generated in reflection, as a result of self-phase modulation (SPM).

- G. Vampa et al. [61] also studied HHG from magnesium oxide (MgO) in reflection and transmission. A comparison between the generated high harmonics from both geometries, shows that the harmonics generated in transmission are spatially (i.e. more divergent) and spectrally broader than those generated in reflection, due to the self-focusing and self-phase modulation effects, respectively. Their measurements are reported in figure 2.9(b).

2.5.4 Manipulation of the HHG Medium

The solid-state nature of the generation medium offers additional degrees of freedom where one can pattern micrometer and nanometer sized structures to enhance the driving field and harmonic efficiency, and spatially manipulate the harmonic beams [22, 26, 77].

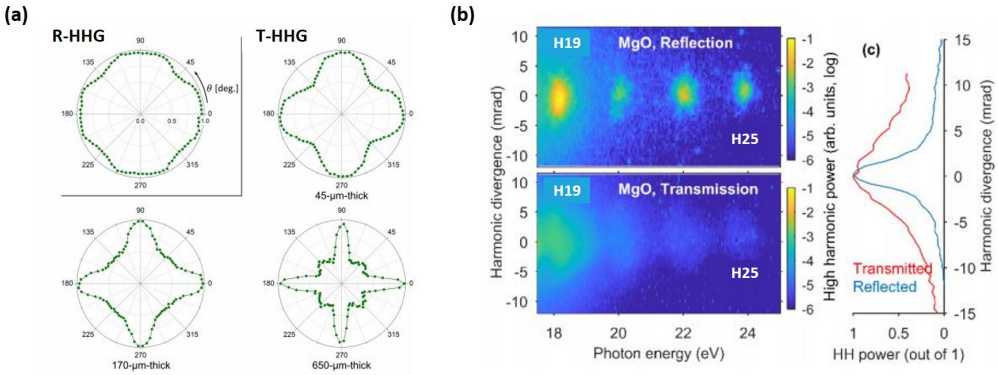

Figure 2.9: (a) Polarization dependences of the harmonics generated from GaAs in reflection (R-HHG) and transmission (T-HHG) geometries [47]. (b) Spectral and spatial comparisons of high order harmonics generated from MgO in reflection and transmission geometries [61].

- Sivis et al. [21] demonstrated the confinement of the laser field in a series of nanostructured cones. In addition, they integrated a Fresnel zone plate at the exit surface of a silicon sample to create self-focused harmonic beams.

- Han et al. [23] reported for the first time on the harmonic generation assisted by plasmonic field enhancement in metal-sappphire nanostructures. The structures are truncated sapphire cones with a thin film of gold deposited on them. High order harmonics (up to the 13^{th} order) of a Ti:sapphire oscillator (800 nm in wavelength) were generated by field enhancement by means of surface-plasmon polaritons along the metal-sapphire interface. The enhancement maximizes at the exit tip of the cone reaching 20 dB (i.e. power factor = 100).

- Vampa et al. [24] observed high order harmonic generation (in the UV-VIS spectral region) in bulk silicon assisted by plasmonic field enhancement through depositing an array of nanosized Au antennas on the surface of a silicon sample. The harmonic signal measured from the region of the nanoantennas was 5-10 times stronger than that measured from the region of no antennas.

Chapter 3

High Harmonic Generation in Graphene

In this chapter, high harmonic generation in graphene is studied. In section 3.1, we start with a motivation behind investigating graphene as a medium of generation. Then, in sections 3.2 and 3.4, we present our preliminary results in high harmonic generation from trilayer of graphene. Two main challenges are encountered, mainly the fast damage of the samples and the generation of a broad fluorescence signal. This will be elaborated upon in section 3.3. Moreover, we compare the harmonic generation in different number of graphene layers in section 3.5 and report for the first time on HHG in freestanding graphene in section 3.6. Finally in section 3.7, we propose solutions that would reduce the damage rate and lead to the generation and detection of higher harmonic orders.

3.1 Objective and Motivation

Graphene is a two dimensional material; it is a material comprising one single layer of carbon atoms arranged in a hexagonal structure. It has attracted great attention and has been the center of research for many years until present due to its extraordinary properties [78]. Graphene is distinguished by its strong light matter interaction owing to its high electron mobility [79, 80] and ultrahigh mechanical strength [81]. Its electric and optical properties has made it a good candidate in the fields of photonics, plasmonics and optoelectronics [82, 83]. As a freestanding monolayer, graphene has a zero band gap energy at its high symmetry point 'K' which is known as the Dirac point. Around this Dirac point the energy dispersion of graphene is linear and thus takes the form of a symmetrical cone, while at high energies the band structure gets deformed (figure 3.1). Opening the band gap in graphene can be easily done, for example by stacking several graphene layers on top of each other or by depositing or transferring the graphene layer on a substrate [84, 85, 86]. Experimentally, having graphene on a substrate can ease its manipulation.

3.2 HHG in Trilayer Graphene

Carrier dynamics in graphene, in response to an intense optical field, were investigated in both the perturbative and the nonperturbative regimes. In the multiphoton regime, terahertz harmonics were generated from graphene driven by a terahertz

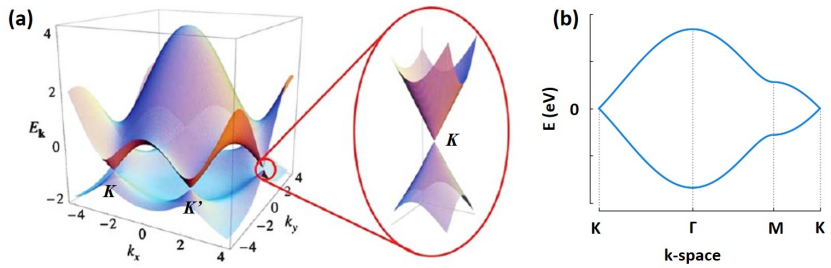

Figure 3.1: 3D representation of the band structure of graphene [87] in the first Brillouin zone. 2D representation of the band structure showing the highest symmetry points K, Γ and M, taken from [88].

field [89, 90], and in the nonperturbative regime, recent studies on HHG from graphene driven by mid-IR laser were investigated, reporting contradicting results about the HHG mechanism and harmonic properties [69, 60, 91]. In the following sections, we study HHG from graphene driven by a near-IR laser field [25].

3.2.1 Experiment with a High-Repetition Rate Mid-IR Fiber Laser

We employ a turnkey mid-infrared femtosecond laser from NOVAE (Appendix B). The laser is a mode-locked thulium-doped fiber oscillator followed by an all-fibered nonlinear amplification stage, which delivers a train of 85 fs and 9 nJ pulses at a repetition rate of 18.66 MHz centered at 2.1 μm wavelength. A sketch of the experimental setup is shown in figure 3.2. The polarization of the laser beam exiting the laser is 10° rotated from the vertical axis, this is why a half-wavelength plate (HWP) is placed in front of the laser exit to correct the polarization to a vertical state and avoid any ellipticity induced by reflections from the mirror. The laser power and polarization are varied by the combination of a HWP and a polarizer. The beam is then reflected and focused by a 2.5 cm focal length off-axis parabola on the graphene samples. The beam size at the focus, at full-width half-maximum

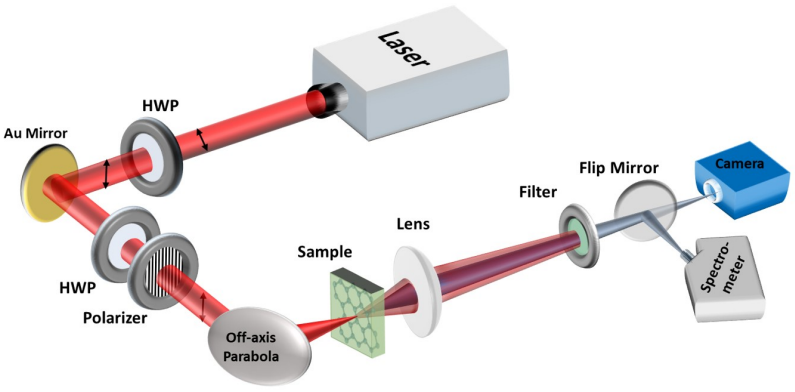

Figure 3.2: Sketch of the NOVAE experimental setup at CEA, Saclay.

(FWHM) is calculated to be 5.9 μm (Appendix A). The generated harmonics diverging from the sample are collected in transmission by a 6 cm focal length lens which focuses them on a CCD camera or a spectrometer for spatial and spectral characterizations, respectively. More details about the detection system are available in Appendix E. To filter out the fundamental laser beam and select individual harmonics, we use bandpass filters whose central wavelengths correspond to each harmonic's wavelength. Although the focusing lens imposes chromatic dispersion on the spatial harmonic mode, it nevertheless helps to seperate the harmonics, as each harmonic focuses at a different lens position. For this reason the lens is placed on a manual translational stage, and translated along the beam propagation direction to optimize the signal of the harmonics. Moreover, the saturation of the third harmonic (H3) can blur the image, therefore, neutral density filters are used to reduce its signal. The maximum laser intensity reached at the focus is estimated to be (in vacuum) ~ 0.2 TW/cm^2. The graphene sample is composed of trilayer of graphene supported by a 500 μm thick quartz substrate, bought from Graphenea. Figure 3.3 shows the harmonic spectrum experimentally obtained from trilayer graphene on quartz at an estimated laser intensity (in vacuum) of 0.17 TW/cm^2. Harmonic 3 (H3), centered at 700 nm, and harmonic 5 (H5) centered at 420 nm are generated from graphene which correspond in photon energies to 1.77 eV and 2.95 eV, respectively. Only harmonic 3 is generated from the quartz substrate at

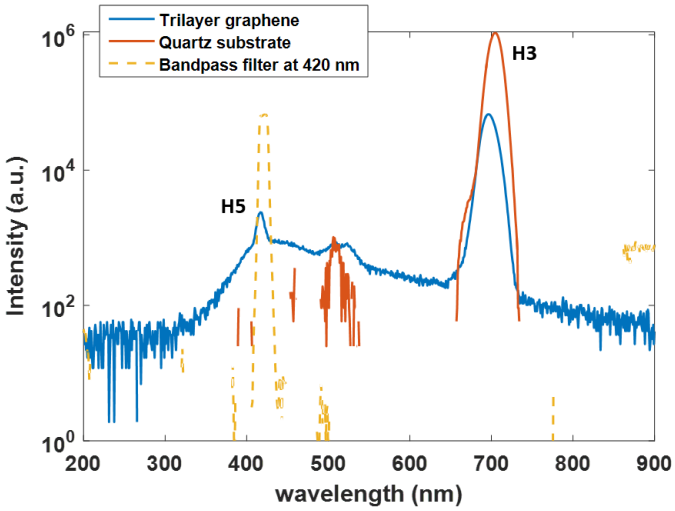

Figure 3.3: Harmonic spectra from trilayer graphene and quartz substrate, at 0.17 TW/cm^2 and 0.18 TW/cm^2, respectively.

the maximum intensity of the laser 0.18 TW/cm^2. During the experiment, the harmonic spectrum from graphene was acquired at an integration time of 200 ms, and the detection was optimized for H5. While the spectrum from quartz was acquired at an integration time of 30 ms and the detection was optimized for H3. This explains why the 3rd harmonic signal from quartz is higher than the signal from graphene, in addition to being measured at a higher laser intensity. In figure 3.3 both spectra are normalized by the integration time. The dashed plot in yellow

in the figure corresponds to the experimentally measured spectral transmission of the bandpass filter of the 5^{th} harmonic. The filter cuts H3 signal and also filters out a significant amount of the broad fluorescence signal permitting precise measurements of H5 later on. A small peak appearing around 520 nm is observed from the quartz spectrum and is also observed on top of the fluorescence signal from graphene. This wavelength matches the wavelength of the 4^{th} harmonic of the 2.1 μm driver. Bearing in mind that quartz is a non-centrosymmetric crystal, it permits the generation of even harmonics, in addition to the odd harmonics [48]. Therefore this peak around 520 nm could be harmonic 4 generated from quartz, however, the investigation on this point was not pushed any further.

3.3 Limitations and Challenges

Photoluminescence

The measured spectra reported above show a broadband photoluminescence (PL) signal which covers the visible spectral range. The broad photoluminescence has been reported by several research groups [92, 93, 94] under the excitation of graphene by femtosecond laser pulses. It is emitted as a result of noncoherent radiative electron-hole recombinations, caused by the rapid scattering between nonequilibrium photoexcited carriers, which occurs on a time scale of tens of femtoseconds [92], less than our laser pulse duration. The photoluminescence signal covers a broad spectral range from the visible to the near UV ($\sim$ 800-300 nm) and exhibits a nonlinear dependence on the laser fluence [93]. This PL signal presents one of the main challenges in the HHG experiment in graphene; its broadband nature makes it difficult to disentangle it from the higher order harmonics.

Graphene Damage

Another main challenge is the fast damage of the graphene samples upon exposure to the laser pulses. Figure 3.4(a) shows the lifetime of the 3^{rd} harmonic signal at 5 different spots on the sample with a low laser intensity, 0.04 TW/cm^2. Indeed, the damage is so fast as H3 decays rapidly in less than 1 second; the measured decay time at half the maximum value of H3 from graphene is 0.35 seconds. Note that the constant signal reached afterwards corresponds to the 3^{rd} harmonic signal generated from the quartz substrate. Besides, the damage rate as a function of the laser intensity is studied and depicted in figure 3.4(b). The decay time decreases exponentially as a function of the laser intensity. Beyond 0.04 TW/cm^2, the damage rate is very high such that the graphene is immediately ablated before generation. These fast decay rates prohibit accurate and long systematic measurements. Working in this low intensity regime limits the detection of higher harmonics since the efficiency of the harmonic generation drops as the harmonic order increases, and thus no harmonics above 2.9 eV have been experimentally detected from graphene. To limit the damage problem we developed an experimental technique that allows systematic measurements even at higher intensities. Using a labview program and motorized piezo stage we continuously refresh our sample in a snake-like pattern. Taking into

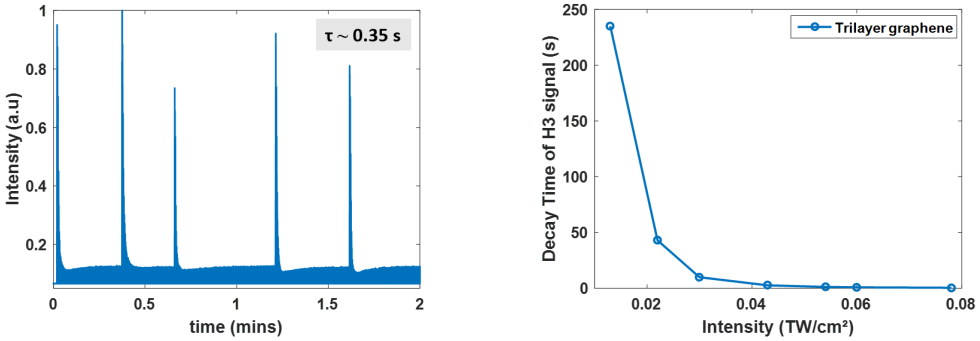

(a) Decay of H3 signal at five different positions on the sample, at a laser intensity of 0.04 TW/cm^2.

(b) Decay time of H3 signal from trilayer graphene as a function of the laser intensity.

Figure 3.4: Damage study of trilayer graphene on quartz exposed to intense laser pulses.

consideration the decay time at each intensity, long measurements are taken by automatically moving to a fresh spot during the acquisition. These laser-traced patterns can be seen in the SEM images in figure 3.5. SEM images supported by EDX measurements have shown that the carbon concentration on radiated graphene areas (white regions) decreased significantly, and confirms the laser-induced local permanent damage on the graphene sample.

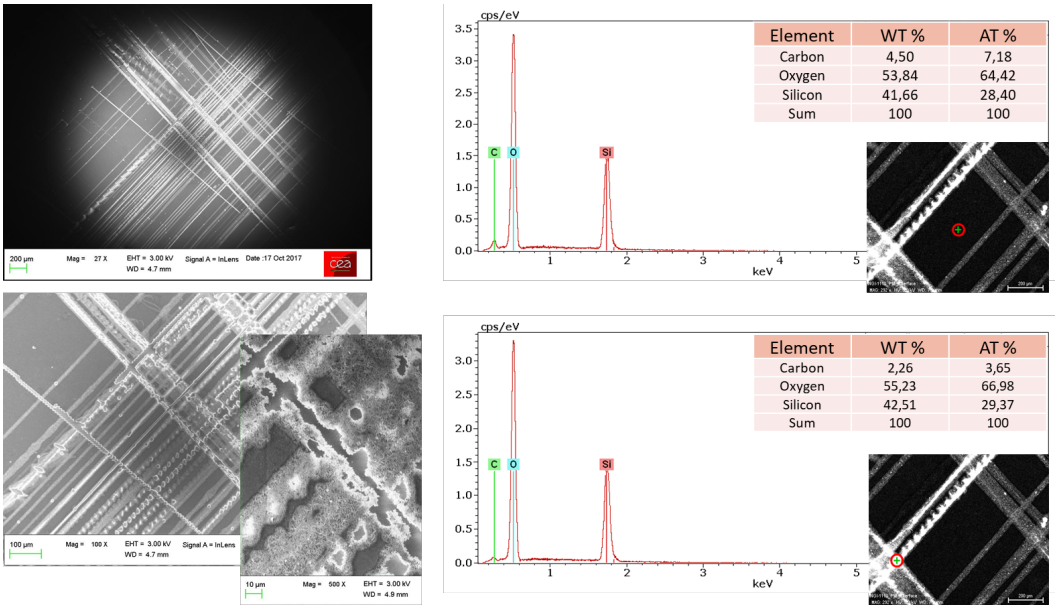

Figure 3.5: Left: SEM images of trilayer graphene samples after exposure to the laser pulses. Right: EDX measurements on nonradiated and radiated trilayer graphene areas.

Furthermore, to characterize accurately our graphene samples before and after laser exposure, we have performed Raman measurements (figure 3.6) in collaboration with Prof. Yannick De Wilde at his laboratory at Institut Langevin, Paris. The excitation wavelength used is 514.5 nm. The Raman measurement on pristine

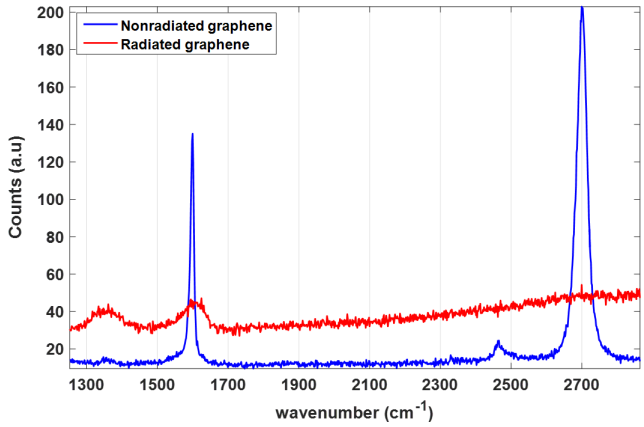

Figure 3.6: Raman measurements on pristine and irradiated monolayer graphene areas.

graphene reveals the two main graphene bands: a G band at 1600 cm^{-1} and a 2D band at $\sim$ 2700 cm^{-1}, which assures a good quality sample with no major defects. However, the main Raman signals on irradiated graphene areas disappear (red spectrum), which indicates complete laser-ablation of graphene. Besides, a pronounced D band at 1300 cm^{-1} represents the presence of defects close to the damaged spots. Interestingly, femtosecond laser pulses in the near-IR have been employed to etch graphene layers and pattern various micro and nanostructures [95, 96] such as graphene microribbons [97]. Kalita et al. [97] argued that Raman characterization at the edge of the etched structures showed a deterioration in the graphene quality and appearance of defects, as a result of the breaking of the sp^2 carbon hybridization due to the oxidation of graphene with the laser pulse [97]. Femtosecond pulsed laser micropatterning on graphene can find potential applications in graphene-based microelectronic devices.

3.4 Laser Dependent HHG in Trilayer Graphene

3.4.1 Intensity Scaling

As discussed in Chapter 2, the laser intensity is a crucial parameter that drives the HHG process and defines the regime in which the process takes place, whether it is multiphoton absorption or tunnel ionization. The scaling law of the harmonic signal with the laser intensity allows one to distinguish the generation regime of the experiment. In mathematical terms, for a harmonic, labelled H, its signal $S_H \propto I^q$, where $q = H$ for a perturbative harmonic. However, in the nonperturbative regime, where tunnel ionization takes place, $q \neq H$. To study the dependence of the harmonic generation in graphene as a function of the laser intensity, we measure the

harmonic signal of H3 and H5 by varying the laser intensity from minimum to maximum. The results are reported in figure 3.7. The measurements are analyzed in a

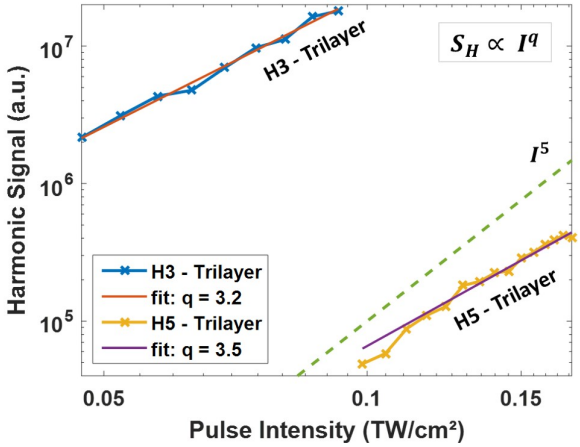

Figure 3.7: Intensity dependence of harmonics 3 and 5 (H3 and H5) generated from monolayer and trilayer graphene on quartz.

double logarithmic scale to fit linearly the scaling law. H3 from trilayer graphene scales as $I^{3.2}$, while H5 scales as $I^{3.5}$. The fits indicate that H3 is a perturbative harmonic, however H5, which is purely generated from graphene is a nonperturbative harmonic ($q = 3.5 \neq 5$).

3.4.2 Ellipticity and Polarization Dependences

The laser ellipticity and polarization studies also give insight into the HHG process in crystals. Both of these laser parameters drive the electron dynamics and determine its direction in the lattice.

Ellipticity Dependences

We perform ellipticity measurements of the harmonics generated from trilayer graphene as well as of harmonic 3 generated from quartz. The measurements are carried out by increasing the ellipticity (e) of the beam using a quarter-wavelength plate (QWP), placed after the polarizer, from linear state (e = 0, QWP angle = 0°) to a circularly polarized state (e = 1, QWP angle = 45°) while recording the harmonic signal on the CCD camera. The laser intensity is estimated to be 0.17 TW/cm^2. The results are summarized in figure 3.8. Note that the ellipticity values correspond to the quarter-wavelength plate angle; for example, at e = 1, the optic axis of the QWP makes an angle of 45° with the incoming linear polarization. Each curve is normalized to its own maximum value at the linear polarization state (i.e. e = 0). The signal of harmonic 3, generated from graphene, decreases as the ellipticity of the driving field increases (figure 3.8(a)); it reaches a minimum value for a circularly polarized state (attenuation by a factor of 5 compared to the linear

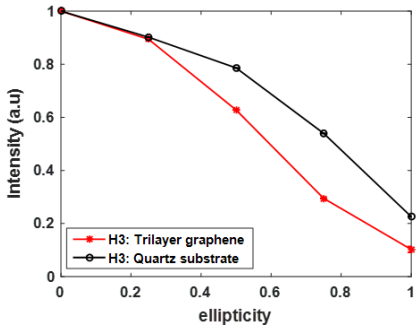

(a) Ellipticity scans of H3 signal generated from trilayer graphene (red curve) and quartz (black curve).

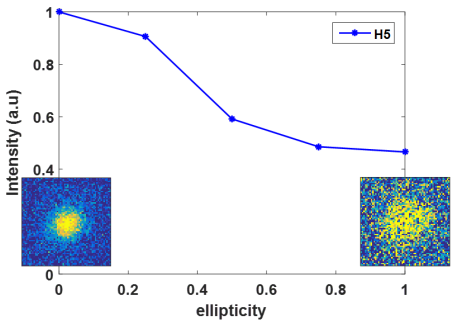

(b) Ellipticity scan of H5 signal generated from trilayer graphene on quartz.

Figure 3.8: Ellipticity dependence of H3 (a) and H5 (b) generated from trilayer graphene on quartz at a laser intensity of 0.17 TW/cm^2. The ellipticity depedence of the quartz substrate is represented by the black curve.

polarization). Besides, the efficiency of harmonic 3 generated from the quartz substrate also decreases as the ellipticity increases. As for the 5$^{\text{th}}$ harmonic generated from graphene, its generation efficiency decreases with the increase of the laser ellipticity, reaching a minimum value for a circularly polarized driver (figure 3.8(b)). Notice that the contrast in the dependence is lower than that of H3, where for e = 1, H5 signal is only attenuated by a factor of 2 compared to the linear case. We verify the spatial modes of H5 at e = 0 and e = 1, and we find that for a linearly polarized state (e = 0), the spatial mode of H5 (shown as an inset in the figure) clearly reveals a Gaussian distribution obeying the spatial mode of the fundamental beam, while for a circularly polarized state (e = 1) the signal is uniform (spatially limited by the aperture of the filter). It is attributed to the fluorescence signal. The ellipticity dependence obtained here agrees with those reported by Taucer et al. [60] and Baudisch et al. [91], but disagee with the results reported by Yoshikawa at al. [69] where the harmonic signals of the 5$^{\text{th}}$ and the 7$^{\text{th}}$ harmonics of the 4.7 μm driver were enhanced for an elliptically polarized beam. Note that, theoretical simulations in the time-dependent density-functional theory (TDDFT) framework have demonstrated the potential of a circularly polarized laser beam to generate circularly polarized high harmonics from graphene [98].

Polarization Dependences

The linear polarization of the laser is also a critical parameter in the HHG process. The generation efficiency is determined by the angle between the crystal axis of the generation medium and the linear polarization of the laser. This dependence not only encodes fundamental information about the HHG process but also reveals the symmetry of the crystal. To study the linear polarization dependence of the harmonics generated from graphene, we rotate the linear polarization of the laser in the plane of the graphene sample while recording the harmonic signal on the CCD

camera for a selected harmonic order. The measurement is performed for harmonic 5 and the result is depicted in the polar plot in figure 3.9. The result shows an

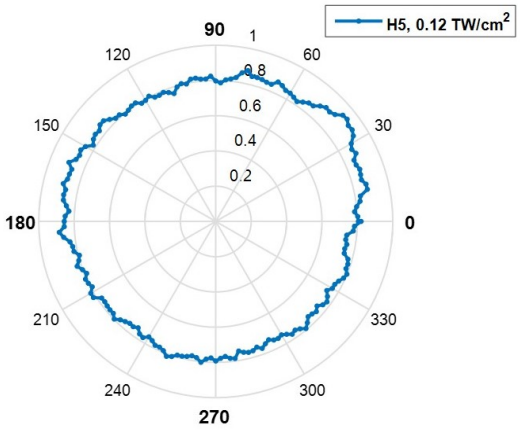

Figure 3.9: Polarization dependence of H5 generated from trilayer graphene on quartz, at 0.12 TW/cm^2 of laser intensity.

isotropic dependence of H5 on the laser polarization; the 5$^{\text{th}}$ harmonic generation in graphene is independent of the angle between the polarization and the graphene axis. Note that, in the perturbative regime, THG (third-harmonic generation) from graphene has been extensively investigated in a number of studies [99, 100] and has shown to exhibit an isotropic dependence on the laser polarization [94].

3.4.3 Polarization Dependences by TDDFT Simulations

In this section, we try to explain the experimental results based on theoretical analysis of the polarization spectroscopy of high order harmonics generated from graphene. Numerical simulations in the Time-Dependent Density-Functional Theory (TDDFT) framework [101, 102] were carried out by our collaborator Nicolas Tancogne-Dejean from the group of Angel Rubio at Max Planck Institute for the Structure and Dynamics of Matter in Hamburg, Germany. The simulations were performed by the Octopus code [103], available from http://www.octopus-code.org. The laser parameters used for the simulations are 2.1 μm laser wavelength, 37.5 fs pulse duration and 0.2 TW/cm^2 laser intensity, similar to our experimental laser parameters. Figure 3.10 shows a 60° polarization spectroscopy scan of the odd harmonics generated from a monolayer of freestanding graphene. The simulation reveals no dependence of the generation efficiency of H3 and H5 on the laser polarization, indeed H3 and H5 polarization dependences are isotropic. However, for the higher order harmonics, particularly, H7 and H9, the generation efficiency is anisotropic. The harmonic signal is maximized only at certain angles between the laser polarization and the graphene axis. The anisotropic dependence of H7 and H9 reveals a 6-fold symmetry which reflects the hexagonal crystal structure of graphene. The simulation of the polarization dependence is in perfect agreement with the theoretical calculations performed by Zurrón-Cifuentes et al. [104] by considering a

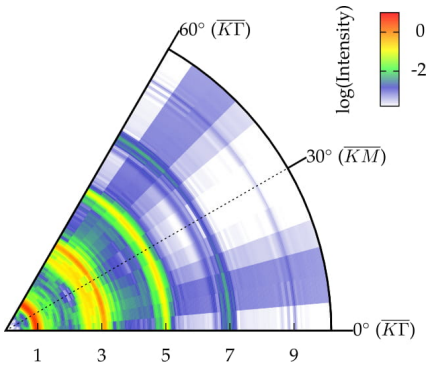

Figure 3.10: Polarization dependent harmonic generation from monolayer of graphene in the UV-VIS spectral range, at 0.2 TW/cm^2 of laser intensity.

driver at 3 μm in wavelength, 28 fs pulse duration and 0.05 TW/cm^2 laser intensity. Similarly, the anisotropy becomes more prominent for higher order harmonics. The reason is that low order harmonics, of low photon energies, are generated when the electron wavepacket oscillates and accelerates in the isotropic conical part of the band structure around the Dirac point, while higher order harmonics are emitted when the electron wavepacket explores higher nonconical regions of the band structure. In general, HHG in solids can probe the band structure of the generation medium through polarization spectroscopy.

3.5 Harmonic Generation from Different Number of Graphene Layers

In this section, we generate harmonics from monolayer and 6-8 layers of graphene supported on a 1 mm thick circular quartz substrate. These samples were bought from ACS Material. The experimental setup is modified according to the following: the off-axis parabola is replaced by a mirror that guides the beam to a 3 cm focal length aspheric coated lens, which focuses the laser pulses on the graphene samples. The diverging generated harmonics are then collected and focused by another 10 cm focal length lens onto the CCD camera and the spectrometer. A sketch of the new experimental setup is illustrated in figure 3.11. The beam size at the focus is calculated to be 7.04 μm at FWHM. With a slightly larger beam size at the focus, we expect to enlarge the generation area, hence more emitters. Therefore, we expect a higher harmonic signal, and consequently a decrease in the damage rate.

The harmonic spectra from monolayer and 6-8 layers of graphene are reported in figure 3.12. Harmonics 3 and 5 (H3 (700 nm) and H5 (420 nm)) are generated from both graphene samples at an estimated laser intensity in vacuum of 0.08 TW/cm^2, in addition to the broadband fluorescence signal in the visible spectral range. However, only harmonic 3 is generated from the quartz substrate at an intensity of 0.12 TW/cm^2. The three spectra are normalized by the integration time (700 ms for the monolayer, 500 ms for the 6-8 layers and 100 ms for quartz), and the background

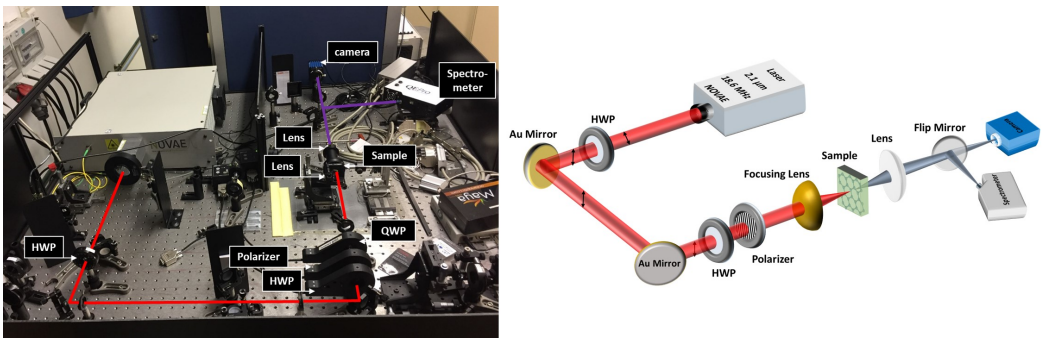

Figure 3.11: Modified experimental setup of the HHG experiement in graphene driven by the NOVAE laser, at CEA, Saclay.

from quartz is subtracted. By comparing the 5$^{\text{th}}$ harmonic signal generated from monolayer and 6-8 layers, we find that the harmonic generation efficiency in the case of monolayer is slightly higher than in the 6-8 layers. This is in agreement with previous experimental and theoretical studies in molybdenum disulfide (MoS_2) [18] and hexagonal boron nitride (h-BN) [105], respectively. The studies have shown the enhanced efficiency in a monolayer of a semiconductor compared to bulk, or even to few stacked layers of the 2D medium.

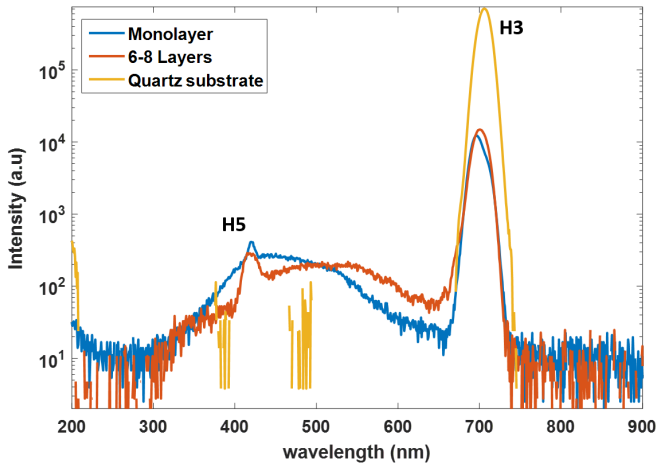

Figure 3.12: Harmonic spectra from monolayer and 6-8 layers of graphene on 1 mm thick quartz substrate, at an estimated laser intensity of 0.08 TW/cm^2. The harmonic spectrum from quartz is measured at a laser intensity of 0.12 TW/cm^2.

Interestingly, we observe that as the number of graphene layers increases the harmonics become spectrally broader. Indeed, the 5$^{\text{th}}$ harmonic generated from few layers of graphene is spectrally broader than the one generated from monolayer graphene. This observation has been reported before by Taucer et al. [60], and has been attributed to the strong self-phase modulation effect in few layers of

graphene ($\sim$ 5 nm), because of the significantly high nonlinear refractive index (n_2) of graphene which is around $-0.5 \times 10^{-9}\text{cm}^2/\text{W}$. In our case, self-phase modulation already comes into play in 6-8 graphene layers ($\sim$ 1.14 nm thick).

3.6 HHG in Freestanding Graphene

In order to avoid any substrate-induced effects on the graphene sample properties, such as band gap opening [84, 86], and on the harmonic generation process, we investigate high harmonic generation from freestanding graphene, employing the NOVAE laser. The freestanding graphene samples are trilayer of graphene transferred on a TEM (Quantifoil) grid. The 300 mesh TEM grid is circular (3 mm in diameter) and Au coated, and supports a Quantifoil R2/4 carbon film (20 nm thickness) consisting of an array of 2 μm diameter holes with a periodicity of 6 μm. The other two samples are monolayer and multilayers (6-8 layers) of graphene on a 2000 mesh copper (Cu) grid with 6.5 μm circular holes and a 12.5 μm periodicity. The Cu grid is supported on a beryllium-copper Synaptek 1 x 2 mm slotted grid. The trilayer freestanding samples were bought from Graphenea, while the monolayer and 6-8 layers were bought from Tedpella. Optical microscopy images of the samples are shown in figure 3.13.

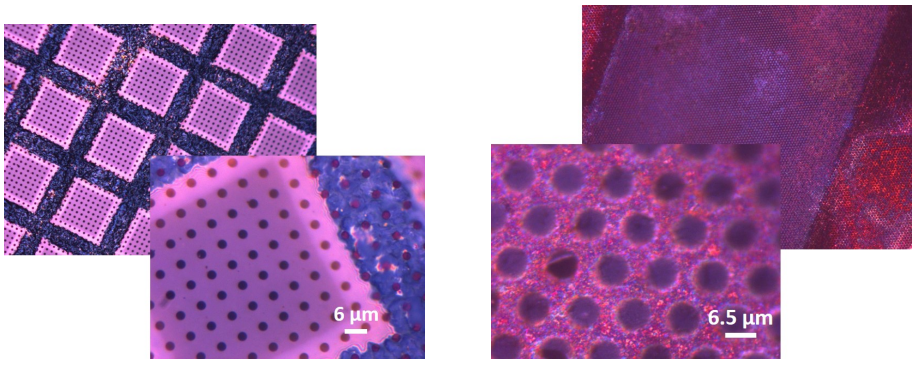

(a) Trilayer graphene on a TEM Quantifoil grid.

(b) Monolayer graphene on a copper (Cu) grid.

Figure 3.13: Optical microscopy images of the freestanding graphene samples. (a) Freestanding trilayer graphene. (b) Freestanding monolayer graphene.

Figure 3.14 shows a bar plot of the harmonic yields generated from freestanding graphene with the NOVAE laser. Harmonic 3 and harmonic 5 are generated from freestanding trilayer graphene, while we report only on the generation of harmonic 3 from monolayer and 6-8 layers of freestanding graphene. The fast damage of the samples in the latter case prevented the detection of higher order harmonics. The freestanding graphene samples on the Cu grid are more fragile and more easily damaged than those on the TEM grid. This is because the hole size of the Cu grid is larger than the hole size of the TEM grid; in fact, the 6.5 μm hole was a limit beyond which the graphene layer would collapse, however, it allows to couple the

full beam to the graphene. On the other hand, the TEM grid may better sustain the bonding with the graphene layer than the copper grid, due to the presence of the Quantifoil carbon film. Note that along the laser propagation direction, the front surface of the sample is the side with no graphene, and the exit surface of the sample is the side where the graphene layer lies; therefore the laser propagates through the grid before reaching the graphene layer. Figure 3.15(a) shows the

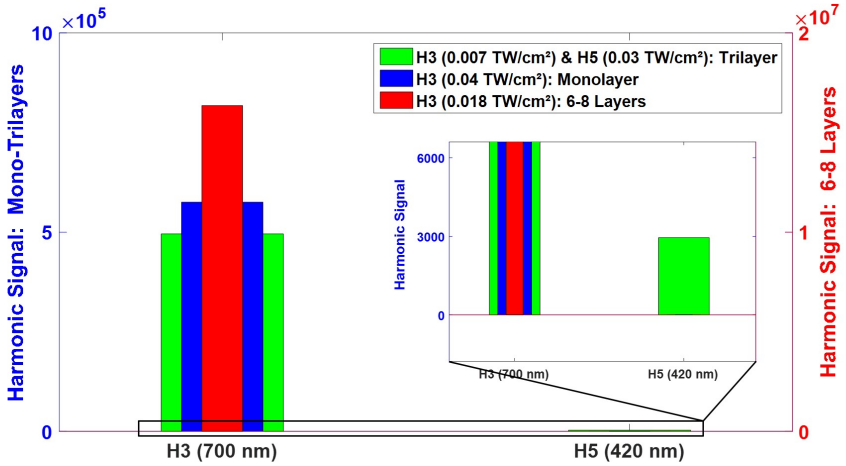

Figure 3.14: Harmonic yields generated from monolayer, trilayer and 6-8 layers of free-standing graphene at different laser intensities of the NOVAE laser vertically polarized. Note that the y-axis on the left is associated with the harmonic signals from trilayer and monolyar graphene, while the y-axis on the right is associated with the harmonic signal from 6-8 layers of graphene.

spatial mode of harmonic 3 generated from 6-8 layers of freestanding graphene on the copper Cu grid with a linearly (vertical) polarized laser beam. The Cu grid acts as a waveguide that guides and confines the laser pulses, which results in a slight enhancement of the laser field at the exit surface. This is illustrated in the FDTD simulation by Lumerical in figure 3.15(c). The mode of the fundamental laser beam at the exit of the grid is shown in figure3.15(d), characterized by an enhancement along the horizontal (x) axis. The feature of the 3rd harmonic mode is therefore associated with the mode of the laser field. With a circularly polarized laser we expect a minimal harmonic generation as previously reported in section 3.4.2, but surprisingly, we generate harmonic 3 from the 6-8 layers of graphene that has a donut-shaped spatial profile as depicted in figure 3.15(b). This is due to the copper grid that enhances the local polarization of the laser beam at the edges of the Cu holes, as shown in the case of vertical polarization. Therefore locally, the polarization of H3 is linear. While with a linear polarization, we generate at the center of the copper hole, the harmonic signal disappears with a circularly polarized driver, in agreement with previous measurements and studies [60].

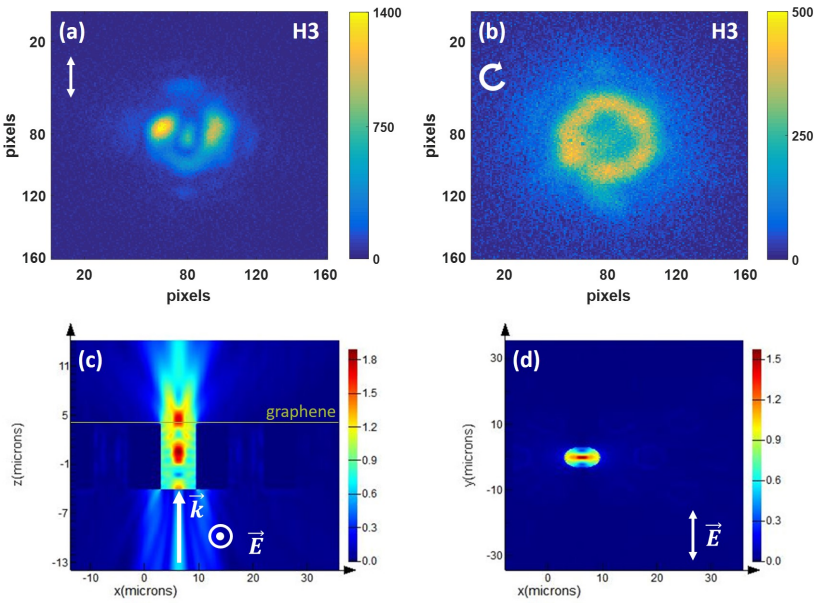

Figure 3.15: Spatial modes of harmonic 3 (700 nm) of the 2.1 μm wavelength driver, generated from 6-8 layers of freestanding graphene with (a) a linearly (vertical) polarized and (b) a circularly polarized laser beam. Each image is taken with an acquisition time of 200 ms. The estimated laser intensity is 0.02 TW/cm^2. (c) and (d) FDTD simulations by Lumerical of the propagation of the NOVAE laser beam in the copper grid in the zx plane and the yx plane, respectively, where z is the propagation direction of the laser beam.

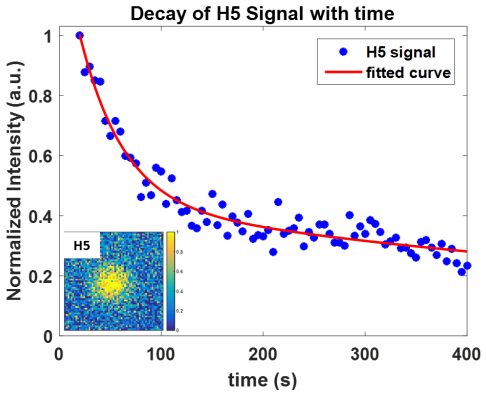

(a) Decay of H5 signal, from freestanding trilayer graphene, with time. The inset figure shows the spatial mode of H5 at a laser intensity of 0.03 TW/cm^2.

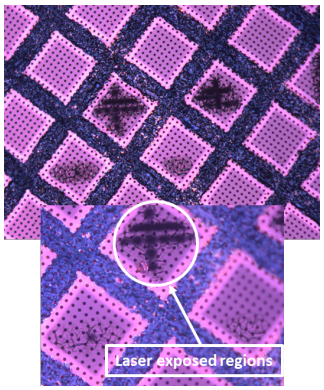

(b) Optical microscope images of the sample showing damaged graphene regions after laser illumination.

Figure 3.16: Damage study of freestanding trilayer graphene supported on a TEM grid.

The damage rate of the trilayer graphene samples is studied as a function of time in figure 3.16(a). At a laser intensity of 0.03 TW/cm^2, the 5$^{\text{th}}$ harmonic signal is recorded over a time duration of 400 s ($\sim$ 6 mins). The decay time is around 30 s, interestingly higher than the decay times of graphene samples deposited on a substrate (10 s at the same laser intensity, figure 3.4(b)). This could be explained as a result of the substrate-induced effect on the high damage rate of the samples. In figure 3.16(b), optical microscopy images reveal the permanent damaged areas caused upon laser exposure.

3.7 Proposed Solutions for Long-standing Graphene

Long wavelength driver: Experiment with an OPCPA laser system

High harmonic generation in graphene is more sustainable using long driving wavelengths. Due to the increase of electronic excitation at short driving wavelengths, the damage is dramatically high and therefore harmonics cannot be efficiently generated in graphene. As the wavelength increases the damage becomes less prominent. Using a near-infrared driver operating at 2.9 μm in wavelength and 125 kHz repetition rate, we generate up to the 7$^{\text{th}}$ harmonic (414 nm $\sim$ 3 eV) from trilayer graphene on quartz (figure 3.17). A broad fluorescence signal dominates the low visible spectral region, nevertheless the 7$^{\text{th}}$ harmonic can be clearly observed. Harmonics beyond 2.5 eV has not been reported before in the previous works, although long wavelength drivers were employed for HHG in graphene, but with low repetition rates 1 kHz [69] and 100 Hz [60].

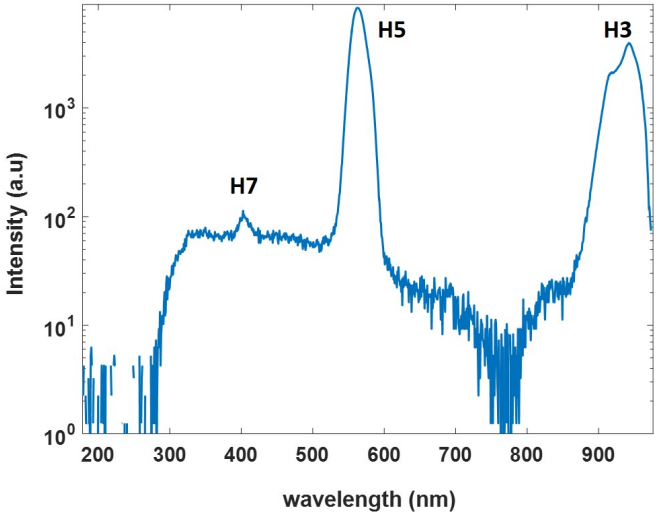

Figure 3.17: Harmonic spectrum from trilayer graphene on quartz with a 2.9 μm driving wavelength. The laser intensity is $\sim 0.05\,\text{TW/cm}^2$.

Isolating graphene samples in an oxygen-free atmosphere

The breaking of the sp^2 carbon hybridization upon laser exposure causes oxidization of the graphene under ambient conditions. The oxidation has been ascertained as a major cause of the fast damage rate. To decrease the damage rate by limiting the oxidation of graphene, we isolate the graphene samples in a nitrogen gas supplied box. The experimental setup is the one shown in figure 3.11, and the nitrogen gas box is shown in figure 3.18.

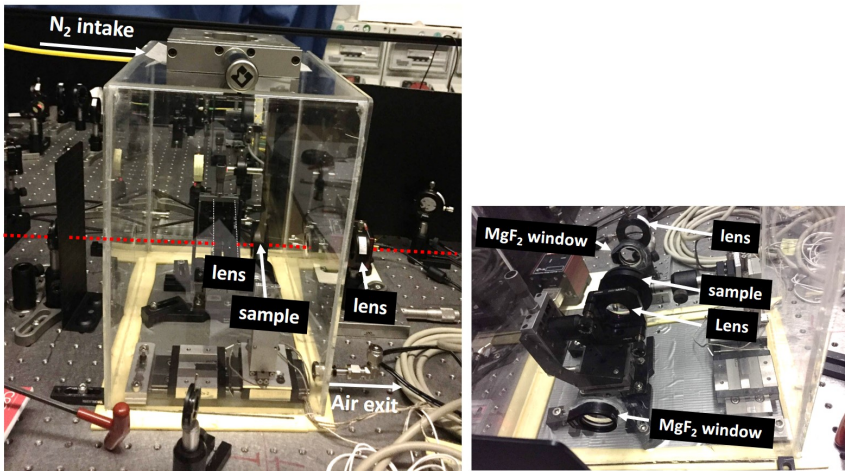

Figure 3.18: Modified experimental setup of the HHG experiment in graphene in nitrogen (N_2) gas.

We compare the harmonic spectra from monolayer graphene on quartz under air versus under nitrogen atmosphere. The results are shown in figure 3.19.

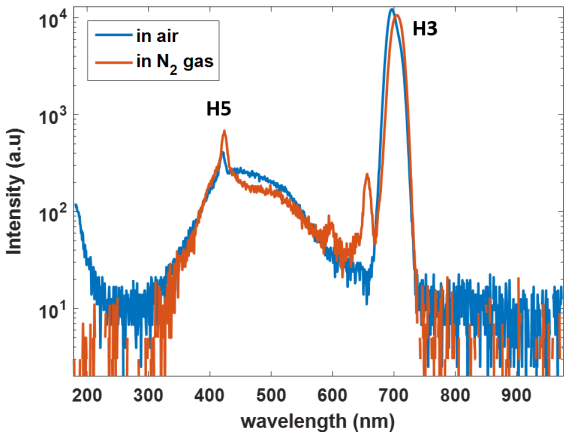

Figure 3.19: Harmonic spectra from monolayer graphene in air and in nitrogen atmosphere, with 2.1 μm driving wavelength at a laser intensity of $\sim 0.08\,\mathrm{TW/cm^2}$.

A slight increase of harmonic 5-to-fluorescence signal is observed when graphene is isolated under nitrogen gas. However, the striking improvement is in the damage rate upon laser exposure of graphene samples when isolated in N_2 gas. The decay time of H3 signal generated from monolayer graphene on quartz is measured and reported in figure 3.20(a). The measurement, which is carried out at low intensity (0.07 TW/cm^2), results in a decay time (τ) of 190 s. The second peak in the figure corresponds to a new refreshed spot on the sample. Note that the decay time is taken as the time during which the harmonic signal drops to half from the constant signal of quartz (at 0.2 (a.u.)). Figure 3.20(b) compares the decay

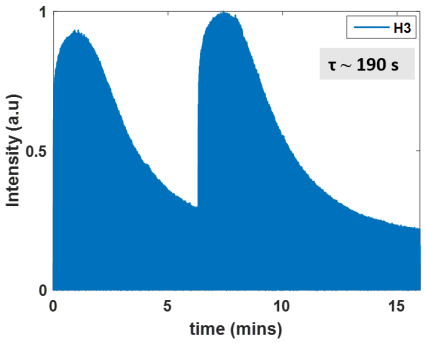

(a) Time evolution of H3 spectra from monolayer graphene on quartz isolated in nitrogen gas, at 0.07 TW/cm^2 of laser intensity.

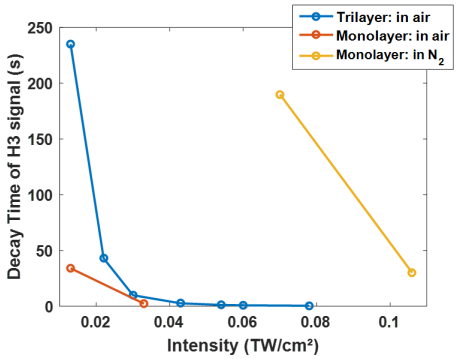

(b) Decay time of H3 signal, generated from trilayer and monolayer graphene samples on quartz, in air and in nitrogen atmosphere, as a function of time.

Figure 3.20: Comparison of the harmonic generation in graphene in ambient conditions of temperature and pressure, and in a nitrogen gas isolation.

times of H3 signal generated from monolayer and trilayer graphene in air and in N_2 gas as a function of the laser intensity. In air, the decay time of H3 signal from monolayer of graphene at 0.01 TW/cm^2 is $\sim$ 35 s (red curve), while in N_2 gas, the decay time is increased by a factor of 4 (190 s) (yellow curve) and at much higher laser intensity (0.07 TW/cm^2). This shows that the oxidation is a critical factor that contributes significantly to the damage rate. Combining the moving sample procedure, explained in section 3.3, together with providing an oxygen-free atmosphere around graphene, permits systematic measurements of a stable harmonic signal from graphene and at higher laser intensities. Another interesting feature is the slower decay rate of H3 signal generated from monolayer graphene in air (red curve), compared to that of trilayer graphene (blue curve) with the increase of the laser intensity. While the decay time of H3 from trilayer of graphene drops rapidly as the laser intensity is increased from 0.01 TW/cm^2 to 0.03 TW/cm^2, the damage seems to be slower in monolayer graphene as the intensity increases. As a future perspective, performing the experiment under vacuum would better solve the damage problem. Although we are able to reduce the damage rate, the broadband fluorescence couldn't be suppressed enough to detect higher harmonic orders which are of our interest to investigate.

3.8 Conclusion and Perspectives

3.8.1 Conclusion

In summary, we reported in this chapter on the high harmonic generation in graphene samples of different number of layers. In the nonperturbative regime, the 3^{rd} and 5^{th} harmonics were generated from monolayer, trilayer and 6-8 layers of graphene on a quartz substrate. Theoretical simulations in the TDDFT framework showed that the polarization dependences of the generated harmonics are sensitive to the band structure of graphene; H3 and H5 generated from the conical region of the band structure showed an isotropic dependence, while higher order harmonics revealed an anisotropic dependence, particularly a 6-fold symmetry consistent with the symmetry of the crystal structure of graphene. In agreement with the simulations, we verified experimentally the isotropic dependence of the 5^{th} harmonic efficiency on the laser polarization. In addition, we demonstrated here for the first time harmonic generation up to the 5^{th} order from freestanding graphene. Those HHG experiments were complicated because of two major challenges: the high damage rate of the graphene samples and the generation of a broadband fluorescence, which limited the ability to sustain the harmonic signal for long acquisition times, detect higher order harmonics and perform systematic measurements. To overcome these limitations, our findings highlight the importance of isolating the graphene samples in an oxygen-free atmosphere in order to prevent their oxidation, their rapid damage and the generation of the broad fluorescence signal in the visible spectral region. Besides, the longer the laser wavelength and, simultaneously, the shorter the pulse duration, the higher the damage threshold and the more efficient the generation process is. The choice of the substrate could also play a role. For example graphene is more persistent being deposited on a silicon carbide (SiC) or hexagonal-boron nitride (h-BN) substrates. SiC and h-BN have a hexagonal crystal structure, which matches the crystal structure of graphene, and results in a stronger interbonding. Studies have shown that the adhesion energy of graphene-SiC is higher than graphene-SiO_2 [106, 107]. Though graphene is not a robust material for the generation of UV and vacuum harmonics, it nevertheless opens a new route to study the nonlinear response of graphene with femtosecond laser pulses in the strong field regime.

3.8.2 Future Perspectives

An interesting study would be to explore HHG in 2D semiconductors driven by an *out-of-plane* polarization. Usually, in a transmission HHG experiment, the surface plane is perpendicular to the propagation direction of the laser beam, and the laser polarization is in the plane of the sample (figure 3.21(a)). This would drive the electron wavepacket to oscillate in the lattice plane. However, in the case of a laser polarization perpendicular to the sample plane (figure 3.21(b)), the electric field would extract the electron out of the lattice, and would drive it to accelerate in the continuum. Interestingly, this behavior recalls the semiclassical electron trajectories of HHG in atomic gases. The 2D nature of the generation medium such as graphene, allows studying the HHG emission with an *out-of-plane*

polarization, a configuration state that cannot be achieved with bulk crystals. This is because in the bulk, except at the surfaces, one cannot free electrons into the vacuum and generate harmonics with them. Tancogne-Dejean et al. [71]

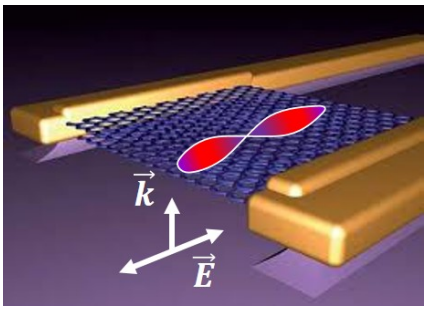

(a) In-plane polarization
Crystal-like response.

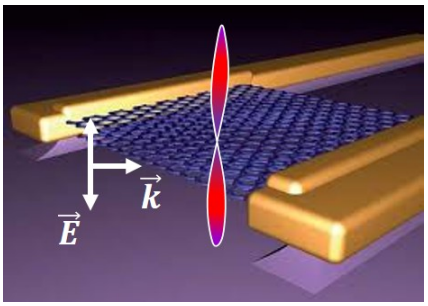

(b) Out-of-plane polarization
Atomic-like response.

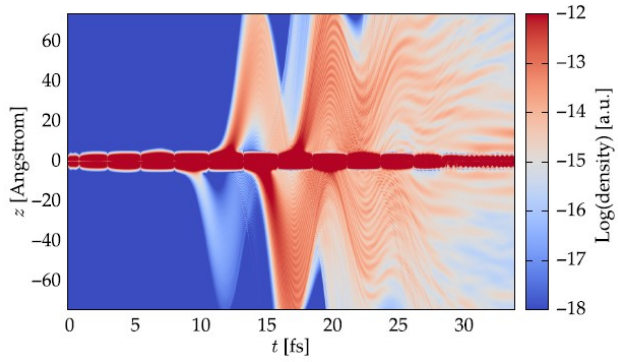

(c) Simulation of electron trajectories in h-BN driven by an out-of-plane polarization, during the HHG process [71].

Figure 3.21: HHG driven by an *out-of-plane* polarization.

explored HHG from a freestanding monolayer of hexagonal-boron nitride (h-BN) with an *out-of plane* polarization by performing TDDFT simulations. The electron trajectories during the HHG process driven by an *out-of plane* polarization are shown in figure 3.21(c). Indeed, the simulations show that during the laser pulse, the electrons leave the lattice (red horizontal part), accelerate in the continuum and some of them return to the monolayer where they emit a harmonic photon. The harmonic spectrum obtained (not shown here) extends to a cutoff energy exactly equal to the one predicted for atomic gas HHG through the expression: $E_{cutoff} = E_w + 3.17U_p$, where E_w is the work energy. This indicates that the HHG mechanism responsible for atoms governs the HHG mechanism of 2D materials for an *out-of plane* polarization. The two polarization configuration states (*in-plane* and *out-of-plane*) allow switching between the two HHG processes to explore for instance, the effect of the electron density.

Experimental trial

In a first attempt to experimentally investigate the harmonic generation in graphene with an *out-of-plane* polarization, we tilt our freestanding graphene sample by $\sim 20°$ from the vertical axis, as shown in figure 3.22. The freestanding graphene sample is a monolayer of graphene on a copper (Cu) grid of 6.5 μm circular holes. In this configuration, a laser beam vertically polarized (s-polarization) decomposes into an out-of-plane and an in-plane polarization components, while a horizontally polarized beam (p-polarization) would be fully in the plane of the graphene layer. One drawback of this configuration lies in a reduced intensity in the sample. We

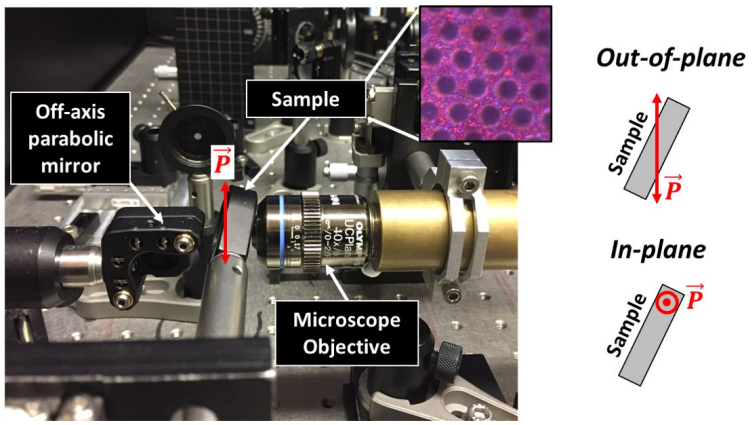

Figure 3.22: Experimental configuration for harmonic generation with an *out-of-plane* polarization.

measure and compare the efficiency of the harmonic generation driven by both polarization states. The NOVAE laser beam at a central wavelength of 2.1 μm is employed. Figure 3.23(a) depicts the spectra of the 3$^{\text{rd}}$ harmonic generated from freestanding monolayer graphene with an in-plane polarization (input horizontal polarization) and an out-of-plane polarization (input vertical polarization), measured at an estimated laser intensity of 0.07 TW/cm^2 at the focus position of the laser. The 3$^{\text{rd}}$ harmonic generation efficiency is lower in the latter case. Indeed, TDDFT simulations by Nicolas Tancogne-Dejean (private communication), shown in figure 3.23(b), reveal a lower harmonic generation efficiency when the HHG process is driven with an out-of-plane polarization. However, our experimental measurement is not of a purely out-of-plane contribution. With this experimental configuration the detected harmonics are also those generated from the in-plane polarization component. The reasonably lower signal in the experimental case of the out-of-plane polarization, is due to the fact that the effective intensity in the graphene sample is lower than the intensity in the case of the full in-plane polarization. Notice that the harmonic signal drops significantly even by a small tilt of the sample ($\sim 20°$). Being limited by the maximum pulse energy of the laser and the low damage threshold of the graphene samples, as previously discussed in the chapter, higher order harmonics couldn't be measured. A signature of the out-of-plane polarization would be detected at the cut-off harmonic energy, which could be achieved with the proposed solutions discussed in section 3.7; that is a

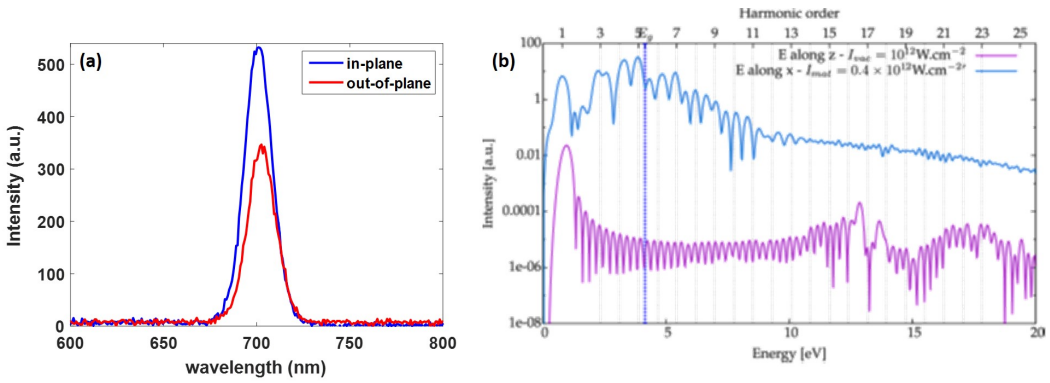

Figure 3.23: (a) Spectra of harmonic 3 (700 nm) generated from freestanding monolayer graphene on Cu grid with an in-plane (blue plot) and an out-of-plane (red plot) polarization states, at a laser intensity at the focus of 0.07 TW/cm^2. (b) TDDFT simulations of the HHG spectra in graphene with an in-plane (bue plot) and an out-of-plane (violet plot) laser polarization (private communication).

long wavelength, short pulse duration driving laser beam, in addition to carrying out the experiment under vacuum. Besides, other 2D materials can be investigated such as h-BN, which has a higher damage threshold than graphene. For a laser pulse in the near-IR spectral range, the calculated damage threshold of h-BN is 7.95 TW/cm^2 [71], while for graphene it is $\sim$ 3 TW/cm^2 in vacuum [108].
Another idea, yet technically more complicated, would be to pattern binary phase lenses on a substrate such as quartz and then transfer graphene or h-BN on top. The binary phase lens serves to focus and transform a radially polarized laser beam into a longitudinally polarized spot [109, 110]. An illustration of the function of such binary lens is shown in figure 3.24 (a). A possible sample configuration to achieve an out-of-plane polarization in 2D materials is schematized in figure 3.24 (b). This configuration ensures a pure response of the 2D layer to the out-of-plane polarization.

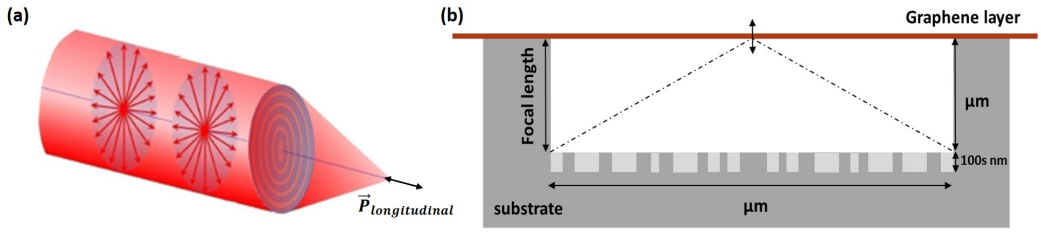

Figure 3.24: (a) Longitudinally polarized spot by focusing a radially polarized beam on a planar binary phase lens [110]. (b) Sample configuration combining the creation of the longitudinal polarization with graphene layer to drive the HHG process with an out-of-plane polarization.

The question then is: how would one experimentally measure the pure harmonic emission driven by an out-of-plane polarization?

Chapter 4

Polarization Spectroscopy of HHG in Crystals

In this chapter, HHG from different semiconductor media are investigated. The dependence of the generation process on the driving laser properties, mainly its polarization, is thoroughly explored. In section 4.2, we investigate the laser dependent harmonic generation from different semiconductor crystals, zinc oxide (ZnO) and silicon (Si), which have different optical and electronic properties. In section 4.3, we study the generation of deep UV and visible harmonics from GaAs in transmission and reflection geometries, and highlight the importance of linear and nonlinear propagation effects in the medium of generation. Besides, HHG in magnesium oxide (MgO) and chromium-doped MgO crystals is also studied in section 4.4, where high emphasis is put on the nonlinear propagation effects, in space and time domains. Finally, in section 4.5, we demonstrate the generation of XUV harmonics from MgO crystals. Making use of the strong anisotropic dependence of vacuum harmonics on the laser polarization, we introduce the *anisotropy gating* technique, in section 4.6, for the generation of isolated solid-state XUV attosecond radiation. This chapter represents the core work of this thesis.

4.1 Introduction

Solid-state HHG process strongly depends on the laser intensity and polarization as discussed in Chapter 2.2.3. These two important variables are the means to control the efficiency of the harmonic generation. The dependence of the HHG process on the laser polarization is studied by measuring the harmonic signal while varying the angle between the linear polarization of the laser field and the crystal axis. The dependence reveals the symmetry of the semiconductor crystal. For example, in cubic or zinc-blende semiconductors a fourfold symmetry is revealed while for hexagonal crystal structures, like the previously studied graphene, the symmetry obtained is a sixfold symmetry. Higher order harmonics exhibit a stronger polarization dependence, as they are generated in higher anisotropic regions of the band structure. In addition, the intensity dictates the excursion of the ionized electrons. Therefore, they can explore higher energy regions of the band structure if the electric field is strong enough. The polarization dependence of the harmonic efficiency can consequently vary with the intensity.

4.2 Anisotropic HHG in Different Semiconductor Crystals

In this section we investigate the polarization dependence of harmonics generated in air i.e. in the deep ultraviolet and visible spectral range from different semiconductor crystals, mainly zinc oxide and silicon.

4.2.1 High Harmonic Generation in ZnO

Zinc oxide (ZnO) is a direct bandgap semiconductor with a gap energy of 3.37 eV. It has proved to be an efficient medium for harmonic generation [16]. Here, we investigate HHG in a zinc oxide crystal driven by the laser pulses of the NOVAE laser.

Experimental Details

A sketch of the experimental setup is shown in figure 4.1. The central wavelength of the laser is 2.1 μm, its repetition rate is 18.66 MHz, and its pulse duration is 82 fs. The telescope, which consists of a 4 cm diverging lens followed by a 15 cm converging lens to collimate the beam, has been introduced in the beam path to enlarge the laser beam diameter by a factor of 3.75. This enlargement allows a tighter focus and consequently higher intensities. The laser is focused by a 3 cm focal length aspheric lens at the exit surface of the sample to maximize the generation of below and above bandgap harmonics. The harmonics generated are then collected by a 10 cm focal length lens and focused on a CCD camera. A flip mirror is mounted before the camera to allow the focusing of the harmonics on a spectrometer. The ZnO

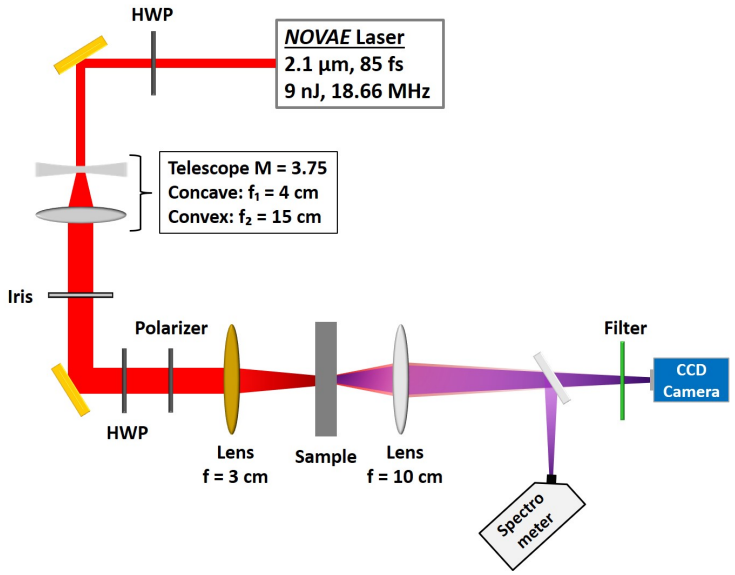

Figure 4.1: Sketch of the experimental setup for HHG experiments in air, with the NOVAE laser.

crystal is 200 μm thick with (0001) orientation i.e. a hexagonal crystal structure unit cell.
We detect up to the 7th harmonic (300 nm) from ZnO. Figure 4.2(a) depicts the harmonic spectrum measured at an estimated laser intensity (in vaccum) of 0.4 TW/cm^2. The band edge of ZnO corresponds to a wavelength of $\sim$ 360 nm, therefore H3 and H5 are below bandgap harmonics, while H7 is above bandgap harmonic. Below bandgap harmonics in ZnO have shown a perturbative dependence on the laser intensity, while above bandgap harmonics show a nonperturbative behavior [111]. Studies of the polarization dependence of H3, H5 and H7 are carried out. The results are shown in figure 4.2(b). The perturbative harmonics, H3 and H5 reveal an isotropic dependence. Moreover, the band structure of ZnO around the bandgap is isotropic up to a conduction band energy of 6 eV [112, 113], which explains why the polarization dependence of H7 (4.1 eV) is also isotropic. Accordingly, using higher intensities would allow detecting higher harmonic orders, and observing their anisotropic laser polarization dependence. Ghimire et al. [16] reported on a strong dependence of the harmonic generation in ZnO on the laser polarization, particularly a fourfold symmetry, but their ZnO crystal had a cubic unit cell, in which the optic axis is not along the laser propagation direction. This permitted the generation of even harmonics, which are not present in our case.

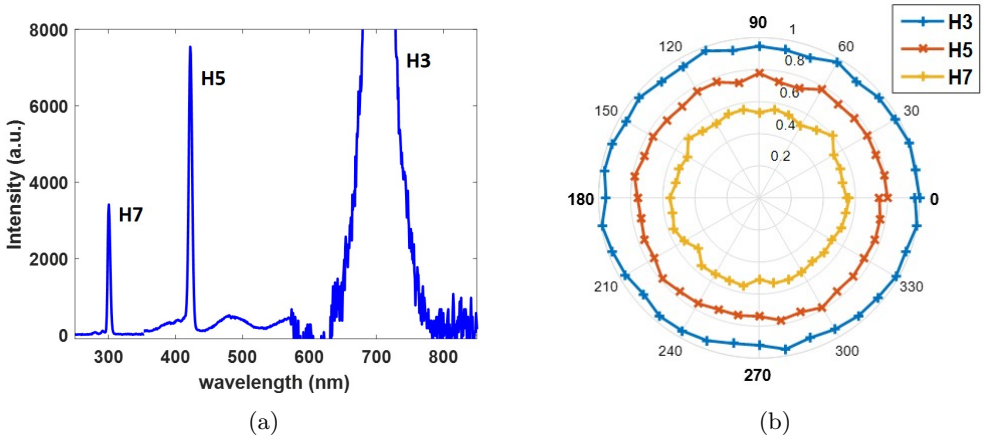

(a) (b)

Figure 4.2: (a) HHG spectrum from ZnO, at an estimated laser intensity (in vacuum) of 0.4 TW/cm^2. (b) Polarization dependences of H3, H5 and H7 generated from ZnO, at 0.28 TW/cm^2 laser intensity.

4.2.2 High Harmonic Generation in Silicon

Silicon is an indirect bandgap semiconductor with an indirect bandgap energy of $E_g \simeq 1.12$ eV. It is a centrosymmetric crystal and has a diamond cubic crystal structure. Although the minimum bandgap in silicon is indirect, tunneling is mostly probable at the Γ point at the direct gap which corresponds to $E_\Gamma \simeq 3.4$ eV [114]. The band structure of silicon is shown in figure 4.3(a). In this section, we study the harmonic generation in a 300 μm thick (100) cut Si sample. The same experimental

setup as the one described in section 4.2.1 was implemented for this study in our laboratory at CEA, Saclay. We generate up to the 9th harmonic from silicon, which is 233 nm in wavelength and corresponds to 5.32 eV of photon energy. Figure 4.4(a) shows the harmonic spectrum measured from the 300 μm thick silicon sample. We

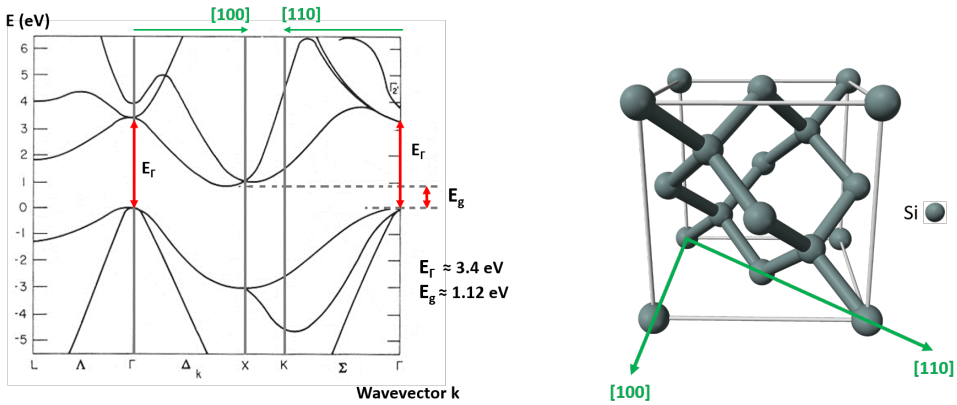

(a) (b)

Figure 4.3: (a) Band structure and (b) a 3D unit cell of the crystal structure of silicon.

perform polarization measurements for harmonics 3, 5, 7, and 9 generated at a laser intensity of 0.29 TW/cm^2. The results are depicted in figure 4.4(b). The laser is initially set to vertical polarization, where in this state the polarization is aligned along the [110] direction of the crystal; this is the 0° point on the polar plot and by every 90° rotation. Polarization dependences of all harmonics reveal a fourfold symmetry. The harmonic signal is maximum when the polarization is aligned along the [110] directions, and is minimum when the polarization is along the [100] directions of the crystal.

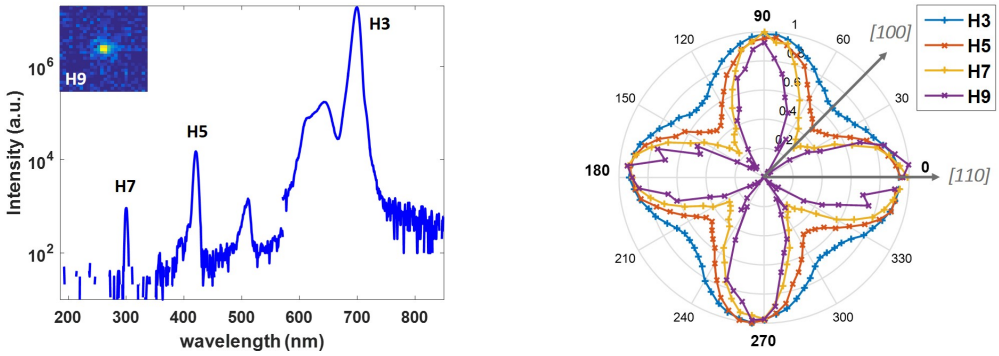

(a) (b)

Figure 4.4: (a) Harmonic spectrum measured from 300 μm thick (100) Si crystal, at a laser intensity of 0.34 TW/cm^2. (b) The polarization dependences of the generated harmonics at an intensity of 0.29 TW/cm^2.

The same result was reported by G. Vampa et al. [68]. This reflects the symmetry of the diamond cubic crystal structure of silicon. The contrast becomes higher as the harmonic order increases, which is due to the fact that higher order harmonics are more sensitive to the curvatures and anisotropy of higher energy regions of the band structure.
It is worth comparing the polarization dependence of single crystals to polycrystalline samples to show how strongly correlated the laser polarization and the crystal structure of the generation medium are. Figure 4.5 shows the harmonic spectra measured from a 100 nm thick polycrystalline silicon sample. The blue spectrum is obtained from a vertically polarized laser beam, and the red one is obtained by a 45° rotation of the laser polarization. The harmonic generation efficiency is identical along the two perpendicular crystal axes. Therefore, no anisotropy is observed in polycrystalline semiconductors. The isotropic polarization dependence of the HHG efficiency in polycrystalline samples could be interpreted as an average of the anisotropic HHG efficiency from single crystals. Notice that the efficiency

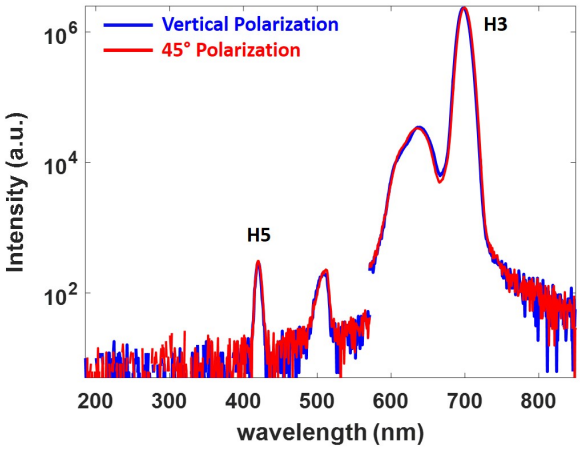

Figure 4.5: Harmonic spectrum from polycrystalline silicon sample with a vertical polarization (blue spectrum) and a 45° polarization (red curve), at 0.34 TW/cm^2.

of the generation in a polycrystalline sample is less than in a single crystal; at the same laser intensity only H3 and H5 are detected from polycrystalline Si, while in a single crystal (100) Si, harmonics up to the 7$^{\text{th}}$ order are detected. If the size of the crystallites of a polycrystalline sample is comparable to a couple of unit cells, one would expect a similar behavior as amorphous solids. Y. S. You et al. [115] have studied the role of the long-range periodicity on the HHG emission, and concluded that coherent collisions over several unit cells contribute significantly to the HHG process.

4.2.3 Nonlinear Propagation Effects in Thick Silicon Crystals

Since the HHG experiment is carried out in transmission, this means that a laser beam focused at the exit surface propagates inside the crystal. Therefore, the

laser may accumulate linear and nonlinear propagation effects. To verify the presence of nonlinear effects, we characterize spatially and spectrally the harmonics generated from a thin 2 μm Si crystal and a thick 300 μm Si crystal in transmission geometry. The nonlinear propagation effects considered here are mainly the Kerr effect (a $\chi^{(3)}$ process) in the spatial and temporal domains. The Kerr effect in the spatial domain refers to the self-focusing effect in the generation medium, and the Kerr effect in the temporal domain is the self-phase modulation (SPM) effect, as discussed in Chapter 2.4.

4.2.3.1 Experiment with a Mid-IR Fiber Laser

In a first part of this study, we employ the NOVAE laser already described. We compare spatially and spectrally the harmonics generated in a silicon sample structured as a 300 μm thick silicon frame supporting a 2 μm thick silicon membrane (Norcada company). The exit plane of the sample is identical for both thicknesses with respect to the laser propagation direction. This particular configuration allows us to shift easily from the thick crystal to the thin one, keeping all experimental parameters identical. Note that both the frame and the membrane have a (100) orientation.

Spatial Characterization

We measure the mode size of harmonic 3 and harmonic 5 at the exit surface of the sample, generated at an estimated laser intensity in vacuum of 0.11 TW/cm^2. The near-field image of the mode is obtained by a microscope objective aligned after the sample which focuses the harmonics on the CCD camera. The microscope objective provides a better resolution of the image and avoids abberation problems. Figure 4.6 shows the harmonic mode size of each of H3 and H5 generated from 300 μm and 2 μm thick Si. As a first look, we can notice that the harmonic mode from the thicker sample is slightly smaller than that from the thinner sample. We precisely compare the mode sizes of the 3$^{\text{rd}}$ and 5$^{\text{th}}$ harmonics. For each harmonic, the image of its spatial mode was smoothed by a Gaussian function, and a vertical cross-section along its center is taken to calculate the mode size at FWHM. A reference sample with a known size was imaged by the microscope objective. The effective image pixel size was found out to be 0.039 μm. An estimation of the spatial modes of harmonic 3 and harmonic 5 at FWHM results in the following: from the thick silicon sample, the mode size of H3 and H5 is 4.21 μm and 3.28 μm, respectively, while from the thin silicon sample, the mode size of H3 and H5 is 4.99 μm and 3.74 μm, respectively. The difference in the mode sizes between the thin and the thick silicon crystals is $\sim$ 0.78 μm for H3 and $\sim$ 0.5 μm for H5, which indicates that the self-focusing effect is present in the thick samples. Although, the difference in the harmonic mode sizes is rather small, it results in an increase of the effective intensity in the 300 μm thick sample by a factor of $\sim$ 1.4. This explains the higher generation efficiency in the thick (300 μm) silicon sample, as can be seen in figure 4.7. Indeed, since we are limited by the maximum pulse energy delivered by the NOVAE laser, the self-focusing effect has turned an advantage in this case.

Due to the low laser intensities involved we expect that the nonlinear absorption is minimal.

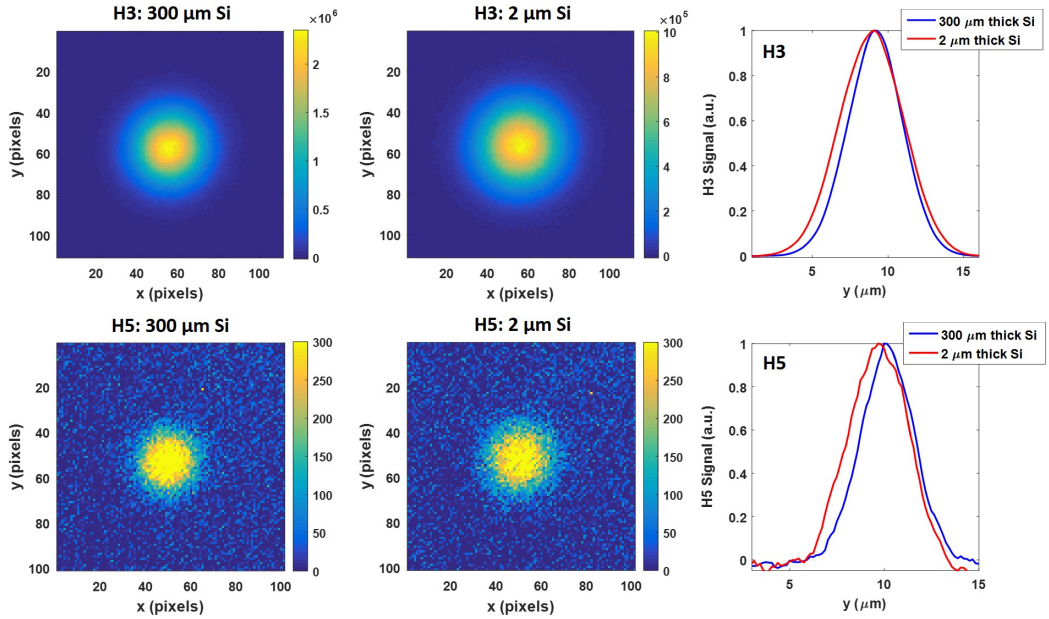

Figure 4.6: Spatial modes of H3 (first row) and H5 (second row) measured at the exit surface of a 300 μm and 2 μm thick silicon samples, at an estimated laser intensity of 0.11 TW/cm^2. The column on the right shows lineouts of the profiles across their centers.

Spectral Characterization

Although in the spatial domain, the self-focusing effect can be noticed, no broadening of the harmonics in the spectral domain is observed (figure 4.7). Note that the spectrometer might not provide a high resolution, but we expect that the self-phase modulation (SPM) effect does not impact significantly the fundamental laser pulse.

4.2.3.2 Experiment with an OPCPA Laser System

In this part, we investigate the harmonic generation in thick and thin silicon samples employing both a 1.55 μm and a 3.1 μm driving wavelength beams. The experiment was carried out at Institut d'Optique Graduate School (IOGS), Palaiseau in 2019 with the group of Marc Hanna. The laser system employed is the OPCPA system providing a signal beam at 1.55 μm wavelength and an idler beam at 3.1 μm wavelength at a repetition rate of 125 kHz. The pulse duration of the signal and idler beams are 30 fs and 130 fs, respectively, as measured with an autocorrelator. A description of the OPCPA laser system is found in Appendix C. The laser beam is focused by a 5 cm focal length lens into the silicon sample. With this laser system

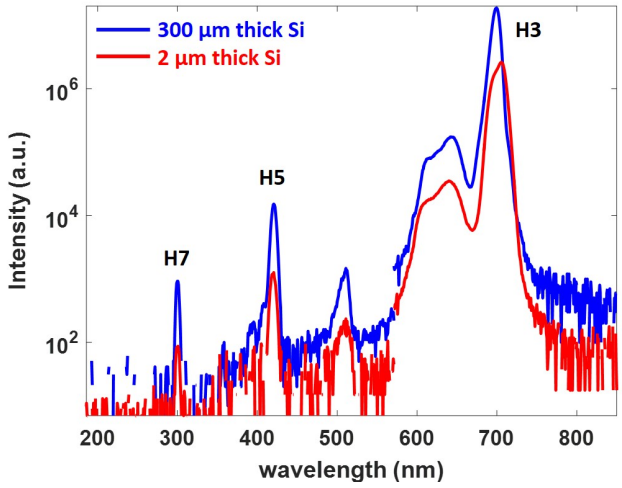

Figure 4.7: Comparison of the harmonic spectra measured from the 300 μm (blue spectrum) and the 2 μm (red spectrum) thick silicon samples, at an estimated laser intensity of 0.11 TW/cm^2.

we have access to higher laser intensities that induce stronger nonlinear propagation effects. Figure 4.8(a) and 4.8(b) show the harmonic spectra of the signal and the idler beams, respectively, measured from silicon, and compare the generation efficiency in the thick (300 μm thickness) and the thin (2 μm thickness) silicon samples. The generation efficiency is higher in the thin sample than in the thick one, contrary to what was observed with the NOVAE (2.1 μm) laser in the previous section. With

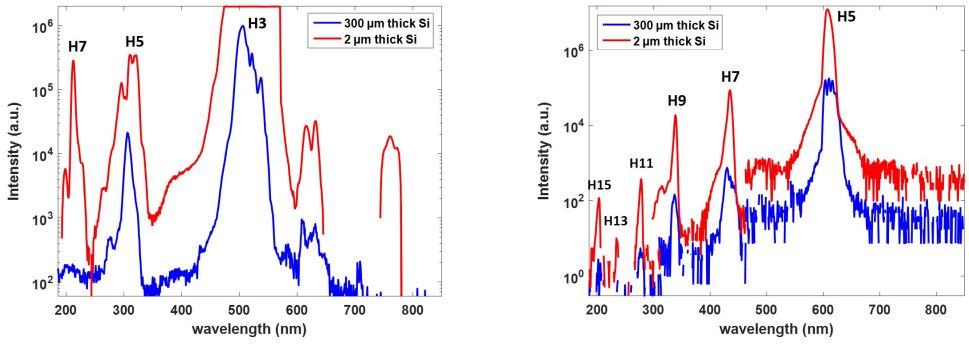

(a) (b)

Figure 4.8: (a) HHG spectra from silicon with a driving wavelength of 1.55 μm, at 4 TW/cm^2 (a), and with a driving wavelength of 3.1 μm, at 3.5 TW/cm^2 (b).

the 1.55 μm wavelength beam, at 4 TW/cm^2, we generate up to the 7$^{\text{th}}$ harmonic from the 2 μm thin sample, while harmonics up to the 5$^{\text{th}}$ order only are generated from the 300 μm thick sample. Similarly, with the 3.1 μm driving wavelength beam,

at an intensity of 3.5 TW/cm^2, we generate efficient harmonics up to the 15$^{\text{th}}$ order from the thin sample, however the efficiency is much lower in the thick one, where up to the 11$^{\text{th}}$ order harmonic only is generated. We attribute the decrease of the HHG efficiency in the thick silicon crystal to the nonlinear absorption at such high intensities, specifically the two-photon absorption (2PA), a $\chi^{(3)}$ process, at 1.55 μm wavelength (0.8 eV), and the three-photon absorption (3PA), a $\chi^{(4)}$ process, at the 3.1 μm wavelength (0.4 eV) [114, 116]. Experimentally, the self-focusing effect was detected; a first indication is that the effective position of the laser focus relative to the sample between the thin and the thick sample was different and had to be corrected to optimize the harmonic signal. Besides, for any change in the input intensity the laser focus position was mainly changing for the thick silicon crystal. Next, we compare the polarization dependences of the harmonics of the 3.1 μm laser generated from the 300 μm and the 2 μm thick Si samples. The laser beam is initially set to vertical polarization, in which the polarization is aligned along the [110] direction of the Si crystal. The results are depicted in figure 4.9. We observe

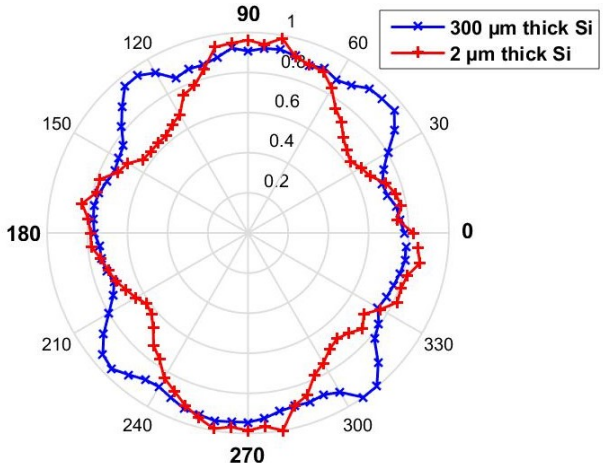

Figure 4.9: Normalized polarization dependence of H5 (620 nm) generated from 300 μm (blue curve) and 2 μm (red curve) thick silicon samples, at an estimated laser intensity of 3.5 TW/cm^2.

a clear difference in the polarization dependences of the harmonics generated from the thin and the thick Si samples. The polarization measurement of harmonic 5 generated from the 2 μm thick sample reveals a fourfold symmetry, similar to what was measured with the NOVAE laser (figure 4.4(b)). The harmonic signal maximizes when the polarization is aligned along the [110] directions, and is minimum when rotating the polarization by 45°, i.e. when the polarization is along the [100] directions of the crystal. As discussed before, the fourfold symmetry results from the symmetry of the cubic crystal structure of silicon. However, for the 300 μm thick sample, a different polarization dependence is revealed. An increase of the harmonic signal is measured at 45°, i.e. along the [100] directions of the Si crystal. We attribute this result to the anisotropy of the nonlinear propagation effects at such high intensities. Indeed, in the wavelength range of 2.3-3.3 μm, the three-

photon absorption in silicon has an anisotropic angular dependence [117].
We conclude that nonlinear Kerr effects in the spatial domain i.e. the self-focusing effect, plays an important role in the case of thick samples as observed with the NOVAE laser, and for higher laser intensities, the nonlinear absorption comes into play, which can significantly impact the high harmonic generation efficiency along different crystal directions due to its anisotropic nature.

4.3 UV-VIS Harmonic Generation in Gallium Arsenide

In this part of the thesis, we investigate the harmonic generation of odd harmonics from a gallium arsenide (GaAs) crystal. GaAs is a low bandgap semiconductor with a band gap energy of $E_g \sim 1.42$eV. It is also characterized by its high linear and nonlinear optical properties. We focus our attention on the polarization dependences of the generated harmonics as a function of the laser intensity. The experimental setup is the same as the one described in section 4.2.1. The laser beam (NOVAE) is focused by the 3 cm focal length lens onto our sample. The GaAs crystal has a (100) orientation and is 500 μm thick. The laser polarization is set to vertical, aligned along the [110] direction of the crystal i.e. ΓK direction in momentum space. Being limited to the maximum pulse energy delivered by the

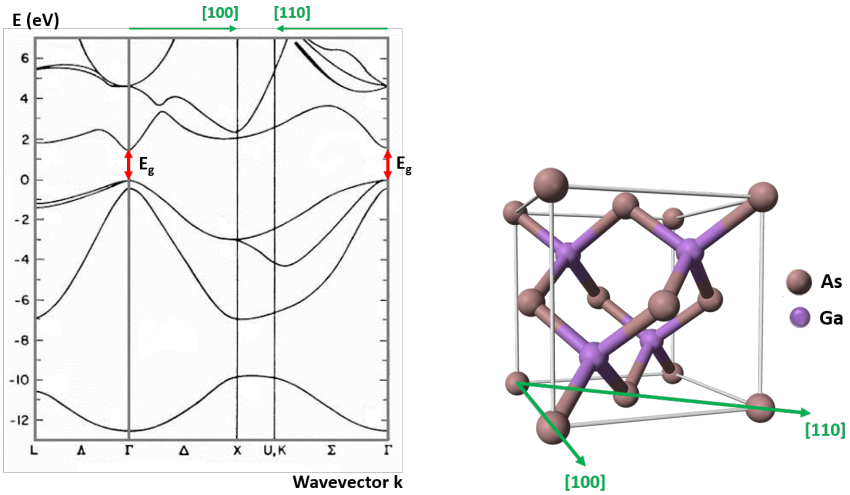

(a) (b)

Figure 4.10: (a) Typical band structure of GaAs, adapted from [118]. (b) 3D unit cell of the crystal structure of GaAs.

laser, harmonics up to the 7^{th} order (300 nm) only are efficiently generated in GaAs. Figure 4.11 shows the measured harmonic spectrum from GaAs. The peak centered at 880 nm corresponds to the fluorescence i.e. the direct band edge emission.

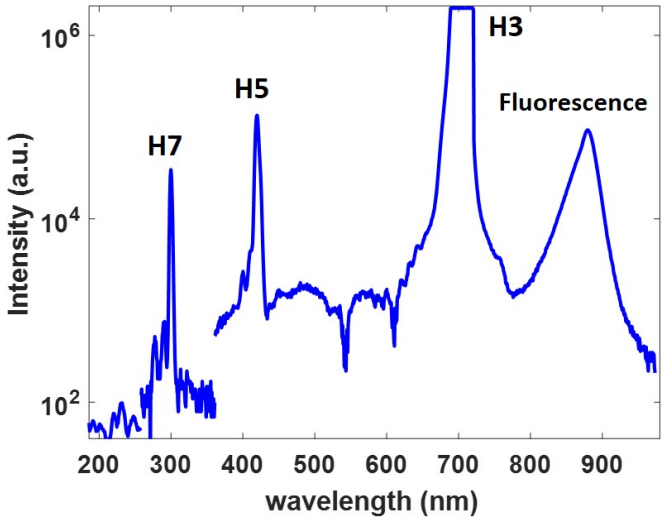

Figure 4.11: HHG spectrum from a 500 μm thick GaAs crystal, measured at an estimated vacuum intensity of 0.47 TW/cm^2.

4.3.1 Intensity Scaling: The Nonperturbative Regime

We measure the intensity scaling of the generated harmonics with the laser intensity. The results are plotted in figure 4.12 in a double logarithmic scale to extract the power law of each harmonic. The harmonic signals, of all three harmonics, scale nonperturbatively with the laser intensity; the scaling power $q \neq$ harmonic order.

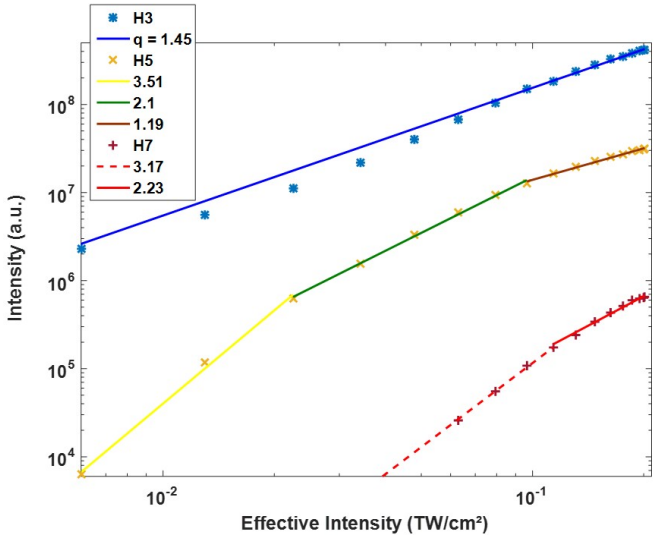

Figure 4.12: Intensity scaling of H3, H5 and H7 generated from GaAs. The laser polarization is aligned along the ΓK direction of the crystal.

The nonperturbative regime is achieved even at low laser intensities. Harmonic 3 scales as $S_{\mathrm{H3}} \propto I^{1.45}$, while the power law of the 5$^{\mathrm{th}}$ and 7$^{\mathrm{th}}$ harmonics differ from one intensity range to another. For intensities between 0.006 TW/cm^2 and 0.02 TW/cm^2, H5 scales as $S_{\mathrm{H5}} \propto I^{3.51}$. As the intensity increases, the scaling power q decreases down to 2.1 between 0.02 TW/cm^2 and 0.1 TW/cm^2. At higher laser intensities I > 0.1 TW/cm^2, the scaling power $q = 1.19$, which corresponds to the regime where the saturation starts to occur. For the 7$^{\mathrm{th}}$ harmonic, the harmonic intensity scales as $S_{\mathrm{H7}} \propto I^{3.17}$, for the intensity range 0.01 TW/cm^2 to 0.11 TW/cm^2. Beyond 0.1 TW/cm^2, the scaling power q decreases to 2.23. Unlike H5, the saturation of H7 occurs at higher intensities which were not accessible by this laser system.

4.3.2 Polarization Dependences

4.3.2.1 Ellipticity Dependences

To verify the dependence of the HHG process in crystals on the ellipticity of the fundamental beam, we perfom ellipticity measurements in which we vary the ellipticity of the driver via a quater-wavelength plate and record the harmonic signal on the CCD camera. The measurements are performed by varying the ellipticity of the laser beam from linear, i.e. vertically polarized (e = 0, QWP angle = 0°), continuously to circular polarization (e = 1, QWP angle = 45°). Note that the reported ellipticity values correspond to the quarter-wavelength plate angle; for instance, at e = 1, the QWP axis makes an angle of 45° with the incoming linear polarization. The measurements are carried out for harmonics 3 (H3), 5 (H5) and 7 (H7) (figure 4.13). All three harmonics reveal a similar dependence, the harmonic

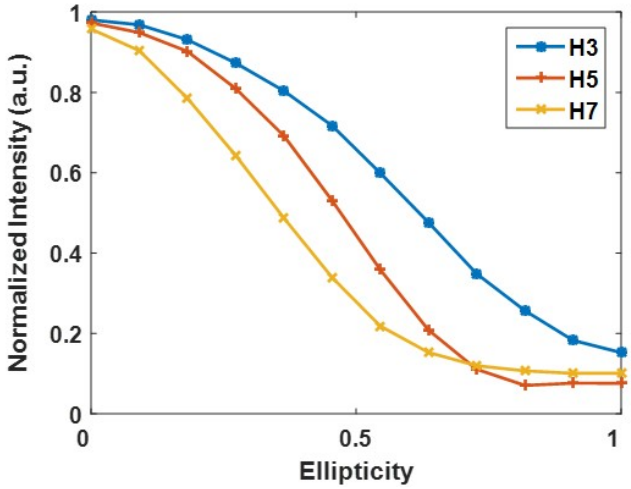

Figure 4.13: Ellipticity dependences of H3, H5 and H7 generated from the 500 μm thick GaAs crystal, at an estimated vacuum intensity of 0.11 TW/cm^2.

signal is maximum for a linearly polarized beam. As we start to introduce some ellipticity to the fundamental beam, the harmonic signal decreases until a minimum

value when the laser beam is completely circularly polarized. Notice that as the harmonic order increases the dependence of the generation efficiency on the laser ellipticity becomes more important. Indeed, the decrease in the harmonic efficiency with the increase of the laser ellipticity gets steeper for higher harmonic orders, yet the harmonic signal does not disappear for a circular polarization. In contrast to HHG in gases, the harmonic generation dependence on the laser ellipticity is less critical for HHG in crystals [44, 76].

4.3.2.2 Linear Polarization Dependences

We study the linear polarization dependence of the harmonic generation in GaAs, by rotating the linear laser polarization with respect to the initial crystal axis (ΓK) and monitoring the harmonic signal on the CCD camera. We perform these measurements for harmonics 3, 5 and 7 at different laser intensities. The laser polarization is initially aligned along the ΓK direction of the crystal; this is the 0° point on the polar plots. The results are depicted in the polar plots in figure 4.14. At low intensity (0.1 TW/cm^2), the polarization dependence of all harmonics reveals a fourfold symmetry, where the harmonic signal is maximized when the laser polarization is aligned along the ΓK directions and is minimized along the ΓX directions. This anisotropy reveals the symmetry of the zinc-blende crystal structure of GaAs. As the laser intensity is increased, we observe a change in the polarization dependent harmonic generation, mainly for harmonic 3 and harmonic 5. For harmonic 3, the contrast in the anisotropy decreases as the intensity increases, and for the maximum reached intensity (0.38 TW/cm^2) the polarization dependence becomes isotropic. Surprisingly, for harmonic 5 the anisotropy rapidly changes with an increase of intensity from 0.1 TW/cm^2 to 0.18 TW/cm^2, where at this latter intensity the dependence becomes more or less isotropic. However, for higher laser intensities the symmetry is rotated by 45°; the harmonic signal maximizes when the polarization is aligned along the ΓX direction. As for H7, the fourfold symmetry revealed consists of a maximum harmonic signal when the polarization is along the ΓK directions, and a minimum signal when the polarization is along the ΓX directions. The same dependence is maintained at any value of the laser intensity. However, in the case of H7, the harmonic emission exhibits a stronger dependence on the laser polarization. Indeed, the contrast in the polar scan of H7 is higher than the contrast in the polar scans of H3 and H5 at 0.1 TW/cm^2.

4.3.3 Nonlinear Propagation Effects

Since the measurements were carried out in transmission geometry we characterize and quantify nonlinear propagation effects, mainly self-focusing and absorption to make sure that they do not impact our results. We measure the 5$^{\text{th}}$ harmonic mode size (ω_{h}) at the exit surface of our GaAs crystal along the two main axes ΓK and ΓX and for different laser intensities (0.1 TW/cm^2 to 0.38 TW/cm^2). The 5$^{\text{th}}$ harmonic is selected for the study, as its polarization dependence at different laser intensities shows different behaviors. Considering the nonperturbative scaling power of H5, $q = 2$ in the intermediate intensity range (figure 4.12), we calculate the fundamental beam size (ω_{f} at FWHM) at the exit surface of the sample

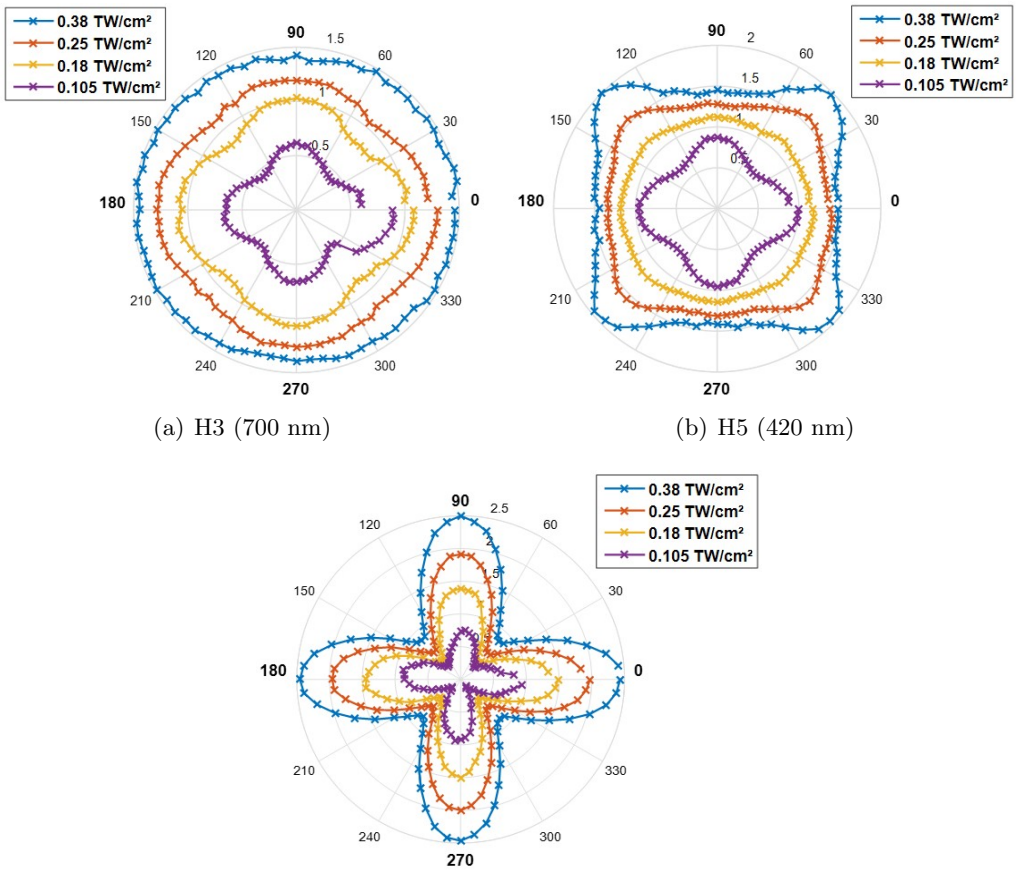

(a) H3 (700 nm)

(b) H5 (420 nm)

(c) H7 (300 nm)

Figure 4.14: Polarization dependences of H3, H5 and H7 of the NOVAE laser, generated from the 500 μm thick GaAs crystal, at different laser intensities. The 0° angle corresponds to a polarization state aligned along the ΓK direction of the crystal.

($\omega_f = \sqrt{q} \times \omega_h$) and measure the ouptut power, for different input powers. Tables 4.1 and 4.2 summarize the measurements and calculations for polarization along the ΓK and ΓX directions, respectively. Taking into account the calculated beam size and the measured output power, we estimate the effective intensity close to the exit surface, $I = \frac{0.83\,P}{\tau \times RepRate \times \omega_f^2}$, where $\tau = 82$ fs is the pulse duration, and RepRate = 18.66 MHz is the repetition rate. The variation of the beam size as a function of the laser intensity is plotted in figure 4.15(a). The measurements show that the fundamental beam size along ΓK decreases at a faster rate than along ΓX as we increase the laser intensity from 0.1 TW/cm^2 to 0.38 TW/cm^2. This means that the self-focusing effect is higher along the ΓK direction. Indeed, W. C. Hurlbut et al. [119] have studied the angular dependence of the nonlinear refractive index, n_2, of GaAs at a wavelength of 2 μm and showed that it is anisotropic; n_2 along ΓK is different than along ΓX, such that $n_2(\Gamma K) = 1.16\ n_2(\Gamma X)$. Theoretical calculations by D. C. Hutchings et al. [120] have also verified the difference

P_{input} (mW)	P_{output} (mW)	H5 mode size (μm)	Fundamental beam size ω_f (μm)	Effective intensity (TW/cm^2)
34	17.91	3.2	4.525	0.049
59	30.75	3.06	4.327	0.092
80	41.35	2.96	4.186	0.133
99	51.03	2.88	4.073	0.173
115	57	2.84	4.016	0.199

Table 4.1: Estimated effective intensities for different input powers, for a vertically polarized beam, i.e. along ΓK.

P_{input} (mW)	P_{output} (mW)	H5 mode size (μm)	Fundamental beam size ω_f (μm)	Effective intensity (TW/cm^2)
34	18.27	3.23	4.568	0.049
59	31.5	3.14	4.441	0.090
80	42.54	3.09	4.370	0.125
99	52.5	3.04	4.299	0.160
115	59	3	4.243	0.184

Table 4.2: Estimated effective intensities for different input powers, for a 45° polarized laser beam, i.e. along ΓX.

in the nonlinear refractive index of GaAs along the main principle axes, whereby $n_2(\Gamma K)/n_2(\Gamma X) = 2$. Then, we measure the output power of the beam exiting our GaAs sample along ΓK and ΓX for the different input intensities. The plot in figure 4.15(b) depicts the ratio of the output power to the input power as a function of the input laser intensity as calculated in vacuum. The decrease, though slow, in the ratio as the laser intensity increases implies that the absorption becomes higher for higher intensities. Moreover, the ratio of the output power to the input power is always lower along ΓK than along ΓX which implies that the absorption is slightly stronger along the ΓK direction, however this difference falls within the experimental error and can be neglected. It is noteworthy to mention that, interestingly, the three photon absorption (3PA) in GaAs at a wavelength of 2 μm also exhibits an angular dependence [119]. The 3PA coefficient along ΓK is larger than the 3PA coefficient along ΓX such that $\gamma(\Gamma K)/\gamma(\Gamma X) \approx 1.24$.
Finally, the variation of the effective intensity close to the exit surface of the sample as a function of the vacuum input intensity is plotted in figure 4.16. The result reveals that the estimated effective intensity increases with the input intensity and is slightly higher along the ΓK direction.
As a conclusion, the contribution of the nonlinear effects in the GaAs crystal does not explain the enhancement of the signal of the 3rd and 5th harmonics along ΓX

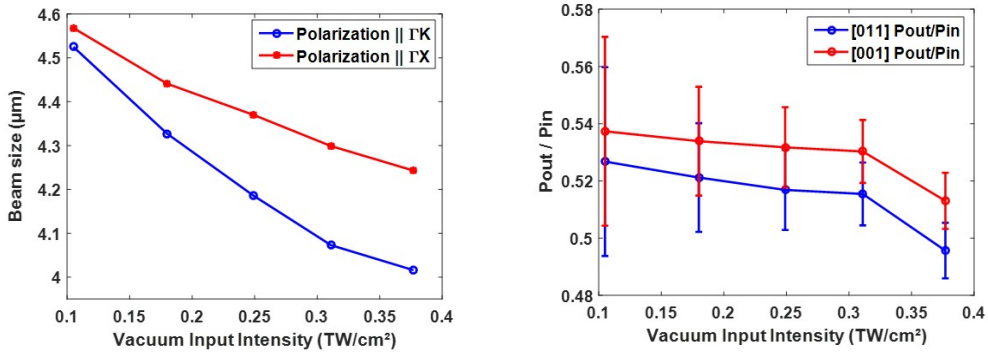

(a) (b)

Figure 4.15: (a) Fundamental beam size in a 500 μm thick GaAs crystal as a function of the laser intensity. (b) Ratio of the output power to the input power as a function with the laser intensity.

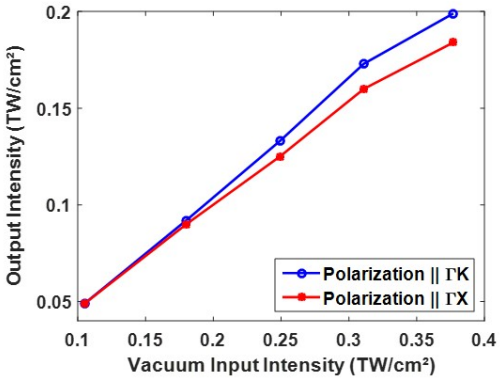

Figure 4.16: The estimated effective intensity at the exit of the GaAs sample as a function of the vacuum input intensity.

directions of the crystal with the increase of the input intensity. Therefore, the nonlinear propagation effects in this observation can be excluded.

4.3.4 Theoretical Calculations of Nonlinear Propagation Effects in the Spatial, Spectral and Temporal Domains

To account for the Kerr effect in the spatial domain, we calculate analytically the evolution of the laser beam $W(z)$ propagating along the z axis in a nonlinear medium of thickness d, as derived by Y. R. Shen [121]:

$$W(z)^2 = W_d^2 \left[\left(1 - \frac{P}{P_{cr}}\right) \frac{2z^2}{k^2 W_d^4} + \left(1 + \theta_d \frac{z}{W_d}\right)^2 \right] \tag{4.1}$$

where, W_d is the beam waist at the input plane, P and P_{cr} are the laser peak power and the critical power, respectively, k is the wavenumber and θ_d is the beam divergence at the input plane. These parameters are calculated as follows:

$$W_d = w_0\sqrt{1+\frac{d}{z_R}};\ P_{cr} = \frac{0.15\lambda^2}{n_0 n_2};\ \theta_d = -\frac{\lambda}{\pi n_0 w_0} \tag{4.2}$$

where w_0 and z_R are the beam waist at focus and the Rayleigh range, respectively. The self-focusing of a laser beam in a crystal occurs when the laser peak power is greater than the so-called critical power [122]. In particular, GaAs possesses high linear and nonlinear refractive indices at wavelengths around 2.1 μm, where n_0 = 3.38 and n_2 = 1.2 $\times 10^{-13}\,\mathrm{cm}^2/\mathrm{W}$ [119]. This corresponds to a critical power P_{cr} = 1.6×10^4 W. For the NOVAE laser, the maximum peak power is $P = 7 \times 10^4$ W $> P_{cr}$, therefore we expect a self-focusing effect inside the GaAs sample. Our experimental configuration, previously described in section 4.2.1, leads to a beam waist at the focus of $w_0 = 3.46\,\mu$m, and a Rayleigh range $z_R = 17.91\,\mu$m (estimated in vacuum). The evolution of the laser beam waist *W(z)* focused at the exit surface of a 200 μm thick GaAs sample, at a transmitted peak power of 5×10^4 W, is shown in the blue curve in figure 4.17. The laser beam indeed experiences the self-focusing effect at distance of ~ 15 μm from the exit surface. This can be compared to what

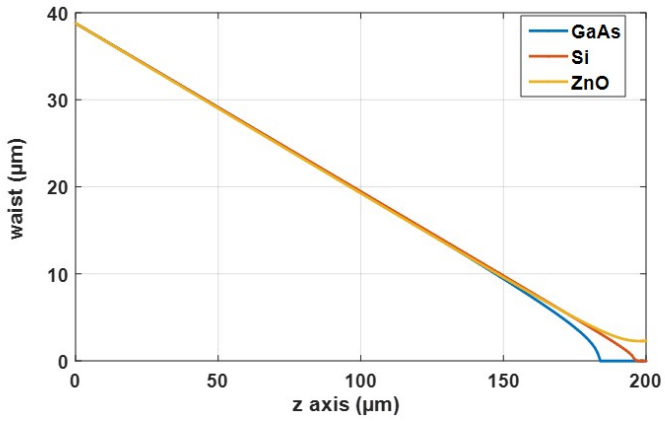

Figure 4.17: The evolution of the laser beam waist W(z) along the propagation direction in 200 μm thick GaAs and Si at a transmitted peak power of $P = 5 \times 10^4$ W and in ZnO at 7×10^4 W. The self-focusing effect appears in GaAs and Si near the exit surface, before the collapse of the beam. In this case, $W(z)^2$ takes non-physical negative values.

happens in a 200 μm thick Si sample. In silicon, $n_0(2.1\,\mu\mathrm{m})$ = 3.45 and $n_2(2.1\,\mu\mathrm{m})$ = $4 \times 10^{-14}\,\mathrm{cm}^2/\mathrm{W}$ [123]. The nonlinear refractive index n_2 is one order of magnitude smaller than in GaAs, yielding a critical power $P_{cr} = 4.6 \times 10^4$ W. The transmitted laser peak power in silicon is 7×10^4 W slightly greater than the critical power, which explains why the self-focusing effect appears later, at a distance of ~ 4 μm from the exit surface. This further validates the self-focusing effect in the thick Si sample observed when comparing the harmonic beam modes at the exit surface of the 2 μm thin and 300 μm thick Si crystals in section 4.2.3. Finally, zinc

oxide (ZnO) possesses lower linear and nonlinear refractive indices than silicon and GaAs ($n_0(2.1\,\mu\text{m}) = 1.92$ and $n_2(2.1\,\mu\text{m}) = 5.5 \times 10^{-15}\,\text{cm}^2/\text{W}$ [124]). Therefore, self-focusing does not occur and the beam propagates with no distortions in the ZnO crystal. Indeed, the transmitted laser peak power is $7 \times 10^4\,\text{W}$, which is less than the critical power of ZnO ($P_{cr} = 6.3 \times 10^5\,\text{W}$) by one order of magnitude. It is worth mentioning that in our experiment, the laser beam propagating in GaAs and silicon does not collapse, hence the calculations could be overestimating the self-focusing effect.
In addition, Kerr effect in the time domain has to be taken into account due to the high nonlinearity of GaAs at our driving laser wavelength. Calculations of nonlinear propagation effects in the spectral and temporal domains were performed by our collaborator Thierry Auguste, from LIDYL at CEA Saclay. The physical model, derived by A. Couairon et al. [125], describes the propagation of an intense pulse in a medium by solving the paraxial wave equation coupled to the time evolution equation for the electron density. The calculations are computed with our experimental parameters of the laser beam and the sample's linear and nonlinear refractive indices at the laser wavelength. The calculations give access to both the spectral and temporal profiles of the laser pulse after propagation in the 500 μm thick GaAs sample which are depicted in figure 4.18 (a) and (b), respectively. The input pulse spectrum and temporal profile are plotted in violet, and the output pulse for a beam focused at the exit surface of the 500 μm thick crystal is plotted in blue. In the spectral domain, a clear blue shift is observed in the output pulse

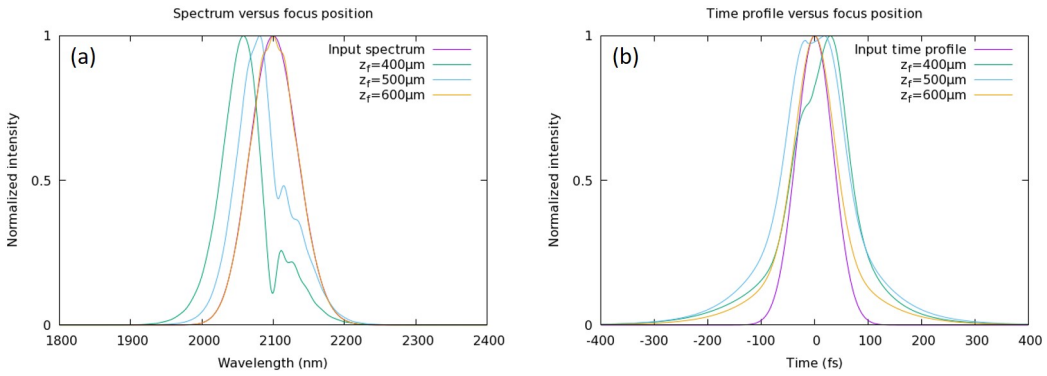

Figure 4.18: Spectral (a) and temporal (b) envelopes of the input laser pulse (violet curves) and after propagation in a 500 μm GaAs sample for different laser focus positions z_f. $Z_f = 500\,\mu$m (blue curves) represents a focus just at the exit surface of the crystal.

which is attributed to the photoionization effect. Moreover, an effect of the self-phase modulation is visible on the spectral pulse, which is narrower than the input pulse, with a spectral width of 55 nm, and a red wing emerging on its spectrum. As a consequence in the time domain, the pulse is much longer, with a pulse duration significantly increased to 130 fs. The focus position in the sample plays an important role. For instance, when the focus is inside the sample, 100 μm from the exit surface (green line), the photoionization induced blue shift is larger, and the self-phase modulation effect is also visible as a narrow spectral width (60 nm)

and a red wing on the pulse. In the temporal domain, the pulse duration is longer, where $\tau = 120$ fs. However, when the laser is focused 100 μm after the exit surface, the photoionization effect is minimal, as the output spectrum is not altered and overlaps with the input pulse. In the temporal domain, the pulse is slightly longer with a pulse duration of 95 fs. This also indicates that when the focus is outside the sample, the nonlinear propagation effects are minimal. Note that, given the nonlinear refractive indices of GaAs by W. C. Hurlbut et al. [119] along ΓX and ΓK directions, $1.2 \times 10^{-13}\,\mathrm{cm}^2/\mathrm{W}$ and $1.4 \times 10^{-13}\,\mathrm{cm}^2/\mathrm{W}$, respectively, the simulations reveal no difference in the output spectrum and temporal properties of the pulse for propagation along both directions of the GaAs crystal.
Even though the pulse energy of the NOVAE laser is low (6 nJ), nonlinear propagation effects play an important role in GaAs both in the spatial domain i.e. the self-focusing effect experimentally demonstrated, and in the temporal domain i.e. the photoionization and the self-phase modulation effects emphasized by the theoretical calculations. In conclusion, since HHG in transmission requires the fundamental pulse to propagate in the crystal to reach the exit surface, spatio-temporal distortions are accumulated by the laser pulses due to linear and nonlinear effects.

4.3.5 High Harmonic Generation in Reflection Geometry

For higher laser intensities, nonlinear propagation effects can alter the HHG mechanism and efficiency, and it is therefore challenging to disentangle these effects from the real physical mechanism of high harmonic generation [47]. To eliminate nonlinear propagation effects two possibilities are foreseen; one is to use very thin crystals if the harmonic generation is carried out in transmission, however, this is not possible for all semiconductor crystals, as some of them are very fragile and difficult to handle. Another possibility is to perform the experiment in reflection geometry. In this case the fundamental laser is focused at an angle of incidence on the sample, and only the backward reflected harmonics are collected. G. Vampa et al. [61] have reported on the observation of backward high harmonic emission from MgO and silicon. In the study, the incidence angle was set at 45° for MgO and 46° for silicon, this is because the harmonic signal decreases above 50° incidence angle. Relying on this study, we set our angle of incidence at $\sim 45°$.

4.3.5.1 Experimental Details

The experiment was realised at CEA with an OPCPA laser system (Appendix D). The idler beam operating at 2.42 μm wavelength, 100 kHz repetition rate, and 75 fs pulse duration is employed for the reflection HHG experiment from GaAs. The laser pulses are focused by a 7.5 cm focal length CaF_2 lens at 45° angle of incidence onto the 500 μm thick GaAs (100) crystal. The harmonic signal is optimized by an iris aperture which is opened to 5 mm in diameter. The estimated beam size at the focus is ~ 40 μm. The sample was placed on both a vertical manual translational stage to be able to refresh it in case of damage, and on a motorized rotational stage to study the dependence of the harmonic yield on the angle between the laser polarization and the crystal axis. A picture of the experimental setup is shown in figure 4.19.

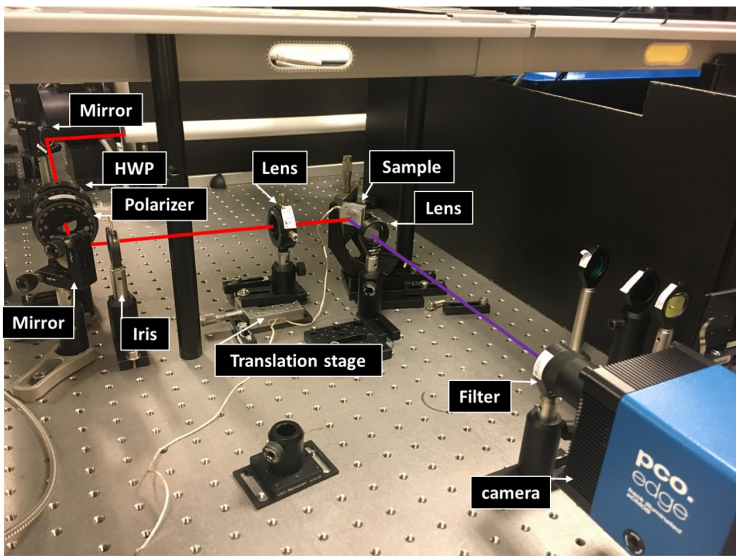

Figure 4.19: Experimental setup of the reflection HHG experiment in crystals with the idler beam (2.42 μm wavelength) of the OPCPA laser system at CEA, Saclay.

4.3.5.2 Theoretical Description

When an electromagnetic wave at an angular frequency ω_0, in a medium (1) of linear refractive index n_{01}, is incident at an angle θ_i on the surface of a bulk material (medium 2) having an index of refraction n_{02}, part of the beam will be reflected at an angle θ_r from the normal axis to the surface, while another part, transmitted in the bulk, will refract at an angle θ_s which is determined by Snell's Law: $n_{01}(\omega_0)\cos\theta_i = n_{02}(\omega_0)\cos\theta_s$. The amplitude of the transmitted refracted ray is determined by the Fresnel law of transmission. The Fresnel transmission (i.e. the power transmission coefficient) varies with the beam polarization and the angle of incidence, and is determined by the Fresnel relations of reflection (R) and transmission (T). For s and p polarizations, the Fresnel relations are given by $T_s = 1 - R_s$ and $T_p = 1 - R_p$, respectively, where $R_s = \left|\frac{n_{01}\cos\theta_i - n_{02}\cos\theta_s}{n_{01}\cos\theta_i + n_{02}\cos\theta_s}\right|^2$ and $R_p = \left|\frac{n_{01}\cos\theta_s - n_{02}\cos\theta_i}{n_{01}\cos\theta_s + n_{02}\cos\theta_i}\right|^2$ [63]. The Fresnel transmission coefficient of the fundamental field in GaAs as a function of the angle of incidence for s and p polarization states is plotted in figure 4.20(a). Note that, for a bulk GaAs sample, the linear index of refraction at the wavelength of our fundamental driving field ($\lambda = 2.42$ μm) is $n_{02} = 3.32$ [62] ($n_{01}(\text{air}) = 1$). The Fresnel coefficient for a s-polarized field (T_s) decreases with increasing angle of incidence, while for a p-polarized field the Fresnel coefficient (T_p) increases up to an angle of incidence of 73°, which is known as the Brewster angle θ_B, i.e. the angle at which the laser field does not reflect and is completely transmitted. The effective intensity close to the surface of the sample is then calculated by taking into account both the Fresnel transmission coefficient and the beam size at an angle of incidence θ_i. The beam area at an angle of incidence θ_i is given by $A_{\theta_i} = A/\cos\theta_i$ where A is the initial beam area at normal

incidence. Hence, the laser intensity at a given angle of incidence (θ_i) is calculated by multiplying the vacuum intensity (I) at normal incidence by the cosine of the incidence angle: $I_{\theta_i} = I \cos\theta_i$. Finally, the transmitted fundamental intensity close to the surface of the GaAs sample is calculated as $I_{transmitted} = I_{\theta_i} \times T$, and is plotted versus the incidence angle in figure 4.20(b).

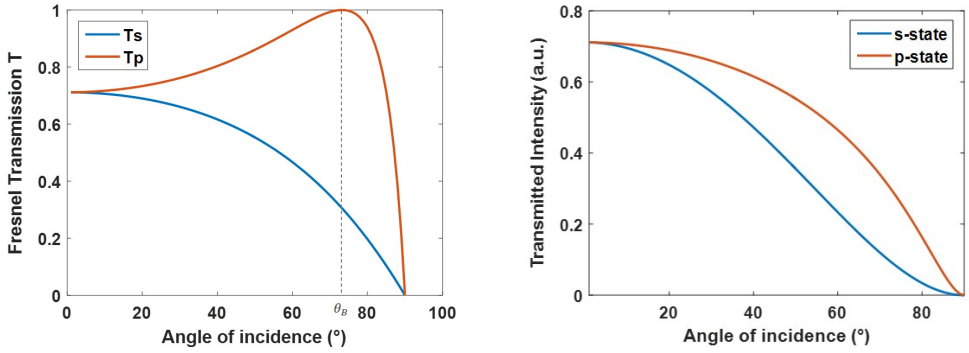

(a) (b)

Figure 4.20: (a) Fresnel transmission coefficient in GaAs at 2.42 μm laser wavelength versus the incidence angle. (b) Transmitted laser intensity in GaAs versus the incidence angle.

The effective intensity for both s and p polarized driver decreases as the incidence angle increases. This is because the beam area at the surface increases. In particular, for a p-polarized driver the surface area increases at a faster rate than the increase in the Fresnel transmission coefficient (red curve in figure 4.20(a)). Interestingly, the effective intensity for a p-polarized field is significantly higher than for the s-polarized one by a factor of ~ 1.4, at 45° incidence angle.
The generated harmonic wave refracts in the medium at an angle of refraction θ_t from the normal, which is determined by Snell's law $n_{02}(n\omega_0)\sin\theta_t = n_{01}(n\omega_0)\sin\theta_i$, while another part reflects and co-propagates with the reflected fundamental field at an angle θ_r, such that $\sin\theta_r = \sin\theta_i$. The amplitude of the reflected harmonic wave is then determined by its nonlinear reflection coefficient and the nonlinear polarization (section 2.1.2). It is given by [126]:

$$E_{n,s} = -4\pi \times r_s P_{NL}\ ,\ s - state$$
$$E_{n,p} = 4\pi \times r_p P_{NL}\ ,\ p - state$$

where r_s and r_p, the nonlinear reflection coefficients of the harmonic wave for s-polarized and p-polarized driver, respectively, are derived, for perturbative harmonics, as [126]:

$$r_s = \sin^2\theta_t \sin\theta_s [\sin(\theta_r + \theta_t)\sin(\theta_s + \theta_t)\sin\theta_r]^{-1} \tag{4.3}$$

$$r_p = \sin^2\theta_t \sin\theta_s \sin(\alpha+\theta_t+\theta_s)[\epsilon_r \sin(\theta_r+\theta_t)\sin(\theta_s+\theta_t)\sin\theta_r \cos(\theta_t-\theta_r)]^{-1} \tag{4.4}$$

ϵ_r being the dielectric constant of the medium (for air, $\epsilon_r = 1$), and α the angle between the nonlinear polarization ($\overrightarrow{P}_{NL}$) and the wave vector $\overrightarrow{k}$, taken to be 90°. Note, that the above equations 4.3 and 4.4 can be applied to nonperturbative harmonics. The dependence of the nonlinear reflection coefficients of the generated harmonics H5, H9 and H11 on the angle of incidence is plotted in figure 4.21, by considering the following linear indices of refraction in GaAs at the harmonic wavelengths of the fundamental field: $n_{02}(5\omega_0) = 4.43$, $n_{02}(9\omega_0) = 3.75$ and $n_{02}(11\omega_0) = 1.34$ [62]. Note that the linear index of refraction of harmonics 3 and 7 in GaAs is very close to that of harmonic 9 ($n_{02}(3\omega_0) = 3.67$, $n_{02}(7\omega_0) = 3.58$), therefore their corresponding nonlinear reflection coefficients, r_s and r_p, are very similar to the ones calculated for H9. The nonlinear reflection coefficients of har-

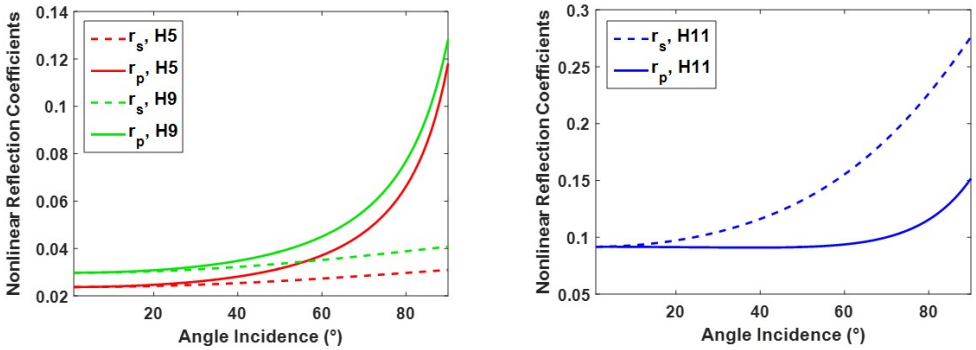

(a) (b)

Figure 4.21: Nonlinear reflection coefficients of harmonics (a) H5, H9, and (b) H11 of the 2.42 μm driving wavelength generated from GaAs.

monics 5 and 9 (figure 4.21(a)) in the case of s-polarization (r_s) only slightly increase as the angle of incidence increases, and are lower than the nonlinear reflection coefficients in the case of p-polarization (r_p). In the latter case, the reflection coefficients increase exponentially. At an angle of incidence of 45°, r_p is slightly higher than r_s, except for harmonic 11, given the fact that the linear index of refraction at the wavelength of H11 ($n_{02}(11\omega_0) = 1.34$) is much lower than that of lower order harmonics. For instance, the nonlinear reflection coefficient of H5 and H9 for p-polarization (solid red and green curves) is 2.97% and 3.65%, respectively, while the nonlinear reflection coefficients for s-polarization (dashed red and green curves) are 2.58% and 3.29%, respectively.

One disadvantage of HHG in reflection as compared to HHG in transmission is when the absorption depth becomes larger than the harmonic wavelength. In this case, forward harmonic emission becomes significant and takes place on a scale of one absorption depth, while backward emission takes place only on a scale comparable to the harmonic wavelength. The absorption depths of the harmonics of the

2.42 μm laser beam generated in reflection from GaAs are summarized in table 4.3 [127, 128]. Except for harmonic 3, the absorption depths of the harmonics in GaAs

Harmonics	Wavelength (nm)	Energy (eV)	Absorption Coefficient (cm^{-1})	Absorption Depth (μm)
H3	807	1.54	9×10^3	1.11
H5	484	2.56	1.45×10^5	0.069
H7	346	3.58	7.5×10^5	0.013
H9	269	4.61	1.75×10^7	0.0057
H11	220	5.64	2×10^6	0.0050

Table 4.3: Absorption depth of the harmonics, of the 2.42 μm driving field, generated from GaAs sample.

are much smaller than their wavelengths. For instance, the absorption depth of the 5^{th} harmonic (484 nm) is $\sim$ 70 nm. As the harmonic order increases, the absorption depth decreases, reaching 5 nm for the 11^{th} harmonic, significantly lower than its wavelength. Therefore, for harmonic orders greater than H3 backward emission only takes place and on a scale of one absorption depth.

4.3.5.3 Results and Discussion

Figure 4.22 depicts the HHG spectra measured from GaAs with a s-polarized (i.e. vertical polarization) and a p-polarized (i.e. horizontal polarization) driving laser incident at an angle of 45°. The estimated vacuum intensity at this angle of incidence is 0.2 TW/cm^2. Harmonics up to the 11^{th} order (218 nm $\equiv$ 5.7 eV) are efficiently generated from GaAs with a p-polarized driver (red spectrum). Moreover, even harmonics up to the 10^{th} order (240 nm wavelength) are detected, but with a signal much lower than the odd harmonics; these are the small peaks located in between the odd harmonics. Even harmonics are generated in GaAs as a result of its non-centrosymmetric crystal nature. Note that the depicted harmonic spectra is obtained without bandpass filters and is optimised for a good visualization of all the generated harmonics. Interestingly, the harmonic generation in the case of a p-polarized driver is more efficient than for the s-polarized one (blue spectrum). Indeed, by considering the Fresnel transmission coefficient (figure 4.20(a)) for s-polarization (T_s = 0.59) and p-polarization (T_p = 0.82), the effective transmitted intensity, near the surface of the GaAs sample, is higher in the latter case (figure 4.20(b)); it is 0.12 TW/cm^2 for s-polarization and 0.16 TW/cm^2 for p-polarization. To increase the efficiency and detect even harmonics with a s-polarized driver, the input power should be increased. Furthermore, the nonlinear reflection coefficients of the harmonics for a p-polarized driver are larger than for a s-polarized one, except for H11 (figure 4.21).

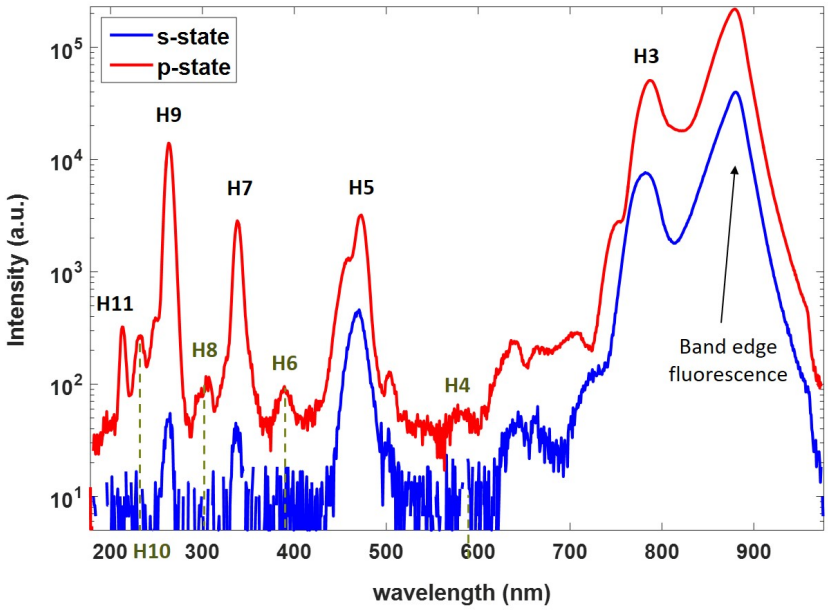

Figure 4.22: HHG spectrum from GaAs in *reflection* geometry measured with s-polarized (in blue) and p-polarized driving laser (in red), incident at an angle of 45° to the normal of the sample surface. The spectra are measured at an estimated laser intensity in vacuum of 0.2 TW/cm^2.

Linear Polarization Dependences

To study the dependence of the generated odd harmonics on the linear polarization of the fundamental driving field, we set the polarization to s-state (i.e. vertical) and rotate the sample, in a complete 360°, while monitoring the harmonic signal. In contrast to the p-polarization, the s-polarization remains completely in the (100) planes of the crystal. It becomes critical when setting a p-polarization in crystals in which the harmonic emission is strongly anisotropic, such as in MgO [20]. This is because while the harmonic emission in MgO is strongly peaked by aligning the polarization along the main crystal axis [001], the p-polarization makes an angle of 24° with respect to the [001] [61], resulting in a reduced harmonic yield. In GaAs, due to its high linear refractive index, the p-polarization refracts and propagates at an angle of 12°, small enough compared to the anisotropy in GaAs. The goal of the present study is to confirm that the results obtained in transmission geometry (discussed in section 4.3.2.2) are not impacted by linear and nonlinear propagation effects of the driving laser. The wavelength of the idler beam (2.4 μm) is close to the wavelength of the NOVAE laser (2.1 μm), hence the corresponding harmonic orders of each laser beam can be directly compared. The polarization measurements are performed for different laser intensities. Initially the s-polarization is aligned along the ΓK direction of the crystal. Taking into account the corresponding Fresnel transmission coefficient ($T_s = 0.59$), the estimated effective intensities for given input powers and incidence angle of 45° are summarized in table 4.4, The

P_{input} (mW)	I_{vacuum} (TW/cm^2)	$I_{45°}$ (TW/cm^2)	$I_{Fresnel}$ (TW/cm^2) (s-state)
25	0.173	0.122	0.073
50	0.346	0.245	0.145
60	0.415	0.293	0.174
80	0.553	0.391	0.232
100	0.692	0.489	0.29
120	0.83	0.587	0.349

Table 4.4: Estimated intensities for different input powers, for an angle of incidence of 45° and taking into consideration the Fresnel transmission coefficient for s polarization.

results of the polarization dependences of harmonics H3, H5, H7, H9 and H11 for different laser intensities are shown in figure 4.23. The 0° angle corresponds to the angle in which the laser polarization is aligned along the ΓK direction, and by 45° rotation of the sample the polarization is aligned along the ΓX direction. Note that the indicated intensities on the polar plots are the estimated effective intensities at an angle of incidence of 45°. The polar scans of all generated harmonics reveal a fourfold symmetry reflecting the zinc-blende structure of the GaAs crystal. The polarization dependence of harmonic 3, shown in figure 4.23(a), does not change as a function of the laser intensity; H3 yield maximizes when the polarization is aligned along ΓK; i.e. at 0° and by every 90° rotation. Moreover, unlike the dependence of harmonic 3 of the NOVAE laser measured in transmission and reported in section 4.3.2.2, harmonic 3 signal maximizes at other angles $\sim 45°$, yet the full polarization dependence still reveals a fourfold symmetry. Interestingly, the 5^{th} harmonic dependence at different laser intensities, shows a similar behavior as the 5^{th} harmonic of the NOVAE laser. Indeed at low laser intensities, 0.072 TW/cm^2 and 0.145 TW/cm^2, the 5^{th} harmonic yield maximizes when the laser polarization is aligned along the ΓK directions. However, as the laser intensity increases the polarization dependence of H5 rotates by around 45°; at 0.232 TW/cm^2 and 0.29 TW/cm^2 laser intensities, H5 yield maximizes when the laser polarization is aligned along the ΓX, i.e. at 45° and by every 90° rotation. For H7, H9 and H11, figure 4.23 (c, d, e), no notable change in the polarization dependences as a function of the laser intensity are observed; the harmonic yield maximizes when the laser polarization is along ΓK and minimizes when aligned along the ΓX directions. For H7 and H9, only the contrast in the polarization plot decreases with the increase of the laser intensity. In addition, by comparing the polarization dependences of all the harmonics generated from GaAs, we observe that as the harmonic order increases the harmonic generation becomes strongly dependent on the angle between the laser polarization and the crystal axis. This reflects the strong anisotropy of the GaAs band structure at higher energies. In conclusion, the measurements in reflection prove that the polarization dependences of the UV-VIS harmonics generated from GaAs are mainly determined by the microscopic response of the crystal.

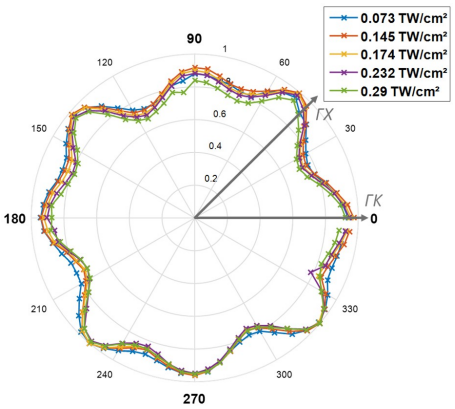

(a) Polarization scans of **H3**.

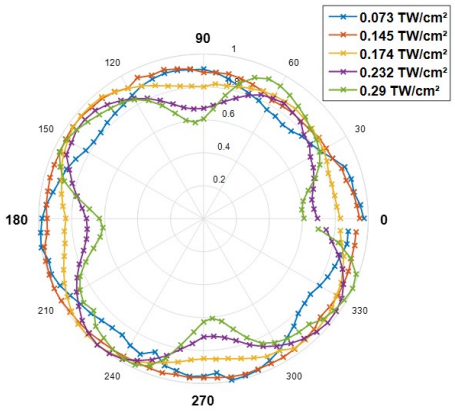

(b) Polarization scans of **H5**.

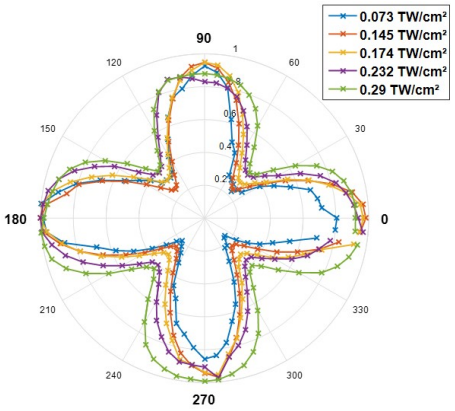

(c) Polarization scans of **H7**.

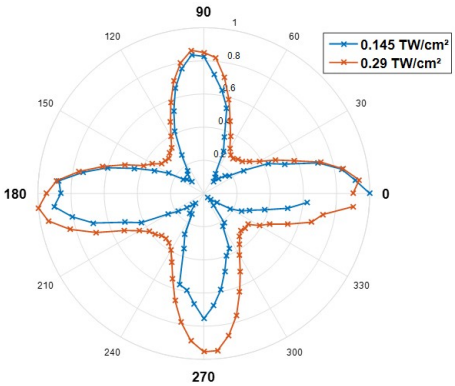

(d) Polarization scans of **H9**.

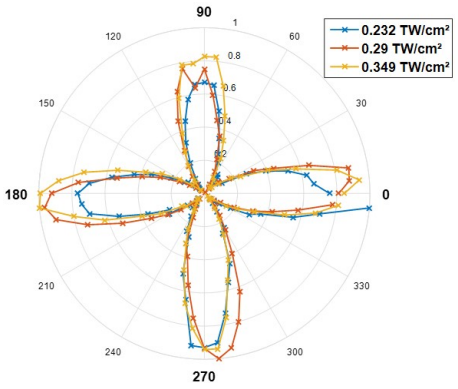

(e) Polarization scans of **H11**.

Figure 4.23: Polarization dependences of the harmonics generated from GaAs in reflection geometry, at different laser intensities. The intensities reported here are the calculated transmitted intensities at an angle of incidence of 45°.

4.3.6 TDDFT Simulations: Polarization Dependences in GaAs

Previously in section 4.3.1, we verified that the harmonics generated from GaAs are nonperturbative harmonics, and proved that in our experimental conditions nonlinear propagation effects do not affect the high harmonic generation mechanism. Characterizing the harmonic emission allows therefore to study electron dynamics at the microscopic level. From an intraband point of view, the anisotropic polarization dependence of the harmonics generated in GaAs is understood as a consequence of the nonparabolic regions of the band structure of GaAs, and consequently of the anisotropy in the electron velocity along the main axes ΓK and ΓX [129]. At this point, numerical simulations would assist in the understanding of the observed phenomena, i.e. the change in the polarization dependence of the harmonics at different laser intensities, particularly for harmonic 5. TDDFT simulations of the polarization dependences of H3 and H5, at different laser intensities, were performed by our collaborator Nicolas Tancogne-Dejean. The simulations are performed with the NOVAE laser wavelength (2.1 μm) at two different intensities 0.1 TW/cm^2 and 0.2 TW/cm^2. In order to make the simulations less time consuming, a band gap energy of 0.6 eV is considered, however the band structure is well reproduced. The results are shown in figure 4.24. The TDDFT simulations include the contributions of both intraband and interband dynamics (section 2.2.1). At a low laser intensity,

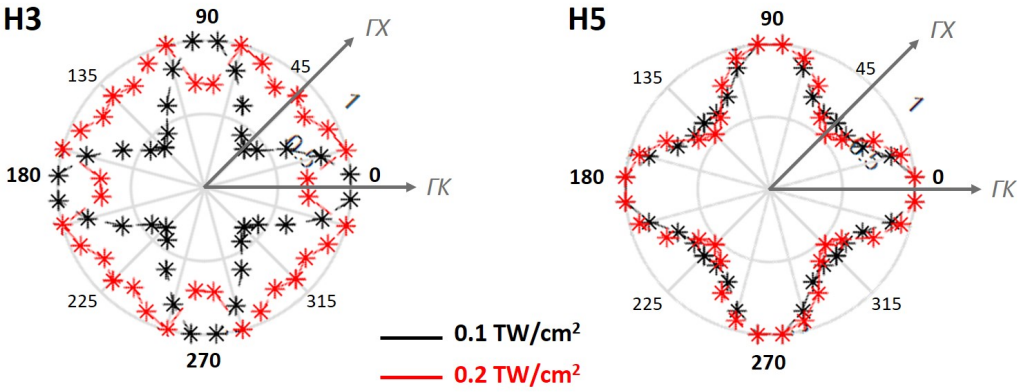

Figure 4.24: TDDFT simulations of the polarization dependences of harmonics 3 and 5 generated from GaAs, at two different laser intensities, 0.1 TW/cm^2 (black) and 0.2 TW/cm^2 (red).

0.1 TW/cm^2, TDDFT simulations of the polarization dependence of H3 and H5, reveal a fourfold symmetry, in which the harmonic efficiency is highest when the laser polarization is aligned along the ΓK directions of the GaAs crystal. This is in perfect agreement with our reported experimental observations of the polarization dependences of the harmonics generated in both transmission (section 4.3.2.2) and reflection (section 4.3.5.3). Interestingly, at a higher laser intensity of 0.2 TW/cm^2, the polarization dependence of H3 exhibits a different behavior; H3 efficiency is highest when the laser polarization is aligned along the ΓX directions of the GaAs

crystal, and is lowest when the polarization is along the ΓK directions. This dependence is similar to the dependence of H5 at higher laser intensities observed experimentally. On the other hand, H5 presents the same fourfold symmetry as observed at lower intensity. Since the band gap energy considered in the simulations is not identical to the real one, which is 1.42 eV, direct harmonic orders between the theory and the experiment cannot be compared. In fact, the electron dynamics responsible for the generation of H3 in the simulation is not the same as in the experiment; in the former case H3 is generated from a higher energy region of the real band structure that is explored by electrons leading to the emission of H5 in the latter case. Particularly for interband emission, the difference between the real and simulated band gap energies (1.42 eV - 0.6 eV = 0.82 eV) should be added to the simulated H3 and H5 photon energies. In this case, it would more or less fit with the experimental H5 (2.95 eV) and H7 (4.13 eV); i.e. E_{H3} (1.55 eV) + 0.82 = 2.37 $\equiv E_{H5}$. With this hypothesis, the theoretically simulated polarization dependences of H3 and H5 resemble those experimentally measured for H5 and H7, respectively. Since the calculated band structure of GaAs is well reproduced, we expect that the reduction of the bandgap does not impact significantly the intraband emission.

4.3.7 Discussions and Analysis

In order to explain the harmonics' polarization dependence in GaAs, and explain the change in the polarization dependence of H5 (of the 2.1 μm and the 2.42 μm drivers) for different laser intensities, we pushed the analysis further. The first question is: In which regime does the process take place, and could the polarization dependence change be related to a transition between the multiphoton and the tunnel ionization? To further confirm that the nonperturbative regime is achieved (section 4.3.1), we calculate the Keldysh parameter at different laser intensities for the two experiments in transmission (at 2.1 μm) and in reflection (2.42 μm). The Keldysh parameter, as defined in Chapter 2, is given by $\gamma_K = \frac{\omega\sqrt{m^* E_g}}{eE_0}$, where $\omega = \frac{2\pi}{\lambda}$ is the angular frequency, $m^* = 0.067 m_e$ is the electron effective mass in GaAs, and E_0 is the electric field strength (Appendix A). The calculations are summarized in table 4.5. For the 2.1 μm driving wavelength, the intensities along the ΓX are chosen for the calculations. Note that along both directions the intensities are very close, and the results of the calculations are almost the same. Except for low laser intensities, $I \leq 0.092\,TW/cm^2$, the Keldysh parameter γ_K is less than 1. This implies that indeed the tunnel ionization regime is achieved in both HHG experiments.
To estimate the contribution of intraband dynamics, we quantify the Bloch oscillations by calculating the β parameter, at the two driving wavelengths and at different laser intensities. The lattice constant in GaAs is taken to be 5.65 Å. β increases with the increase of the laser intensity, implying that the Bloch oscillation frequencies increase during the subcycle of the laser. Moreover, the Bloch oscillations reflect the electron excursion in the conduction band. Following the acceleration theorem, we estimate the percentage of the Brillouin zone (BZ) excusion by the electron. With the NOVAE laser wavelength, the electron explores only up to $\sim 17\%$ of the conduction band, while with the OPCPA laser wavelength the electron explores a maximum of $\sim 26\%$ of the conduction band. Therefore, in both cases full Bloch os-

$\lambda_{\mathrm{NOVAE}} = 2.1\mu$m				$\lambda_{\mathrm{OPCPA}} = 2.42\mu$m			
Intensity ($\mathrm{TW/cm^2}$)	γ_{K}	β_{B}	% BZ	Intensity ($\mathrm{TW/cm^2}$)	γ_{K}	β_{B}	% BZ
0.049	1.44	0.16	9%	0.073	1.04	0.23	12%
0.092	1.05	0.22	12%	0.145	0.74	0.32	17%
0.133	0.88	0.26	14%	0.23	0.59	0.4	22%
0.173	0.77	0.3	16%	0.29	0.52	0.45	24%
0.199	0.72	0.32	17%	0.35	0.48	0.49	26%

Table 4.5: The calculated Keldysh parameter γ_{K}, the β_{B} parameter, and the percentage of the Brillouin zone (BZ) excursion by the electron wavepacket, for the two driving wavelengths and at different laser intensities.

cillations are not achieved. Since Bloch oscillations are associated to the intraband current due to electron acceleration, they are influenced by the band curvature. By examining the conduction band in figure 4.25, we notice that the band along the ΓX is steeper than along the ΓK direction. This signifies a higher electron velocity [129], and consequently higher intraband current along the ΓX direction of the crystal. Yet this does not explain the signal of higher order harmonics along the ΓK direction and the fourfold symmetric polarization dependence of the harmonics generated in GaAs.

Next, we turn the analysis to the interband contribution. The recombination could take place by coupling of the conduction band to different valence bands, namely the heavy hole, light hole or split-off bands. To easily image these couplings, the arrows in figure 4.25 represent harmonic energies (close to the harmonic energies of the two driving wavelengths) along the principal crystal axes ΓX and ΓK. The red dashed lines denote the maximum excursion of the electron in the first Brillouin zone for the two driving wavelengths, 2.1 μm and 2.42 μm. Notice that the heavy and light hole bands overlap along the ΓX direction, while along the ΓK direction the electron has to travel much farther to emit high order harmonic energies, in case the interband transitions involve the heavy hole band. This is pictured by the yellow and blue dotted arrows corresponding to the emission energies of H7 and H9. However, the transitions involving the heavy hole band is less probable than the transitions involving the light hole band [130]. If we consider the interband transitions between the conduction band and the light hole band along the ΓK, the electron can recombine and emit harmonic energies close to the region of the maximum excursion of the electron (dotted red lines). It is important to point out a special feature of the band structure of GaAs; along the ΓX direction, the 9^{th} harmonic (blue solid arrow) can be emitted only at very far regions close to the border of the first Brillouin zone because the interband energy before is lower. With the intensities provided by our lasers, the electron does not reach this region. However, the light hole band along the ΓK direction is much steeper, and the interband energies as high as the 11^{th} harmonic energy of the 2.42 μm driver are close to the maximum electron excursion. This could explain why the harmonic emission of H9

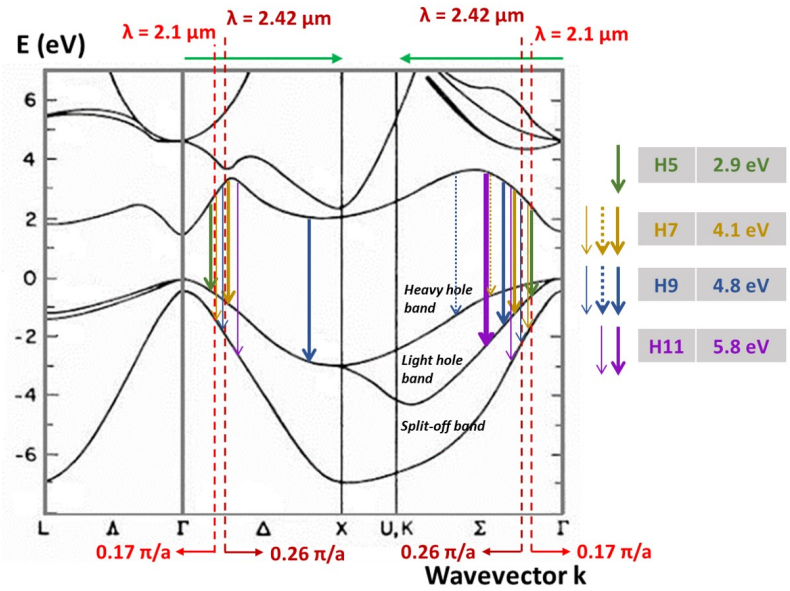

Figure 4.25: Band structure of GaAs (adapted from [118]) showing interband transitions for each harmonic energy. The red arrow denotes the position of the maximum excursion of the electron in the Brillouin zone, which is 17% at the maximum laser intensity 0.2 TW/cm^2. The solid arrows represent the emission of harmonic energy by the electron recombination with a light hole, the dotted arrows represent the emission of harmonic energy by the electron recombination with a heavy hole, and the thin arrows represent the emission of harmonic energy by the electron recombination with a split-off hole.

and H11 along the ΓK direction is more efficient, which also explains the fourfold symmetry. Besides, there is also a probability that interband mechanisms couple the conduction band and the split-off band. The recombinations that correspond to these couplings are indicated by the thin arrows. Interestingly, in this case high order harmonics are emitted even if the electron explores only 25% of the Brillouin zone. Yet, along the two crystal directions the probability of recombination seems similar, and the fourfold symmetry can not be explained in this case. Indeed, the two main anisotropic properties of the band structure are the steepness of the light hole band and the curvature of the heavy hole band [131], which are stronger along the ΓK direction of the crystal.

Lastly, a hypothesis to explain the change in the polarization dependence of harmonic 5 is based on the propagation of the harmonics in the GaAs sample. Note that we exclude the propagation effect of the fundamental although the nonlinear refractive index of GaAs and the three-photon absorption are anisotropic [119], because the change in the polarization dependence appears only for the 3$^{\text{rd}}$ and 5$^{\text{th}}$ harmonics and not for the higher order ones. Despite the thin absorption length in GaAs (order of tens of nanometers), the question is: could the absorption of the harmonics be different along the two main crystal axes? C. Schmidt et al. [132] have performed THz pump-probe experiments to study the transient transmission and absorption of a broad energy range of the probe. Having their pump aligned

along the ΓL direction of the crystal, they reported on the Franz-Keldysh electro-absorption effect due to the pump field. More precisely they observed Wannier-Stark localization and a significant transient absorption in the energy range 2.5 eV - 3.4 eV, which includes our 5^{th} harmonic energy. This effect could be different with respect to the orientation of the crystal axis, possibly explaining the experimental results.

4.4 High Order Harmonic Generation in MgO and Chromium-Doped MgO

In this section, we investigate high harmonic generation in magnesium oxide (MgO) and chromium-doped magnesium oxide (Cr-MgO) crystals. We study the polarization dependence of the harmonics generated in air i.e. in the deep UV-Visible spectral range. We also highlight the impact of nonlinear propagation effects in undoped and doped MgO crystals in both space and time domains.

4.4.1 Motivation and Objective

MgO is a wide direct bandgap semiconductor with a band gap energy of $E_g = 7.8$ eV and a cubic crystal structure. In general, dopants introduce defects and impurities in the crystals which causes a change in the optical and electronic properties of the resulting doped semiconductor [133]. This presents a big advantage for the crystal band structure engineering. For low concentrations, dopings can decrease the effective bandgap keeping the band structure more or less identical. In this case, during the HHG process one expects to enhance the ionization and consequently increase the HHG yield. HHG in such doped semiconductors paves the way to understand intraband and interband electron dynamics at the fundamental level [55, 134]. Moreover, it can serve as an efficient XUV source for experiments such as coherent diffractive imaging, that requires a strong high harmonic signal. Figure 4.26 illustrates the measured transmission properties of pure MgO and different

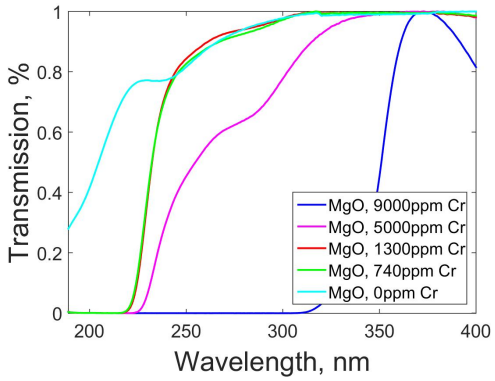

Figure 4.26: Transmission measurements, in the UV-violet spectral range, of undoped and Cr-doped MgO crystals.

levels of chromium-doped MgO. The percentage of the doping level is reported in ppm units (parts-per-million). The optical transmission measurements confirm that the band gap energy of MgO lies in the UV spectral range, < 200 nm in wavelength. However, for a chromium-doped MgO crystal with a Cr dopant level of 740 ppm, the bandgap shifts to above 200 nm (~ 6.2 eV), and as the doping level increases the band gap energy decreases, i.e. shifts to larger wavelengths.

4.4.2 Laser Dependent UV-VIS Harmonics from MgO

We investigate high harmonics generated from MgO and Cr-doped MgO samples in air. We study each laser intensity, ellipticity and polarization dependences of the harmonics.

Experimental Setup and Details

The HHG experiment was carried out at IOGS in 2018 with the OPCPA laser system. The driving laser beam is the signal beam centered at 1.6 μm wavelength, 80 fs pulse duration and 125 kHz repetition rate. The laser is focused in air by a 5 cm focal length off-axis parabolic mirror at the exit surface of the MgO samples. The generated harmonics are collected and focused by another off-axis parabolic mirror (5 cm focal length) onto a VIS-UV spectrometer (QE Pro spectrometer). A half-wavelength plate (HWP), a polarizer and a quarter-wavelength plate (QWP), inserted before the focusing off-axis parabola, are employed to vary the laser power, polarization and ellipticity of the driving laser beam. The beam size at the focus is calculated to be 10.7 μm at FWHM. The undoped and doped MgO samples are 5×5 mm and are 200 μm thick with (100) orientation. Samples with different doping levels were grown. The different doping concentrations are 740 ppm, 1300 ppm, 5000 ppm and 9500 ppm. They were bought from SurfaceNet. The harmonic

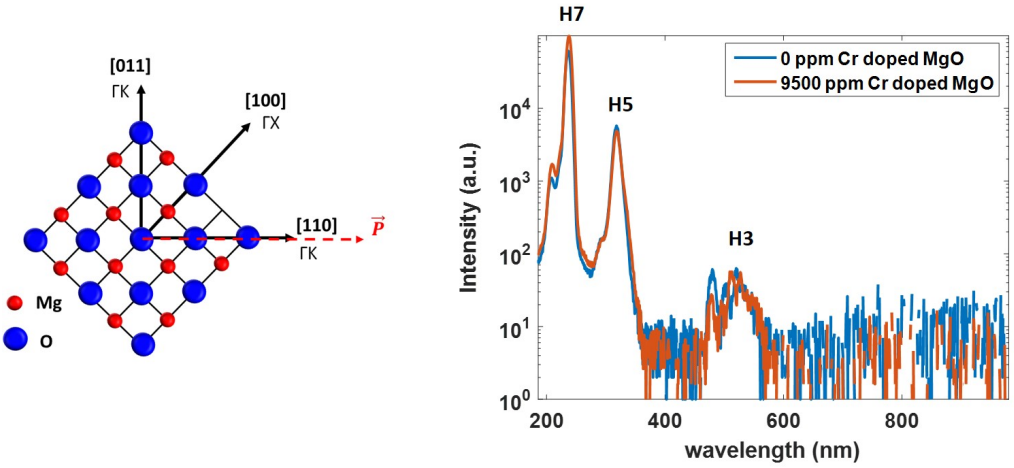

Figure 4.27: Left: Crystal structure of MgO. Right: Harmonic spectra of the 1.6 μm driving laser beam, measured from undoped and Cr-doped (9500 ppm) MgO crystals, at a laser intensity of 9.28 TW/cm^2.

spectra measured from undoped MgO and 9500 ppm Cr-doped MgO crystals, at an estimated laser intensity of 9.28 TW/cm^2, are shown in figure 4.27. The laser beam is vertically polarized (i.e. s-polarized) and aligned along the ΓK ([110]) direction of the MgO crystals. A bandpass filter centered at 239 nm wavelength was used to attenuate the saturation of the 3$^{\text{rd}}$ harmonic signal. H3 (533 nm ≡ 2.33 eV), H5 (320 nm ≡ 3.87 eV) and H7 (228 nm ≡ 5.44 eV) are efficiently generated from both samples but no obvious differences in the generation efficiencies between undoped and doped crystals. Note that both spectra are measured at an integration time of 1 second. MgO is a centrosymmetric crystal, therefore only odd harmonics can be generated. The harmonics generated from undoped MgO are below bandgap harmonics ($E_{H7} < E_g$), while in reference to the transmission measurements in figure 4.26, H5 and H7 generated from the 9500 ppm Cr-doped MgO should be above bandgap harmonics.

4.4.2.1 Intensity Dependences

We study the dependence of the strength of the harmonics generated from undoped and doped MgO crystals on the laser intensity. The measurements of the 5$^{\text{th}}$ and 7$^{\text{th}}$ harmonics are depicted in figures 4.28(a) and 4.28(b), respectively. For a clear

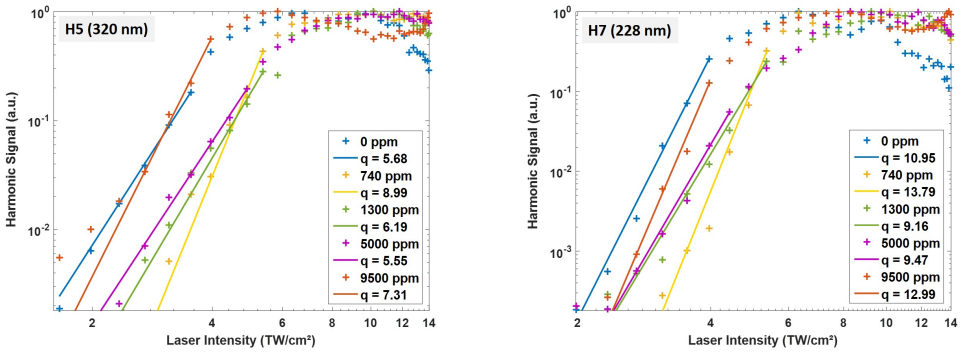

(a) Intensity scaling of H5 (320 nm) generated from MgO crystals for different doping levels.

(b) Intensity scaling of H7 (288 nm) generated from MgO crystals for different doping levels.

Figure 4.28: Dependence of the strength of harmonics 5 (a) and 7 (b) of the 1.6 μm driving wavelength generated from different Cr-doped MgO samples on the laser intensity.

comparison, the power laws corresponding to the scaling of the harmonic signal as a function of the laser intensity are summarized in table 4.6 below. Harmonic 5, generated from the undoped and the 5000 ppm doped MgO samples, scales as a perturbative harmonic, where the scaling power q is close to 5, however, from the crystals with the other doping concentrations (740 ppm, 1300 ppm and 9500 ppm) the scaling power q is > 5. As for harmonic 7 which is generated from undoped and different Cr-doped MgO crystals, the scaling power q is $\gg 7$. The resulting high scaling powers of the harmonics do not only represent the nonperturbative dependence of the harmonic yield, but could also be due to nonlinear propagation effects on the laser. Saturation of the harmonic efficiency is reached for a laser

	MgO Doping Level				
Harmonics	0 ppm	740 ppm	1300 ppm	5000 ppm	9500 ppm
H5 (320 nm)	5.68	8.99	6.19	5.55	7.31
H7 (228 nm)	10.95	13.79	9.16	9.47	12.99

Table 4.6: Power scaling law of the harmonics with the laser intensity of the 1.6 μm driver generated from MgO.

intensity higher than 6 TW/cm^2 calculated in vacuum. A decrease in the harmonic signal is observed above $\sim$ 10 TW/cm^2, which indicates the damage of the sample at such high laser intensities.

4.4.2.2 Ellipticity Dependences

According to Y. S. You et al. [20], the ellipticty dependence of HHG in MgO changes along different crystal axes. For instance, when the linear polarization of the driving laser is aligned along the [110] direction, the HHG yield is not maximized and increases with the increase of the laser ellipticity reaching a maximum value for an ellipticity of 0.65. To explore this special feature and study the effect of doping in MgO on the ellipticity dependence of the generated high harmonics, we perform ellipticity measurements in which we vary the ellipticity of the laser from linear (e = 0) to circular (e = 1) by a quarter-wavelength plate. The measurements depicted in figure 4.29 consist of a full rotation of the QWP, where e = 0 corresponds to a 0° angle between the optic axis of the QWP and the incoming linear polarization, and e = 1 corresponds to an angle of 45°. Initially, the linear laser polarization is aligned along the ΓK ([110]) direction of the MgO crystals, hence at e = 0. The

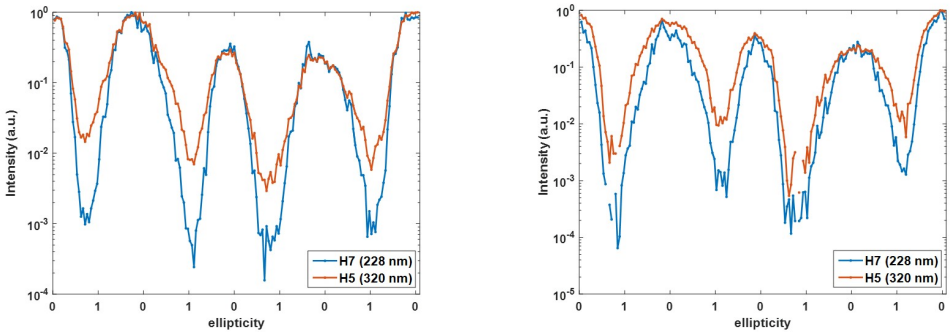

(a) Ellipticity measurements of the harmonics generated in **undoped** MgO.

(b) Ellipticity measurements of the harmonics generated in **9500 ppm** Cr-doped MgO.

Figure 4.29: Dependence of the generation efficiency on the ellipticity of the driving laser beam in undoped and Cr-doped MgO samples, at 6.52 TW/cm^2 laser intensity. The curves are normalized by the maximum harmonic signal at linear polarization and by the integration time which is 200 ms.

harmonic generation efficiency of H5 (320 nm) in undoped MgO (figure 4.29(a)) is maximum for a linear laser polarization and decreases as the ellipticity increases i.e. towards circularly polarized state. As the harmonic order increases, the dependence of the generation efficiency on the laser ellipticity becomes stronger. This is why the contrast in the ellipticity dependence of H7 (228 nm) is larger than that of H5 (320 nm), yet the harmonic signal for a circularly polarized laser beam does not completely go to zero. The same behavior is observed for the case of the 9500 ppm Cr-doped MgO sample (figure 4.29(b)); the harmonic generation efficiency of the 5^{th} and 7^{th} harmonics decreases with the increase of the laser ellipticity, and is minimal for a circularly polarized beam. Similar to the dependence of H7 generated from the undoped MgO sample, the contrast in the ellipticity dependence of H7 is larger than that of H5. Hence, we don't observe an influence of the doping on the ellipticity dependence of the UV harmonics generated from Cr-doped MgO crystals. The results reported here at this laser intensity are typical results of the ellipticity dependence of the harmonics generated in undoped and Cr-doped MgO crystals, and do not vary with the intensity. It is worth emphasizing that the ellipticity dependence of HHG in crystals is less critical than in atomic gas, where the harmonic signal in the latter case drops rapidly with the increase of the driver ellipticity and reaches zero for a circular polarization [40, 41].

4.4.2.3 Linear Polarization Dependences

The linear polarization dependence of the UV-visible harmonics generated in MgO and Cr-doped MgO crystals is also studied. The laser polarization is initially aligned along the ΓK direction of the MgO crystal (0° on the polar plots), and the polarization measurement is performed by rotating the linear polarization by 360°. The laser intensity is estimated to be 10.44 TW/cm^2. Figures 4.30(a) and 4.30(b) depict the results of the polarization measurements of both harmonics H5 (320 nm) and H7 (228 nm) generated from undoped MgO and 9500 ppm Cr-doped MgO, respectively. The polarization measurements reveal a fourfold symmetry, which is a direct consequence of the cubic crystal structure of MgO. The harmonic signal is highest when the laser polarization is aligned along the ΓK directions of the MgO crystal (figure 4.27), and is minimum when the polarization is rotated by 45°, i.e. when it is along the ΓX directions. The results obtained are in agreement with the polarization dependences of low order harmonics generated from MgO and reported by Y. S. You et al. [20]. Similar to the measurements reported previously from GaAs, as the harmonic order increases the dependence of the harmonic generation on the angle between the laser polarization and the crystal axis becomes more critical; this is observed by comparing the polarization dependences of harmonic 5 and harmonic 7, in which the lobes of the polar scan of H7 are narrower than those of H5. Besides, the contrast in the polarization dependences of higher order harmonics is larger than the one of lower orders. The results reported here do not change as a function of the laser intensity. To study the effect of different doping concentrations on the polarization dependences of the harmonics (deep UV and visible harmonics) generated from MgO in air, we perform polarization measurements for the different Cr-doped MgO samples. A comparison of the polarization dependences of harmonic 5 (320

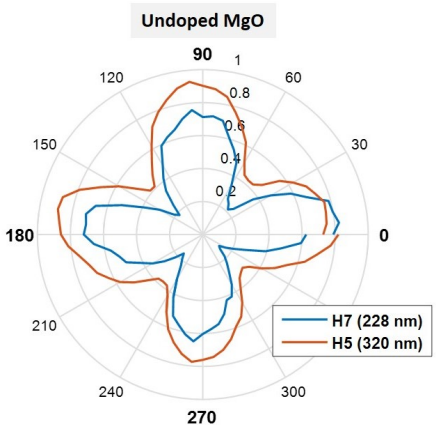

(a) Polarization dependence of H5 (320 nm) and H7 (228 nm) generated in **undoped** MgO crystal.

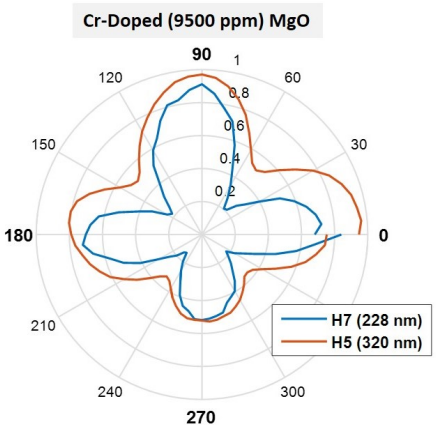

(b) Polarization dependence of H5 (320 nm) and H7 (228 nm) generated in **9500 ppm** Cr doped MgO crystal.

Figure 4.30: Dependence of the generation efficiency, of harmonics 5 and 7 in undoped and 9500 ppm Cr-doped MgO samples, on the linear polarization of the driving laser beam, at 10.44 TW/cm^2 laser intensity.

nm) and harmonic 7 (228 nm) generated from undoped MgO and doped MgO with different doping concentrations is shown in figures 4.31(a) and 4.31(b). The results

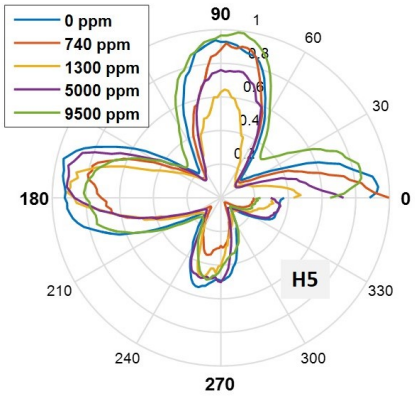

(a) Polarization dependence of **H5 (320 nm)** generated in undoped and different Cr doping levels of MgO samples.

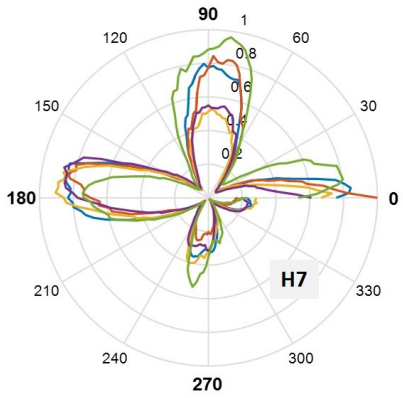

(b) Polarization dependence of **H7 (228 nm)** generated in undoped and different Cr doping levels of MgO samples.

Figure 4.31: Dependence of the generation efficiency in undoped and Cr-doped MgO samples on the linear polarization of the driving laser beam, at 6.52 TW/cm^2 laser intensity.

reveal no particular trend in the polarization dependences of the generated harmonics. The high harmonic generation efficiencies, from all samples, exhibit a fourfold symmetric dependence on the laser polarization. Note that the assymmetric fourfold symmetry is an experimental artifact, due to the misalignment of the beam into the spectrometer as we rotate the polarizer to carry out the measurements. In conclusion, these chromium doping concentrations in MgO seems to maintain the polarization dependence of low order harmonic generation.

4.4.3 Nonlinear Propagation Effects in Space and Time Domains

Propagation effects are important to be examined when studying HHG in crystals. In this subsection, we draw the attention to the occurrence of the nonlinear Kerr effect in MgO crystals both in space and time domains, that is self-focusing and self-phase modulation (SPM), respectively. The experimental study employs the signal beam, centered at 1.78 μm wavelength, of the OPCPA laser system at CEA, which is focused by a 5 cm focal length CaF_2 lens, with an anti-reflective coating, into the undoped and doped MgO crystals. A microscope objective is then aligned to image the focus at the exit surface of the sample on a CMOS camera from Imaging Source (Appendix E).

4.4.3.1 Characterization in the Spatial Domain

To study nonlinear propagation effects in the spatial domain, we characterize the beam size of the fundamental and the harmonics at the exit surface of the crystals; this is where the beam focus is placed to optimize the harmonic efficiency. To estimate the waist of the mode, we define the center of the recorded image and then take a vertical and a horizontal cross sections to fit them by a Gaussian function, as illustrated in figures 4.32 (a) and (b). The Gaussian function is of the following form $f(x) = a\exp\left(\frac{x-b}{c}\right)^2$, where a = 1 since we normalize the image, and the constants b and c are in pixels. For example, the fitted curve in (figure 4.32 (b)) is represented by $f(x) = \exp\left(\frac{x-406}{97}\right)^2$. The waist is then calculated as $\omega = \sqrt{2}\,c$. Figures 4.32 (c) and (d) depict typical results of the spatial mode of the fundamental beam at the exit surface of the MgO crystals. By observing the modes in figure 4.32, we can notice that the beam size is much smaller at the exit of the MgO samples, indeed it is relatively less than half of the size of the mode without a sample. This is a clear indication of the self-focusing effect in the MgO crystals. Moreover, by comparing the undoped case to the doped MgO case, we can notice that the beam mode at the exit of the 5000 ppm Cr-doped MgO sample is slightly smaller than the mode at the exit of the undoped MgO sample. This indicates that the self-focusing effect is more important in the doped MgO crystal than in the undoped one. Since the nonlinear propagation effects act on the fundamental driving beam, which then generates the harmonics, their consequences should also be revealed in the characteristics of the generated harmonics. Figure 4.33 depicts the spatial modes of harmonics 3 (600 nm) and 5 (360 nm) generated in the MgO crystals. We observe that the modes of H3 and H5 are smaller when generated in doped crystals. To quantify the change in the spatial modes of the harmonics we estimate their areas, calculated as $A = \pi\omega_1\omega_2$

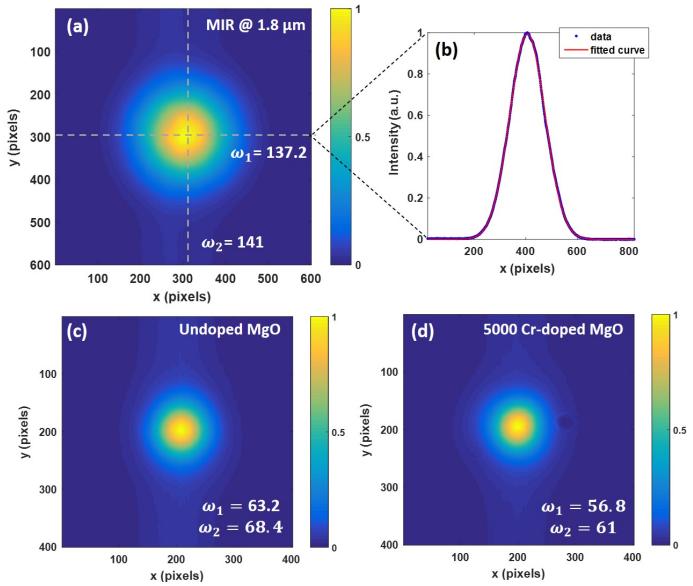

Figure 4.32: Spatial mode of the fundamental signal beam without a sample (a), and at the exit of the the undoped MgO crystal (c) and the 5000 ppm Cr-doped MgO crystal (d). The estimated vacuum laser intensity at the focus is 21 TW/cm^2.

in pixel^2. The results are summarized in table 4.7. We compare the change in the area of the spatial modes, obtained from the undoped crystal and the doped one, to the area of spatial mode from the undoped crystal A_1, and therefore we calculate the percentage change as $\%\,\text{change} = \frac{A_1 - A_2}{A_1} \times 100$.

	Undoped MgO	**Doped MgO**	
Spatial mode area	A_1 (in pixel^2)	A_2 (in pixel^2)	% change in Area
Signal	1.36e4	1.09e4	19.7 %
H3	5.6e3	4.3e3	22.8 %
H5	1.88e3	1.65e3	12.2 %

Table 4.7: Area of the mode of the fundamental signal beam and harmonics H3 and H5.

For the fundamental beam, the percentage change is $\sim$ 20 %, while for H3 and H5, the percentage change is 23 % and 12 %, respectively. This difference again proves that the self-focusing effect in Cr-doped MgO crystal is higher than in the undoped one. Doping induces a change in the optical properties of the material, not only by influencing the linear absorption and transmission properties (figure 4.26), but also by impacting the nonlinear properties.

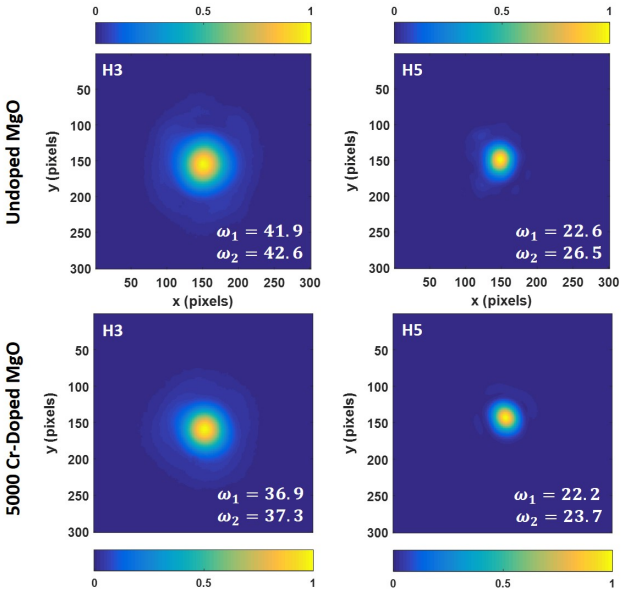

Figure 4.33: Spatial mode of harmonic 3 and harmonic 5 generated from the undoped MgO crystal and the 5000 ppm Cr-doped MgO crystal, at a laser intensity of 21 TW/cm^2.

4.4.3.2 Characterization in the Temporal Domain

Nonlinear propagation effects in the crystal can also influence the temporal properties of the fundamental beam, because of the high intensity reached at its focus. In order to get insight on this aspect, we characterize spectrally the fundamental beam after the MgO samples. The laser is focused by the same 5 cm focal length CaF_2 lens into the undoped and the 5000 ppm Cr-doped MgO samples. Another lens is aligned after the sample to collimate the diverging beam which is then guided into a Mozza spectrometer from Fastlite for pulsed IR laser sources. The measured spectra at an estimated laser intensity of 21 TW/cm^2 is depicted in figure 4.34(b). The spectra of the fundamental beam after propagation in the MgO samples are narrower and reveal two small bumps around the central peak as compared to the spectrum measured without a sample (figure 4.34(a)). This indicates that nonlinear propagation effects in the MgO crystals, particularly self-phase modulation (SPM), has a significant impact on the laser pulses. Moreover, figure 4.34(b) shows identical spectra from both the undoped and the doped crystals, which means that SPM effect on the laser beam after propagation through the undoped and the 5000 ppm Cr-doped MgO samples is similar. We employ a FROG (Frequency Resolved Optical Gating) technique to characterize more precisely the laser pulse in the spectral and temporal domains after propagation in the MgO samples. The FROG allows retrieving the spectral and temporal phases of the laser pulse. Regarding the experimental setup, after collimation, the beam is guided to a home-made FROG setup (Appendix F). The FROG results are summarized in figure 4.35, where the first column shows the reconstructed traces of the FROG measurements, the second and

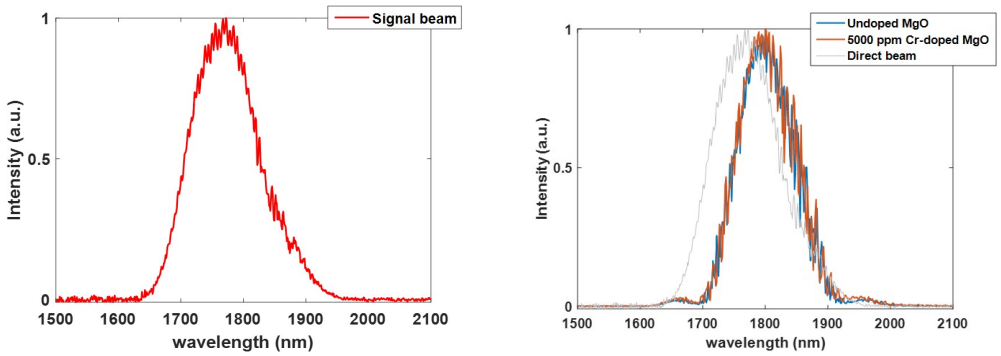

(a) (b)

Figure 4.34: (a) Spectra of the fundamental signal beam exiting the OPCPA 4.34(a), and (b) after propagating in the undoped and the 5000 Cr-doped MgO crystal 4.34(b). The estimated laser intensity in vacuum is 21 TW/cm^2.

third columns represent the spectral and temporal characterizations of the laser pulse, respectively. The spectral (figure 4.35 (column b)) and temporal (figure 4.35 (column c)) pulse envelopes are plotted in blue, while the spectral and temporal phases are plotted by the red dashed curve on the second y-axis. The case of no sample, i.e. the first row, corresponds to the case where the laser is focused and collimated in air, i.e. no sample at the focus position. In this case we characterize the fundamental beam and consider it as our reference. In the spectral domain, the measurement reveals a bandwidth of $\Delta\omega = 137$ nm at FWHM, and a spectral phase with a negative curvature which implies that our laser pulse is initially negatively chirped. This chirp includes the chirp coming from the laser, exiting the OPCPA, and any linear dispersion effects induced by the optics. As a consequence in the time domain, the pulse duration at FWHM is $\tau = 51$ fs and the temporal phase has a positive curvature. Next, by placing the undoped sample in the optimal generation position, the pulse is strongly modified both spectrally and temporally (second row of figure 4.35). In the spectral domain, the spectral envelope shrinks, the bandwidth is reduced to 96 nm and two small arms are observed around the central peak. Moreover, a reduction in the curvature of the spectral phase is observed. This is due to the self-phase modulation effect on a negatively chirped pulse. The SPM effect in the undoped MgO crystal is revealed in the time domain, and is evidenced by the appearance of the small negative curvature at the central part of the temporal phase. Note that the SPM effect impacts the temporal phase; the SPM phase denoted by γ_{SPM} is directly proportional to the time-dependent pulse intensity $I(t)$, $\gamma_{\text{SPM}} \propto n_2 I(t)$. For a Gaussian pulse, γ_{SPM} takes a negative curvature form. This modulation in the temporal phase results in a shorter spectrum and a longer pulse $\sim \tau = 75$ fs. Likewise, for the 5000 ppm Cr-doped MgO crystal (third row of figure 4.35), the SPM effect, at the optimal generation position, strongly modulates the laser pulse. A small negative curvature is also revealed at the center of the temporal phase, resulting in a shorter spectrum with $\Delta\omega = 97$ nm and a longer pulse $\tau = 75$ fs. In conclusion, the SPM effect seems to be identical in undoped and doped MgO

crystals. Therefore, the doping by itself does not influence the spectral and temporal properties of the pulse, however, its effect is more pronounced in the spatial domain as discussed in the previous section.

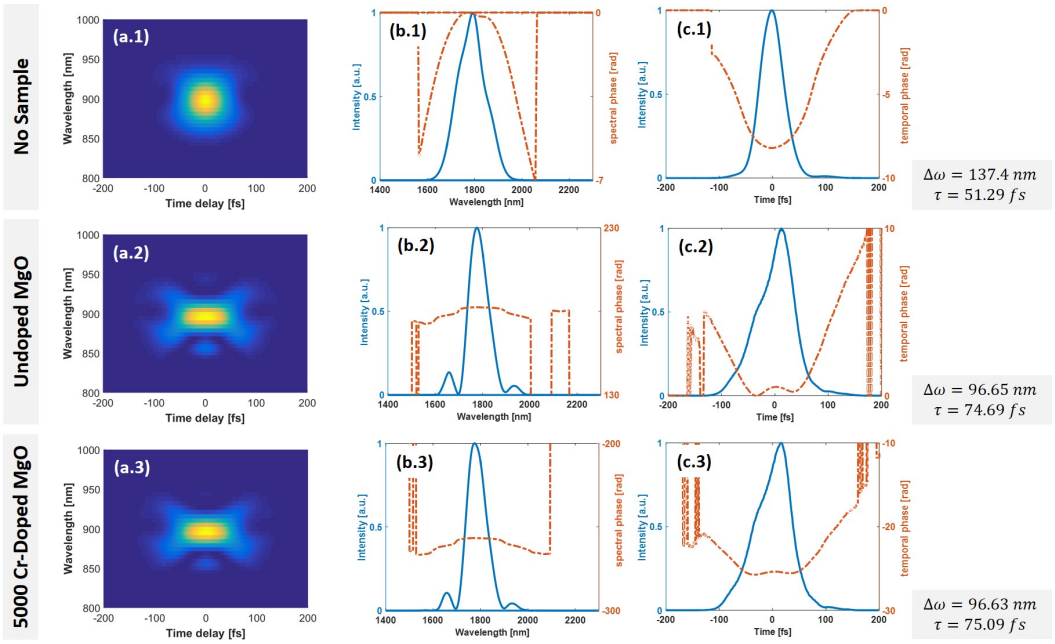

Figure 4.35: Spectral and temporal characterization of the signal beam through the undoped MgO crystal and the Cr-doped MgO crystal, at an estimated laser intensity in vacuum of 25 TW/cm^2. The first column represents the reconstructed FROG traces, while the second and third columns represent the spectral and temporal characterizations of the fundamental signal beam, respectively.

Long pulse durations present a limitation for solid-state HHG experiments as the effective intensity decreases and the damage rate increases. To shorten the pulses, one solution is to compensate the negatively chirped pulse by adding a material that induces a positive GDD (group delay dispersion). For that we have selected a zinc selenide crystal of 3 mm thickness. At the wavelength of our signal beam, $\lambda = 1.78$ μm, ZnSe possesses a positive group velocity dispersion, GVD, ~ 300 fs^2/mm, which imposes a GDD of 900 fs^2 in the 3 mm thick ZnSe crystal, large enough to compensate for the initially chirped pulse. The ZnSe crystal is placed in the beam path before the focusing lens. We then carry out FROG measurements similar to the ones shown in figure 4.35. The results with the ZnSe crystal are summarized in figure 4.36. For the case of no sample, which is shown in the first row of figure 4.36, an obvious dispersion effect of the ZnSe crystal is observed. Compared to the previous case without the ZnSe (first row of figure 4.35), the quadratic term of the spectral phase is significantly reduced with the ZnSe. In the time domain, this leads to a shorter pulse duration, that is reduced from 51 fs, without the ZnSe, to 37 fs with the ZnSe in the beam path. This means that the ZnSe imposes a positive GDD strong enough to compensate the spectral phase and to shorten the pulse duration. Taking this case as our reference we proceed to

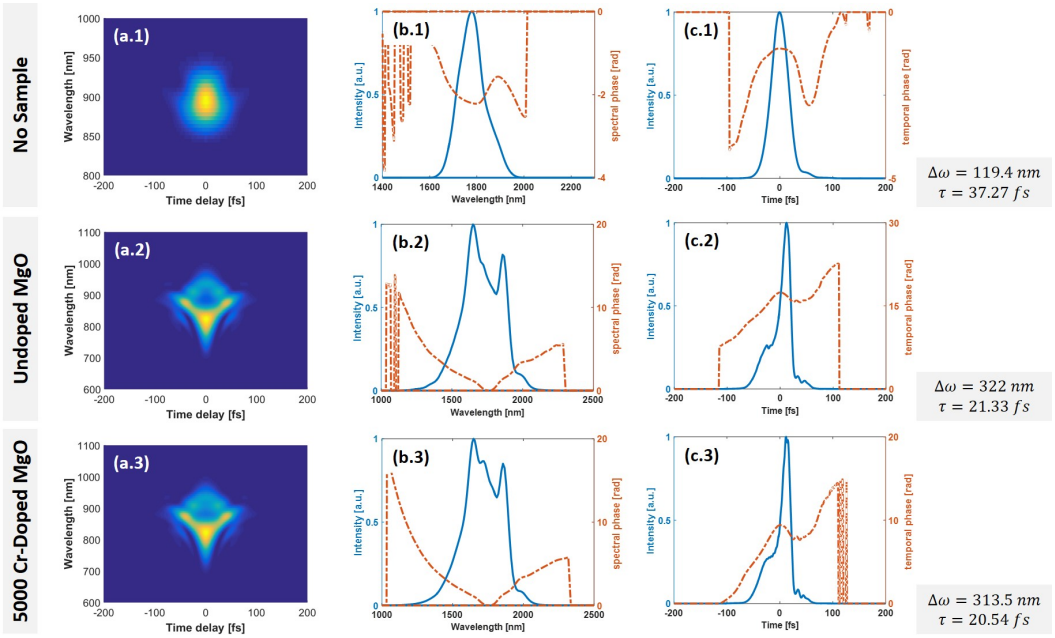

Figure 4.36: Spectral and temporal characterization of the signal beam through the undoped MgO crystal and the Cr-doped MgO crystal, with a 3 mm thick ZnSe crystal in the beam path, at an estimated laser intensity in vacuum of 20 TW/cm^2. The first column represents the reconstructed FROG traces, while the second and third columns represent the spectral and temporal characterizations of the fundamental signal beam, respectively.

investigate the self-phase modulation effect in the medium of generation (undoped and doped MgO) on the laser pulses. The samples are also placed at the focus position at the optimal generation position. The case of the undoped MgO sample is shown in the second row of figure 4.36. A drastic SPM effect takes place; the spectrum becomes broader (figure 4.36 (b.2)), almost three times the reference spectrum (figure 4.36 (b.1)), where the bandwidth $\Delta\omega$ increases from 119 nm (case of no sample) to 322 nm. In the time domain, an important self-compression is observed that significantly shrinks the pulse duration down to $\tau = 21$ fs. This effect is probably a result of the combination of the SPM and the negative dispersion of MgO at this laser wavelength (1.78 μm). Note that a significant ionisation could be involve in the process as the spectrum is blue shifted. For the 5000 ppm Cr-doped MgO sample, a similar SPM effect occurs; the spectrum becomes broader with a bandwith $\Delta\omega = 314$ nm and pulse duration $\sim \tau = 21$ fs, i.e. close to 3 optical cycles. This observation of pulse compression presents an interesting advantage for solid-state HHG experiments, as it can finally lead to the desired requirement of shorter pulse durations at the optimal harmonic generation position.

4.5 XUV High Order Harmonic Generation in Magnesium Oxide

Contribution to the harmonic emission from higher energy bands of the band structure can be studied experimentally by extending the high order harmonic detection range to the XUV spectral domain [135]. You et al. [135] have observed two spectral plateaus from MgO; the first one consists of harmonics generated from the first conduction band, while the second plateau consists of harmonics at higher photon energies generated from the second conduction band, and less intense than the harmonics of the first plateau, as shown in figure 4.37. This is a particular and interesting feature of solid-state HHG (section 2.2.3).

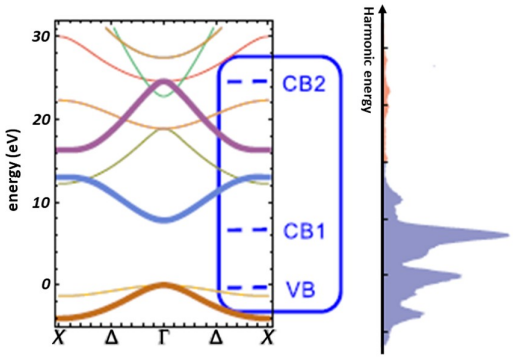

Figure 4.37: HHG in MgO involving different energy bands in momentum space [135].

4.5.1 Experimental Setup and Details

Since harmonics of photon energies above 6.2 eV (200 nm in wavelength) are absorbed in air, we set up an *in vacuum* HHG experiment to detect vacuum harmonics generated from MgO. The experimental setup, implemented by other colleagues in the group, is shown in figure 4.38. The driving laser beam is the signal beam of the OPCPA laser system at CEA, Saclay. Its wavelength is centered at 1.78 μm, the pulse duration is 40 fs and the repetition rate is 100 kHz. The laser beam enters the chamber through a fused silica vacuum window, and is guided then focused by a 10 cm focal length CaF_2 lens onto the MgO samples, which are mounted on a 3D translational and a rotational stage. The (001) oriented MgO sample is 1×1 cm and is 200 μm thick. The harmonics generated hit a grating which angularly disperses the generated harmonics and focuses them on a photomultiplier. The configuration and the characteristics of the grating and photomultiplier are available in Appendix E. During the measurements, the voltage on the photomultiplier is set to 2.8 kV. The vacuum inside the chamber is achieved by a roughing pump that reduces the pressure to $\sim 10^{-2}$ mbar, and a turbo pump that additionnally reduces it down to 10^{-6} mbar. Note that an iris aperture is aligned in front of the entrance window of the chamber (outside the vacuum chamber) to control the laser beam size and intensity. In our case, the iris is open to 4-5 mm in diameter.

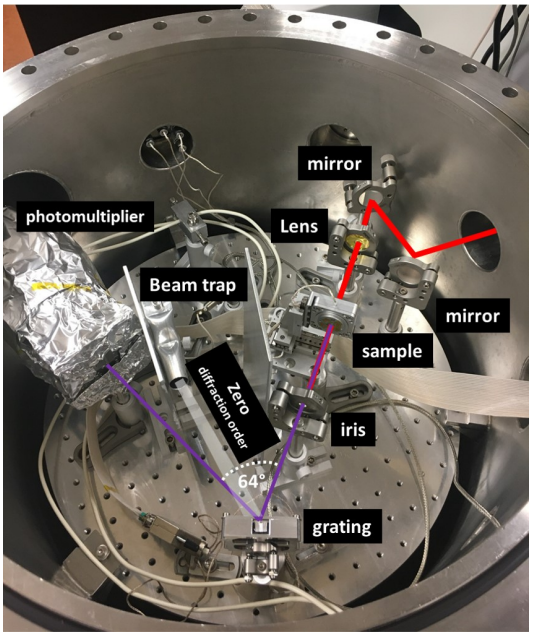

Figure 4.38: Picture of the *in-vacuum* HHG experiment, at CEA Saclay.

4.5.2 Results and Discussion

Figure 4.39 depicts the high order harmonic spectrum generated from a 200 μm thick MgO crystal, for a laser beam vertically polarized and aligned along the ΓX direction of the MgO crystal. The laser intensity is estimated to be 8 TW/cm^2 at the beam focus. High order *vacuum* harmonics are generated in MgO; we detect up to the 33$^{\text{rd}}$ harmonic order which corresponds to a photon energy of $\sim$ 23 eV and 54 nm in wavelength. The first plateau includes the low order harmonics up

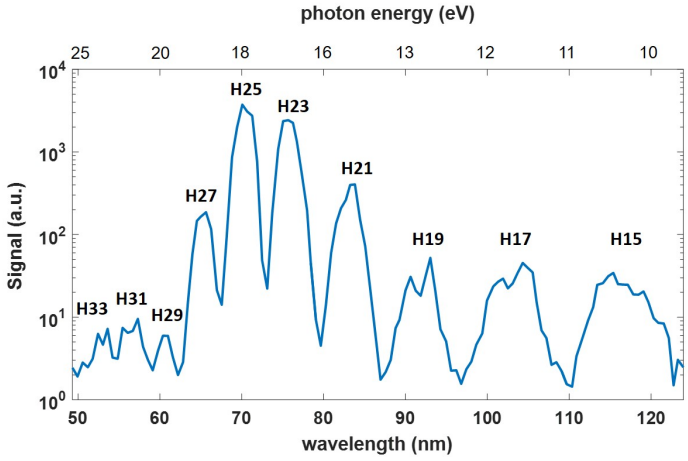

Figure 4.39: High order harmonic spectrum generated from MgO, at a laser intensity of 8 TW/cm^2.

to harmonic 27 (66 nm ≡ 18.8 eV), while the second plateau includes harmonics H29 to H33, the highest detectable harmonic here. Note that the difference in the harmonic signals in the first plateau is not attributed to the detection system, but it seems it's a particular feature of the HHG in MgO (figure 4.37 [135]). The high order harmonic generation mechanism in the vacuum UV spectral range is highly sensitive to the angle between the linear polarization and the crystal axis. To investigate the polarization dependence of high order harmonics generated from MgO, we perform polarization measurements by setting a vertical polarization of the laser beam and rotate the sample over 90° of angular range. The measurements are carried out for an estimated laser intensity of 8 TW/cm^2, and the results are depicted in figure 4.40. The figure highlights the HHG efficiencies along the ΓX and ΓK directions within the fourfold symmetry. The polarization dependence of all generated harmonics

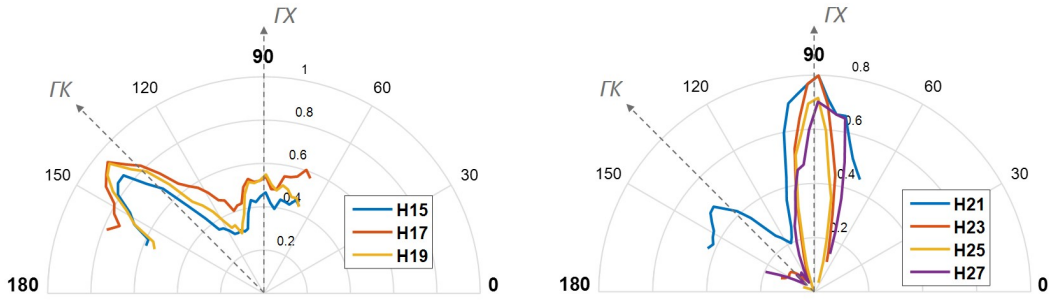

Figure 4.40: Polarization dependences of VUV harmonics generated from a 200 μm thick MgO sample, at a laser intensity of 8 TW/cm^2. (a) Polarization dependences of H15-H19 and (b) Polarization dependences of H21-H27.

reveals a fourfold symmetry, reflecting the cubic crystal structure of MgO. The low order harmonics of the first plateau, particularly harmonics 15, 17 and 19, have their maximum generation efficiency when the laser polarization is aligned along the ΓK directions of the crystal, similar to the polarization dependences of the visible and deep UV harmonics generated in air (section 4.4.2). However, for higher harmonic orders of the first plateau, H21 to H27, their maximum generation efficiency is obtained when the polarization is along the ΓX directions of the crystal, which is in agreement with the results reported by Y. S. You et al. [20]. This is because low and high order harmonics are generated from different regions of the band structure. Furthermore, higher order harmonics exihibit a stronger dependence on the laser polarization, as they are generated from higher anisotropic regions of the band structure.

4.6 The Anisotropy Gating Technique

4.6.1 Introduction

This section aims at taking advantage of the laser polarization dependence of the high harmonic generation efficiency in crystals to generate isolated attosecond ra-

diation. Isolated attosecond pulses have been generated from atomic gas HHG in several ways, mainly by gating the fundamental driving field [136, 137, 39, 138]. "Gating" refers to restructuring of the fundamental pulse to allow the generation only within a very short temporal window of the pulse, ideally, the generation within one optical cycle. One of the techniques is the polarization gating, in which two optical pulses, orthogonally polarized, are delayed such that the relative phase difference ϕ is $\pi/2$. The two electric field pulses $\overrightarrow{E}_1$ and $\overrightarrow{E}_2$ can then be expressed in the time domain as:

$$E_1 = E_0 \mathrm{e}^{-\frac{(t-t_1)^2}{\tau^2}} \cos(\omega t) \tag{4.5}$$

$$E_2 = E_0 \mathrm{e}^{-\frac{(t-t_2)^2}{\tau^2}} \cos(\omega t + \phi) \tag{4.6}$$

where the delay between the two pulses is given by $\delta t = t_1 - t_2$. E_0, τ and ω are the field amplitude, pulse duration and angular frequency of the electric fields, respectively. Around the peak of the created pulse a circularly polarized state is produced, while at the tails of the pulse the polarization remains linear, as illustrated in the upper diagram in figure 4.41. If this pulse is passed through a quarter-wavelength plate, the central cycles of the pulse will be converted into a linearly polarized state, while the tails would be converted into circularly polarized states. The interaction of this highly intense pulse with gas atoms results in the generation of a burst of light only at the linearly polarized cycle, hence the emission of an XUV attosecond radiation [136]. However, if we introduce a π delay between the two pulses, the result is a rotating linear polarization within the pulse envelope, as shown in the lower diagram of figure 4.41. The combination of this pulse with the highly

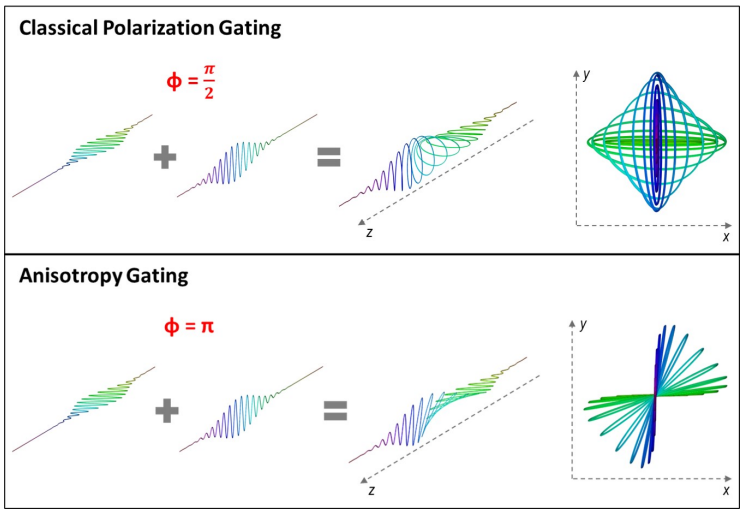

Figure 4.41: Illustration of the polarization gating and the anisotropy gating pulses.

anisotropic polarization dependence of the harmonics generated in MgO should result in a gated state, where the generation should take place ideally only when the

polarization of one cycle is aligned along the proper crystal axis. We call this the *Anisotropy Gating* technique. It is illustrated in figure 4.42. The optical cycle that is of our interest is the central one at the peak of the pulse, and will be referred to as the "gated" optical cycle.

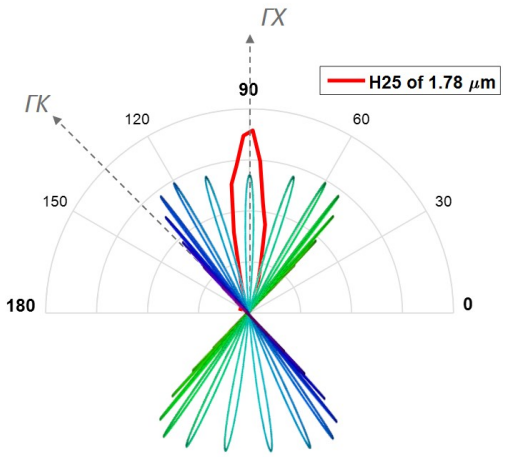

Figure 4.42: Illustration of the *Anisotropy Gating* technique. The semi-polar plot shows the polarization dependence of harmonic 25 of the 1.78 μm laser generated from the MgO crystal. The "gated" pulse is superposed on the polar plot in such a way that the "gated" cycle is aligned along the ΓX direction i.e. the crystal direction along which the generation efficiency is maximum.

4.6.2 Experimental Setup and Details

To produce two laser beams delayed in time with a precise control over the relative phase, we implement the TWINS interferometer, inspired by A. Oriana et al. [139]. The TWINS interferometer consists of a pair of birefringent wedges and a birefringent crystal with an optic axis perdendicular to the optic axis of the wedges. A representation of the TWINS setup is shown in figure 4.43. The birefringent material composing the wedges and the crystal is an $\alpha - \mathrm{BBO}$ crystal with an AR coating at 1.78 μm to maximize the transmission of the fundamental beam. The crystal is 4.25 mm thick with dimensions 20 x 10 mm, while the wedges' maximum thickness is 3 mm and their minimum thickness is 1.25 mm. The wedges' angle is 5°. The optic axis of the wedges is perpendicular to the 10 mm x 3 mm side, while the optic axis of the crystal is parallel to the 10 mm side. The TWINS setup is placed in the beam path outside the vaccum chamber, as shown in figure 4.43. The crystal and the wedges were ordered from Newlight Photonics Inc. When a linearly polarized beam at 45° angle from the optic axis of the wedges enters the pair of wedges, due to their birefringence, it is split into two perpendicular components, a vertical one (s-polarized) and a horizontal one (p-polarized) that travel at different

speeds. As a result a large delay between the two components is created. The crystal with the optic axis perpendicular to the optic axis of the wedges serves to reset the delay back to zero and combine the pulses. To vary the delay δt between the two perpendicular polarizations, the second wedge is placed on a translation stage in order to vary the effective combined thickness of the wedges d_B. The group delay between the two pulses is then given by: $\delta t = (d_A - d_B)\left(\frac{1}{v_{go}} - \frac{1}{v_{ge}}\right)$, where v_{go} and v_{ge} are the ordinary and extraordinary group velocities of the fundamental field inside the $\alpha - \mathrm{BBO}$ material. Likewise, the relative phase difference ϕ between the cycles of the optical pulses is given by:

$$\phi = (d_A - d_B)\left(\frac{1}{v_{po}} - \frac{1}{v_{pe}}\right) \tag{4.7}$$

where v_{po} and v_{pe} are the ordinary and extraordinary phase velocities. Experimentally, the phase delay is set by monitoring the temporal interference. We express in the following the delay as the phase delay in number N of cycles. The biggest advantage of the TWINS interferometer as compared to other interferometric techniques, is that the phase is very stable. Another advantage is that the two delayed beams are directly aligned along the propagation axis, and both pass through the same material, hence their wavefronts are immediately aligned and they experience the same dispersion effect from the $\alpha - \mathrm{BBO}$ crystals. To spectrally and temporally characterize the fundamental field exiting the sample, a mirror and a lens are placed on a motorized translation mount inside the vacuum chamber, aligned after the sample as shown in figure 4.43; the lens collimates the beam which exits the chamber, and is guided to the FROG setup. A lens also focuses the beam onto a CMOS camera for spatial characterization of the two beams. The characterization of the optical pulse after the sample permits the characterization of the real pulse inside the sample, including the induced GDD (group delay dispersion) from all the optics, and any induced nonlinear effects from the sample. To set the phase delay and characterize the pulses, a polarizer is placed outside the chamber at the exit of the collimated beam. Note that since the grating efficiency for a s-polarization is greater than that for a p-polarization by almost a factor of 3, we place a half-wavelength plate (HWP) just after the TWINS stage to rotate the "gated" optical cycle by 45° (i.e. to s-polarization), so that it is aligned along the best grating efficient axis. The sample's axis ΓX is aligned along the "gated" cycle, to optimize the harmonic generation efficiency. The other optical cycles at the tails of the "gated" pulse match the minimal generation efficiency along the ΓK directions, and therefore should not generate harmonics. To compensate for the negative GDD imposed by all the optics, we place a 3 mm thick ZnSe crystal in the beam path before the vacuum chamber. The MgO sample is 100 μm thick with (001) orientation.

4.6.3 Gated Pulse Characterization

To get insight into the effect of the delay on the outcome of the "gated" pulse, figure 4.44 summarizes simulated optical pulses with different phase delay values between the two beams: (a) 5 cycles ($\sim$ 30 fs), (b) 7 cycles ($\sim$ 41 fs) and (c) 9 cycles ($\sim$ 53 fs). The simulations are computed given the signal wavelength $\lambda = 1.78$ μm and a

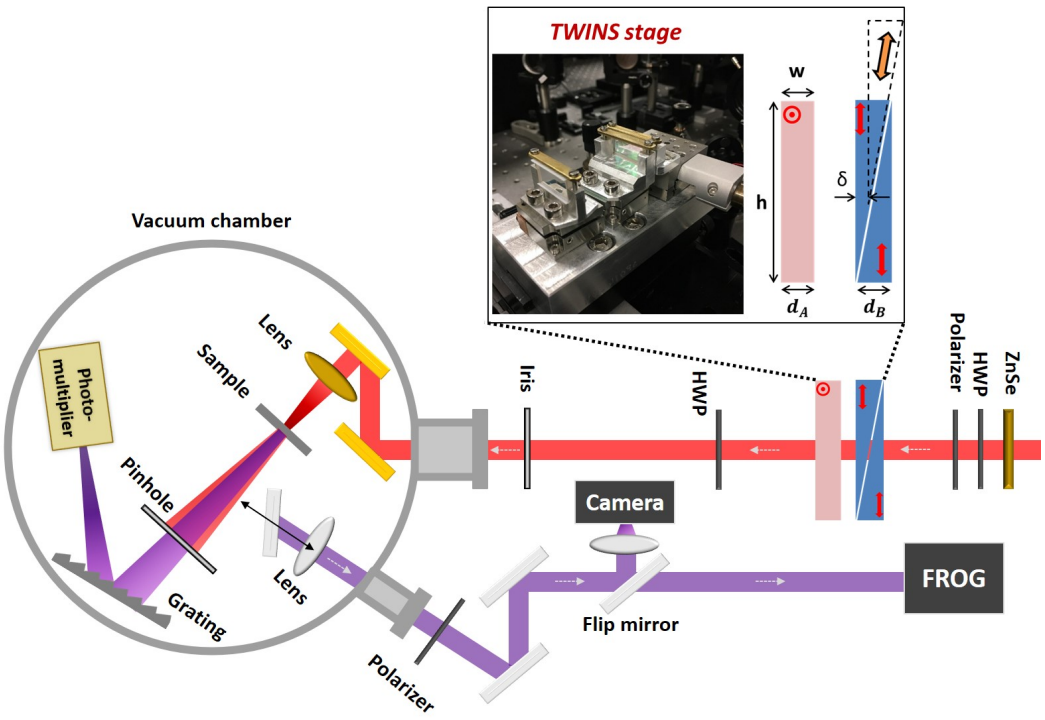

Figure 4.43: Sketch of the experimental setup of the *Anisotropy Gating* technique, showing the TWINS interferometer, the vacuum HHG setup and the spatiotemporal characterization beam line.

pulse duration τ of 30 fs. When the delay is small, the optical cycles at the central part of the two pulses interfere, resulting in several intense cycles at the center of the "gated" pulse. This does not support the anisotropy gating technique which requires the generation with ideally one optical cycle, while most of the other cycles align to the improper crystal axes. For larger delays, such as a delay of 9 cycles (figure 4.44(c)), very few cycles at the tails of the pulses interfere which results in a strong rotating polarization with a minimal intensity at the center of the resulting optical pulse, as can be seen in the polar plot. In fact, a compromise between the two delays would be recommended. Indeed, the 7 cycles delay (figure 4.44(b)) seems to be a compromise between the velocity of rotation of the polarization states within the "gated" pulse and the intensity of the central cycles.
Experimentaly, the characterization of the "gated" pulse from the TWINS is done using different projections (vertical, horizontal and 45°) on the analyzer, which is the polarizer placed at the output of the chamber. For instance, the zero delay is verified using the 45° projection in which a contructive interference is observed on the camera. Then, to set the proper delay and relative phase, we use the $-45°$ projection and optimize for the destructive interferences which are more sensitive and easily visible. As we translate the second wedge we clearly see constructive and destructive interference fringes. To set a certain number of delayed cycles, we count the number of times the destructive interference fringes occur. The two

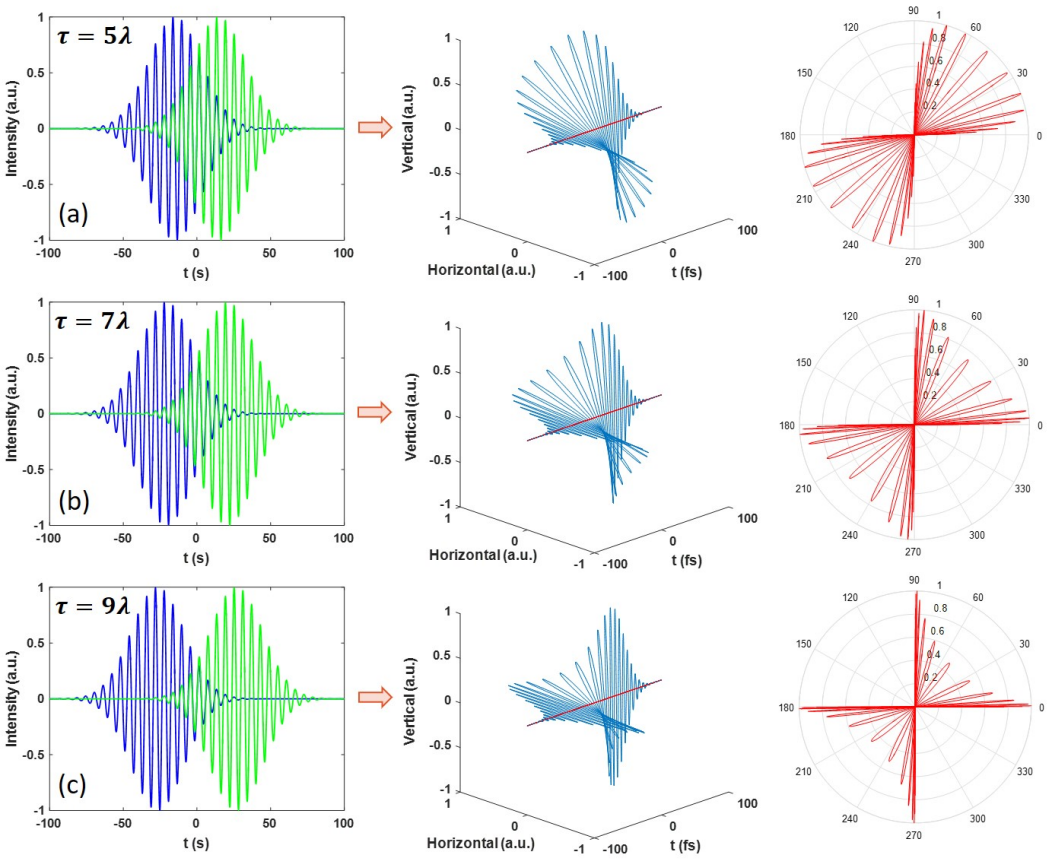

Figure 4.44: Simulation of the "gated" pulse obtained by different delays between the two beams, (a) 5 cycles (b) 7 cycles and (c) 9 cycles. The second column shows the resulting "gated" pulse in three dimensions, and the third column is its representation in the plane perpendicular to the time axis.

main perpendicular components of the "gated pulse" exiting the TWINS are then analyzed through the polarizer by the FROG technique, which gives us access to the temporal and spectral envelopes and phases. Figure 4.45 shows (a) the horizontal component of the "gated pulse" in the spectral domain as retrieved from the FROG and (b) its corresponding pulse envelope and electric field in the temporal domain. The pulse duration is around 40 fs. The "gated" pulse is reconstructed from the two projected pulses, i.e. the TWINS horizontal and vertical components, by a MATLAB code. For a 7.5 cycles delay the resulting computed "gated" pulse is shown on the right of figure 4.46.

4.6.4 Results and Discussion

The strong anisotropy in the polarization dependence of vacuum harmonics, especially of harmonics H23, H25 and H27, offers a gating window within a very small angular range. Upon the interaction of the rotated polarization pulse with MgO, the

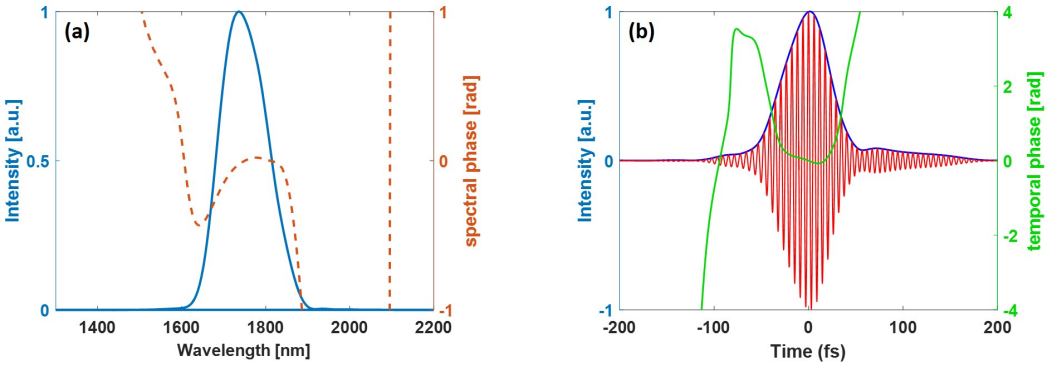

Figure 4.45: (a) Spectral characteristics of the horizontal component of the "gated" pulse retrieved from the FROG measurement. (b) Temporal characteristics of the corresponding electric field by Fourier transform.

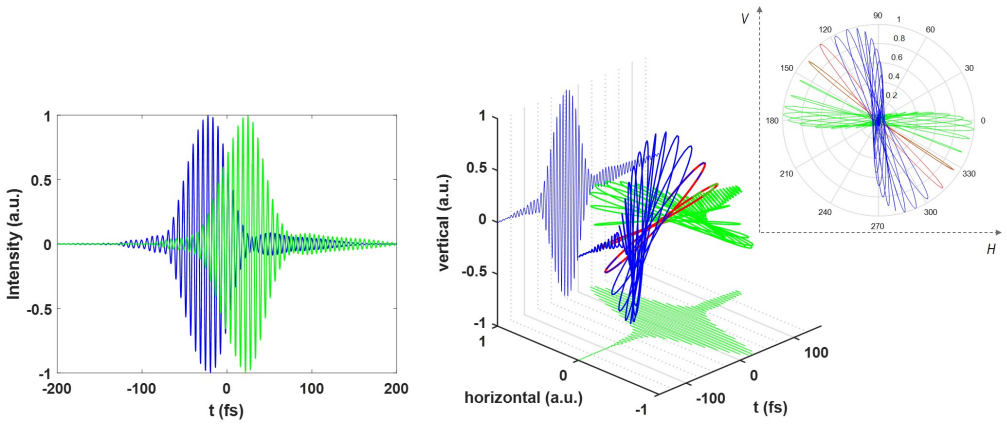

Figure 4.46: Left: The vertical and horizontal components of the two beams delayed by 7.5 cycles with respect to each other. Right: Reconstruction of the "gated" pulse.

high harmonic emission would take place only when the instantaneous polarization state of the optical cycle is aligned along the proper crystal axis (ΓX), thus confining the harmonic emission on a sub-optical cycle time scale. This should result in spectrally broader and complex harmonic structure. Figure 4.47 compares the HHG spectra generated with vertically polarized laser pulses (blue spectrum), i.e. zero delay between the two beams, and with 7.5 cycles delay (red spectrum). The pulse duration of the resulting pulse with 7.5 cycles delay is measured with its projection at 45° by the FROG. The pulse duration is around 70 fs. The corresponding measurements are carried out at an estimated input (vacuum) intensity at focus of 10 TW/cm^2. For a zero delay, the measured HHG spectrum (in blue) from the MgO crystal consists of well-resolved odd harmonics up to the 27$^{\text{th}}$ order. The estimated input intensity at focus is 12 TW/cm^2. Interestingly, the HHG process driven by the "gated" pulse obtained for 7.5 cycles delay, results in a modulated spectrum

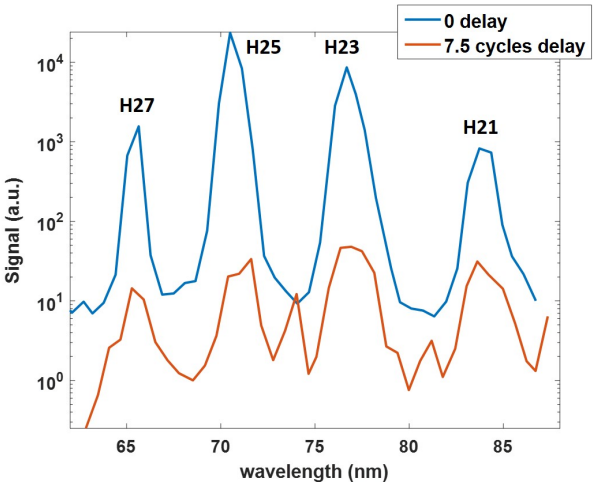

Figure 4.47: HHG spectra measured from MgO with zero delay between the two laser beams (blue spectrum) and with 7.5 cycles delay (red spectrum). The estimated input intensity in the former case is 13 TW/cm^2, while in the latter case it is 10 TW/cm^2.

consisting of spectrally broader harmonics, in addition to signal measured between odd harmonics occuring at even harmonic wavelengths. This is a first indication of the symmetry breaking of the HHG process. In addition, the high harmonic generation efficiency is lower than that measured for zero delay. We attribute this result to the efficiency of the HHG process driven by the "gated" pulse. Ideally, one would expect a continuous spectrum from the generation with one optical cycle.
To study the effect of the delay on the harmonic emission, we measure the harmonic spectra for different values of the delay between the two beams. The delay is varied between 6 and 8.5 cycles, and the harmonic spectra are measured and reported in figure 4.48. The HHG process driven by the "gated" pulse is highly sensitive

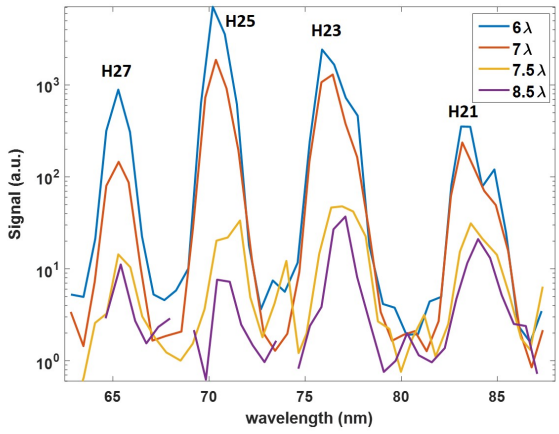

Figure 4.48: HHG spectra measured from MgO with gated pulses obtained from different delays between the two laser beams. The estimated input intensity is $\sim 10\,\mathrm{TW/cm^2}$.

to the delay. The HHG spectrum becomes less intense and less contrasted as we increase the delay from 6 cycles to 7.5 cycles delay. Indeed, for a delay of 7.5λ the HHG spectra is broader and more modulated than that measured with 7λ delay. By varying the delay from 7 to 7.5 cycles, the polarization of the cycles flips by 90°. Moreover, some of the optical cycles could be elliptically polarized, hence the 7.5λ delay would reverse the handedness of the ellipticity inside the pulse. Interestingly, Y. S. You et al. [20] have observed an enhancement in the harmonic generation for an elliptically polarized beam, and demonstrated that the handedness of the ellipticity is important to determine the electron trajectories in the MgO crystal to connect to the proper atomic sites, and consequently enhance the harmonic efficiency. It is important to bear this in mind, especially as we would need to avoid recombination on other efficient generation sites than the principle one. For larger values of the delay, the optical cycles at the center of the "gated" pulse are less intense (as illustrated in figure 4.44(c)), which explains the low efficiency of the generated harmonics.
To align the "gated" optical cycle with the proper crystal axis, we rotate the sample around its vertical axis in the surface plane by few degrees and notice that the HHG process is also very sensitive to this alignment. The high harmonic generation process, in this study, is driven by the "gated" pulse, obtained by a 7.5 cycles delay between the two beams. The sample is rotated in steps of ±3° around the 0° angle, which initially corresponds to an alignment of the vertical laser polarization with the ΓX direction of the crystal. The measured HHG spectra are summarized in figure 4.49. At angles of ±6°, the resulting spectrum reveal only odd harmon-

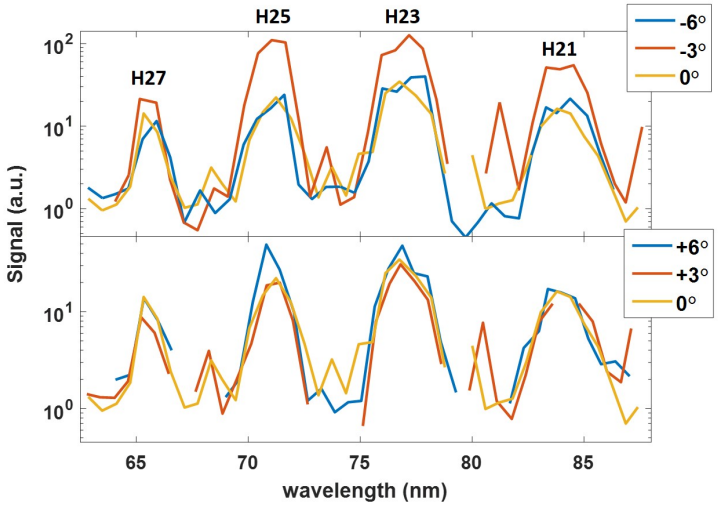

Figure 4.49: HHG spectra measured from MgO by rotating the crystal around the vertical direction, at an estimated input intensity of $\sim 10\,\mathrm{TW/cm^2}$. The HHG process is driven by the gated pulses obtained from 7.5 cycles delay between the two beams.

ics. However, around the 0° angle the spectra becomes less contrasted and more modulated. Particularly, we observe some peaks at the positions of the even order harmonics. The highest signal is obtained at an angle of −3°, which seems to cor-

respond to a better alignment of the "gated" optical cycle with the proper crystal axis (ΓX).
The CEP (carrier-envelope phase) of the laser plays a similar role as the sample alignment. The CEP of the laser is defined as the phase between the pulse envelope and the carrier wave. In this experiment a stable CEP is an important requirement to better define our "gated" pulse. By varying the CEP, the polarization of the cycles within the pulse rotates slightly, which allows a fine alignment of the "gated" cycle with the proper crystal axis. Figure 4.50 compares two HHG spectra obtained both with a 7.5λ delay between the pulses but with a CEP shift of 1.6 rad between the two measurements. Interestingly, the slight change of the CEP on the laser sig-

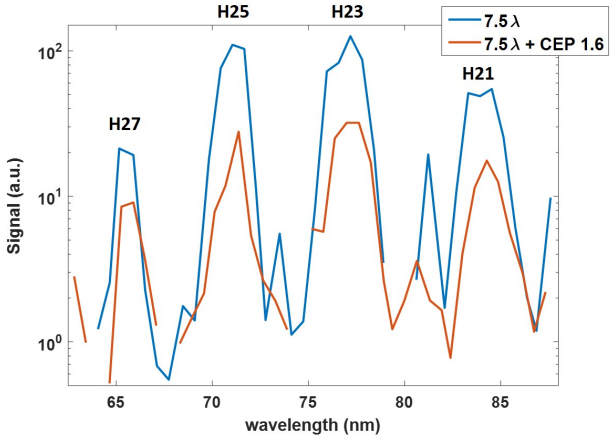

Figure 4.50: HHG spectra measured from MgO with gated pulses obtained from 7.5 cycles delay between the two beams (blue curve) and by a change of the CEP of the laser by 1.6 rad (red curve). The estimated input intensity is $\sim 10\,\mathrm{TW/cm^2}$.

nificantly impacts the generation process driven by the "gated" pulse. The strong modulations of the spectrum i.e. the peaks at the positions of even harmonic orders observed with the 7.5λ delay disappear, and the efficiency becomes lower.
One limiting parameter could be the pulse duration which is long in our case. Consequently, several half cycles are closely aligned with the best crystal axis. The next step would be to compress our fundamental laser pulses before creating the "gated" pulse. Despite some promising preliminary results of the anisotropy gating technique, we haven't yet observed the clear signature of generation by a single optical cycle, that would lead to the emission of a broadband XUV radiation. Nevertheless, the study reported in this section sets a first attempt for the generation of isolated attosecond pulses through polarization spectroscopy of solid-state HHG.

4.7 Conclusion

In this chapter, we have successfully shown that high harmonic generation in semiconductor crystals exhibits a strong dependence on an entangled relation between the laser properties and the structural and optical properties of the generation

medium. We have seen that the laser intensity guides electron dynamics and defines the regime in which the HHG process takes place. The HHG efficiency dependence on the ellipticity of the driving field reveals a less critical dependence than in atomic gas HHG; the efficiency of the harmonics generated from silicon, gallium arsenide (GaAs) and magnesium oxide (MgO) decreases with increasing laser ellipticity. The generation efficiency is minimal for a circularly polarized driver, yet not zero. In addition, the linear laser polarization also determines the directions along which the electron excursions take place during the HHG process. Because of the atomic arrangement inside the solid and the crystal symmetry, the HHG efficiency varies along different directions of the crystal. We have demonstrated the anisotropic dependence of the generated harmonics in different semiconductors on the laser polarization. Cubic crystals like silicon and magnesium oxide, as well as zinc-blende semiconductors such as gallium arsenide lead to a harmonic generation with a fourfold symmetric dependence on the laser polarization. Moreover, as the harmonic order increases the generation becomes strongly dependent on the angle between the laser polarization and the crystal axis, since they are generated from more anisotropic regions of the band structure. Polarization spectroscopy of HHG in crystals not only encodes fundamental information about the generation mechanism, but also provides a mean to study the properties of the generation medium and map its band structure. Finally, we have exploited the strong anisotropy in the polarization dependence of high order harmonics and proposed the *Anisotropy Gating* technique as a scheme for the generation of isolated XUV attosecond radiation.

Since the driving laser field propagates inside the medium of generation towards the exit surface before it generates, it can accumulate linear and nonlinear propagation effects. These macroscopic effects should be carefully treated; we have confirmed the presence of the Kerr effect in the spatial and temporal domains of the laser field in silicon, GaAs and MgO, and explored its effect on the laser properties and the generation mechanism. In silicon, the self-focusing effect permitted the enhancement of the intensity of a nanojoule laser inside a thick silicon sample, which led to a stronger harmonic signal. In GaAs, the self-focusing was proved to be stronger along the ΓK crystal directions than along the ΓX directions. Besides, theoretical calculations emphasized the important role of the photoionization effect in GaAs. We have shown that at very high laser intensities, Kerr effect can lead to self-compression of the laser pulse in the generation medium, which can further increase the HHG efficiency. This was demonstrated upon the interaction of the intense driving laser beam with an MgO crystal. In order to eliminate macroscopic effects, we have investigated HHG in two experimental configuration states, firstly in transmission geometry from a very thin silicon sample (2 μm), and secondly in reflection geometry from a GaAs crystal.

Chapter 5

Enhancement and Spatial Manipulation of Solid-State HHG

5.1 Introduction and Motivation

One of the great advantages of HHG in crystals, as compared to HHG in atomic gases, is the additional degrees of freedom provided by the solid-state nature of the generation medium. Indeed, it can be structured to tailor the harmonic radiation. In section 5.2, we explore the local confinement and enhancement of the laser electric field in micrometer sized ZnO cones patterned at the exit surface of the crystal, which results in an enhancement of high order harmonics. In section 5.3, we introduce orbital angular momentum (OAM) to the harmonic beams by patterning diffractive phase objects on the generation medium, and by transferring the OAM from the fundamental laser to the harmonics. Finally in section 5.4, we perform a Coherent Diffraction Imaging (CDI) experiment based on harmonic radiation generated from ZnO, to prove the coherence of the solid-state harmonics and image a micrometer sized structure as a proof of principle.

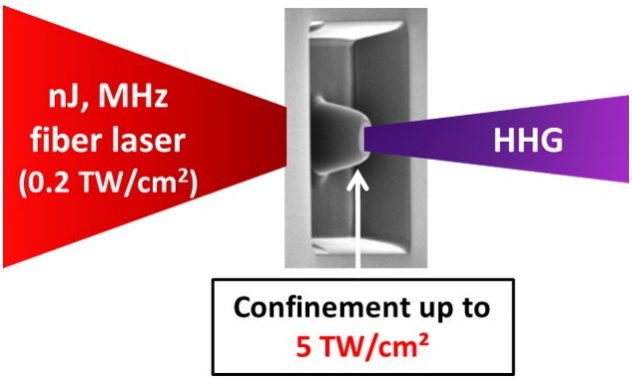

Figure 5.1: Motivation scheme of high harmonic generation in nanostructured crystals.

5.2 HHG Enhancement by Field Confinement in Nanostructured Cones

5.2.1 FDTD Simulations by Lumerical

The goal of generating harmonics in nanostructured truncated cones is to enhance the electric field of the laser pulses of nanojoule energies, in order to reach the intensity range required for efficient high order harmonic generation (figure 5.1) [22]. Starting with a maximum intensity at focus provided by a nanojoule laser of 0.2 TW/cm^2, the confinement of the laser field inside a nanostructured cone can boost the laser intensity up to 5 TW/cm^2, that is an enhancement factor of 25.
The confinement and enhancement of the electric field in nanostructured cones is simulated by a commercial solution for FDTD calculations, developed by Ansys Inc./Lumerical (Appendix G). The dimensions of the truncated microcones are optimized to obtain the highest possible enhancement of the electric field. A cross-section of the simulated microcone along the propagation direction (z) of the laser field is shown in figure 5.2(a). Figures 5.2(b) and 5.2(c) summarize the results

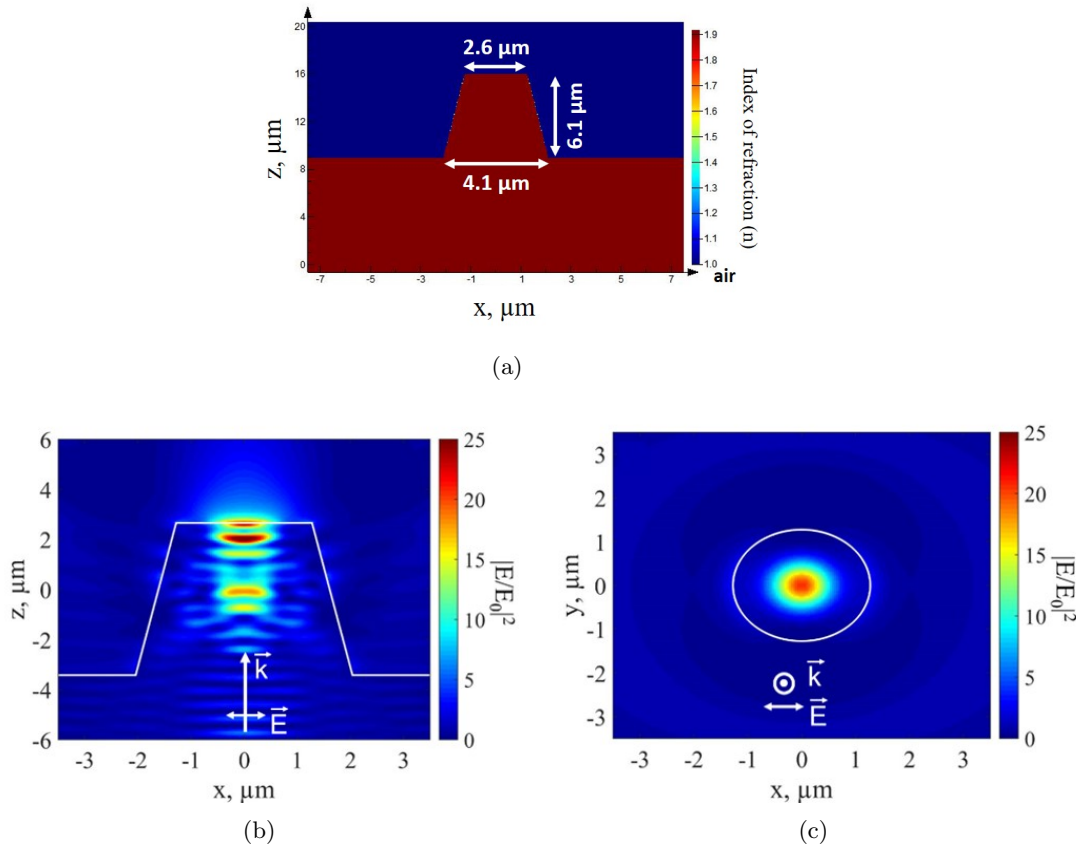

Figure 5.2: Lumerical simulations of the nanostructured ZnO truncated cone. The intensity at the top of the microcone is enhanced by a factor of 25.

obtained from the simulations. The ($\overrightarrow{k}$) vector denotes the propagation direction and the ($\overrightarrow{E}$) vector represents the laser polarization. Figure 5.2(b) shows that the electric field is confined near the top surface of the truncated cone, where the modulus square of the laser field $|\overrightarrow{E}|^2$, i.e. the intensity, is enhanced by a factor of 25. A cross-section in the yx plane (perpendicular to the propagation direction) at the top surface of the truncated cone shows the intensity distribution with a nearly Gaussian mode. As a result, given an initial intensity of 0.2 TW/cm^2, the laser intensity can reach a maximum value of 5 TW/cm^2 in our truncated microcone.

5.2.2 Experimental Setup and Details

The nanostructured cones are patterned by the Focused Ion Beam (FIB) technique. A description of this technique is found in appendix H. SEM images taken at 0° and 60° of the patterned truncated cones are shown in figure 5.3(b). The NOVAE laser is employed for the study; a picture of the experimental setup is shown in figure 5.3(a), which was schematized in figure 3.2 in Chapter 3. The laser pulses are focused by a 2.5 cm focal length off-axis parabola onto the cones. The harmonics generated are collected by a 6 cm focal length lens which then focuses them on a CCD camera and a spectrometer.

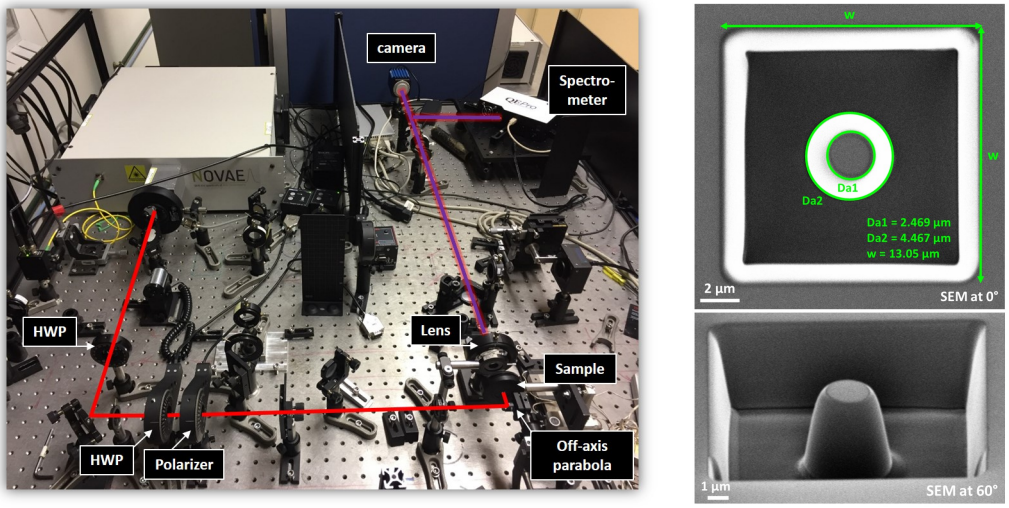

(a) Sketch of the experimental setup.

(b) SEM images.

Figure 5.3: HHG experiment in nanostructured truncated cones. The experimental setup is shown on the left (figure 5.3(a)) and the patterned cones are shown in the SEM images on the right (figure 5.3(b)).

5.2.3 Enhancement of Harmonics in the UV-Visible Spectral Range

To experimentally verify the enhancement of the laser field in our nanostructured cone we measure the harmonics generated in the microcones and compare their

efficiency to the harmonics generated in bulk ZnO at low and high intensities, 0.045 TW/cm^2 and 0.17 TW/cm^2, respectively. The harmonic spectra measured from the ZnO microcones versus bulk ZnO are depicted in figure 5.4. At a very low laser intensity, 0.045 TW/cm^2, harmonics up to the 9th order (at 233 nm) are efficiently generated from the microcones, whereas only harmonic 3 (at 700 nm) is generated from the bulk (figure 5.4 (a)). Note that the band edge of ZnO corresponds to a

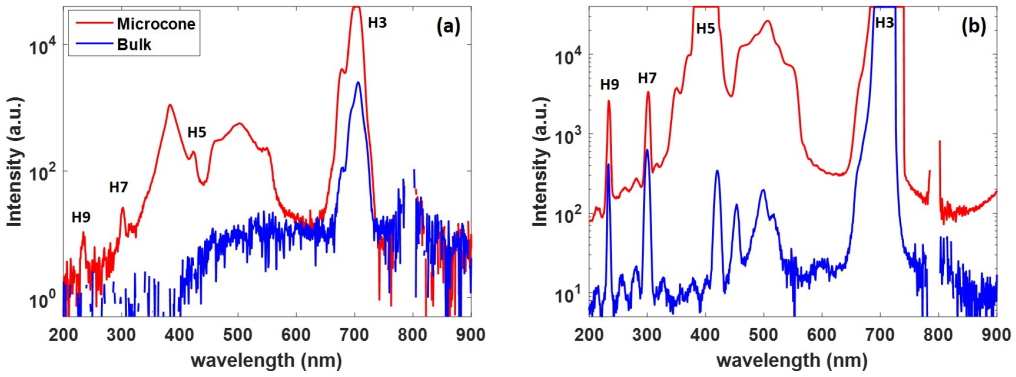

Figure 5.4: Enhancement of the harmonic generation in the nanostructured truncated ZnO cones. The spectra on the left (a) is measured at a laser intensity of 0.045 TW/cm^2, while the spectra on the right (b) is measured at a laser intensity of 0.17 TW/cm^2.

photon energy of 3.2 eV, which is the peak situated at a wavelength of $\sim$ 380 nm, whose tail overlap with that of the 5th harmonic (H5, 2.95 eV). The band edge emission is an incoherent emission, referred to as fluorescence, which explains why its spectral envelope does not follow the spectral envelope of the fundamental or the coherent harmonics. Another strong incoherent signal situated at a wavelength of $\sim$ 500 nm is detected, which corresponds to luminescence from defect states in ZnO. At a higher laser intensity, 0.17 TW/cm^2 (figure 5.4 (b)), which is almost the maximum intensity provided by the laser at its focus, harmonics up to the 9th order are generated in the bulk, however, the harmonics generated in the microcone are enhanced by one order of magnitude for above band gap harmonics (H9 and H7) and by two orders of magnitude for below band gap harmonics (H5 and H3). Moreover, the incoherent fluorescence is further enhanced in the microcone which saturates and completely overlaps harmonic 5.

5.2.4 Damage of Truncated Cones

One limitation of solid-state HHG as compared to atomic gas HHG is the damage of the medium of generation upon laser exposure. This sets a threshold intensity beyond which the semiconductor crystal will be damaged. Nevertheless, even with an intensity lower than the threshold intensity, exposing the medium of generation to laser pulses for a long time can also restructure and damage it. In order to study the lifetime of our nanostructured cones with this laser system, we monitor the signals of harmonics 9 and 7, generated from the microcone and from the bulk, during a time duration of 3 hours. Figure 5.5(a) and 5.5(b) reveal the decay of

H9 (red curve) and H7 (blue curve) signals, respectively, as a function of time. The harmonic signals, H9 and H7, generated from the bulk are also monitored within a time duration of 3 hours (black curve in figure 5.5). H9 and H7 signals generated from the microcone show a continuous increase during the first half an hour after which the signal starts to decrease gradually to reach the value from the bulk emission. On the other hand, H9 and H7 signals generated from the bulk are constant throughout the whole 3 hours.

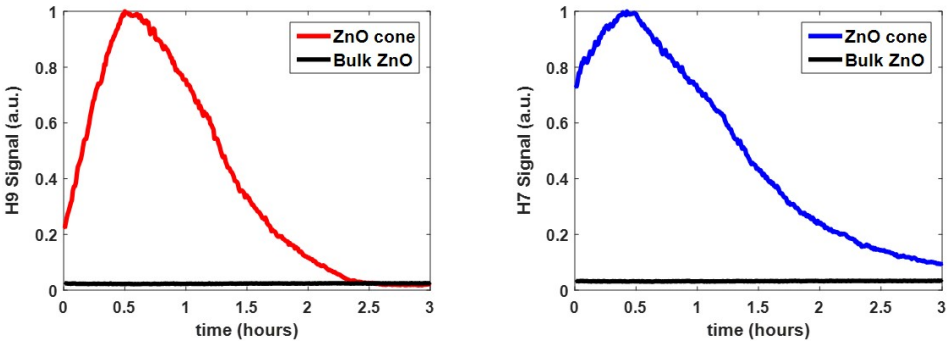

(a) Decay of H9 signal with time.

(b) Decay of H7 signal with time.

Figure 5.5: Temporal evolution of the harmonic emission (H9 and H7), from the ZnO cone, for a time duration of 3 hours. The harmonic signal generated from the bulk (black curve) is normalized to the maximum harmonic signal generated from the nanostructured ZnO cone. The laser intensity is 0.175 TW/cm^2.

In order to understand and visualize the temporal evolution of the harmonic signal generated from the microcones, a set of three identical cones were patterned with the FIB. The first one is used as a reference and hence not exposed to laser pulses, while the second and the third are continuously exposed to laser pulses for a time duration of 30 minutes and 3 hours, respectively. SEM measurements of the top surface and inner body of the microcones are then performed (figure 5.6). The cone is vertically cut in half by the FIB. In figure 5.6(b), SEM images show that structural modification at the top surface of the cone occurs during the first half an hour of laser exposure. Two main cracks appear at the surface center of the cone. Interestingly, those cracks are perpendicular to the linear laser polarization. Femtosecond laser-induced periodic structures described as ripples, on the surface of ZnO crystals have been reported in different studies [140, 141]. Note that the two thin channels along the cone's central height are a result of the cut with the FIB, as the highly energetic ions penetrate from the top cracks. The reshaping of the surface of the cone seems to favor the enhancement of the harmonic signal, and that could explain its increase during the first half an hour. The restructuring of the cone persists for longer exposure times, and the top surface of the cone starts to be ablated and becomes porous. Consequently, the harmonic signal decreases. The damage at the top surface occurs at the position of the maximum field enhancement (figure 5.2(c)), where the laser fluence in the microcone is boosted up to $\sim$ 0.2 J/cm^2, close to the damage threshold [140]. As compared to the bulk, no

damage or restructuring is observed at the surface of the ZnO crystal for the same experimental conditions of input laser intensity and exposure time interval (figure 5.6(d)). This explains why the harmonic signal generated from the bulk remains constant during the whole 3 hours. Although these nanoemitters have a limited lifetime, yet they efficiently offer a nanoscale high harmonic source for compact solid-state EUV sources and applications.

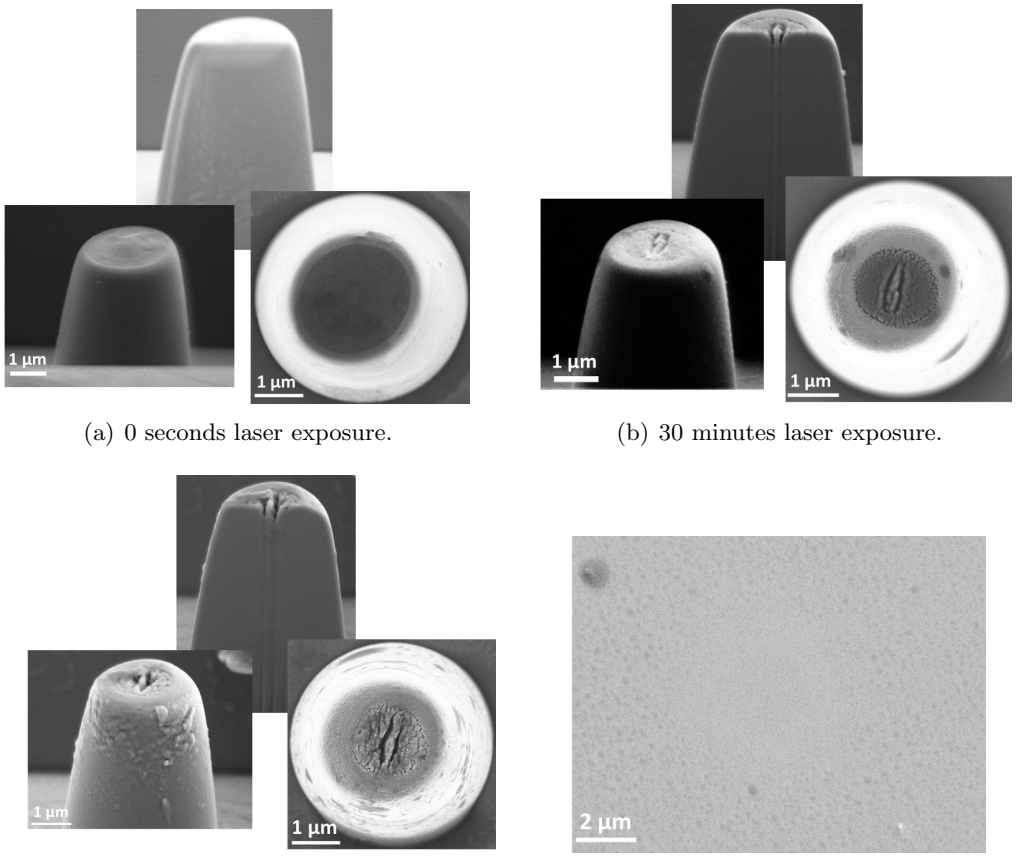

(a) 0 seconds laser exposure.

(b) 30 minutes laser exposure.

(c) 3 hours laser exposure.

(d) Bulk ZnO: 3 hours laser exposure.

Figure 5.6: SEM images at 60° and 0° of the nanostructured cones before and after laser exposure. No restructuring or damage has been observed on the surface of the bulk ZnO.

5.3 HHG with Orbital Angular Momentum (OAM)

In this section, we report on the generation of harmonic beams carrying an orbital angular momentum through two different approaches [26]; first by patterning diffractive optics on the exit surface of the ZnO crystal (section 5.3.1), and second by the transfer of the OAM from the fundamental laser to its harmonics (section 5.3.2). Previous work has already verified the transfer and conservation of the OAM from the generating laser to the harmonics [142, 143, 144]. Beams carrying

an orbital angular momentum possess a helical wavefront with a phase singularity at their center, yielding the well-known optical vortices [145]. Their spatial profile is thus characterized by a donut-shaped intensity profile. They are usually defined mathematically by Laguerre-Gaussian functions in the paraxial approximation [146]. Orbital angular momentum can be introduced into optical beams using different elements, such as the common spiral phase plates, fork gratings or q-plates. With the recent developments of coherent light sources, the generation of beams carrying OAM have triggered significant investigations on a fundamental level and for applications [147, 148, 149, 150]. OAM beams in the IR and visible spectral range have found vast applications in the fields of quantum information, optical trapping as well as microscopy and spectroscopy. Extending optical vortices to the XUV and X-ray attosecond pulses allows to bring these applications to the nanometer and atomic scale, and combine time-resolved studies [151].

5.3.1 Spatial Manipulation of the Generation Medium

5.3.1.1 Patterned Spiral Zone Plates (SZPs)

Spiral zone plates, labelled as SZPs, are diffractive objects that combine beam focusing, just like an ordinary Fresnel zone plate along with OAM mode conversion to create optical votices at their focus with an arbitrary topological charge. The SZPs, considered in this study, are pure phase objects computed numerically by combining the phase profiles of a helical and a spherical wave. The resulting phase of the SZP is described by the following relation $\mathrm{P} = \exp(-\mathrm{i}l\phi)\exp(\mathrm{i}2\pi\sqrt{\mathrm{R}^2+\mathrm{r}^2}/\lambda)$, where $\exp(-\mathrm{i}l\phi)$ is the azimuthal phase dependence of the OAM wave (l being the topological charge), λ is the wavelength of the spherical wave of radius of curvature R which determines the focal length of the SZP, and r is the radial coordinate. All the SZPs that we designed generate optical vortices with a topological charge $l = 1$. From the computed phase P, two types of etching profile can be defined: the *binary* SZP, obtained by the binarization of the phase, P, at 0 and π, and the *non-binary* SZP which corresponds to the wrapping of P within $0 - 2\pi$. For below band gap harmonic energies, the harmonic radiation is generated in the bulk and then propagates towards the exit surface, so the etching depth d in the crystal can be defined as $\mathrm{d} = \lambda\mathrm{P}/2\pi(\mathrm{n}-1)$, where n is the index of refraction of the ZnO material at the harmonic wavelength. For instance, the index of refraction of ZnO at the wavelength of the 5^{th} harmonic (420 nm) is $\mathrm{n} \approx 2.1$.

Binary and Non-Binary Spiral Zone Plates (SZP)

The experimental setup is shown in figure 5.7. It consists of focusing the laser pulses of our NOVAE laser by an off-axis parabolic mirror (2.5 cm focal length) on the patterned *binary* and *non-binary* spiral zone plates, at the exit surface of the ZnO crystal. The SZPs are etched by the FIB technique on a 500 μm thick ZnO crystal. The diameter of each SZP is 10 μm. The harmonic beam generated in the crystal propagates and diffracts through the SZP, and consequently the OAM mode is then created at its focus, set at 6 μm from the sample with our design. To image the

OAM mode at the focus position, a microscope objective lens (numerical aperture NA = 0.65) is aligned and coupled to a CCD camera.

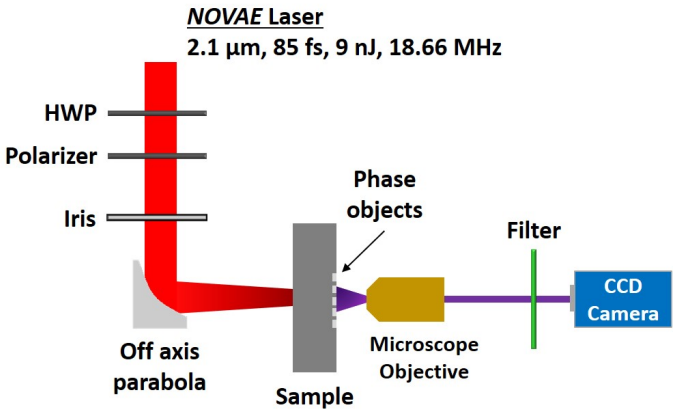

Figure 5.7: Schematic representation of the experimental setup to generate and measure the OAM harmonic beams from spiral zone plates (SZPs).

Figures 5.8 (a) and (c) show the SEM images of our etched *binary* and *non-binary* SZPs, respectively. The corresponding spatial mode of the 5^{th} harmonic at the focal plane of the binary SZP is depicted in figure 5.8 (b). The characteristic donut-shaped profile is observed though it is imperfect. The main cause of the imperfect mode is the restricted number of illuminated zones (grooves) of the SZP that limits an efficient build-up of the diffracted wave at the focus. This is because the harmonic beam diameter is ≈ 3 μm, so only the central part of the 10 μm SZP is indeed illuminated. One proposed solution would be to increase the number of illuminated zones, by either increasing the size of the laser beam or decreasing the zone periodicity. In the first case one has to ensure that the laser intensity stays high enough to generate high harmonics, however we are limited by the maximum power delivered by the NOVAE laser, while the latter case would result in decreasing the focal length of the SZP, thus leading to a tighter focus. Therefore, the design of the SZP was a tradeoff between the laser energy available and the image resolution allowed with our objective lens. Another source of imperfection is coming from the fabrication defaults; the etched depth is about 205 nm, inducing a phase step about 7% larger than requested. Moreover, the gallium ions contamination and the ruggedness induced by the etching process with the focused ion beam (FIB) might have modified the transmittance of the optics. The last source of imperfection is coming from residual aberrations in the generating laser and misalignments. In comparison to the result obtained from the *non-binary* SZP (figure 5.8 (d)), the measured donut-shaped intensity profile of harmonic 5, with a radius of 380 nm, is better defined. This *non-binary* SZP is based on the principle of a Fresnel lens, so it does not suffer from the problem of limited number of illuminated zones. Yet, due to small errors in the etching depth, it also shows a diffractive behavior with the presence of diffraction orders, visible as the parasitic signal surrounding the main mode similar to the *binary* SZP. One improvement could be to design instead

spiral zone plates that are pure amplitude objects; this means that instead of the etched step of the phase SZP one can deposit gold or silver or even pollute the surface in a SZP form. The advantage of an amplitude spiral zone plate is that it eliminates etching defaults and structural modifications induced by the driving laser. In addition, waveguiding effects of the laser field in such phase structures, such as the one exploited in the nanostructured cone, can limit an appropriate diffraction of above band gap harmonics that are generated within the last few tens of nanometers of the structure.

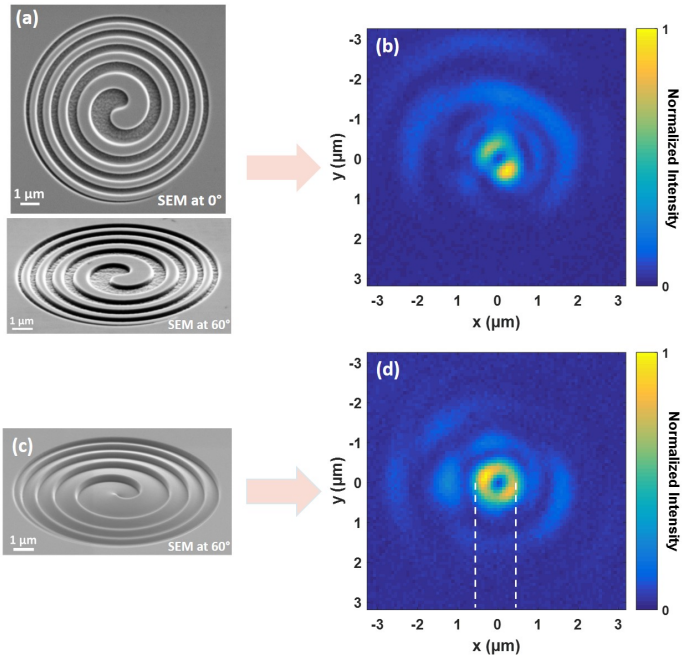

Figure 5.8: Spatial intensity distribution of harmonic 5 (420 nm) at the focal plane of the binary (a) and the non-binary (c) spiral zone plates, etched at the exit surface of the ZnO crystal.

Binary and Non-Binary Off-Axis Spiral Zone Plates (OA-SZP)

Off-axis spiral zone plates, labelled as OA-SZPs, are another type of SZPs that are designed by considering a transversal shift between the centers of the spherical and helical waves. We design our OA-SZP with a shift of 6 μm for a radius of curvature of 10 μm. As a result, unlike the previous on-axis SZPs, the diffraction orders are focused and spread along a horizontal axis. For instance, the first diffraction order is tilted by an angle of 31° from the main optical axis. Hence, to image it, the microscope objective is placed at 31° from the propagation axis, as can be seen in the experimental sketch in figure 5.9. Similarly, both *binary* and *non-binary* OA-SZPs can be achieved. SEM images of our etched *binary* and *non-binary* OA-SZPs are shown in figure 5.10 (a) and (b), respectively. These have been particularly designed at the wavelength of harmonic 5 (420 nm) and to obtain a topological

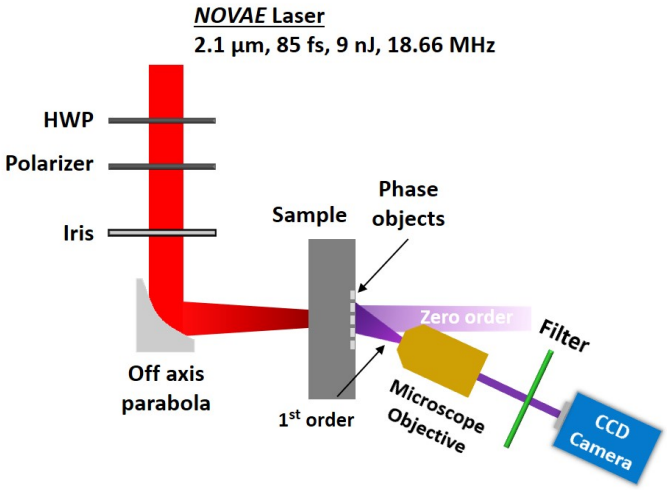

Figure 5.9: Schematic representation of the experimental setup to generate and measure the OAM harmonic beams from off-axis spiral zone plates (OA-SZPs).

charge of 1. The resulting intensity distribution, in the focal plane of the first diffraction order of the 5^{th} harmonic, is shown below each of the corresponding SEM images of the OA-SZPs in figure 5.10. Compared to the previous *binary* on-axis SZP, the mode quality (figure 5.10(a)) is significantly improved, because the off-axis design leads to a larger density of illuminated zones in the center of the optics, hence optimizing the diffracted signal. Moreover, because the diffraction orders are spatially separated, there are no parasitic signals surrounding the main mode. For properly chosen parameters, beams from different harmonic orders can be split as well. OAM beams from adjacent harmonic orders are generated from the same SZP and share the same topological charge. However, the efficiency in our case is rather low, because the etching is not optimized for a broad wavelength range. For the *non-binary* off-axis SZP (figure 5.10 (b)), the blazed grating profile optimizes the flux diffracted in the first order, which contains 76% of the detected photons, when this number is only of 9% for the binary case.

Characterization of the Optical Harmonic Vortices

To measure and verify the topological charge of the 5^{th} harmonic optical vortex, we perform interferometric measurements in which a reference beam interferes with the OAM beam. This reference beam is provided by the zero order that spreads over the first order by means of a knife-edge, as depicted in figure 5.11. The resulting interference mode (shown on the right) possesses a fork grating pattern with one bifurcation, as emphasized with the white-dashed line on the mode; one fringe splits in two, yielding a topological charge of 1. This confirms the generation of the 5^{th} harmonic optical vortex with a unitary topological charge ($l = 1$).

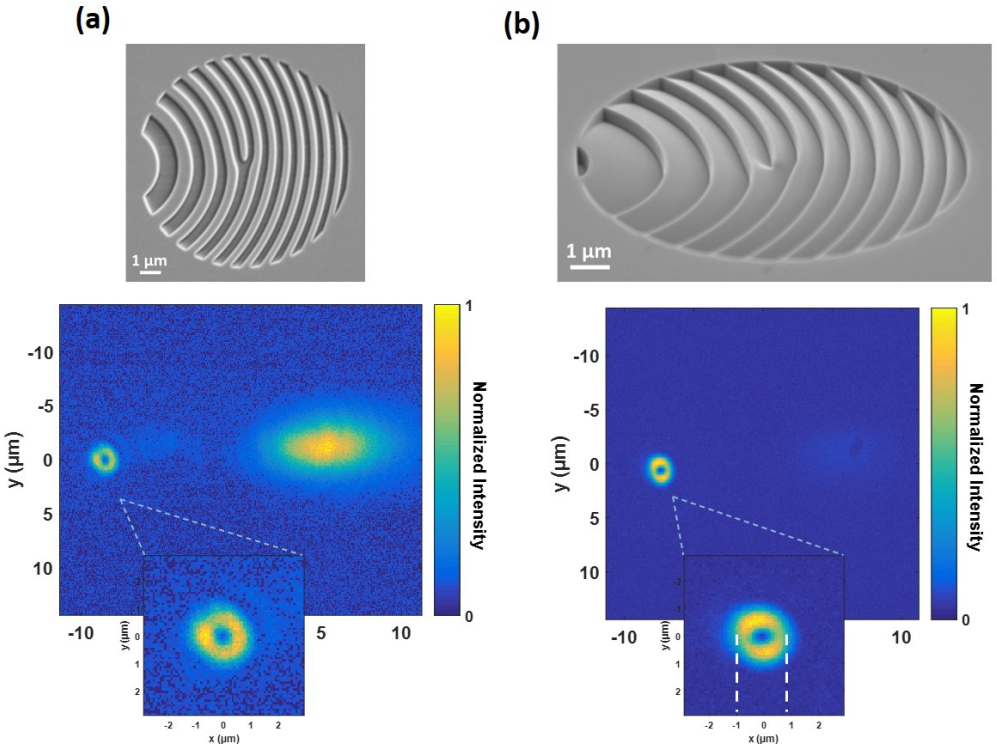

Figure 5.10: Spatial intensity distributions of harmonic 5 (420 nm) at the focal plane of the binary (a) and the non-binary (b) off-axis spiral zone plates etched at the exit surface of the ZnO crystal.

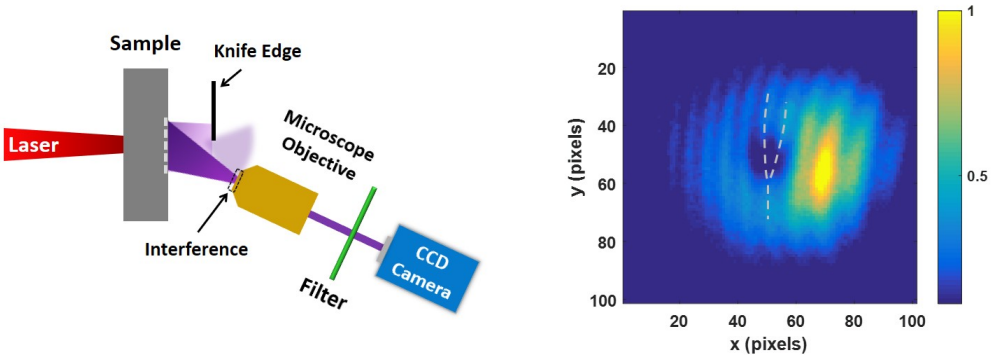

Figure 5.11: Knife edge method to characterize the 5^{th} harmonic optical vortex generated from the off-axis spiral zone plate (OA-SZP).

5.3.2 *OAM*, from the Fundamental Laser to the Harmonics

In this study, we consider the generation of harmonics carrying an orbital angular momentum by means of a Laguerre-Gaussian driving laser field in a bare ZnO crystal. In this case, the laser beam initially carrying an OAM of topological charge

l_f transfers the OAM to the generated harmonics by obeying the law of conservation of orbital angular momentum. This means that the generated harmonics carry an OAM of topological charge l_{Hq}, that is multiple of the harmonic order (q) according to the following relation: $l_{Hq} = q \times l_f$.

Experimental Details

The experiment was conducted at Institut d'Optique Graduate School (IOGS) in 2018 at Palaiseau. A sketch of the experimental setup is shown on the left of figure 5.12. An OPCPA laser system emitting a signal beam at a wavelength of 1.55 μm, 80 fs pulse duration, 125 kHz repetition rate and $\sim$ 2 μJ pulse energy is employed for the study. The initial Gaussian laser beam is converted to a Laguerre-Gaussian mode via a q-plate [152]; resulting in a beam carrying an orbital angular momentum with a unitary topological charge ($l_f = 1$). A q-plate is a phase retarder element with spatially variable optical axes orientations. The q-plate used in the experiment is a variable spiral plate (VSP), from ARCoptix company, composed of a liquid crystal. The output polarization is determined by the input polarization and the phase retardation which can be adjusted by a bias voltage. For an input beam with a circular polarization and a phase retardation of π, the ouput beam is circularly polarized and carries a topological charge of 1. In our experimental setup, figure 5.12, the first quarter-wavelength plate (QWP) serves to set the input beam to circular polarization, while the second QWP (after the q-plate) sets back the polarization to linear, which is the polarization state recommended for an efficient harmonic generation in ZnO. The laser is focused by a 5 cm focal length off-axis parabolic mirror near the rear surface of a 500 μm thick zinc oxide crystal. The calculated intensities at the focus range from 0.2 to 1.5 TW/cm^2. An aspheric lens, with a numerical aperture NA = 0.63, and a CCD camera are used to image the harmonic beams at the exit of the crystal.

Results and Discussions

The spatial modes of the fundamental beam and the generated harmonics H3 (517 nm), H5 (310 nm) and H7 (221 nm) imaged at the exit of the crystal are displayed on the right of figure 5.12. The modes show the expected donut-shaped intensity distribution with a radius of about 15 μm. Notice that the thickness of the rings decreases with an increase of the harmonic order. This is a result of the nonlinear response to the annular fundamental intensity distribution in the sample; the harmonic field $\mathrm{E_H}$ is proportional to the fundamental field $\mathrm{E_f} \propto \mathrm{e}^{\frac{-\mathrm{x}^2}{\omega^2}}$, $\mathrm{E_H} \propto \left|\mathrm{e}^{\frac{-\mathrm{x}^2}{\omega^2}}\right|^{\mathrm{q}}$, therefore the harmonic beam waist is reduced, following the relation: $\omega_{\mathrm{H}} = \frac{\omega}{\sqrt{\mathrm{q}}}$. Moreover, the imperfections in the fundamental mode are enhanced for high harmonics, which results in a decrease of the Laguerre-Gaussian mode purity.

Characterization of the OAM Harmonic Beams

To determine the topological charge of each mode we performed self-referenced spatial interferometric measurements [153]. The principle is illustrated in figure 5.13

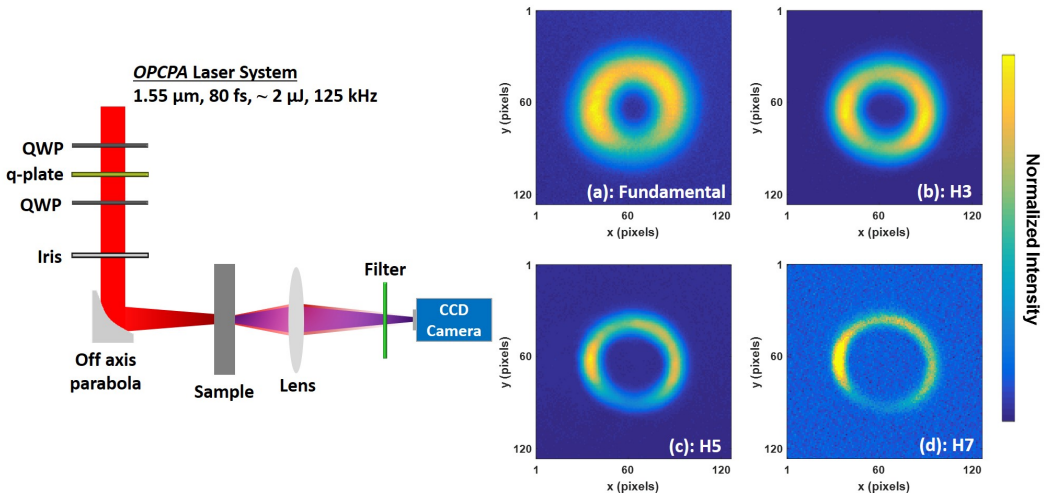

Figure 5.12: Left: Sketch of the experiment setup to prove the transfer and conservation of the OAM from the fundamental laser to the harmonics. Right: Experimental results of the spatial modes of the fundamental, and harmonics 3, 5 and 7 measured at the exit surface of the ZnO crystal.

(a). A part of the donut-shaped mode, mainly its arc, is aligned to hit and diffract from a rectangular slit (15 $\times$ 1 μm in size) which is patterned on the exit surface of the crystal, as demonstrated in the figure. At a distance of about 100 μm from the crystal, the diffraction of the local field from the slit spreads over the harmonic beam which is not affected by the slit and that propagates outside the crystal. The slit is small enough with respect to the OAM mode such that the diffracted wavefront does not contain any phase singularity, and can be approximated by a spherical wavefront. Interference of the latter with the helical wavefront of the main OAM beam produces a characteristic fork grating pattern, as depicted in figure 5.13 (b). The topological charge of the mode is deduced directly from the number of bifurcations, which are emphasized on the figure by the small white dashes. Figures 5.13 (c) and (d) display the experimental results for the 3$^{\text{rd}}$ and 5$^{\text{th}}$ harmonics, respectively. For harmonic 3 (figure 5.13 (c)), one fringe splits in 4 fringes which gives a topological charge of 3, $l_{H_3} = 3$, while for harmonic 5 (figure 5.13 (d)), one fringe splits in 6 corresponding to a topological charge of 5, $l_{H_5} = 5$. These results validate the *multiplicative* rule of the OAM transfer from the generation laser to the harmonics. Note that, the measurements are obtained with laser peak intensity estimated (in vacuum) to be 0.8 TW/cm^2, which corresponds to a Keldysh parameter near the tunneling limit of strong-field ionization [43]. As a conclusion, in this highly nonlinear regime, the orbital angular momentum conservation rules for harmonics below and above the ZnO band gap (E_g = 3.3 eV) are still obeyed by the mechanisms of HHG in semiconductors.

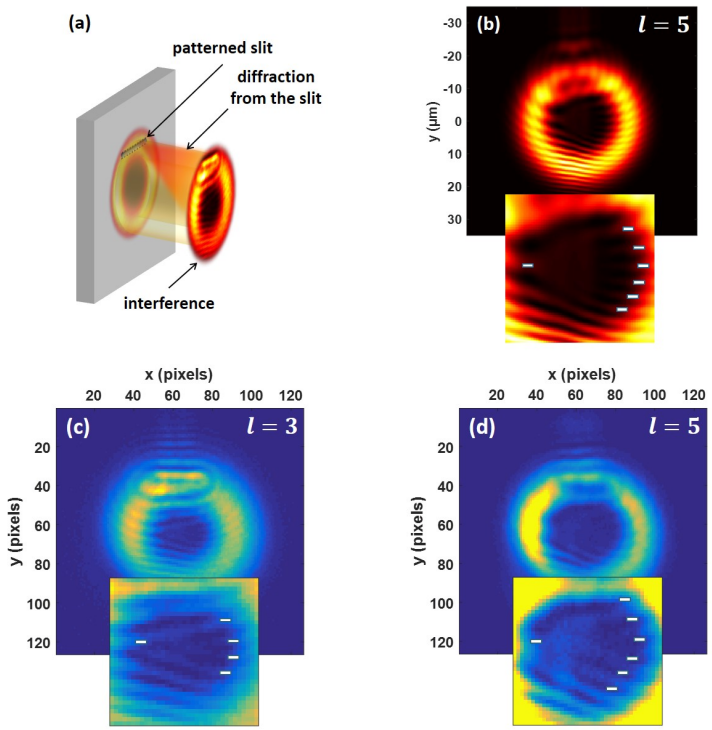

Figure 5.13: Measurement of the topological charge of the OAM harmonic modes using self-referenced interferences via a patterned slit (a). Simulation (b) with the experimental parameters of the self-referenced interferogram for harmonic 5. Experimental results of H3 (c) and H5 (d).

5.4 Solid-State Harmonic Source Applications

5.4.1 Coherent Diffractive Imaging (CDI)

The past two decades have marked successful achievements in the field of lensless imaging, in particular the coherent diffractive imaging technique (CDI), that was pioneered at CEA Saclay in 2009 in single-shot using gas HHG [154, 155, 156, 157]. In a CDI experiment, a micrometer or nanometer sized sample is illuminated by a coherent XUV radiation that scatters from the sample, and creates a diffraction pattern which is collected by a detector. The measured diffraction pattern is then provided to a phase retrieval algorithm. The algorithm basically does the job of a normal lens; Fourier transforming the reciprocal space diffraction from the object to a real space image of the object. In general, two parameters are needed to reconstruct an image from a diffracted radiation, namely the amplitude and the phase. In CDI experiments, the amplitude is the measured signal of the diffraction pattern. However, the field spatial phase is unknown, because spatial detectors in this energy range are only sensitive to field intensity. Therefore, algorithms have been developed to retrieve the missing phase. Basically, the algorithm starts with a random phase, associated with the experimental diffraction pattern. It then

alternates from the reciprocal space to the real one, applying known constraints. The standard constraints are the measured intensity and the sample size. Finally, the exit field from the sample is reconstructed, leading to a high resolution image of the sample transmittance [158].
We perform a CDI experiment in which the coherent source used is a harmonic beam emitted by the previously patterned ZnO nanostructured cones (section 5.2). The experimental setup is shown in figure 5.14. Harmonic beams are selected by transmission bandpass filters, mainly of harmonic 3 (H3) and harmonic 5 (H5), which are then focused by a lens onto a cross-shaped sample. The sample, shown in the SEM image in figure 5.14, was patterned by the focused ion beam (FIB) milling on a very thin opaque membrane composed of 75 nm of Si_3N_4 and 150 nm of Au. Due to the high divergence of the scattered radiation, the sample is placed very closely to the CCD camera. The diffraction pattern of the 3rd and 5th harmonics

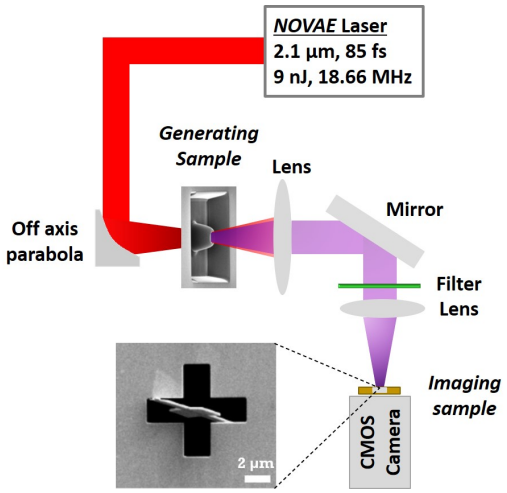

Figure 5.14: *Coherent Diffraction Imaging* experimental setup from solid-state harmonics.

collected by the CCD camera are shown in figure 5.15(a) and 5.15(b), respectively. After subtracting the background noise, the diffraction pattern of H5 is provided to a Hybrid input output (HIO) phase retrieval algorithm for image reconstruction. The reconstructed image is shown in figure 5.16. It is obtained by a coherent average over 50 independent runs of the algorithm, around 500 iterations each. From the phase retrieval transfer function criterion, the spatial resolution is estimated to be 1.6 μm. This CDI experiment was limited by the low number of photons of harmonic 5, due to the limited maximum intensity reached by the nanojoule NOVAE laser, which is 0.2 TW/cm^2. Nevertheless, the CDI demonstration here assures the coherence of the harmonics generated in solid crystals and proves that they are suitable sources for imaging applications. An exclusive and interesting CDI experiment based on solid-state HHG could be to image a sample that is itself the source of high harmonic emission. In such a case the generated and diffracted harmonics from the sample to be imaged are directly collected. This would lead to high resolution images (as the resolution limit is set by the wavelength) without the need of short wavelength laser sources. Lensless imaging applications based on solid-state high harmonics could

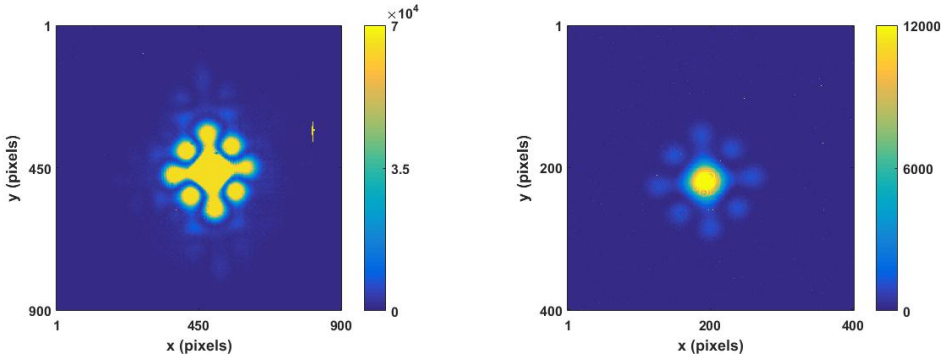

(a) Diffraction of H3.

(b) Diffraction of H5.

Figure 5.15: Diffraction patterns of harmonic 3 (700 nm ≡ 1.77 eV) (figure 5.15(a)), and harmonic 5 (420 nm ≡ 2.95 eV) (figure 5.15(b)), from the sample.

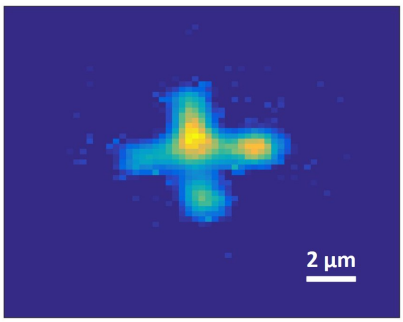

Figure 5.16: Reconstructed cross structure from the diffraction pattern of H5.

be extended to the *ptychography* technique [159]. Similar to the CDI technique, ptychography is also a computational imaging method. However, the ptychography technique requires several diffraction patterns obtained by scanning the sample in the xy plane relative to the beam focus; hence acquiring a set of consecutive diffraction data on different positions on the sample, where each two consecutive focus positions must be overlapping. As a result, ptychography allows imaging bigger dimensions of large-sized specimens with no loss of resolution.

5.5 Conclusion and Perspectives

5.5.1 Conclusion

To sum up, the studies explored in this chapter aimed at manipulating the solid-state generation medium. First, we investigate the local confinement and enhancement, by a factor of 25, of a nanojoule laser field in a nanostructured ZnO truncated cone, which potentially led to the enhancement of the harmonic generation even at low electric field strengths. At a low laser intensity (0.045 TW/cm^2, calculated in

vacuum) harmonics up to the 9^{th} order were efficiently generated in the ZnO cones while only harmonic 3 was generated from the bulk. This avoids the need for expensive and large laser amplifiers, and proves the capability of a modest femtosecond oscillator to generate high order harmonics in crystals. Second, we manipulate the fundamental properties of the harmonics generated from bulk ZnO by inducing an orbital angular mometum with an arbitrary topological charge, through patterning diffractive phase objects at the exit surface of the sample. The diffractive phase object is itself the source of the harmonic radiation and the optics component that creates the OAM mode. Moreover, we proved that the conservation rules of orbital angular momentum are obeyed by the HHG mechanisms in crystals. Indeed, the *multiplicative* rule of the harmonic's topological charge, $l_{\text{q}} = q \times l_{\text{f}}$, was valid. In addition, we verified the coherence of the harmonics generated from ZnO by performing a CDI experiment based on the generated 5^{th} harmonic beam as the radiation source, and demonstrated that HHG in crystals is a good candidate for table-top nanoscale imaging applications. The studies carried out in this chapter lead to the development of fully-integrated compact solid-state emitters and sources of optical votices, that sets a basis for a new branch of ultrafast solid-state optoelectronic devices.

5.5.2 Future Perspectives

Photoemission Electron Microscopy (PEEM)

Spatial and spectroscopic correlation between emitted electrons and photons would assist in the fundamental understanding of the HHG mechanism in crystals. This could be achieved by studying the hot electron emission via ***p****hotoemission* ***e****lectron* ***m****icroscopy* (PEEM). A first PEEM attempt, with our ZnO truncated cone as the sample, was realized in collaboration with Ludovic Douillard at CEA Saclay. Photoemission electron microscopy measurements are carried out on a LEEM/PEEM III instrument (Elmitec GmbH) operating under ultra-high vacuum conditions. The laser source is a mode-locked Ti:sapphire oscillator with wavelength range 680 nm–1000 nm, repetition rate 80 MHz and pulse duration 130 fs. The ZnO cone is back illuminated by a 775 nm pulsed laser beam at an angle of incidence of 45°, and the emitted electrons from the top of the cone are collected and analyzed. A preliminary photoemission electron microscopy (PEEM) measurement is shown in figure 5.17(a). The spatial resolution of the image is about 35 nm. The PEEM image shows a central bright spot which corresponds to the strong field electron emissions with energies ranging from 6 to 12 eV. The source size is 590 nm measured at full-width half-maximum (FWHM). Notice that the hot electrons are emitted at the position of the maximum local field enhancement (figure 5.2(c)). On the other hand, the nanoscale local field enhancement results in a nanoscale harmonic source localized at the position of maximum enhancement, with a mode size of 800 nm at FWHM, measured here particularly for harmonic 7 (H7), as shown in figure 5.17(b). This is a clear signature that the harmonic emission during the HHG process is spatially correlated to the electron emission. The PEEM measurement further confirms the electric field localization at the top of the microcone by measuring the spatial distribution of the hot electrons emitted during the strong-field interaction. This

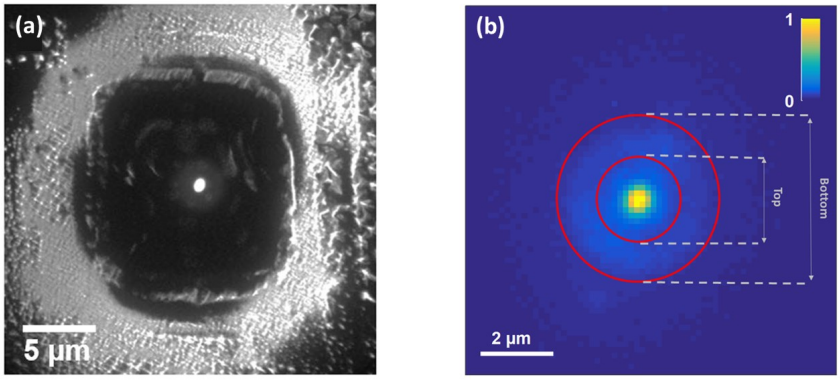

Figure 5.17: (a): Photoemission electron microscopy (PEEM) image of hot electrons emitted at the top surface of the cone, at a laser excitation wavelength of 775 nm. The spatial resolution is 35 nm. (b): Spatial mode of H7 at the top surface of the nanostructured cone, measured via a microscope objective. H7 mode size is measured to be 800 nm at FWHM. The top and base of the cone are highlighted.

also illustrates the potential of our semiconductor waveguide to create nanoscale source of hot electrons. Preliminary measurements of the energy distribution of photoemitted electrons is shown in figure 5.18. At an excitation wavelength of 725

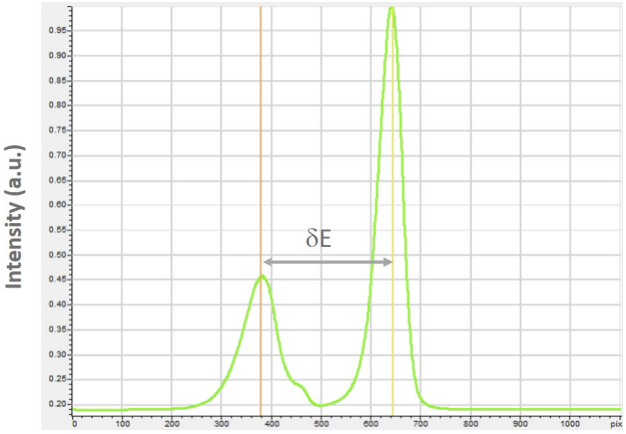

Figure 5.18: Spectrum of the photoemitted electrons at an excitation wavelength of 725 nm (preliminary result).

nm (1.7 eV) and selecting a narrow energy part of the electron spectrum for analysis, the energy distribution of the electrons shows two main peaks. Interestingly, the energy seperation between the two peaks (δE) $\sim$ 1.33 eV is very close to the photon energy of the excitation laser (the exact energy calibration of the spectrum is still underway). This clearly reminds above-threshold ionization (ATP), a process long identified in gas phase strong-field interaction. The signature of ATP peaks

reveals that the process is driven by the strong laser field at the sub-optical cycle level. We believe that the coherent nature of the HHG process offers the possibility of tailoring a nanoscale attosecond electron source from nanostructured semiconductors. Future investigations linking the HHG and the PEEM results, with deeper analyses, could correlate the harmonic emission to the electron emission and give more insight into the HHG process. Another exciting initiative would be to explore the intensity and polarization dependences of the emitted hot electrons.

Chapter 6

Conclusion and Perspectives

Conclusion

In this work we investigated high harmonic generation in graphene, a 2D material, and in different 3D semiconductor crystals such as ZnO, silicon, GaAs and MgO. We studied the dependence of the generation process on the driving laser properties such as its intensity, polarization and ellipticity. Besides, by manipulating the generation medium, we were able to tailor the properties of the laser and the generated harmonics. For a simple illustration, figure 6.1 points out the photon energy of our maximum detected high order harmonic as a function of the driving laser wavelength, achieved in this thesis with respect to the state-of-the-art (figure 2.7).

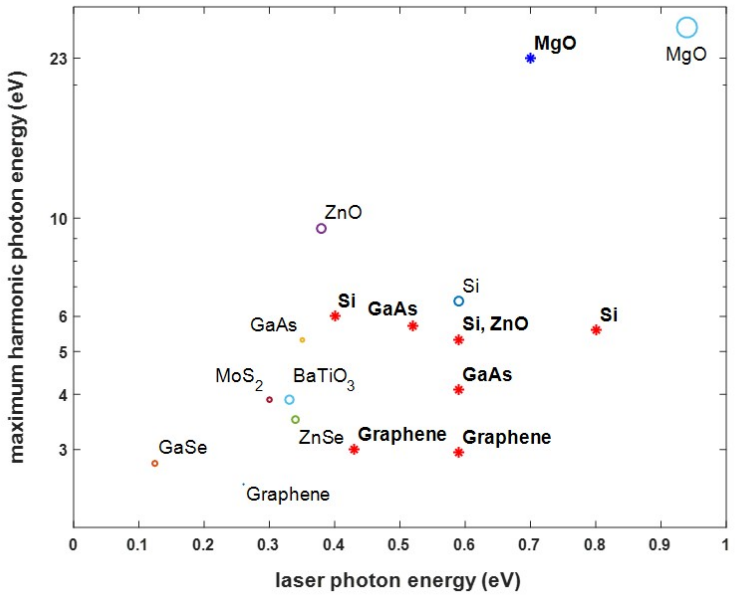

Figure 6.1: The HHG detection of this thesis's experiments with respect to the state-of-the art, marked in red stars for harmonics generated in air, and in blue for XUV higher order harmonics.

In chapter 3, harmonics up to the 5^{th} order of a 2.1 μm driving laser beam were generated from different graphene layers on a quartz substrate. The interaction of the intense laser with the graphene samples imposed two major challenges; the broadband fluorescence signal which dominates in the UV-Visible spectral range (2 - 6 eV), and the rapid damage of the samples preventing systematic and statistical measurements. The fluorescence signal due to the rapid scattering of nonequilibrium photoexcited carriers couldn't be avoided with our relatively long pulses preventing the detection of harmonic orders higher than the 5^{th} order. Laser induced ablation on the graphene samples was verified by Raman measurements and SEM images. The damage rate was less than a second even at very low laser intensity, 0.043 TW/cm^2. We proved that the oxidation of the graphene layers was a leading factor for the damage upon laser exposure in air. By isolating graphene in N_2 gas, an oxygen free ambiance, the decay time of the harmonic signal was increased to few minutes ($\sim$ 3 mins). Nevertheless, we studied the dependence of the 5^{th} harmonic generated from trilayer graphene on the laser intensity, ellipticity and polarization. Experimental measurements reavealed that the generation efficiency of H5 has an isotropic dependence on the laser polarization, as it is generated from the isotropic conical region of the band structure of graphene. This was confirmed by TDDFT simulations, which further showed that higher order harmonics such as the 7^{th} and the 9^{th} orders exhibit an anisotropic dependence on the laser polarization, particularly a sixfold symmetry, which reflects the hexagonal crystal symmetry of graphene. Finally, we reported for the first time on the harmonic generation, up to the 5^{th} harmonic order, from trilayers of freestanding graphene.

In chapter 4 we investigated HHG in different semiconductor crystals, mainly zinc oxide (ZnO), silicon (Si), gallium arsenide (GaAs) and magnesium oxide (MgO). These crystals have different structural, linear and nonlinear optical properties. We explored the HHG mechanism for different experimental conditions of the driving laser and generation medium. An entangled relation between the laser parameters and the crystal properties determines the HHG process. In a ZnO crystal, below bandgap perturbative harmonics and nonperturbative above bandgap harmonics generated in energy regions close to the bandgap revealed an isotropic efficiency with the laser polarization direction. However, in silicon, a fourfold symmetry in the polarization dependence of the generated harmonics was observed, which reflects the cubic crystal structure of silicon. A comparison between the harmonic generation from a nanojoule pulse energy laser in a 2 μm and a 300 μm thick silicon samples, displayed a higher efficiency in the latter case. We attributed this result to the Kerr effect in the spatial domain, i.e. the self-focusing of the laser beam. However, this effect significantly altered the HHG process at higher laser intensities in which the harmonic generation efficiency became lower in the thick sample than the thin one, and different dependences on the laser polarization was observed. Moreover, we explored the harmonic generation in the deep-UV and visible spectral range generated from gallium arsenide, a low bandgap semiconductor with high linear and nonlinear optical properties. A special feature of HHG

in GaAs is the change in the polarization dependences of the nonperturbative harmonics, mainly harmonic 3 and harmonic 5, at different laser intensities. We proved that the nonlinear propagation effects, mainly self-focusing and absorption of the laser are not the reason behind this observation. Theoretical calculations confirmed the presence of the photoionization and the self-phase modulation effects in the GaAs sample, however no difference was observed between the main crystal axes. Avoiding nonlinear propagation effects was achieved by carrying out the HHG in GaAs experiment in reflection geometry. The backward reflected harmonics originating only from the microscopic response of the HHG process, also exhibited different polarization dependences with the laser intensity, similar to the transmission case. This presents HHG in crystals as a tool to obtain information about the band structure of the generation medium [74, 134] and map generated petahertz electron currents [59]. Besides, we have also investigated HHG in magnesium oxide (MgO) and chromium-doped MgO samples in the UV-visible spectral range. Transmission measurements showed a decrease in the band gap energy as the doping level increases, however, the generation efficiency of the harmonics generated in air from the undoped and the doped samples was the same. In addition, no change in the polarization and ellipticity dependences was reported. Interestingly, we have exploited nonlinear effects, in the temporal domain, in these MgO crystals to achieve self-compression of the laser pulses with an appropriate compensation of the initially chirped pulses, thus shortening the pulse duration to around 20 fs. Finally, we demonstrated the strong anisotropy of vacuum harmonics generated from MgO of photon energies ≥ 10 eV, and exploited this dependence as an angular gate to generate attosecond XUV radiation through the *Anisotropy Gating technique*. Preliminary results of this technique revealed a decrease in the harmonic efficiency and a significant broadening and modulation of the harmonic spectrum, an indication of the driven HHG process by only few optical cycles. The *Anisotropy Gating technique* is currently still under deeper investigations. Primarily, a compression stage is being set to compress the laser pulses of the signal beam (1.78 μm) down to $\sim$ 20 fs, in order to decrease the number of optical cycles aligned with the best crystal axis which favors the highest generation efficiency.

In chapter 5 we exploit the 3D nature of the zinc oxide (ZnO) generation medium to enhance the intensity of a nanojoule energy laser by confining the laser pulses in a single nanostructured truncated ZnO cone. The maximum laser intensity provided by the laser, 0.2 TW/cm^2, is enhanced by a factor of 25, which leads to efficient generaton of high harmonics up to the 9$^{\text{th}}$ order (5.3 eV photon energy). This presents an alternative to large and expensive amplifiers usually needed to reach the high intensities that are required for the HHG process. Moreover, we also illustrated the potential to alter fundamental properties of the generated harmonics, specifically introducing orbital angular momentum, through the manipulation of the generation medium at the harmonic source. This was accomplished by patterning spiral phase objects, binary and nonbinary spiral zone plates, at the exit surface of the ZnO crystal. The generated harmonics get diffracted by these phase objects, which combine focusing of the harmonic beam while introducing an OAM mode. The spatial characterization of the harmonic

mode at the focus of the SZP which is at few micrometers ($\sim 6\,\mu$m) from the exit surface of the sample revealed a donut-shaped intensity profile. In addition, we also proved the laws of conservation of orbital angular momentum during the HHG process in crystals in the strong field regime. The HHG process driven by a laser beam carrying an orbital angular momentum with a topological charge (l) of 1, gave rise to high harmonic emission with harmonics carrying a topological charge which is proportional to their harmonic order (q), $l_q = q \times l$. Finally, we demonstrated the spatial coherence of solid-state harmonics through the Coherent Diffraction Imaging (CDI) technique, using the 5^{th} harmonic of the 2.1 μm driving laser generated from the ZnO cone, to illuminate and image a microstructure.

Future Perspectives

High Harmonic generation in unconventional materials
High harmonic emission in crystals originates from ultrafast petahertz carrier dynamics in the crystal band structure. On this basis, research can be built upon this particular fundamental field to develop optoelectronic devices operating at petahertz frequencies from standard semiconductors (MgO, SiO_2, ZnO, Si) to unconventional ones, such as strongly correlated materials like vanadium dioxide, or topological insulators. An interesting feature of vanadium dioxide is that it undergoes a reversible metal-insulator phase transition. Therefore, HHG in such materials can provide a petahertz switch, as their phase transition (insulator$\leftrightarrow$metal) can be initiated by the driving laser of the HHG process.
Other remarkable and promising materials that have attracted the scientific community are transition metal dichalcogenides (TMDs) such as monolayers of molybdenum disulphide (MoS_2) and tungsten diselenide (WSe_2). TMDs are atomically thin semiconductors that have "valleys" i.e. local minima in their band structure. They are currently known as valleytronic systems as their "valleys" can offer the ability to store and process information. Ultrafast carrier dynamics in transition metal dichalcogenides driven by SAM (spin angular momentum) or OAM laser pulses promote switching of their intrinsic quantum properties, particularly the valley pseudo spin at the subcycle level [160], which consequently enables the petahertz switching of encoded information. This paves the way to fast lightwave valleytronics which could take the lead in semiconductor technology. Understanding strong field processes in such materials requires temporal characterization of the attosecond electron dynamics. This could be achieved by the RABBIT technique (**R**esolution of **A**ttosecond **B**eating **B**y **I**nterference of **T**wo-photon transitions) [161, 162] which provides access to the temporal phase and duration of the electronic processes.

Appendices

Appendix A

Beam Size Measurements and Intensity Calculations

Given a Gaussian pulsed laser beam of pulse duration τ, its intensity at the focus is defined as:

$$I(r,t) = I_0 e^{-4ln2\left(\frac{r}{\Gamma}\right)^2} e^{-4ln2\left(\frac{t}{\tau}\right)^2} \tag{A.1}$$

where Γ is the beam size at full-width half-maximum (FWHM) at the focus position. The energy stored in this pulse is then given by:

$$E = \int I \,\mathrm{d}A\,\mathrm{d}t = \int_{-\infty}^{+\infty}\int_{0}^{2\pi}\int_{0}^{\infty} I\, r\mathrm{d}r\,\mathrm{d}\phi\,\mathrm{d}t \tag{A.2}$$

For laser pulses at a repetition rate *RepRate* and average input power P_{av}, the pulse energy is also calculated as:

$$E = \frac{P_{av}}{RepRate} \tag{A.3}$$

By solving equation A.2, and integrating equation A.3, the peak laser intensity at the focus of the Gaussian beam is:

$$I = 0.83\frac{P_{av}}{\tau \times RepRate \times \Gamma^2} \tag{A.4}$$

The electric field strength E_0 is then calculated according to the following equation:

$$I = \frac{1}{2}\epsilon_0 cnE_0 \tag{A.5}$$

where ϵ_0, c and n are the electric vacuum permittivity, speed of light in vacuum, and index of refraction of the material, respectively.
To experimentally estimate the laser beam size before focus, we measure the laser power for different iris apertures, which is set in the beam path before the first focusing lens for alignment. The plot of the power of the NOVAE laser (2.1 μm wavelength) as a function of the iris radius is shown in figure A.1. The power of a

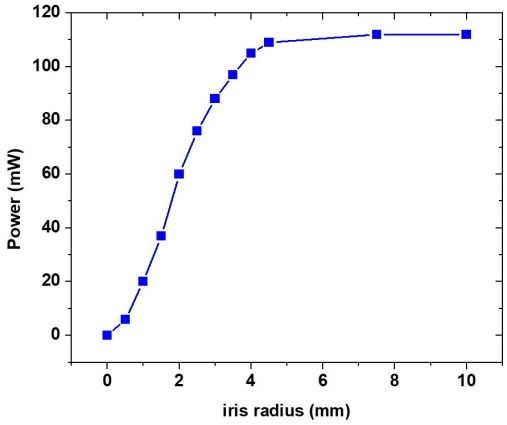

Figure A.1: NOVAE laser power versus the iris radius.

collimated Gaussian beam passing through an aperture of radius r, *P(r)*, is given by:

$$P(r) = P_0(1 - e^{-2r^2/w^2}) \tag{A.6}$$

where w is the beam waist. By subtracting the graph (i.e. $P(r)$) from the maximum measured power (P_0) and taking the mirror image of it, we obtain the black curve on the left of figure A.2 which corresponds, from equation A.6, to a Gaussian distribution proportional to the laser intensity: $P_0 e^{-2r^2/w^2} = P_0 - P(r) \propto I(r)$. The beam waist ($w$) is then extracted by fitting the plot with a Gaussian function through the Origin software.

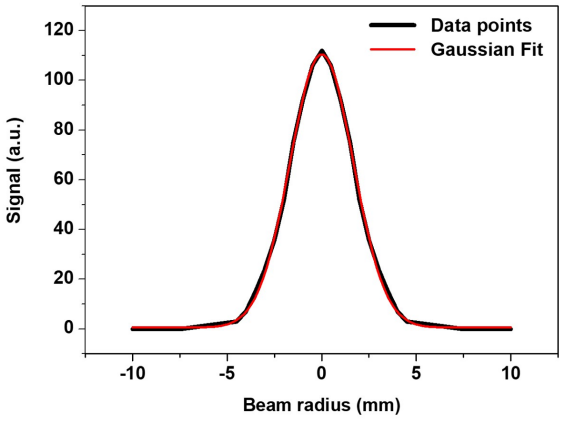

Gauss Fit Equation: $y = y_0 + \frac{A}{w\sqrt{\frac{\pi}{2}}} e^{-2\left(\frac{x-x_c}{w}\right)^2}$

Adj R^2	0.99903	
	Value	Standard Error
y_0	0.563	0.5
x_c	0	0
w	3.35	0.03
A	461.54	5.06
sigma	1.67	
FWHM	3.94	
Height	110.07	

Figure A.2: Beam size measurement of the NOVAE laser. The beam waist before focus is 3.35 mm, and its size at FWHM is 3.94 mm.

Finally, the beam waist at the focus and the beam size at FWHM are calculated as:

$$w_{focus} = \frac{\lambda f}{\pi w} \tag{A.7}$$

$$\Gamma = \omega_{focus}\sqrt{2\ ln(2)} \tag{A.8}$$

where λ and f are the laser wavelength and focal length of the focusing optics, respectively.

Appendix B

NOVAE Laser System

The description of the NOVAE laser system was detailed by Jean-Thomas Gomes from the NOVAE company.
The approach for production of high-energy mid-infrared pulses relies on generating a train of temporal solitons at a short wavelength and tuning its carrier frequency towards the spectral region of interest in nonlinear optical fibers via intrapulse stimulated Raman scattering. In a Raman-active medium such as fused silica, the high-frequency part of sub-picosecond pulses is absorbed while the low-frequency part is amplified, yielding a continuous red-shift in the pulse carrier frequency. Fundamental solitons are stable in standard single-mode fibers for nanojoule energy, which is however insufficient for high harmonic generation in solids. In order to build a laser delivering high-energy 100 fs pulses in the mid-infrared, the company implements the concept of nonlinear femtosecond master-oscillator power-amplifier in a fully fusion-spliced fiber format. The experimental setup is depicted in figure B.1.

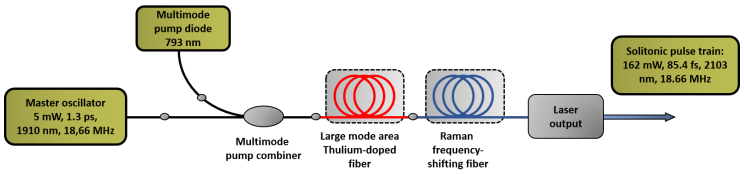

Figure B.1: Laser experimental setup

The seed mode-locked thulium-doped fiber oscillator delivers a train of 1.3 ps hyperbolic secant squared (sech^2) shaped pulses centered at 1910 nm with a repetition rate of 18.66 MHz. The average power is 4 mW, corresponding to E = 0.2 nJ. In order to increase the energy to levels appropriate for high harmonic generation in solids, the pulses are further amplified in a cladding-pumped amplifier based on LMA TDF. The pulse energy is directly amplified to tens of nanojoules. Multisolitonic effects lead to the pulse fission followed by ejection of high-energy (8.7 nJ) sech^2 pulse frequency-shifted up to 2100 nm. The laser spectrum with 2103 nm peak wavelength is measured with an optical spectrum analyzer (AQ6375, Yokogawa, Japan) and displayed in figure B.2(a). The average power of the pulse train is 162 mW with a linear polarization state (PER>15dB). The autocorrelation trace of the output pulse after the filter is recorded using a second-harmonic generation

autocorrelator (FR-103XL, Femtochrome Inc., USA), and the results are plotted in figure B.2(b). The deduced FWHM pulse duration is 85.4 fs assuming a sech^2 pulse shape. The estimated pulse peak power is thus 101.6 kW. Finally, the stability of the laser (figure B.2(c)) is analyzed. The variation in average power over a period of seven hours is below 0.5% rms. The laser footprint is 56 cm × 57 cm × 43 cm.

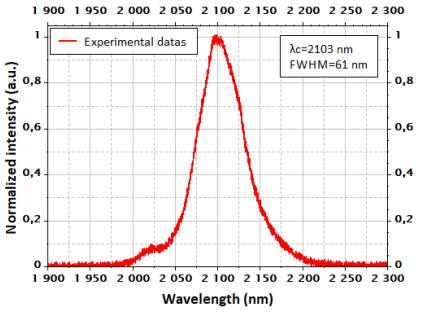

(a) Measured optical spectrum after a long-pass filter.

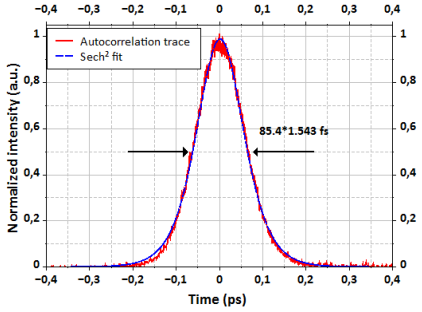

(b) Autocorrelation trace.

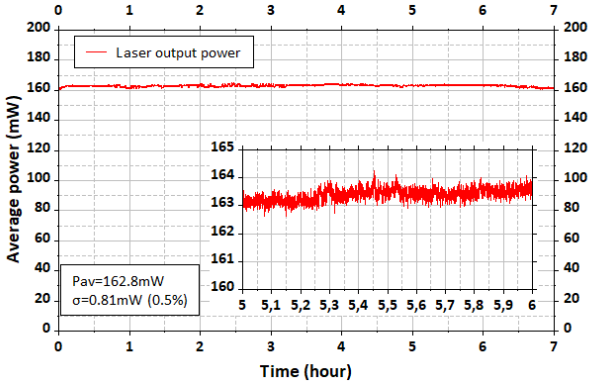

(c) Laser average power measured over a period of seven hours. Excellent stability corresponding to 0.5% rms.

Figure B.2: Results of the NOVAE laser pulse characterization.

Appendix C

OPCPA Laser System at IOGS

The OPCPA, acronym for **O**ptical **P**arametric **C**hirped **P**ulse **A**mplification, concept allows high energy laser pulses by amplifying chirped pulses. The OPCPA laser system employed during the beamtime in 2018 was developed by the group of Marc Hanna at the Institut d'Optique Graduate School (IOGS), at Palaiseau. The system is seeded by a femtosecond ytterbium-doped fiber amplifier system (Tangerine, from Amplitude Systèmes), delivering laser pulses of 400 μJ energy, 400 fs pulse duration at 125 kHz repetition rate and 1.03 μm central wavelength. The output of the system is a signal beam centered at 1.55 μm wavelength, 20 μJ pulse energy and 49 fs pulse duration, and an idler beam centered at 3.07 μm wavelength, 10 μJ pulse energy and 72 fs pulse duration. A detailed description of the OPCPA laser system can be found in [163].
For the beamtime in 2019, the group modified the system by using a multipass cell (MPC), in the net anomalous dispersion regime, to take advantage of soliton dynamics and self-compress the laser pulses generated by the OPCPA [164]. The MPC is introduced in the beam path of the Signal beam at 1.55 μm central wavelength. The nonlinear propagation of the laser pulses in the MPC leads to the compression of the 19 μJ, 63 fs pulses down to 22 fs pulse duration, with 14 μJ pulse energies and a transmission of 73%.

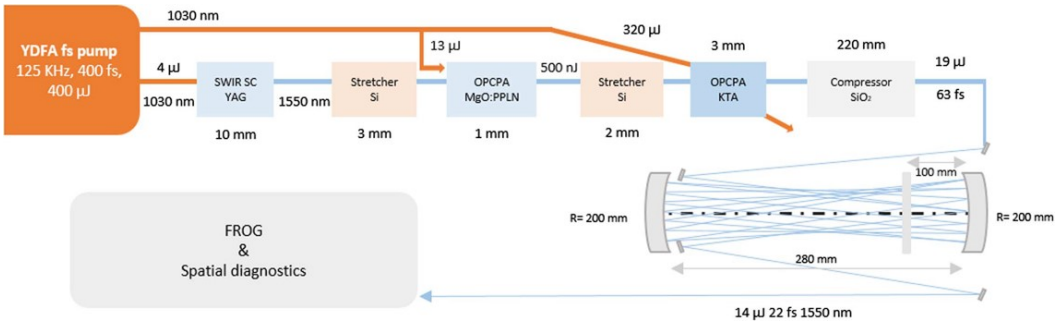

Figure C.1: Experimental setup of the OPCPA system at IOGS in 2019. Taken from [164].

Appendix D

OPCPA Laser System at CEA Saclay

The OPCPA laser system installed in our laboratory at CEA, Saclay (June 2019) was developed by Fastlite. The pump laser is a Tangerine provided by Amplitude Systèmes which is characterized by the following:

Central wavelength = 1030 nm
Pulse duration < 350 fs
Repetition rate = 100 kHz
Power > 20 W
Pulse energy > 200 μJ
M^2 factor < 1.3

A Dazzler system from Fastlite is inserted in the OPCPA setup for better, cleaner and shorter pulses The output Signal and Idler beams are spectrally measured at central wavelengths of 1.78 μm and 2.42 μm, respectively. An important feature of this laser system is that the signal beam is CEP stable. The characteristics of the Signal and Idler are summarized in table D.1 below.

	Signal Output	Idler Output
Central wavelength	1780 nm	2422 nm
Average power	1.65 W	1.29 W
Repetition rate	100.2 kHz	100.2 kHz
Pulse duration FWHM	38.4 fs	60 fs
Pulse-to-pulse stability (over 1 second)	1.13 %	2.3 %
CEP stability (over 1 hour)	120 mrad	NA mrad
Strehl ratio	> 0.743	0.743
Pointing stability	X:2.4, Y:4.4 (urad rms/°C)	X:0.8, Y:0.7 (urad rms/°C)

Figure D.1: Characteristics of the signal and idler beams of the OPCPA system as provided by Fastlite.

Appendix E

Detection System

PCO Ultraviolet Camera

The image sensor is a CCD, **c**harged **c**oupled **d**evice, with a chip size of 1392 × 1040 pixels. The pixel size is 4.65 μm × 4.65 μm. The camera's quantum efficiency over the ultraviolet to near-infrared range is shown in figure E.1 below. Its operating temperature is between 10°C and 35°C. During our HHG experiments, it was operated at ambient conditions of temperature and pressure. To optimize the detected signal, we vary the integration time and the binning options.

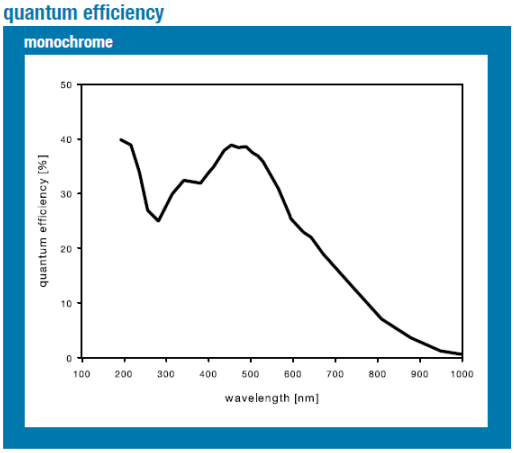

Figure E.1: Quantum efficiency of the PCO ultraviolet camera.

Imaging Source Camera

The Imaging Source Camera was used to study the spatial mode of the fundamental infrared beams. The image sensor is a CMOS, **c**omplementary **m**etal **o**xide **s**emiconductor. For long wavelength laser beams (near-IR wavelengths), the imaging is based on a two-photon absorption in a silicon detector. Therefore, the real size of the image is larger than the measured one by a factor of $\sqrt{2}$. The chip size is 744 × 480 pixels with a pixel size of 6 μm × 6 μm. Its operating temperature range

is −5°C to 45°C. During our experiments, it was operated at ambient conditions of temperature and pressure.

Spectrometers

QE Pro series from Ocean Insight
This high sensitivity spectrometer was used for spectral characterization of the harmonics generated from solid crystals at ambient conditions. It consists of a UV-VIS dual blaze grating with groove density of 300 grooves/mm. Its polarization efficiency is reported in figure E.2.

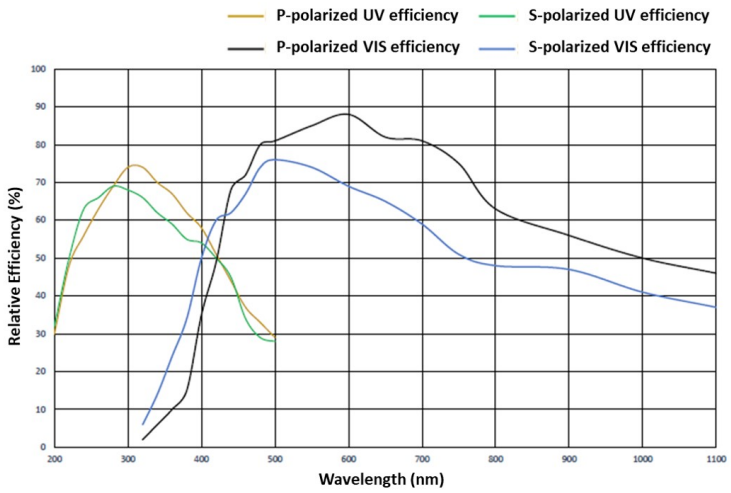

Figure E.2: Polarized efficiency of the grating of the QE pro spectrometer used in the UV-VIS spectral range.

Diffraction Grating for *vacuum* HHG experiment

The dispersive diffraction grating used in the *vacuum* HHG experiment (Chapter 4, section 4.5) is a concave corrected grating bought from McPherson Inc. It is platinum (Pt) coated with groove density d = 2400 grooves/mm. This grating is designed to be used in a vacuum monochromator (Model 234/302), such that the total angle between the incident beam and the reflected focused one is well-defined and has to be set to 64°, in this case $\alpha + |\beta| = 64°$. The experimental configuration is shown in figure E.3. The focal plane of the grating is 20 cm. The grating's dimensions are 40 × 45 mm. The wavelength of the spectrum is calculated following equation E.1 [165]:

$$m\lambda = 2d\cos(K)\sin(\phi) \tag{E.1}$$

where m is the diffraction order ($m = 1$ in our case), d is the groove density, $K = \frac{\alpha-\beta}{2}$ = constant = 32°, and $\phi = \frac{\alpha+\beta}{2}$, which is varied experimentally, by

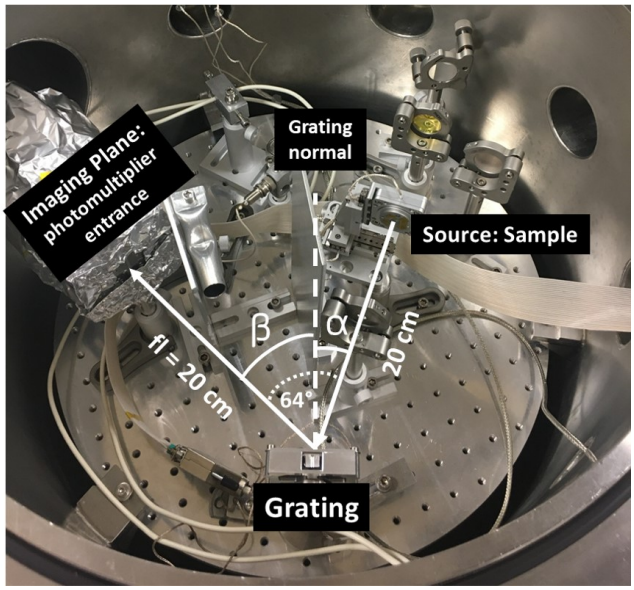

Figure E.3: Experimental configuration of the grating in the *vacuum* HHG experiment.

rotating the grating to scan the high harmonic spectrum. The grating quantum efficiency, for s-polarized and p-polarized radiation is shown in figure E.4.

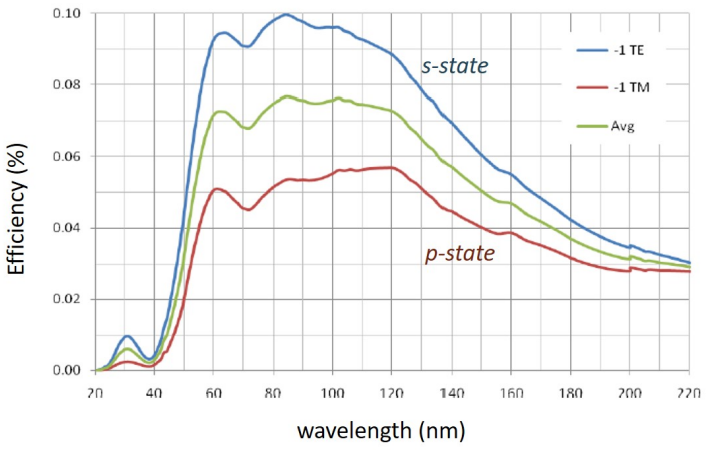

Figure E.4: Quantum efficiency of the grating.

Photomultiplier

The photomultiplier tube used in the *vaccum* HHG experiment to detect high energy photon harmonics consists of a CuBe photocathode. Its quantum efficiency is shown in figure E.5.

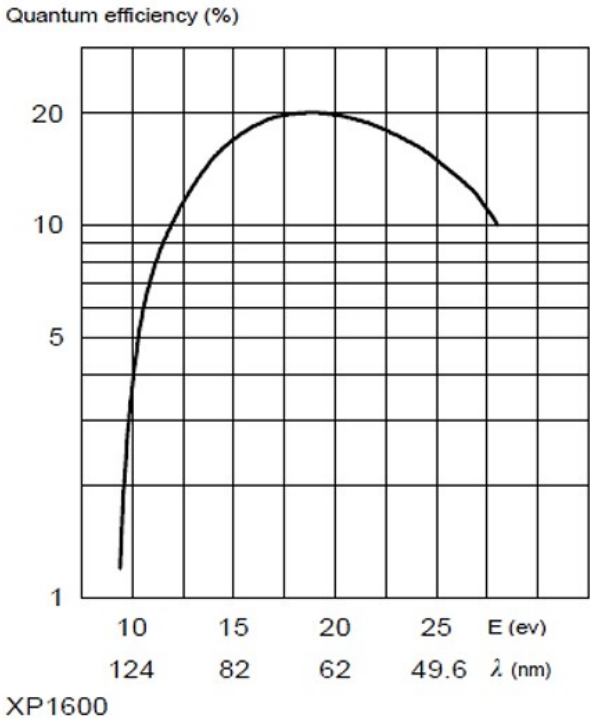

Figure E.5: Quantum efficiency of the photomultiplier used in the *vacuum* HHG experiment.

Appendix F

The FROG Technique

FROG Method and Theory

FROG, acronym for **F**requency **R**esolved **O**ptical **G**ating, is a technique widely used for a full temporal characterization of ultrashort pulses with durations ranging from nanosecond to femtosecond. This technique allows the retrieval of the spectral phase of the optical pulse and its temporal properties including the temporal phase and duration.

Setup

The setup was set by Dr. Dominik Franz from our group (figure F.1). The beam is incident at the center of two half mirrors which are closely placed. One of the half mirrors is placed on a motorized translational stage (indicated by the two-sided yellow arrow in figure F.1). The beam reflects from the two half mirrors as two separate semi-Gaussian beams. These two beams are then focused by an off-axis parabolic mirror of 2.5 cm focal length onto a nonlinear second harmonic generation (SHG) crystal, an α-BBO crystal in our case. When the delay between these two beams is zero, the second harmonic of the fundamental beam will be generated along the central axis normal to the surface of the crystal. Thanks to an iris placed far enough to allow the fundamental beams to diverge, only the second harmonic generated along the central axis is selected (marked in blue line in figure F.1). The second harmonic is then focused by a lens onto the spectrometer (Maya2000 Pro spectrometer).

Measurements

The FROG trace is obtained by varying the delay between the two beams through translating the half mirror with respect to the other half. In my studies, the delay was usually scanned over a range of ~ 60 fs by a labview program where the FROG trace is finally obtained. This FROG trace is then inserted into a user-friendly interface, "FROG3" program of Femtosoft Technologies (Version 3.2.2), to extract the spectral phase and the optical pulse in the time domain. An example of a FROG measurement of the signal beam, at 1.78 μm wavelength, of the OPCPA laser system

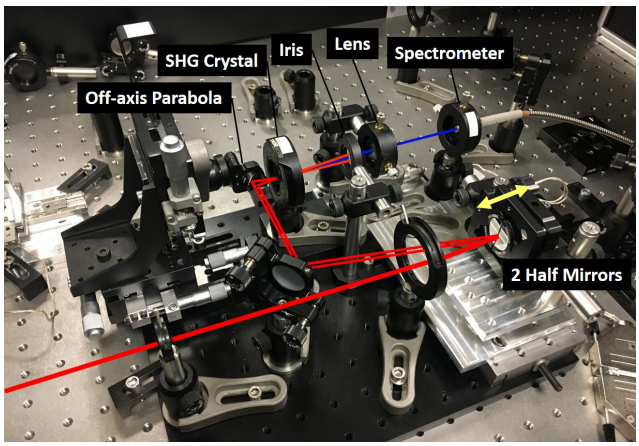

Figure F.1: FROG setup.

at CEA is shown in figure F.2. The resulting pulse duration at FWHM is ~ 45 fs, and the bandwidth is ~ 130 nm (FWHM).

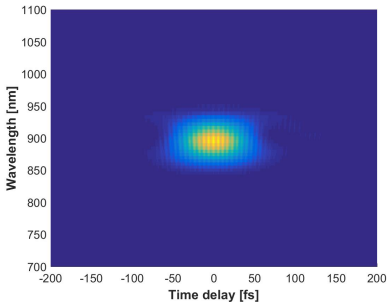

(a) Measured FROG trace.

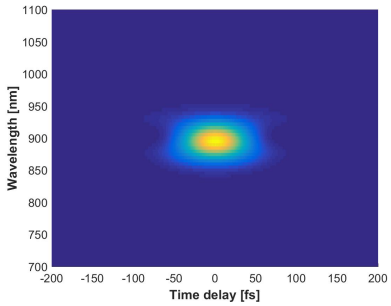

(b) Reconstructed FROG trace.

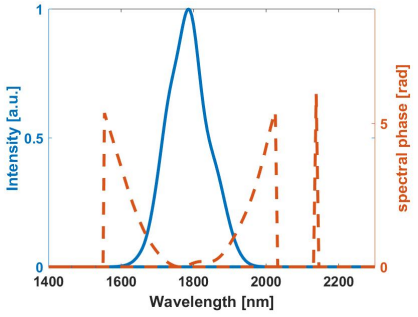

(c) Extracted spectral intensity and spectral phase.

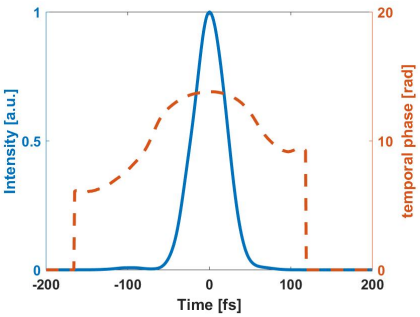

(d) Extracted temporal intensity and temporal phase.

Figure F.2: FROG measurement and pulse reconstruction of the 1.78 μm wavelength laser beam.

Appendix G

FDTD Simulations by Lumerical

The finite-difference time-domain (FDTD) method is a numerical method for solving Maxwell's equations in complex geometries. In this method, the time-dependent Maxwell's equations are discretized by replacing the space and time partial derivatives by central-difference approximations. The finite-difference equations are solved in a leapfrog manner: the electric field vector components in a spatial volume in space are solved at a given instant in time, then the magnetic field vector components in the same spatial volume are solved at the next instant in time. This process is repeated until the electromagnetic field behavior has fully evolved. Maxwell's equations tell us that a change of the electric field in time depends on a change of the magnetic field across space. Hence at each point in space, the new value of the electric field in time depends on the stored value of the electric field and the curl of the local distribution of the magnetic field in space. Similarly, the updated value of the magnetic field at any point in time is dependent on the previous value of the magnetic field and the curl of the local distribution of the electric field in space [166].
Lumerical is a user-friendly interface that performs FDTD simulations, where one can define the problem specifying the source, material and the computational domain in which both the electric and magnetic fields are determined at every point in space. The desired spectral and temporal properties of the electromagnetic wave can be chosen. A large database provides the choice of numerous materials including air, metals, dielectrics and semiconductors. Missing materials can be added by inserting their properties, mainly their permeability, permittivity and conductivity. When setting the computational region, the boundary conditions are an important part that depend on the medium and the electromagnetic field under study. Besides, the mesh or grid size of the computational region must be specified as well. For a quick yet relatively accurate simulation, the mesh should be a fraction ($\sim$ one tenth) of the wavelength of the electromagnetic field and the structure size. The smaller the mesh the higher the accuracy of the simulation, however the more time consuming it is. The user adds the frequency domain field and power monitors within the computational domain to read the output of the simulation. One can select to view the result of the electric or magnetic field in their three dimensions. The simulations were carried out on a bi-processor Intel Haswell 10C E5-2650V3 computer (10 cores, 20 threads, max. frequency 3 GHz, Bus speed 9.6 GT/s QPI, 768 Gb registered SDRAM (DDR4 2133, 68GB/s bandpass)).

Appendix H

Focused Ion Beam Technique

The FIB (**F**ocused **I**on **B**eam) technique is a milling technique that uses a high energy focused ion beam to nanostructure the surface of a solid. When the high energy ions hit the sample, they sputter atoms from the surface. Imaging resolutions of 5 nm can be achieved by the FIB technique. The ZnO truncated cones and the spiral phase objects were milled by Dr. Willem Boutu using the FIB technique installed at the CSNSM Laboratory in Orsay. The equipment consists of a LEO 1530 MEB (field effect gun) equipped with an Orsay Physics FIB column of gallium ions (Ga^+). The beam width is in the order of 15 nm. The energy of the ion beam (Ga^+) is usually set to 30 keV. The SEM provides a simultaneous image of the sample during the patterning process. A schematic illustration is shown in figure H.1.

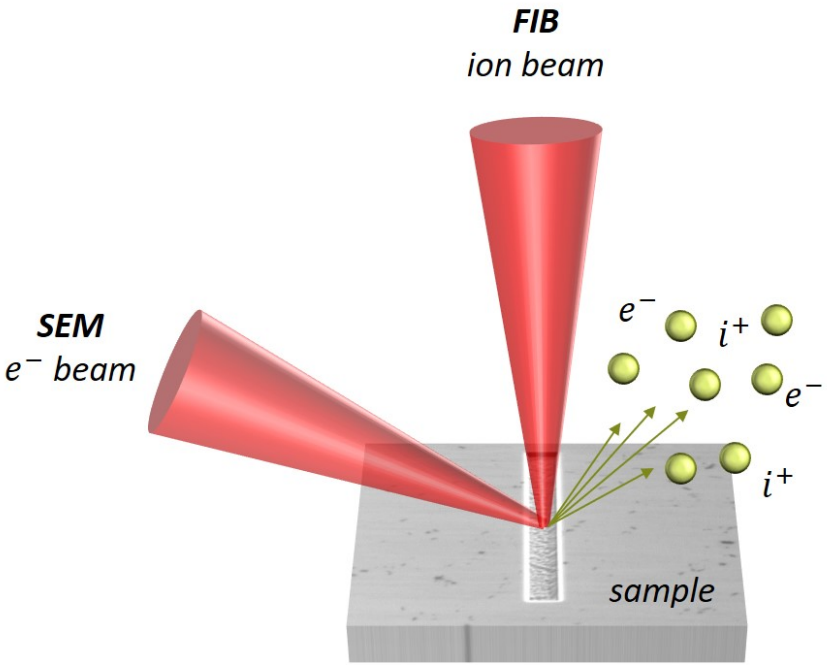

Figure H.1: Schematic illustration of the FIB system.

List of Figures

List of Tables

Bibliography

[1] J. M. Glownia, A. Natan, J. P. Cryan, R. Hartsock, M. Kozina, M. P. Minitti, S. Nelson, J. Robinson, T. Sato, T. van Driel, G. Welch, C. Weninger, D. Zhu, and P. H. Bucksbaum. Self-Referenced Coherent Diffraction X-Ray Movie of Ångstrom- and Femtosecond-Scale Atomic Motion. *Physical Review Letters*, 117(15):153003, October 2016.

[2] Philip H. Bucksbaum, Matthew R. Ware, Adi Natan, James P. Cryan, and James M. Glownia. Characterizing Multiphoton Excitation Using Time-Resolved X-ray Scattering. *Physical Review X*, 10(1):011065, March 2020.

[3] Simone Peli, Denny Puntel, Damir Kopic, Benjamin Sockol, Fulvio Parmigiani, and Federico Cilento. Time-resolved VUV ARPES at 10.8 eV photon energy and MHz repetition rate. *Journal of Electron Spectroscopy and Related Phenomena*, 243:146978, August 2020.

[4] A. P. Mancuso, O. M. Yefanov, and I. A. Vartanyants. Coherent diffractive imaging of biological samples at synchrotron and free electron laser facilities. *Journal of Biotechnology*, 149(4):229–237, September 2010.

[5] Jianwei Miao, Keith O. Hodgson, Tetsuya Ishikawa, Carolyn A. Larabell, Mark A. LeGros, and Yoshinori Nishino. Imaging whole Escherichia coli bacteria by using single-particle x-ray diffraction. *Proceedings of the National Academy of Sciences*, 100(1):110–112, January 2003.

[6] Changyong Song, Huaidong Jiang, Adrian Mancuso, Bagrat Amirbekian, Li Peng, Ren Sun, Sanket S. Shah, Z. Hong Zhou, Tetsuya Ishikawa, and Jianwei Miao. Quantitative Imaging of Single, Unstained Viruses with Coherent X Rays. *Physical Review Letters*, 101(15):158101, October 2008.

[7] Tomas Ekeberg, Martin Svenda, Chantal Abergel, Filipe R. N. C. Maia, Virginie Seltzer, Jean-Michel Claverie, Max Hantke, Olof Jönsson, Carl Nettelblad, Gijs van der Schot, Mengning Liang, Daniel P. DePonte, Anton Barty, M. Marvin Seibert, Bianca Iwan, Inger Andersson, N. Duane Loh, Andrew V. Martin, Henry Chapman, Christoph Bostedt, John D. Bozek, Ken R. Ferguson, Jacek Krzywinski, Sascha W. Epp, Daniel Rolles, Artem Rudenko, Robert Hartmann, Nils Kimmel, and Janos Hajdu. Three-Dimensional Reconstruction of the Giant Mimivirus Particle with an X-Ray Free-Electron Laser. *Physical Review Letters*, 114(9):098102, March 2015.

[8] Anna Munke, Jakob Andreasson, Andrew Aquila, Salah Awel, Kartik Ayyer, Anton Barty, Richard J. Bean, Peter Berntsen, Johan Bielecki, Sébastien Boutet, Maximilian Bucher, Henry N. Chapman, Benedikt J. Daurer, Hasan DeMirci, Veit Elser, Petra Fromme, Janos Hajdu, Max F. Hantke, Akifumi Higashiura, Brenda G. Hogue, Ahmad Hosseinizadeh, Yoonhee Kim, Richard A. Kirian, Hemanth K. N. Reddy, Ti-Yen Lan, Daniel S. D. Larsson, Haiguang Liu, N. Duane Loh, Filipe R. N. C. Maia, Adrian P. Mancuso, Kerstin Mühlig, Atsushi Nakagawa, Daewoong Nam, Garrett Nelson, Carl Nettelblad, Kenta Okamoto, Abbas Ourmazd, Max Rose, Gijs van der Schot, Peter Schwander, M. Marvin Seibert, Jonas A. Sellberg, Raymond G. Sierra, Changyong Song, Martin Svenda, Nicusor Timneanu, Ivan A. Vartanyants, Daniel Westphal, Max O. Wiedorn, Garth J. Williams, Paulraj Lourdu Xavier, Chun Hong Yoon, and James Zook. Coherent diffraction of single Rice Dwarf virus particles using hard X-rays at the Linac Coherent Light Source. *Scientific Data*, 3(1):160064, August 2016.

[9] Ahmad Hosseinizadeh, Ghoncheh Mashayekhi, Jeremy Copperman, Peter Schwander, Ali Dashti, Reyhaneh Sepehr, Russell Fung, Marius Schmidt, Chun Hong Yoon, Brenda G. Hogue, Garth J. Williams, Andrew Aquila, and Abbas Ourmazd. Conformational landscape of a virus by single-particle X-ray scattering. *Nature Methods*, 14(9):877–881, September 2017.

[10] A. P. Mancuso, Th Gorniak, F. Staier, O. M. Yefanov, R. Barth, C. Christophis, B. Reime, J. Gulden, A. Singer, M. E. Pettit, Th Nisius, Th Wilhein, C. Gutt, G. Grübel, N. Guerassimova, R. Treusch, J. Feldhaus, S. Eisebitt, E. Weckert, M. Grunze, A. Rosenhahn, and I. A. Vartanyants. Coherent imaging of biological samples with femtosecond pulses at the free-electron laser FLASH. *New Journal of Physics*, 12(3):035003, March 2010.

[11] Emelie Fogelqvist, Mikael Kördel, Valentina Carannante, Björn Önfelt, and Hans M. Hertz. Laboratory cryo x-ray microscopy for 3D cell imaging. *Scientific Reports*, 7(1):13433, October 2017.

[12] Yoshinori Nishino, Yukio Takahashi, Naoko Imamoto, Tetsuya Ishikawa, and Kazuhiro Maeshima. Three-Dimensional Visualization of a Human Chromosome Using Coherent X-Ray Diffraction. *Physical Review Letters*, 102(1):018101, January 2009.

[13] A. McPherson, G. Gibson, H. Jara, U. Johann, T. S. Luk, I. A. McIntyre, K. Boyer, and C. K. Rhodes. Studies of multiphoton production of vacuum-ultraviolet radiation in the rare gases. *JOSA B*, 4(4):595–601, April 1987.

[14] M. Ferray, A. L\textquotesingleHuillier, X. F. Li, L. A. Lompre, G. Mainfray, and C. Manus. Multiple-harmonic conversion of 1064 nm radiation in rare gases. *Journal of Physics B: Atomic, Molecular and Optical Physics*, 21(3):L31–L35, February 1988.

[15] Zenghu Chang, Andy Rundquist, Haiwen Wang, Margaret M. Murnane, and

Henry C. Kapteyn. Generation of Coherent Soft X Rays at 2.7 nm Using High Harmonics. *Physical Review Letters*, 79(16):2967–2970, October 1997.

[16] Shambhu Ghimire, Anthony D. DiChiara, Emily Sistrunk, Pierre Agostini, Louis F. DiMauro, and David A. Reis. Observation of high-order harmonic generation in a bulk crystal. *Nature Physics*, 7:138, December 2010.

[17] Shambhu Ghimire and David A. Reis. Publisher Correction: High-harmonic generation from solids. *Nature Physics*, 15(2):197–197, February 2019.

[18] Hanzhe Liu, Yilei Li, Yong Sing You, Shambhu Ghimire, Tony F. Heinz, and David A. Reis. High-harmonic generation from an atomically thin semiconductor. *Nature Physics*, 13(3):262–265, March 2017.

[19] G. P. Zhang, M. S. Si, M. Murakami, Y. H. Bai, and Thomas F. George. Generating high-order optical and spin harmonics from ferromagnetic monolayers. *Nature Communications*, 9(1):3031, August 2018.

[20] Yong Sing You, David A. Reis, and Shambhu Ghimire. Anisotropic high-harmonic generation in bulk crystals. *Nature Physics*, 13(4):345–349, April 2017.

[21] Murat Sivis, Marco Taucer, Giulio Vampa, Kyle Johnston, André Staudte, Andrei Yu. Naumov, D. M. Villeneuve, Claus Ropers, and P. B. Corkum. Tailored semiconductors for high-harmonic optoelectronics. *Science*, 357(6348):303–306, 2017.

[22] Dominik Franz, Shatha Kaassamani, David Gauthier, Rana Nicolas, Maria Kholodtsova, Ludovic Douillard, Jean-Thomas Gomes, Laure Lavoute, Dmitry Gaponov, Nicolas Ducros, Sebastien Février, Jens Biegert, Liping Shi, Milutin Kovacev, Willem Boutu, and Hamed Merdji. All semiconductor enhanced high-harmonic generation from a single nanostructured cone. *Scientific Reports*, 9(1):5663, December 2019.

[23] Seunghwoi Han, Hyunwoong Kim, Yong Woo Kim, Young-Jin Kim, Seungchul Kim, In-Yong Park, and Seung-Woo Kim. High-harmonic generation by field enhanced femtosecond pulses in metal-sapphire nanostructure. *Nature Communications*, 7:ncomms13105, October 2016.

[24] G. Vampa, B. G. Ghamsari, S. Siadat Mousavi, T. J. Hammond, A. Olivieri, E. Lisicka-Skrek, A. Yu Naumov, D. M. Villeneuve, A. Staudte, P. Berini, and P. B. Corkum. Plasmon-enhanced high-harmonic generation from silicon. *Nature Physics*, advance online publication, April 2017.

[25] Shatha Kaassamani, Rana Nicolas, David Gauthier, Dominik Franz, Willem Boutu, and Hamed Merdji. High harmonic generation in graphene (conference presentation). In *Advances in Ultrafast Condensed Phase Physics*, volume 10673, page 106730G. International Society for Optics and Photonics.

[26] David Gauthier, Shatha Kaassamani, Dominik Franz, Rana Nicolas, Jean-Thomas Gomes, Laure Lavoute, Dmitry Gaponov, Sébastien Février, Gaëtan Jargot, Marc Hanna, Willem Boutu, and Hamed Merdji. Orbital angular momentum from semiconductor high-order harmonics. *Optics Letters*, 44(3):546–549, February 2019.

[27] M. Lewenstein, Ph. Balcou, M. Yu. Ivanov, Anne L'Huillier, and P. B. Corkum. Theory of high-harmonic generation by low-frequency laser fields. *Physical Review A*, 49(3):2117–2132, March 1994.

[28] L. V. Keldysh. Ionization in the field of a strong electromagnetic wave. *Journal of Experimental and Theoretical Physics*, 20:1307, May 1965.

[29] Pascal Salières, Anne L'Huillier, and Maciej Lewenstein. Coherence Control of High-Order Harmonics. *Physical Review Letters*, 74(19):3776–3779, May 1995.

[30] J.-F. Hergott, M. Kovacev, H. Merdji, C. Hubert, Y. Mairesse, E. Jean, P. Breger, P. Agostini, B. Carré, and P. Salières. Extreme-ultraviolet high-order harmonic pulses in the microjoule range. *Physical Review A*, 66(2):021801, August 2002.

[31] P. Rudawski, C. M. Heyl, F. Brizuela, J. Schwenke, A. Persson, E. Mansten, R. Rakowski, L. Rading, F. Campi, B. Kim, P. Johnsson, and A. L'Huillier. A high-flux high-order harmonic source. *Review of Scientific Instruments*, 84(7):073103, July 2013.

[32] Tenio Popmintchev, Ming-Chang Chen, Oren Cohen, Michael E. Grisham, Jorge J. Rocca, Margaret M. Murnane, and Henry C. Kapteyn. Extended phase matching of high harmonics driven by mid-infrared light. *Optics Letters*, 33(18):2128, September 2008.

[33] E. L. Falcão-Filho, V. M. Gkortsas, Ariel Gordon, and Franz X. Kärtner. Analytic scaling analysis of high harmonic generation conversion efficiency. *Opt. Express, OE*, 17(13):11217–11229, June 2009.

[34] Eiji J. Takahashi, Yasuo Nabekawa, and Katsumi Midorikawa. Low-divergence coherent soft x-ray source at 13 nm by high-order harmonics. *Applied Physics Letters*, 84(1):4–6, January 2004.

[35] Eiji Takahashi, Yasuo Nabekawa, Tatsuya Otsuka, Minoru Obara, and Katsumi Midorikawa. Generation of highly coherent submicrojoule soft x rays by high-order harmonics. *Physical Review A*, 66(2):021802, August 2002.

[36] E. Constant, D. Garzella, P. Breger, E. Mével, Ch. Dorrer, C. Le Blanc, F. Salin, and P. Agostini. Optimizing High Harmonic Generation in Absorbing Gases: Model and Experiment. *Physical Review Letters*, 82(8):1668–1671, February 1999.

[37] H. Eichmann, A. Egbert, S. Nolte, C. Momma, B. Wellegehausen, W. Becker, S. Long, and J. K. McIver. Polarization-dependent high-order two-color mixing. *Physical Review A*, 51(5):R3414–R3417, May 1995.

[38] I Jong Kim, Chul Min Kim, Hyung Taek Kim, Gae Hwang Lee, Yong Soo Lee, Ju Yun Park, David Jaeyun Cho, and Chang Hee Nam. Highly Efficient High-Harmonic Generation in an Orthogonally Polarized Two-Color Laser Field. *Physical Review Letters*, 94(24):243901, June 2005.

[39] Hamed Merdji, Thierry Auguste, Willem Boutu, J.-Pascal Caumes, Bertrand Carré, Thomas Pfeifer, Aurélie Jullien, Daniel M. Neumark, and Stephen R. Leone. Isolated attosecond pulses using a detuned second-harmonic field. 32(21):3134–3136.

[40] K. S. Budil, P. Salières, Anne L'Huillier, T. Ditmire, and M. D. Perry. Influence of ellipticity on harmonic generation. *Physical Review A*, 48(5):R3437–R3440, November 1993.

[41] N. H. Burnett, C. Kan, and P. B. Corkum. Ellipticity and polarization effects in harmonic generation in ionizing neon. *Physical Review A*, 51(5):R3418–R3421, May 1995.

[42] Mengxi Wu, Shambhu Ghimire, David A. Reis, Kenneth J. Schafer, and Mette B. Gaarde. High-harmonic generation from Bloch electrons in solids. *Physical Review A*, 91(4):043839, April 2015.

[43] Shambhu Ghimire, Georges Ndabashimiye, Anthony D. DiChiara, Emily Sistrunk, Mark I. Stockman, Pierre Agostini, Louis F. DiMauro, and David A. Reis. Strong-field and attosecond physics in solids. *Journal of Physics B: Atomic, Molecular and Optical Physics*, 47(20):204030, October 2014.

[44] Nicolas Tancogne-Dejean, Oliver D. Mücke, Franz X. Kärtner, and Angel Rubio. Ellipticity dependence of high-harmonic generation in solids originating from coupled intraband and interband dynamics. *Nature Communications*, 8(1):745, December 2017.

[45] G. Vampa, C. R. McDonald, G. Orlando, D. D. Klug, P. B. Corkum, and T. Brabec. Theoretical Analysis of High-Harmonic Generation in Solids. *Physical Review Letters*, 113(7):073901, August 2014.

[46] Shambhu Ghimire, Anthony D. DiChiara, Emily Sistrunk, Georges Ndabashimiye, Urszula B. Szafruga, Anis Mohammad, Pierre Agostini, Louis F. DiMauro, and David A. Reis. Generation and propagation of high-order harmonics in crystals. *Phys. Rev. A*, 85(4):043836, April 2012.

[47] Peiyu Xia, Changsu Kim, Faming Lu, Teruto Kanai, Hidefumi Akiyama, Jiro Itatani, and Nobuhisa Ishii. Nonlinear propagation effects in high harmonic generation in reflection and transmission from gallium arsenide. *Optics Express*, 26(22):29393–29400, October 2018.

[48] Tran Trung Luu, Valerio Scagnoli, Susmita Saha, Laura J. Heyderman, and Hans Jakob Wörner. Generation of coherent extreme ultraviolet radiation from α–quartz using 50 fs laser pulses at a 1030 nm wavelength and high repetition rates. *Optics Letters*, 43(8):1790–1793, April 2018.

[49] Giulio Vampa, Hanzhe Liu, Tony F. Heinz, and David A. Reis. Disentangling interface and bulk contributions to high-harmonic emission from solids. *Optica*, 6(5):553, May 2019.

[50] Mengxi Wu, Dana A. Browne, Kenneth J. Schafer, and Mette B. Gaarde. Multilevel perspective on high-order harmonic generation in solids. *Physical Review A*, 94(6):063403, December 2016.

[51] Xi Liu, Xiaosong Zhu, Xiaofan Zhang, Dian Wang, Pengfei Lan, and Peixiang Lu. Wavelength scaling of the cutoff energy in the solid high harmonic generation. *Optics Express*, 25(23):29216–29224, November 2017.

[52] Edyta N. Osika, Alexis Chacón, Lisa Ortmann, Noslen Suárez, Jose Antonio Pérez-Hernández, Bartłomiej Szafran, Marcelo F. Ciappina, Fernando Sols, Alexandra S. Landsman, and Maciej Lewenstein. Wannier-Bloch Approach to Localization in High-Harmonics Generation in Solids. *Physical Review X*, 7(2):021017, May 2017.

[53] Nicolas Tancogne-Dejean, Oliver D. Mücke, Franz X. Kärtner, and Angel Rubio. Impact of the Electronic Band Structure in High-Harmonic Generation Spectra of Solids. *Physical Review Letters*, 118(8):087403, February 2017.

[54] Giulio Vampa, Gianfranco Orlando, P Corkum, T Brabec, and C McDonald. Theory of high-harmonic generation in solids. *Journal of Physics: Conference Series*, 594, March 2015.

[55] Zhou Wang, Hyunwook Park, Yu Hang Lai, Junliang Xu, Cosmin I. Blaga, Fengyuan Yang, Pierre Agostini, and Louis F. DiMauro. The roles of photocarrier doping and driving wavelength in high harmonic generation from a semiconductor. *Nature Communications*, 8(1):1686, December 2017.

[56] J. Tate, T. Auguste, H. G. Muller, P. Salières, P. Agostini, and L. F. DiMauro. Scaling of Wave-Packet Dynamics in an Intense Midinfrared Field. *Physical Review Letters*, 98(1):013901, January 2007.

[57] A. D. Shiner, C. Trallero-Herrero, N. Kajumba, H.-C. Bandulet, D. Comtois, F. Légaré, M. Giguère, J-C. Kieffer, P. B. Corkum, and D. M. Villeneuve. Wavelength Scaling of High Harmonic Generation Efficiency. *Physical Review Letters*, 103(7):073902, August 2009.

[58] Hyunwoong Kim, Seunghwoi Han, Yong Woo Kim, Seungchul Kim, and Seung-Woo Kim. Generation of Coherent Extreme-Ultraviolet Radiation from Bulk Sapphire Crystal. *ACS Photonics*, 4(7):1627–1632, 2017.

[59] A. A. Lanin, E. A. Stepanov, A. V. Mitrofanov, D. A. Sidorov-Biryukov, A. B. Fedotov, and A. M. Zheltikov. High-order harmonic analysis of anisotropic petahertz photocurrents in solids. *Optics Letters*, 44(8):1888–1891, April 2019.

[60] M. Taucer, T. J. Hammond, P. B. Corkum, G. Vampa, C. Couture, N. Thiré, B. E. Schmidt, F. Légaré, H. Selvi, N. Unsuree, B. Hamilton, T. J. Echtermeyer, and M. A. Denecke. Nonperturbative harmonic generation in graphene from intense midinfrared pulsed light. *Physical Review B*, 96(19):195420, November 2017.

[61] G. Vampa, Y. S. You, H. Liu, S. Ghimire, and D. A. Reis. Observation of backward high-harmonic emission from solids. *Optics Express*, 26(9):12210–12218, April 2018.

[62] Mikhail N. Polyanskiy. Refractive index database. Retrieved from `https://refractiveindex.info`. Accessed on: 2020-08-28.

[63] Wikipedia contributors. Fresnel equations. Retrieved from `https://en.wikipedia.org/w/index.php?title=Fresnel_equations&oldid=975836365`. Accessed on: 2020-08-28.

[64] Georges Ndabashimiye, Shambhu Ghimire, Mengxi Wu, Dana A. Browne, Kenneth J. Schafer, Mette B. Gaarde, and David A. Reis. Solid-state harmonics beyond the atomic limit. *Nature*, 534(7608):520–523, June 2016.

[65] Shima Gholam Mirzaei, John Beetar, and Michael Chini. High harmonic generation in ZnO with a high-power mid-IR OPA. *Applied Physics Letters*, 110:061101, February 2017.

[66] Shima Gholam-Mirzaei, John E. Beetar, Alexis Chacón, and Michael Chini. High-harmonic generation in ZnO driven by self-compressed mid-infrared pulses. *JOSA B*, 35(4):A27–A31, April 2018.

[67] Keisuke Kaneshima, Yasushi Shinohara, Kengo Takeuchi, Nobuhisa Ishii, Kotaro Imasaka, Tomohiro Kaji, Satoshi Ashihara, Kenichi L. Ishikawa, and Jiro Itatani. Polarization-Resolved Study of High Harmonics from Bulk Semiconductors. *Physical Review Letters*, 120(24):243903, June 2018.

[68] Giulio Vampa, Thomas J. Hammond, Nicolas Thiré, Bruno E. Schmidt, Francois Légaré, Dennis D. Klug, and Paul B. Corkum. Generation of high harmonics from silicon. *arXiv:1605.06345 [physics]*, May 2016.

[69] Naotaka Yoshikawa, Tomohiro Tamaya, and Koichiro Tanaka. High-harmonic generation in graphene enhanced by elliptically polarized light excitation. *Science*, 356(6339):736–738, May 2017.

[70] Shima Gholam-Mirzaei, Erin Crites, John E. Beetar, Aiping Chen, Michael Chini, and Michael Chini. Anisotropic Polarization Dependent High Harmonic Generation in the Ferroelectric Crystal BaTiO3. In *Conference on Lasers*

and Electro-Optics (2018), paper FF3P.6, page FF3P.6. Optical Society of America, May 2018.

[71] Nicolas Tancogne-Dejean and Angel Rubio. Atomic-like high-harmonic generation from two-dimensional materials. *Science Advances*, 4(2):eaao5207, February 2018.

[72] H. K. Avetissian, A. K. Avetissian, B. R. Avchyan, and G. F. Mkrtchian. Multiphoton excitation and high-harmonics generation in topological insulator. *Journal of Physics: Condensed Matter*, 30(18):185302, April 2018.

[73] Seunghwoi Han, Lisa Ortmann, Hyunwoong Kim, Yong Woo Kim, Takashi Oka, Alexis Chacon, Brent Doran, Marcelo Ciappina, Maciej Lewenstein, Seung-Woo Kim, Seungchul Kim, and Alexandra S. Landsman. Extraction of higher-order nonlinear electronic response in solids using high harmonic generation. *Nature Communications*, 10(1):3272, December 2019.

[74] G. Vampa, T. J. Hammond, N. Thiré, B. E. Schmidt, F. Légaré, C. R. McDonald, T. Brabec, D. D. Klug, and P. B. Corkum. All-Optical Reconstruction of Crystal Band Structure. *Physical Review Letters*, 115(19):193603, November 2015.

[75] A. A. Lanin, E. A. Stepanov, A. B. Fedotov, and A. M. Zheltikov. Mapping the electron band structure by intraband high-harmonic generation in solids. *Optica*, 4(5):516–519, May 2017.

[76] N. Klemke, N. Tancogne-Dejean, G. M. Rossi, Y. Yang, F. Scheiba, R. E. Mainz, G. Di Sciacca, A. Rubio, F. X. Kärtner, and O. D. Mücke. Polarization-state-resolved high-harmonic spectroscopy of solids. *Nature Communications*, 10(1):1319, March 2019.

[77] Dominik Franz, Rana Nicolas, Willem Boutu, Liping Shi, Quentin Ripault, Maria Kholodtsova, Bianca Iwan, Ugaitz Elu Etxano, Milutin Kovacev, Jens Biegert, and Hamed Merdji. Amplification of high harmonics in 3D semiconductor waveguides. *arXiv:1709.09153 [physics]*, September 2017.

[78] K. S. Novoselov, V. I. Falko, L. Colombo, P. R. Gellert, M. G. Schwab, and K. Kim. A roadmap for graphene. *Nature*, 490(7419):192–200, October 2012.

[79] K. I. Bolotin, K. J. Sikes, Z. Jiang, M. Klima, G. Fudenberg, J. Hone, P. Kim, and H. L. Stormer. Ultrahigh electron mobility in suspended graphene. *Solid State Communications*, 146(9):351–355, June 2008.

[80] Alexander S. Mayorov, Roman V. Gorbachev, Sergey V. Morozov, Liam Britnell, Rashid Jalil, Leonid A. Ponomarenko, Peter Blake, Kostya S. Novoselov, Kenji Watanabe, Takashi Taniguchi, and A. K. Geim. Micrometer-Scale Ballistic Transport in Encapsulated Graphene at Room Temperature. *Nano Letters*, 11(6):2396–2399, June 2011.

[81] Changgu Lee, Xiaoding Wei, Jeffrey W. Kysar, and James Hone. Measurement of the Elastic Properties and Intrinsic Strength of Monolayer Graphene. *Science*, 321(5887):385–388, July 2008.

[82] K. S. Novoselov, A. K. Geim, S. V. Morozov, D. Jiang, M. I. Katsnelson, I. V. Grigorieva, S. V. Dubonos, and A. A. Firsov. Two-dimensional gas of massless Dirac fermions in graphene. *Nature*, 438(7065):197–200, November 2005.

[83] A. K. Geim and K. S. Novoselov. The rise of graphene. *Nature Materials*, 6(3):183–191, March 2007.

[84] S. Y. Zhou, G.-H. Gweon, A. V. Fedorov, P. N. First, W. A. de Heer, D.-H. Lee, F. Guinea, A. H. Castro Neto, and A. Lanzara. Substrate-induced bandgap opening in epitaxial graphene. *Nature Materials*, 6(10):770–775, October 2007.

[85] Gianluca Giovannetti, Petr A. Khomyakov, Geert Brocks, Paul J. Kelly, and Jeroen van den Brink. Substrate-induced band gap in graphene on hexagonal boron nitride: Ab initio density functional calculations. *Physical Review B*, 76(7):073103, August 2007.

[86] Jeil Jung, Ashley M. DaSilva, Allan H. MacDonald, and Shaffique Adam. Origin of band gaps in graphene on hexagonal boron nitride. *Nature Communications*, 6(1):6308, February 2015.

[87] Hongtao Liu, Yunqi Liu, and Daoben Zhu. Chemical doping of graphene. *J. Mater. Chem.*, 21(10):3335–3345, 2011.

[88] Dean Moldovan. Band structure - pybinding. Retrieved from `http://docs.pybinding.site/en/stable/tutorial/bands.html`. Accessed on: 2020-08-13.

[89] P. Bowlan, E. Martinez-Moreno, K. Reimann, T. Elsaesser, and M. Woerner. Ultrafast terahertz response of multilayer graphene in the nonperturbative regime. *Physical Review B*, 89(4):041408, January 2014.

[90] Hassan A. Hafez, Sergey Kovalev, Jan-Christoph Deinert, Zoltán Mics, Bertram Green, Nilesh Awari, Min Chen, Semyon Germanskiy, Ulf Lehnert, Jochen Teichert, Zhe Wang, Klaas-Jan Tielrooij, Zhaoyang Liu, Zongping Chen, Akimitsu Narita, Klaus Müllen, Mischa Bonn, Michael Gensch, and Dmitry Turchinovich. Extremely efficient terahertz high-harmonic generation in graphene by hot Dirac fermions. *Nature*, 561(7724):507–511, September 2018.

[91] Matthias Baudisch, Andrea Marini, Joel D. Cox, Tony Zhu, Francisco Silva, Stephan Teichmann, Mathieu Massicotte, Frank Koppens, Leonid S. Levitov, F. Javier García de Abajo, and Jens Biegert. Ultrafast nonlinear optical response of Dirac fermions in graphene. *Nature Communications*, 9(1):1018, March 2018.

[92] Wei-Tao Liu, S. W. Wu, P. J. Schuck, M. Salmeron, Y. R. Shen, and F. Wang. Nonlinear broadband photoluminescence of graphene induced by femtosecond laser irradiation. *Physical Review B*, 82(8):081408, August 2010.

[93] Chun Hung Lui, Kin Fai Mak, Jie Shan, and Tony F. Heinz. Ultrafast Photoluminescence from Graphene. *Physical Review Letters*, 105(12):127404, September 2010.

[94] Tao Jiang, Di Huang, Jinluo Cheng, Xiaodong Fan, Zhihong Zhang, Yuwei Shan, Yangfan Yi, Yunyun Dai, Lei Shi, Kaihui Liu, Changgan Zeng, Jian Zi, J. E. Sipe, Yuen-Ron Shen, Wei-Tao Liu, and Shiwei Wu. Gate-tunable third-order nonlinear optical response of massless Dirac fermions in graphene. *Nature Photonics*, 12(7):430–436, July 2018.

[95] Zhi-Bo Liu, Li Li, Yan-Fei Xu, Jia-Jie Liang, Xin Zhao, Shu-Qi Chen, Yong-Sheng Chen, and Jian-Guo Tian. Direct patterning on reduced graphene oxide nanosheets using femtosecond laser pulses. *Journal of Optics*, 13(8):085601, August 2011.

[96] Tianqi Dong, Martin Sparkes, Colm Durkan, and William O'Neill. Evaluating femtosecond laser ablation of graphene on SiO $_2$ /Si substrate. *Journal of Laser Applications*, 28(2):022202, May 2016.

[97] Golap Kalita, Litao Qi, Yoshiharu Namba, Koichi Wakita, and Masayoshi Umeno. Femtosecond laser induced micropatterning of graphene film. *Materials Letters*, 65(11):1569–1572, June 2011.

[98] Zi-Yu Chen and Rui Qin. Circularly polarized extreme ultraviolet high harmonic generation in graphene. *Optics Express*, 27(3):3761–3770, February 2019.

[99] Nardeep Kumar, Jatinder Kumar, Chris Gerstenkorn, Rui Wang, Hsin-Ying Chiu, Arthur L. Smirl, and Hui Zhao. Third harmonic generation in graphene and few-layer graphite films. *Physical Review B*, 87(12):121406, March 2013.

[100] Giancarlo Soavi, Gang Wang, Habib Rostami, David G. Purdie, Domenico De Fazio, Teng Ma, Birong Luo, Junjia Wang, Anna K. Ott, Duhee Yoon, Sean A. Bourelle, Jakob E. Muench, Ilya Goykhman, Stefano Dal Conte, Michele Celebrano, Andrea Tomadin, Marco Polini, Giulio Cerullo, and Andrea C. Ferrari. Broadband, electrically tunable third-harmonic generation in graphene. *Nature Nanotechnology*, 13(7):583–588, July 2018.

[101] Erich Runge and E. K. U. Gross. Density-functional theory for time-dependent systems. 52(12):997–1000.

[102] Robert van Leeuwen. Causality and symmetry in time-dependent density-functional theory. 80(6):1280–1283.

[103] Xavier Andrade, David Strubbe, Umberto De Giovannini, Ask Hjorth Larsen, Micael J. T. Oliveira, Joseba Alberdi-Rodriguez, Alejandro Varas, Iris

Theophilou, Nicole Helbig, Matthieu J. Verstraete, Lorenzo Stella, Fernando Nogueira, Alán Aspuru-Guzik, Alberto Castro, Miguel A. L. Marques, and Angel Rubio. Real-space grids and the Octopus code as tools for the development of new simulation approaches for electronic systems. *Physical Chemistry Chemical Physics*, 17(47):31371–31396, November 2015.

[104] Óscar Zurrón-Cifuentes, Roberto Boyero-García, Carlos Hernández-García, Antonio Picón, and Luis Plaja. Optical anisotropy of non-perturbative high-order harmonic generation in gapless graphene. *Optics Express*, 27(5):7776, March 2019.

[105] Guillaume Le Breton, Angel Rubio, and Nicolas Tancogne-Dejean. High-harmonic generation from few-layer hexagonal boron nitride: Evolution from monolayer to bulk response. *Physical Review B*, 98(16):165308, October 2018.

[106] Steven P. Koenig, Narasimha G. Boddeti, Martin L. Dunn, and J. Scott Bunch. Ultrastrong adhesion of graphene membranes. *Nature Nanotechnology*, 6(9):543–546, September 2011.

[107] G. H. Wells, T. Hopf, K. V. Vassilevski, E. Escobedo-Cousin, N. G. Wright, A. B. Horsfall, J. P. Goss, A. G. O'Neill, and M. R. C. Hunt. Determination of the adhesion energy of graphene on SiC(0001) via measurement of pleat defects. *Applied Physics Letters*, 105(19):193109, November 2014.

[108] Adam Roberts, Daniel Cormode, Collin Reynolds, Ty Newhouse-Illige, Brian J. LeRoy, and Arvinder S. Sandhu. Response of graphene to femtosecond high-intensity laser irradiation. *Applied Physics Letters*, 99(5):051912, August 2011.

[109] Haifeng Wang, Luping Shi, Boris Lukyanchuk, Colin Sheppard, and Chong Tow Chong. Creation of a needle of longitudinally polarized light in vacuum using binary optics. *Nature Photonics*, 2(8):501–505, August 2008.

[110] An-ping Yu, Gang Chen, Zhi-hai Zhang, Zhong-quan Wen, Lu-ru Dai, Kun Zhang, Sen-lin Jiang, Zhi-xiang Wu, Yu-yan Li, Chang-tao Wang, and Xiangang Luo. Creation of Sub-diffraction Longitudinally Polarized Spot by Focusing Radially Polarized Light with Binary Phase Lens. *Scientific Reports*, 6(1):38859, December 2016.

[111] Dominik Franz. *High harmonic generation in crystals assisted by local field enhancement in nanostructures*. PhD thesis, Université Paris-Saclay, May 2018.

[112] Li Honglin, Lv Yingbo, Li Jinzhu, and Yu Ke. First-principles study of p-type conductivity of N-Al/Ga/In co-doped ZnO. *Physica Scripta*, 90(2):025803, January 2015.

[113] Linda Y. Lim, Stephan Lany, Young Jun Chang, Eli Rotenberg, Alex Zunger, and Michael F. Toney. Angle-resolved photoemission and quasiparticle calculation of ZnO: The need for d band shift in oxide semiconductors. *Physical Review B*, 86(23):235113, December 2012.

[114] Alan D. Bristow, Nir Rotenberg, and Henry M. van Driel. Two-photon absorption and Kerr coefficients of silicon for 850–2200nm. *Applied Physics Letters*, 90(19):191104, May 2007.

[115] Yong Sing You, Yanchun Yin, Yi Wu, Andrew Chew, Xiaoming Ren, Fengjiang Zhuang, Shima Gholam-Mirzaei, Michael Chini, Zenghu Chang, and Shambhu Ghimire. High-harmonic generation in amorphous solids. *Nature Communications*, 8(1):724, September 2017.

[116] Ting Wang, Nalla Venkatram, Jacek Gosciniak, Yuanjing Cui, Guodong Qian, Wei Ji, and Dawn T. H. Tan. Multi-photon absorption and third-order nonlinearity in silicon at mid-infrared wavelengths. *Optics Express*, 21(26):32192–32198, December 2013.

[117] Shaul Pearl, Nir Rotenberg, and Henry M. van Driel. Three photon absorption in silicon for 2300–3300nm. *Applied Physics Letters*, 93(13):131102, September 2008.

[118] Saeed Ullah. *Optical control and detection of spin coherence in multilayer systems.* PhD thesis, University of São Paulo-Institute of Physics, April 2017.

[119] W. C. Hurlbut, Yun-Shik Lee, K. L. Vodopyanov, P. S. Kuo, and M. M. Fejer. Multiphoton absorption and nonlinear refraction of GaAs in the mid-infrared. *Optics Letters*, 32(6):668–670, March 2007.

[120] D. C. Hutchings and B. S. Wherrett. Theory of the anisotropy of ultrafast nonlinear refraction in zinc-blende semiconductors. *Physical Review B*, 52(11):8150–8159, September 1995.

[121] Y. R. Shen. *The Principles of Nonlinear Optics*, chapter 17: Self-Focusing, pages 303–313. John Wiley & Sons, New York, 1984.

[122] Dr Rüdiger Paschotta. Self-focusing. Retrieved from `https://www.rp-photonics.com/self_focusing.html`. Accessed on: 2020-08-28.

[123] Yang Yue, Lin Zhang, HAO HUANG, Raymond Beausoleil, and Alan Willner. Silicon-on-Nitride Waveguide With Ultralow Dispersion Over an Octave-Spanning Mid-Infrared Wavelength Range. *IEEE Photonics Journal*, 4:126, February 2012.

[124] Robert Adair, L. L. Chase, and Stephen A. Payne. Nonlinear refractive index of optical crystals. *Physical Review B*, 39(5):3337–3350, February 1989.

[125] A. Couairon, L. Sudrie, M. Franco, B. Prade, and A. Mysyrowicz. Filamentation and damage in fused silica induced by tightly focused femtosecond laser pulses. *Physical Review B*, 71(12):125435, March 2005.

[126] N. Bloembergen and P. S. Pershan. Light Waves at the Boundary of Nonlinear Media. *Physical Review*, 128(2):606–622, October 1962.

[127] H. C. Casey, D. D. Sell, and K. W. Wecht. Concentration dependence of the absorption coefficient for n - and p - type GaAs between 1.3 and 1.6 eV. *Journal of Applied Physics*, 46(1):250–257, January 1975.

[128] Absorption coefficient. Retrieved from `https://www.pveducation.org/pvcdrom/pn-junctions/absorption-coefficient`. Accessed on: 2020-09-07.

[129] P. Pfeffer and W. Zawadzki. Five-level k\ensuremath{\cdot}p model for the conduction and valence bands of GaAs and InP. *Physical Review B*, 53(19):12813–12828, May 1996.

[130] Isak Kilen, Miroslav Kolesik, Jorg Hader, Jerome V. Moloney, Ulrich Huttner, Maria K. Hagen, and Stephan W. Koch. Propagation Induced Dephasing in Semiconductor High-Harmonic Generation. *Physical Review Letters*, 125(8):083901, August 2020.

[131] S. M. Golin, S. E. Kirkwood, D. D. Klug, D. M. Villeneuve, D. M. Rayner, C. A. Trallero Herrero, and P. B. Corkum. Strong field processes inside gallium arsenide. *Journal of Physics B: Atomic, Molecular and Optical Physics*, 47(20):204025, October 2014.

[132] C. Schmidt, J. Bühler, A.-C. Heinrich, J. Allerbeck, R. Podzimski, D. Berghoff, T. Meier, W. G. Schmidt, C. Reichl, W. Wegscheider, D. Brida, and A. Leitenstorfer. Signatures of transient Wannier-Stark localization in bulk gallium arsenide. *Nature Communications*, 9(1):2890, December 2018.

[133] M. O. Henry, J. P. Larkin, and G. F. Imbusch. Nature of the broadband luminescence center in MgO:${\mathrm{Cr}}^{3+}$. *Physical Review B*, 13(5):1893–1902, March 1976.

[134] S. Almalki, A. M. Parks, G. Bart, P. B. Corkum, T. Brabec, and C. R. McDonald. High harmonic generation tomography of impurities in solids: Conceptual analysis. *Physical Review B*, 98(14):144307, October 2018.

[135] Yong Sing You, Mengxi Wu, Yanchun Yin, Andrew Chew, Xiaoming Ren, Shima Gholam-Mirzaei, Dana A. Browne, Michael Chini, Zenghu Chang, Kenneth J. Schafer, Mette B. Gaarde, and Shambhu Ghimire. Laser waveform control of extreme ultraviolet high harmonics from solids. *Optics Letters*, 42(9):1816, May 2017.

[136] O. Tcherbakoff, E. Mével, D. Descamps, J. Plumridge, and E. Constant. Time-gated high-order harmonic generation. *Physical Review A*, 68(4):043804, October 2003.

[137] I. J. Sola, E. Mével, L. Elouga, E. Constant, V. Strelkov, L. Poletto, P. Villoresi, E. Benedetti, J.-P. Caumes, S. Stagira, C. Vozzi, G. Sansone, and M. Nisoli. Controlling attosecond electron dynamics by phase-stabilized polarization gating. *Nature Physics*, 2(5):319–322, May 2006.

[138] Giuseppe Sansone, Luca Poletto, and Mauro Nisoli. High-energy attosecond light sources. *Nature Photonics*, 5(11):655–663, November 2011.

[139] Aurelio Oriana, Julien Réhault, Fabrizio Preda, Dario Polli, and Giulio Cerullo. Scanning Fourier transform spectrometer in the visible range based on birefringent wedges. *Journal of the Optical Society of America A*, 33(7):1415, July 2016.

[140] T. Shih, M. T. Winkler, T. Voss, and E. Mazur. Dielectric function dynamics during femtosecond laser excitation of bulk ZnO. *Applied Physics A*, 96(2):363–367, August 2009.

[141] D. Dufft, A. Rosenfeld, S. K. Das, R. Grunwald, and J. Bonse. Femtosecond laser-induced periodic surface structures revisited: A comparative study on ZnO. *Journal of Applied Physics*, 105(3):034908, February 2009.

[142] Genevieve Gariepy, Jonathan Leach, Kyung Taec Kim, T. J. Hammond, E. Frumker, Robert W. Boyd, and P. B. Corkum. Creating High-Harmonic Beams with Controlled Orbital Angular Momentum. *Physical Review Letters*, 113(15):153901, October 2014.

[143] R. Géneaux, A. Camper, T. Auguste, O. Gobert, J. Caillat, R. Taïeb, and T. Ruchon. Synthesis and characterization of attosecond light vortices in the extreme ultraviolet. *Nature Communications*, 7(1):12583, August 2016.

[144] A. Denoeud, L. Chopineau, A. Leblanc, and F. Quéré. Interaction of Ultraintense Laser Vortices with Plasma Mirrors. *Physical Review Letters*, 118(3):033902, January 2017.

[145] Miles Padgett, Johannes Courtial, and Les Allen. Light's Orbital Angular Momentum. *Physics Today*, 57(5):35–40, May 2004.

[146] L. Allen, M. W. Beijersbergen, R. J. C. Spreeuw, and J. P. Woerdman. Orbital angular momentum of light and the transformation of Laguerre-Gaussian laser modes. *Physical Review A*, 45(11):8185–8189, June 1992.

[147] V. Petrillo, G. Dattoli, I. Drebot, and F. Nguyen. Compton Scattered X-Gamma Rays with Orbital Momentum. *Physical Review Letters*, 117(12):123903, September 2016.

[148] J. Vieira, R. M. G. M. Trines, E. P. Alves, R. A. Fonseca, J. T. Mendonça, R. Bingham, P. Norreys, and L. O. Silva. High Orbital Angular Momentum Harmonic Generation. *Physical Review Letters*, 117(26):265001, December 2016.

[149] Primož Rebernik Ribič, Benedikt Rösner, David Gauthier, Enrico Allaria, Florian Döring, Laura Foglia, Luca Giannessi, Nicola Mahne, Michele Manfredda, Claudio Masciovecchio, Riccardo Mincigrucci, Najmeh Mirian, Emiliano Principi, Eléonore Roussel, Alberto Simoncig, Simone Spampinati, Christian David, and Giovanni De Ninno. Extreme-Ultraviolet Vortices from a Free-Electron Laser. *Physical Review X*, 7(3):031036, August 2017.

[150] D. Gauthier, P. Rebernik Ribič, G. Adhikary, A. Camper, C. Chappuis, R. Cucini, L. F. DiMauro, G. Dovillaire, F. Frassetto, R. Géneaux, P. Miotti, L. Poletto, B. Ressel, C. Spezzani, M. Stupar, T. Ruchon, and G. De Ninno. Tunable orbital angular momentum in high-harmonic generation. *Nature Communications*, 8(1):14971, April 2017.

[151] Carlos Hernández-García, Jorge Vieira, Jose T. Mendonça, Laura Rego, Julio San Román, Luis Plaja, Primoz R. Ribic, David Gauthier, and Antonio Picón. Generation and Applications of Extreme-Ultraviolet Vortices. *Photonics*, 4(2):28, June 2017.

[152] L. Marrucci, C. Manzo, and D. Paparo. Optical Spin-to-Orbital Angular Momentum Conversion in Inhomogeneous Anisotropic Media. *Physical Review Letters*, 96(16):163905, April 2006.

[153] D. G. Lee, J. J. Park, J. H. Sung, and C. H. Nam. Wave-front phase measurements of high-order harmonic beams by use of point-diffraction interferometry. *Optics Letters*, 28(6):480, March 2003.

[154] A. Ravasio, D. Gauthier, F. R. N. C. Maia, M. Billon, J-P. Caumes, D. Garzella, M. Géléoc, O. Gobert, J-F. Hergott, A-M. Pena, H. Perez, B. Carré, E. Bourhis, J. Gierak, A. Madouri, D. Mailly, B. Schiedt, M. Fajardo, J. Gautier, P. Zeitoun, P. H. Bucksbaum, J. Hajdu, and H. Merdji. Single-Shot Diffractive Imaging with a Table-Top Femtosecond Soft X-Ray Laser-Harmonics Source. *Physical Review Letters*, 103(2):028104, July 2009.

[155] D. Gauthier, M. Guizar-Sicairos, X. Ge, W. Boutu, B. Carré, J. R. Fienup, and H. Merdji. Single-shot Femtosecond X-Ray Holography Using Extended References. *Physical Review Letters*, 105(9):093901, August 2010.

[156] J. Duarte, R. Cassin, J. Huijts, B. Iwan, F. Fortuna, L. Delbecq, H. Chapman, M. Fajardo, M. Kovacev, W. Boutu, and H. Merdji. Computed stereo lensless X-ray imaging. *Nature Photonics*, 13(7):449–453, July 2019.

[157] Julius Huijts, Sara Fernandez, David Gauthier, Maria Kholodtsova, Ahmed Maghraoui, Kadda Medjoubi, Andrea Somogyi, Willem Boutu, and Hamed Merdji. Broadband coherent diffractive imaging. *Nature Photonics*, 14(10):618–622, October 2020.

[158] John C. H. Spence. Diffractive Imaging of Single Particles. In Peter W. Hawkes and John C. H. Spence, editors, *Springer Handbook of Microscopy*, Springer Handbooks, pages 2–2. Springer International Publishing, Cham, 2019.

[159] Pierre Thibault, Martin Dierolf, Andreas Menzel, Oliver Bunk, Christian David, and Franz Pfeiffer. High-resolution scanning x-ray diffraction microscopy. 321(5887):379–382.

[160] F. Langer, C. P. Schmid, S. Schlauderer, M. Gmitra, J. Fabian, P. Nagler, C. Schüller, T. Korn, P. G. Hawkins, J. T. Steiner, U. Huttner, S. W. Koch,

M. Kira, and R. Huber. Lightwave valleytronics in a monolayer of tungsten diselenide. *Nature*, 557(7703):76–80, May 2018.

[161] H.G. Muller. Reconstruction of attosecond harmonic beating by interference of two-photon transitions. *Applied Physics B*, 74(1):s17–s21, June 2002.

[162] Y. Mairesse. Attosecond Synchronization of High-Harmonic Soft X-rays. *Science*, 302(5650):1540–1543, November 2003.

[163] Philippe Rigaud, Aymeric Van de Walle, Marc Hanna, Nicolas Forget, Florent Guichard, Yoann Zaouter, Khmaies Guesmi, Frédéric Druon, and Patrick Georges. Supercontinuum-seeded few-cycle mid-infrared OPCPA system. *Optics Express*, 24(23):26494, November 2016.

[164] Gaëtan Jargot, Nour Daher, Loïc Lavenu, Xavier Delen, Nicolas Forget, Marc Hanna, and Patrick Georges. Self-compression in a multipass cell. *Optics Letters*, 43(22):5643–5646, November 2018.

[165] Christopher Palmer. *Diffraction Grating Handbook (7th edition)*, chapter 2: The Grating Equation, pages 21–25. Richardson Gratings, Newport Corporation, 2014.

[166] Wikipedia contributors. Finite-difference time-domain method. Retrieved from `https://en.wikipedia.org/wiki/Finite-difference_time-domain_method`. Accessed on: 2020-09-15.

Publications

SCIENTIFIC REPORTS

OPEN

All semiconductor enhanced high-harmonic generation from a single nanostructured cone

Received: 11 December 2018
Accepted: 8 March 2019
Published online: 05 April 2019

Dominik Franz[1], Shatha Kaassamani[1], David Gauthier[1], Rana Nicolas[1], Maria Kholodtsova[1], Ludovic Douillard[2], Jean-Thomas Gomes[3], Laure Lavoute[3], Dmitry Gaponov[3], Nicolas Ducros[3], Sebastien Février[3,4], Jens Biegert[5], Liping Shi[6], Milutin Kovacev[6], Willem Boutu[1] & Hamed Merdji[1]

The enhancement and control of non-linear phenomena at a nanometer scale has a wide range of applications in science and in industry. Among these phenomena, high-harmonic generation in solids is a recent focus of research to realize next generation petahertz optoelectronic devices or compact all solid state EUV sources. Here, we report on the realization of the first nanoscale high harmonic source. The strong field regime is reached by confining the electric field from a few nanojoules femtosecond laser in a single 3D semiconductor waveguide. We reveal a strong competition between enhancement of coherent harmonics and incoherent fluorescence favored by excitonic processes. However, far from the band edge, clear enhancement of the harmonic emission is reported with a robust sustainability offering a compact nanosource for applications. We illustrate the potential of our harmonic nano-device by performing a coherent diffractive imaging experiment. Ultra-compact UV/X-ray nanoprobes are foreseen to have other applications such as petahertz electronics, nano-tomography or nano-medicine.

Ultrafast nano-photonics science is emerging thanks to the extraordinary progresses in nano-fabrication and ultrafast laser science. Boosting laser fields in nanostructured photonic devices to the strong field regime has the potential of creating nano-localized sources of energetic photons or particles, opening vast applications. Nowadays, optoelectronics is extending to the highly non-linear regime where electron currents can be optically controlled under strong fields in semiconductors. A recent impact of this capability is the emergence of high-harmonic generation (HHG) in crystals[1–5]. High harmonics are emitted when electrons undergo either intra-band or inter-band processes. These above bandgap phenomena occur efficiently in a crystal exit layer of sub-micrometer thickness[2] down to an atomically thin layer[6–10]. The strong electron currents from which HHG originates can be manipulated in space and time. This, in turn, allows to localize the HHG process in time at the single optical cycle scale[4] and in space at a nanometer scale to create for example beams that carry orbital angular momentum[11]. This control can not only revolutionize attosecond science but also prepare a new generation of ultrafast visible to X-ray optoelectronic devices operating at petahertz frequencies.

The high intensity needed for HHG in solids requires large laser amplification systems which limits the integration of the source in advanced devices. However, nanoscale field enhancement is nowadays a technology used to stimulate non-linear phenomena[12,13]. Different meta-surfaces of metallic[14–16], dielectric and semiconductor[17–19] as well as metallic/dielectric and metallic/semiconductor hybrid structures[20–22] were successfully used to boost non-linear processes. In 2016, Han *et al.* showed the enhancement of high harmonics from a 800 nm femtosecond oscillator operating at 75 MHz repetition rate using plasmonic resonances in hybrid sapphire-metal waveguides[23]. Enhancement of high-harmonic generation induced by an array of metallic nano-rods has been observed[24,25]. Plasmonic resonances ensure extremely high enhancement of the local electric field with sub-diffraction-limited hot spots. Another route for HHG enhancement is to use a full semiconductor structure. This is not the first time that such structures are used. Indeed, recent works have studied samples composed of an array of structures and

[1]LIDYL, CEA, CNRS, Université Paris-Saclay, CEA Saclay, Saclay, 91191, Gif sur Yvette, France. [2]SPEC, CEA, CNRS, Université Paris-Saclay, CEA Saclay, Saclay, 91191, Gif sur Yvette, France. [3]Novae, ZA du Moulin Cheyroux, Moulin, 87700, Aixe-sur-Vienne, France. [4]University Limoges, CNRS, XLIM, UMR 7252, 87000, Limoges, France. [5]ICFO–The Institute of Photonic Sciences, Mediterranean Technology Park, Av. Carl Friedrich Gauss 3, 08860, Castelldefels, Spain. [6]Leibniz Universität Hannover, Institut für Quantenoptik, Welfengarten 1, D-30167, Hannover, Germany. Correspondence and requests for materials should be addressed to H.M. (email: hamed.merdji@cea.fr)

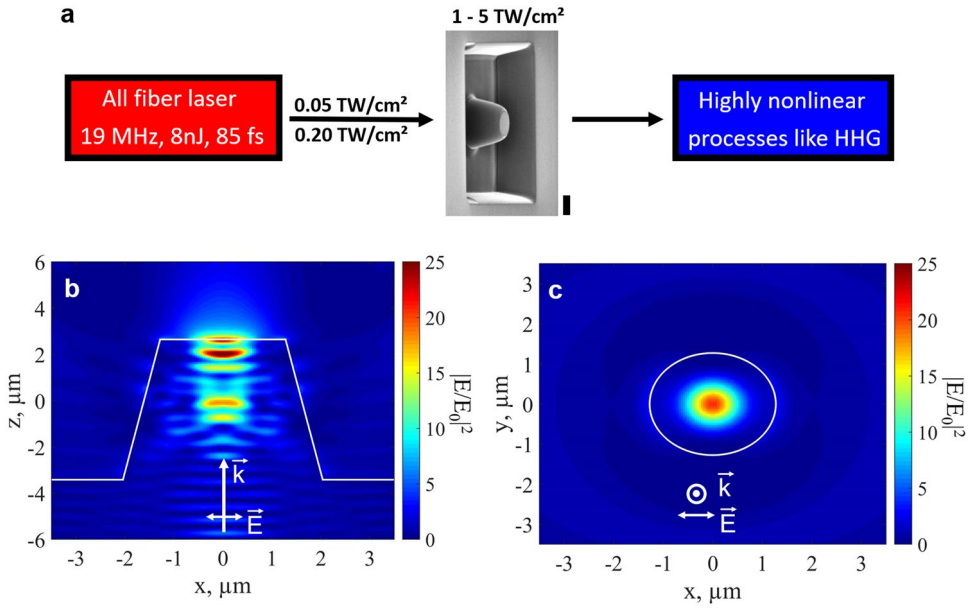

Figure 1. Field enhancement in the semiconductor waveguide. (**a**) Schematics of the field enhancement. The local field enhancement increases moderate pump intensities of 0.05–0.2 TW/cm^2 provided by the laser to up to 5 TW/cm^2 and allows for HHG. The SEM picture shows our structure patterned on a bulk ZnO crystal with the dimensions: base size of 4.1 µm in diameter, height of 6.1 µm and top of 2.6 µm. The vertical black thick bar represents 2 µm. (**b**) Simulation of the intensity distribution in the cone (plane spanned by k- and E-vectors). Significant intensity enhancement occurs on the tip of the cone by a factor larger than 20. The simulation has been done with the experimental parameters. **c** Intensity enhancement at the exit of the cone (plane perpendicular to the propagation direction) 100 nm below the top surface of the cone.

for light emitted around the crystal bandgap[26–28]. Liu *et al.* have recently reported on the enhancement of harmonics using an array of structures patterned on an all-dielectric 2D surface[29]. The main difference of our work is that we use a single nanostructure to create a nanoscale size HHG source opening the path for a compact ultrafast extreme UV (EUV) nano-probe. In addition, we explore the enhancement regime of above band gap harmonics which are relevant for further extension of the HHG nanosource to the EUV. We also illustrate the potential of the nanostructured cone to produce a nanosource of hot electrons.

Results

The principle is based on the confinement of the laser light in an integrated structure to reach the intensity threshold that allows for high-harmonic generation from a few nanojoules mid-infrared fiber laser. The effective laser intensity is raised up from the sub-TW/cm^2 to the TW/cm^2 regime inside a single zinc oxide (ZnO) nanostructured waveguide as illustrated in Fig. 1a. The design of the structure and the results from finite-difference time-domain (FDTD) simulations of the intensity enhancement are shown in Fig. 1b. As the beam propagates towards the tip of the ZnO nanostructured cone, the fundamental intensity is enhanced by more than one order of magnitude in a sub-laser-wavelength volume. The simulation of the laser confinement at the output surface in the plane perpendicular to the propagation direction shows a regular centered mode (see Fig. 1c). Note that intensity enhancement close to the exit surface is mandatory for efficient above bandgap HHG because high harmonics cannot propagate more than few 100 nanometers in the bulk crystal due to their strong absorption[1].

The layout of the experimental setup is shown in Fig. 2 (see methods). The laser, of few nanojoules energy, is coupled into the cone entrance to seed the harmonic emission. Using a UV/VIS spectrometer, we have measured emission spectra at different pump intensities. The results are displayed in Fig. 3a,b. At low pump intensity of 0.07 TW/cm^2 only H3 is generated from the bare crystal and emission from the defect states (450–550 nm band) is noticeable (blue curve, Fig. 3a). While this intensity is not sufficient to trigger above-band gap harmonic generation in the bare crystal, H5, H7 and H9 are efficiently generated when the laser is focused into the cone (red curve, Fig. 3a). The Supplementary Movie S1 shows the dynamic enhancement when the isolated truncated cone is scanned across the laser beam focus. In Fig. 3a, we notice a very strong enhancement of the luminescence generated at the excitonic band edge (385 nm) and the defect states spectral regions. When increasing the pump intensity to 0.17 TW/cm^2, we notice that H5, H7 and H9 and the luminescence are generated from the bare crystal (blue curve, Fig. 3b). When focusing into the nanostructured cone, all harmonic orders and the luminescence are dramatically enhanced with respect to the bare crystal (red curve, Fig. 3b). We see that the luminescence from the band edge, which could be barely measured from the bare crystal, is strongly enhanced. The 5th harmonic, although distinguishable, cannot be used to retrieve quantitative information of the full intensity dependence. Moreover, Fig. 3c reports the non-perturbative intensity dependence of the luminescence which scales as $I^{3.1}$. This does not allow us to clearly identify the strong field origin of the harmonic emission such as reported by Sivis *et al.*[28].

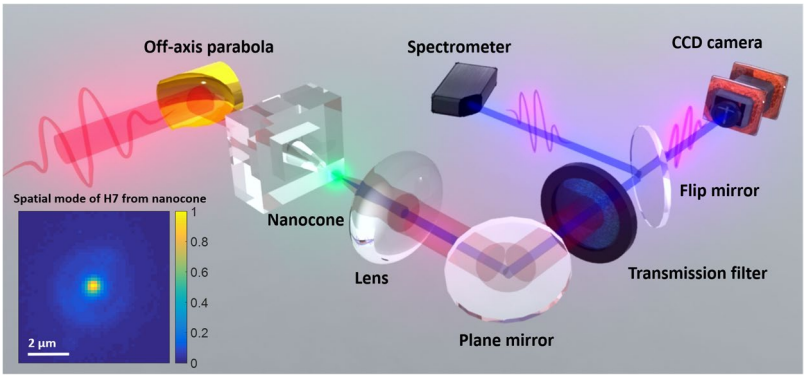

Figure 2. Experimental setup. The laser used in this experiment is an all fiber laser with 2.1 µm operating wavelength, 85 fs pulse duration, 19 MHz repetition rate and 8.7 nJ maximum pulse energy. The laser is focused with an off-axis parabola (f = 25 mm) into the sample to a spot size of 5.9 µm (FWHM) at normal incidence. The intensity range used in the experiment is 0.05–0.2 TW/cm^2. The light exiting the cone is collected by a lens towards a spectrometer or a CCD camera. Different transmission filters can be used to select a specific harmonic order. The spatial profile of H7 emitted from the cone is shown as an inset.

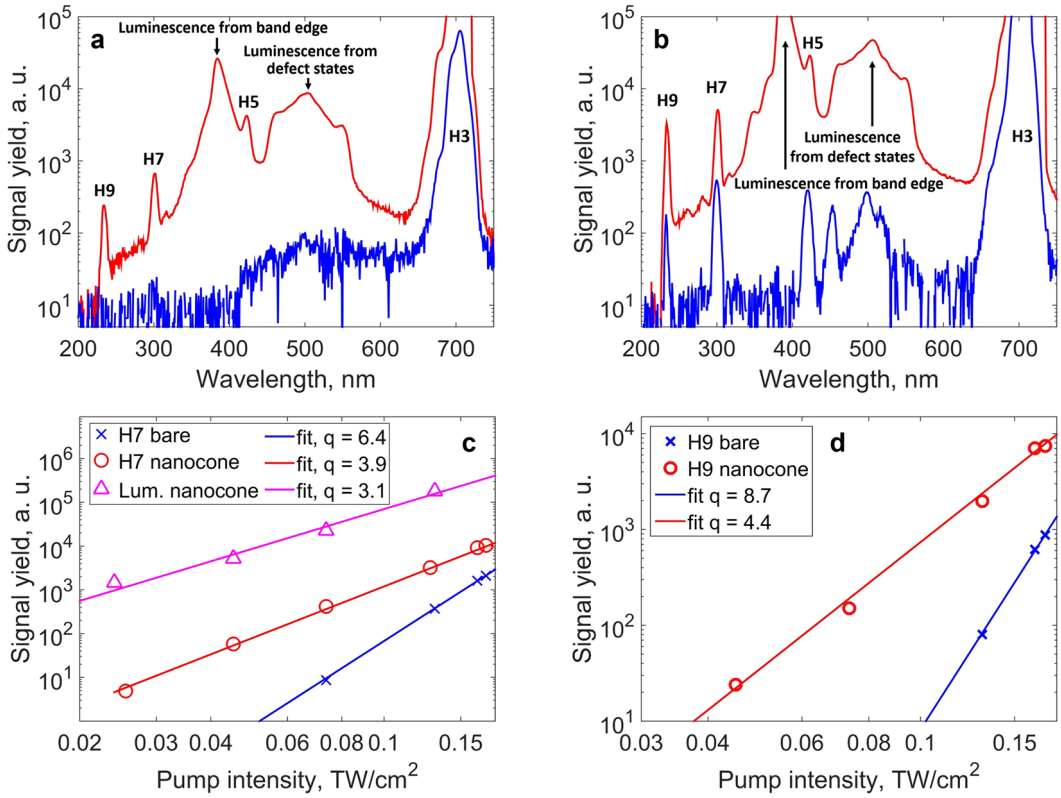

Figure 3. Intensity-dependent signal yield. (**a**,**b**) Spectra emitted from the ZnO cone (red curve) and from the bare crystal (blue curve) measured at pump intensities of 0.07 TW/cm^2 and 0.17 TW/cm^2, respectively. The harmonics H3, H5, H7 and H9 are highlighted as well as the luminescence from the band edge at 385 nm and from defect states. (**c**,**d**) Intensity dependence and power law of the harmonic yield for H7 and H9 from the bare crystal (blue crosses) and the cone (red circles), respectively. The power law for the luminescence from the band edge generated in the cone is shown in (**c**) as magenta triangles.

In order to discriminate between coherent and incoherent enhancement, we concentrated our study on higher harmonic orders. H7 (300 nm) and H9 (233 nm) stand well above the ZnO excitonic band edge which allows for a clear observation of the coherent enhancement process. H7 and H9 are enhanced in the cone (red curve) by more than two orders of magnitude with respect to the bare crystal (blue curve) at low intensity (Fig. 3a) and by around one order of magnitude at higher intensity (Fig. 3b). Figure 3c,d report the intensity power law dependencies of H7 and H9, respectively. Note that the background produced by the saturated 3rd harmonic is below H7 and H9 signals and its subtraction was efficiently achieved during the analysis. While H7 and H9 behave perturbatively

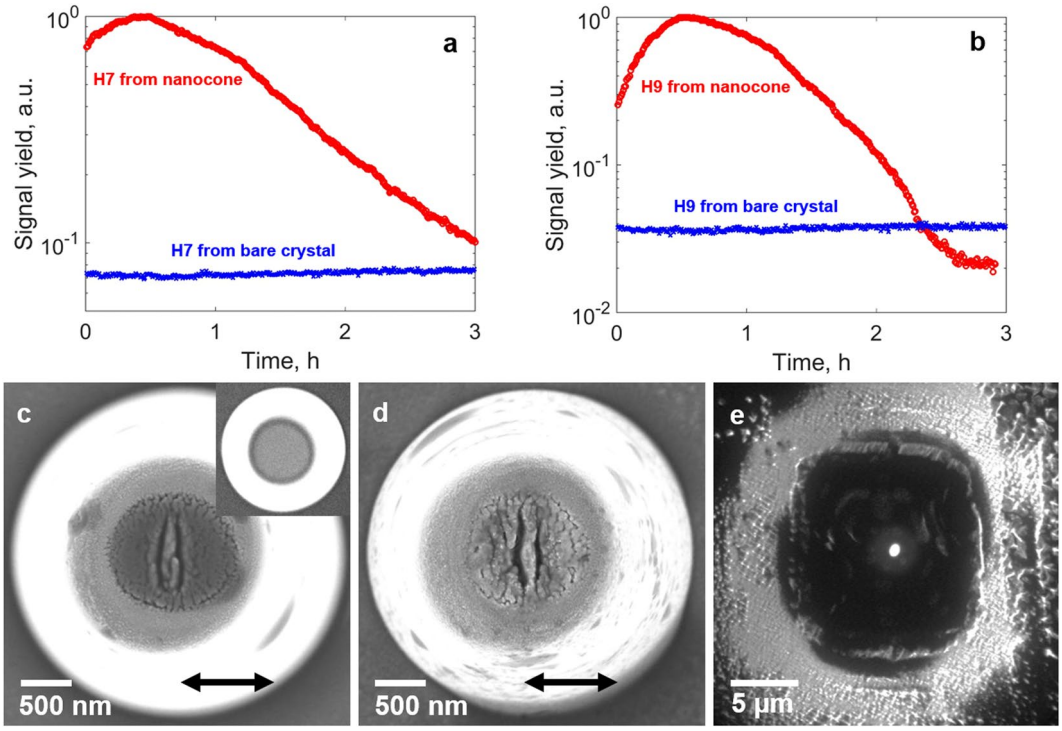

Figure 4. Temporal evolution of the harmonic emission. Temporal evolution of (**a**) H7 and (**b**) H9 from a cone at an intensity of 0.17 TW/cm^2 (red curve). The signal is observed over a time of 3 hours. SEM-images of the top of a cone after an exposure time of half an hour and 3 hours, respectively at an intensity of 0.17 TW/cm^2 are shown in (**c**,**d**). The polarization direction is indicated by a black arrow. The initial cone, before irradiation, is shown as an inset in (**c**). (**e**) Image of hot electrons emitted by the cone taken by photo-emission electron microscopy (PEEM). The cone is back illuminated by a 775 nm pulsed laser beam under an angle of 45°. The image is a superposition of two simultaneously acquired images, one recorded in low energy electron microscopy imaging mode (LEEM, topographic signature) and one in PEEM imaging mode (photoelectron signature).

with the laser intensity when generated in the bulk (with close to I^q dependencies for harmonic order q), their yield scales non-perturbatively when enhanced in the cone.

To investigate the sustainability of the harmonic nano-source, we have monitored the temporal evolution of the harmonic signal which exhibits unexpected dynamics. For intensities below one TW/cm^2, the harmonic signal emitted from the nanostructured cone was enhanced during hours as shown in Fig. 4a,b for H7 and H9, respectively. After exposure of a pristine cone to the laser, the harmonic signal first increases during a time span of up to half an hour and then decreases and tends towards a constant value. The temporal evolution of the harmonic emission is related to a structural modification of the cone, similarly to a study in bow-tie antenna recently reported[30]. Two deep subwavelength cracks appear close to the center of the cone after half an hour of exposure (SEM-image in Fig. 4c)[31]. Due to the local field enhancement self-organized reshaping occurs which leads to a higher field enhancement than in the initial pristine cone. This explains the initial increase of the harmonic signal. For longer exposure the reshaping continues and the top surface of the cone becomes porous (SEM-image in Fig. 4d), which leads to a decrease of the harmonic signal. We found that the damages occur at the position of highest field enhancement (Fig. 1b,c), i.e. in the center of the output surface of the cone, and that the linear cracks are perpendicular to the laser polarization. Those cracks are associated to emission of ions and electrons. We have further confirmed the field localization at the top of the nanoprobe by measuring the spatial distribution of hot electrons emitted during the strong field interaction (see Fig. 4e). The measurement is realized using photoemission electron microscopy (PEEM, see methods) with a spatial resolution of about 35 nm[32]. The central bright spot corresponds to the non-linearly photo-emitted electrons with an energy ranging from 6 to 12 eV and a source size of 590 nm full width at half maximum (FWHM). Note that this illustrates another potential of our semiconductor waveguide to create nanoscale source of hot electrons.

The strong localization of the electron emission reflects the nanoscale field enhancement inside the structure and is correlated to the harmonic source size. From the simulation shown in Fig. 1c, the transverse mode of the fundamental beam at the top of the cone has a size of 900 nm. The diameter of H7 emission from the cone was measured to be 800 nm (FWHM) (see inset in Fig. 2). This opens perspectives in the realization of UV/EUV nano-probes for spectroscopy or imaging applications. As an example, HHG can be used to image nanoscale objects in a femtosecond snapshot[33,34]. Here, we selected H5 emitted from the cone by using a narrow bandwidth filter to investigate the feasibility of coherent diffractive imaging (CDI). A generic layout is displayed in Fig. 5. The beam is focused onto a sample consisting in a nanoscale pattern realized on a thin opaque membrane (see methods). The coherence of

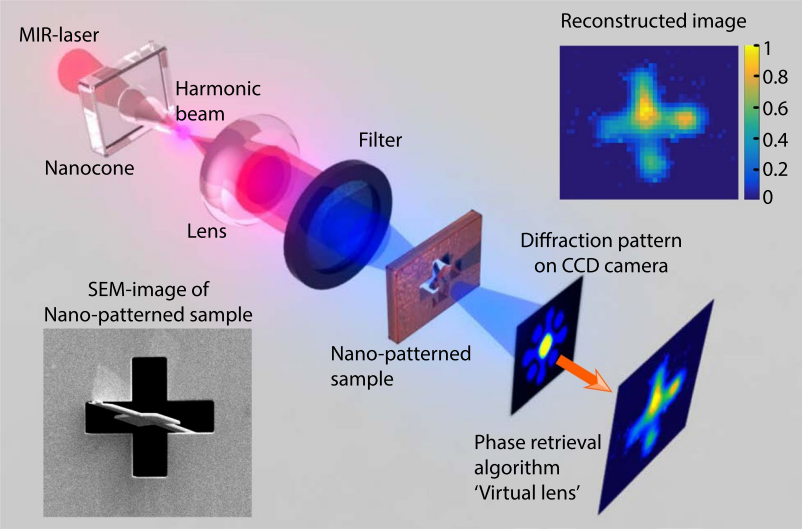

Figure 5. Generic layout of the coherent diffractive imaging setup. Few nano-joules of our 2.1 µm femtosecond laser are injected in the cone. The emission from the cone was filtered in the far field to select the 5th harmonic and then focused on a nano-patterned test sample consisting in a partially occulted cross. The diffraction pattern is collected in the far field using a CCD detector. A phase retrieval algorithm is then applied to reconstruct the image of the sample. The white bars on the SEM images of the sample and the reconstructed image correspond to a distance of 2 µm.

the harmonic source allows to measure a well contrasted diffraction pattern in the far field. The incoherent part of the emission due to fluorescence creates a constant background that does not contribute to the diffraction pattern. The image of the sample was reconstructed using a phase retrieval hybrid input-output algorithm which acts as a virtual lens (see methods). The CDI reconstruction reproduces well the cross-shape of the sample with a spatial resolution of 1.6 µm. This proof-of-principle can be extended to the sub-100 nanometer range by using higher band gap material to push the HHG spectrum to shorter wavelengths[2]. Besides illustrating the coherence of the harmonics generated in the semiconductor cone, we propose the realization of a very compact ultrafast nanoscale microscope. Other techniques such as ptychography could allow generalizing the method to extended objects[35].

Discussion

In conclusion, we have shown that high-harmonic generation can be confined in a single nanostructured semiconductor. We have shown the severe competition between the enhancement of incoherent fluorescence versus coherent harmonics. We report that the fluorescence dominates harmonics around the zinc oxide band gap. At energies well above the band gap, we demonstrated a clear enhancement of harmonics by at least two orders of magnitude. Our semiconductor harmonic nano-source shows a good sustainability, with hours long lifetime. Nanoscale enhancement can replace external laser amplifiers using few nano-joules femtosecond laser systems to boost non-linear processes to the strong field regime. Other control such as terahertz, two-color or DC field can be applied to our strong field optoelectronic device[36–38]. Single nano-emitters generate coherent UV/XUV radiation which offers a wide field of applications as, for example, ultrafast nanoscale imaging. Our nanostructured crystal can offer also an appealing source of hot electrons of nanometer scale size, the localization of which is directly controlled by the confinement of the electric field. Finally, our demonstrations pave the way towards a stable source of novel all-solid-state attosecond optoelectronic devices operating at petahertz frequencies. Additionally, the control of the laser phase gradient should also favor tailoring the spatial and spectral phases of the harmonic emission allowing controlled emission of attosecond pulses[39].

Methods

Laser. The seed mode-locked oscillator delivers a train of 1.3 ps hyperbolic secant squared (sech^2) shaped pulses centered at 1910 nm with a repetition rate of 19 MHz. The average power is 4 mW, corresponding to E = 0.2 nJ. The pulses are further amplified in a cladding-pumped amplifier based on large mode area thulium-doped fiber to tens of nano-joules. Multisolitonic effects lead to the pulse fission followed by ejection of high-energy (8.7 nJ) pulses that are frequency-shifted to 2100 nm. The spectrum has a central wavelength of 2103 nm and was measured with an optical spectrum analyzer (AQ6375, Yokogawa, Japan). The average power of the pulse train is 162 mW with a linear polarization state. The pulse duration was measured via autocorrelation to be 85 fs.

Experimental setup. The laser is focused using a 25 mm focal length off-axis parabola either in bulk or nanostructured ZnO. Harmonic spatial profiles can be imaged in the near-field (crystal sample exit) by a lens (f = 60 mm) and a CCD-camera (Photonlines, PCO.Ultraviolet). Harmonic spectra can be detected from the near infrared down

to the deep UV (Ocean Optics QE Pro, cooled). For the imaging experiment, H5 is selected with a FB420-10 transmission filter from Thorlabs and focused by a f = 50 mm lens onto the PCO ultraviolet CCD camera.

Sample. The surface of a ZnO [0001] crystal is patterned with isolated truncated waveguide structures via focused ion beam (FIB) milling. The cone has a height of 6.1 μm, a bottom diameter of 4.1 μm and a top diameter of 2.6 μm. It is illuminated from the bottom with the 2.1 μm laser beam.

Simulations. Finite difference time domain (FDTD) calculations using LUMERICAL Solutions have been performed to optimize the local enhancement of the electromagnetic field in the cone at a wavelength of 2.1 μm. The material of both the cone and its substrate is ZnO. Its optical parameters were imported from Bond *et al*., 1965, to LUMERICAL and used throughout the simulations. The surrounding medium is air. The structure is illuminated by a Gaussian beam with ω = 5.0 μm wave at 2.1 μm wavelength from below the substrate. We used perfectly matching layers at the boundaries. A finite mesh of 40 nm was used on x, y and z. The calculation time is about 3 hours on a bi-processors Intel Haswell 10C E5-2650V3 (10 cores, 20 threads, max. frequency 3 GHz, Bus speed 9.6 GT/s QPI, 768 GB registered SDRAM (DDR4 2133, 68GB/s bandpass)).

CDI. The CDI sample has been patterned on a thin opaque membrane (75 nm Si_3N_4 + 150 nm Au) by focused ion beam milling. The raw diffraction data is shown in the Supplementary Information. The diffraction patterns take about 1/3 of the full CCD dimensions so that it is possible to measure the background associated to the luminescence which covers the whole CCD. Indeed, the luminescence is isotropic and adds a constant background to the diffraction pattern. Other source noise like light scattering is also included in the background. The background is subtracted to the diffraction pattern which is then inverted using a hybrid input output algorithm. The reconstruction image is the coherent average over 50 independent runs of the algorithm, of around 500 iterations each. From the phase retrieval transfer function criterion, the spatial resolution is estimated at 1.6 μm.

PEEM. Photoemission electron microscopy measurements are carried out on a LEEM/PEEM III instrument (Elmitec GmbH) operating under ultra-high vacuum conditions. In PEEM imaging mode the spatial resolution routinely achieved is 20 nm. The laser source is a mode-locked Ti:Al_2O_3 oscillator (Chameleon Ultra II, Coherent Inc., repetition rate 80 MHz, pulse width 130 fs, wavelength range 680 nm–1000 nm). In addition to PEEM imaging, the instrument can be operated in low energy electron microscopy (LEEM) mode where backscattered electrons are used to create an image reflecting the topography of the sample.

References

1. Ghimire, S. *et al*. Observation of high-order harmonic generation in a bulk crystal. *Nat. Phys.* **7**, 138–141 (2011).
2. Luu, T. T. *et al*. Extreme ultraviolet high-harmonic spectroscopy of solids. *Nature* **521**, 498–502 (2015).
3. Hohenleutner, M. *et al*. Real-time observation of interfering crystal electrons in high-harmonic generation. *Nature* **523**, 572–575 (2015).
4. Schubert, O. *et al*. Sub-cycle control of terahertz high-harmonic generation by dynamical Bloch oscillations. *Nature Photonics* **8**, 119–123 (2014).
5. Ndabashimiye, G. *et al*. Solid-state harmonics beyond the atomic limit. *Nature* **534**, 520–523 (2016).
6. Liu, H. *et al*. High-harmonic generation from an atomically thin semiconductor. *Nature Physics* **13**, 262–265 (2016).
7. Baudisch, M. *et al*. Ultrafast nonlinear optical response of Dirac fermions in graphene. *Nature. Communications* **9**, 1018 (2018).
8. Kaassamani, S. *et al*. High harmonic generation in graphene. Proceedings Volume 10673, Advances in Ultrafast Condensed Phase Physics; 106730G, https://doi.org/10.1117/12.2306789 (2018)
9. Yoshikawa, N., Tamaya, T. & Tanaka, K. High-harmonic generation in graphene enhanced by elliptically polarized light excitation. *Science* **356**, 736–738 (2017).
10. Hafez, H. A. *et al*. Extremely efficient terahertz high-harmonic generation in graphene by hot Dirac fermions. *Nature* **561**, 507–511 (2018).
11. Gauthier *et al*. Orbital angular momentum from semiconductor high order harmonics. *Optics Letters* **44**(3), 546–549 (2019).
12. Gramotnev, D. K. & Bozhevolnyi, S. I. Plasmonics beyond the diffraction limit. *Nat. Photon.* **4**, 83–91 (2010).
13. Schuller, J. A. *et al*. Plasmonics for extreme light concentration and manipulation. *Nat. Mater.* **9**, 193–204 (2010).
14. Zhang, S. *et al*. Pronounced Fano Resonance in Single Gold Split Nanodisks with 15 nm Split Gaps for Intensive Second Harmonic Generation. *ACS Nano* **10**, 11105–11114 (2016).
15. Metzger, B., Hentschel, M. & Giessen, H. Probing the Near-Field of Second-Harmonic Light around Plasmonic Nanoantennas. *Nano Lett.* **17**, 1931–1937 (2017).
16. Butet, J., Brevet, P.-F. & Martin, O. J. F. Optical Second Harmonic Generation in Plasmonic Nanostructures: From Fundamental Principles to Advanced Applications. *ACS Nano* **9**, 10545–10562 (2015).
17. Razdolski, I. *et al*. Resonant Enhancement of Second-Harmonic Generation in the Mid-Infrared Using Localized Surface Phonon Polaritons in Subdiffractional Nanostructures. *Nano Lett.* **16**, 6954–6959 (2016).
18. Tong, W. *et al*. Enhanced third harmonic generation in a silicon metasurface using trapped mode. *Opt. Express, OE* **24**, 19661–19670 (2016).
19. Shorokhov, A. S. *et al*. Multifold Enhancement of Third-Harmonic Generation in Dielectric Nanoparticles Driven by Magnetic Fano Resonances. *Nano Lett.* **16**, 4857–4861 (2016).
20. Metzger, B. *et al*. Doubling the Efficiency of Third Harmonic Generation by Positioning ITO Nanocrystals into the Hot-Spot of Plasmonic Gap-Antennas. *Nano Lett.* **14**, 2867–2872 (2014).
21. Aouani, H., Rahmani, M., Navarro-Cía, M. & Maier, S. A. Third-harmonic-upconversion enhancement from a single semiconductor nanoparticle coupled to a plasmonic antenna. *Nat. Nanotech.* **9**, 290–294 (2014).
22. Ning, T., Tan, C., Niemi, T., Kauranen, M. & Genty, G. Enhancement of second-harmonic generation from silicon nitride with gold gratings. *Opt. Express* **23**, 30695–30700 (2015).
23. Han, S. *et al*. High-harmonic generation by field enhanced femtosecond pulses in metal-sapphire nanostructure. *Nature Communications* **7**, 13105 (2016).
24. Vampa, G. *et al*. Plasmon-enhanced high-harmonic generation from silicon. *Nat. Phys.* **13**, 659–662 (2017).
25. Imasaka, K. *et al*. Antenna-enhanced high harmonic generation in a wide-bandgap semiconductor ZnO. *Optics Express* **26**(16), 21364 (2018).
26. Franz, B. *et al*. Amplification of high harmonics in 3D semiconductor waveguides. *arXiv* **1709**, 09153v1 (2017).

27. Franz, B. *et al.* Amplification of solid high harmonics in semiconductor nanostructures, Proc. SPIE 10673, Advances in Ultrafast Condensed Phase Physics, 106730L, https://doi.org/10.1117/12.2306896 (29 May 2018).
28. Sivis, M. *et al.* Tailored semiconductors for high-harmonic optoelectronics. *Science* **357**, 303–306 (2017).
29. Liu, H. *et al.* Enhanced high-harmonic generation from an all-dielectric metasurface. *Nature Physics* **14**, 1006 (2018).
30. Shi, L. *et al.* Self-optimization of plasmonic nanoantennas in strong femtosecond fields. *Optica* **4**, 1038–1043 (2017).
31. Min, H. & Zhizhan., X. Spontaneous scaling down of femtosecond laser-induced apertures towards the 10-nanometer level: the excitation of quasistatic surface plasmons. *Laser & Photonics Reviews* **8**, 633–652 (2014).
32. Hrelescu, C. *et al.* Selective Excitation of Individual Plasmonic Hotspots at the Tips of Single Gold Nanostars. *Nano Lett.* **11**, 402–407 (2011).
33. Ravasio, A. *et al.* Single-shot diffractive imaging with a table-top femtosecond soft X-ray laser-harmonics source. *Phys. Rev. Lett.* **103**, 028104 (2009).
34. Gauthier, D. *et al.* Single-shot Femtosecond X-Ray Holography Using Extended References. *Phys. Rev. Lett.* **105**, 093901 (2010).
35. Rodenburg, J. M. & Faulkner, H. M. L. A phase retrieval algorithm for shifting illumination. *Appl. Phys. Lett.* **85**, 4795–4797 (2004).
36. Langer, F. *et al.* Lightwave-driven quasiparticle collisions on a subcycle timescale. *Nature* **533**, 225–229 (2016).
37. Wang *et al.* The roles of photo-carrier doping and driving wavelength in high harmonic generation from a semiconductor. *Nature Communications* **8**, 1686 (2017).
38. Vampa, G. *et al.* Strong-field optoelectronics in solids. *Nature Photonics* **12**(8), 465–468 (2018).
39. Shaaran, T., Nicolas, R., Iwan, B., Kovacev, M. & Merdji, H. Nano-plasmonic near field phase matching of attosecond pulses. *Scientific Reports* **7**, 6356 (2017).

Acknowledgements

We acknowledge Franck Fortuna and Laurent Delbecq for access and support to the nano-focused ion beam at the CSNSM laboratory (IN2P3, Paris Saclay University). We acknowledge support from the PETACom FET Open H2020, support from the French ministry of research through the ANR grants 2014"IPEX", 2016 "HELLIX", 2016 "BISCOT", 2017 "PACHA", the DGA RAPID grant "SWIM" and from the C'NANO research program through the NanoscopiX grant, and the LABEX "PALM" (ANR-10-LABX-0039-PALM) through he grants"Plasmon-X", "STAMPS" and "HILAC". We acknowledge the financial support from the French ASTRE program through the "NanoLight" grant. We aknowledge support from Conseil Régional de Nouvelle-Aquitaine grant 2017 "FLOWA". Financial support by the Deutsche Forschungsgemeinschaft, grant KO 3798/4-11 and from Lower Saxony through "Quanten- und Nanometrologie" (QUANOMET), project NanoPhotonik are acknowledged. J.B. acknowledges financial support from the Spanish Ministry of Economy and Competitiveness (MINECO), through the "Severo Ochoa" Programme for Centres of Excellence in R&D (SEV-2015- 0522) and the Fundació Cellex Barcelona.

Author Contributions

D.F., S.K., D.G., R.N., W.B. and H.M. carried out the experiment. The samples were produced by W.B. The laser was developed by N.D., S.F., J.-T.G., L.L. and D.Gap. Simulations were performed by D.F., S.K., R.N. and D.G. The PEEM measurements were made by L.D. Data analysis was performed by D.F., S.K., D.G., R.N., M.Kh., W.B., J.B., L.S., M.K. and H.M. H.M. proposed the physical concept. All authors discussed the results and contributed to the writing of the manuscript.

Additional Information

Supplementary information accompanies this paper at https://doi.org/10.1038/s41598-019-41642-y.

Competing Interests: The authors declare no competing interests.

Publisher's note: Springer Nature remains neutral with regard to jurisdictional claims in published maps and institutional affiliations.

Optics Letters

Orbital angular momentum from semiconductor high-order harmonics

David Gauthier,[1,*] Shatha Kaassamani,[1] Dominik Franz,[1] Rana Nicolas,[1] Jean-Thomas Gomes,[2] Laure Lavoute,[2] Dmitry Gaponov,[2] Sébastien Février,[3] Gaëtan Jargot,[4,5] Marc Hanna,[4] Willem Boutu,[1] and Hamed Merdji[1]

[1]LIDYL, CEA, CNRS, Université Paris-Saclay, CEA-Saclay, 91191 Gif-sur-Yvette, France
[2]Novae, ZI du Moulin Cheyroux, 87700 Aixe-sur-Vienne, France
[3]Université de Limoges, CNRS, XLIM, UMR 7252, 87000 Limoges, France
[4]Laboratoire Charles Fabry, Institut d'Optique Graduate School, CNRS, Université Paris-Saclay, 91127 Palaiseau, France
[5]Fastlite, 165 rue des Cistes, Pôle entreprise 95, 06600 Antibes, Sophia Antipolis, France
*Corresponding author: david.gauthier@cea.fr

Received 20 September 2018; revised 20 December 2018; accepted 25 December 2018; posted 2 January 2019 (Doc. ID 346402); published 23 January 2019

Light beams carrying orbital angular momentum (OAM) have led to stunning applications in various fields from quantum information to microscopy. We examine OAM from the recently observed high-harmonic generation (HHG) in semiconductor crystals. HHG from solids could be a valuable approach for integrated high-flux short-wavelength coherent light sources. First, we verify the transfer and conservation of the OAM in the strong-field regime of interaction from the generation laser to the harmonics. Secondly, we create OAM beams by etching a spiral zone structure directly at the surface of a zinc oxide crystal. Such diffractive optics act on the generated harmonics and produces focused optical vortices with sub-micrometric size.

https://doi.org/10.1364/OL.44.000546

Interaction between matter and photons carrying an orbital angular momentum (OAM) is an intensively studied topic in a large variety of applications [1]. Light beams carrying OAM have a helical wavefront accompanied by a phase singularity in their center [2]. They show an azimuthal phase dependence $\exp(-il\phi)$, where l is the topological charge, and ϕ is the azimuthal coordinate in the plane perpendicular to the beam propagation. Such beams carry an OAM of $l\hbar$ per photon [3]. The most common light beams carrying OAM display Laguerre–Gaussian modes characterized by a donut-shaped intensity profile. There is currently a large theoretical and experimental effort towards the generation of vortex beams with new coherent light sources [4–8]. Among the challenges involving OAM beams, increasing attention is devoted to the fundamental studies in highly nonlinear light-matter interactions. High-harmonic generation (HHG) based on frequency upconversion of a high intensity visible-IR femtosecond laser can generate coherent beams down to few nanometer wavelength and attosecond pulse duration [9]. This light source is now very common, and the underlying mechanisms are well understood for generation in various media, particularly for atomic gases and plasma targets. Recently, in both media, the transfer and conservation of the OAM from the driving laser to the high harmonics has been verified [10–12].

Reported for the first time in 2011 [13], HHG in solids, namely, bulk semiconductor crystals, has triggered numerous studies focused on the understanding of the phenomenon, proposing different models, and pushing experimental setups [14,15]. The harmonic generation mechanism is different from the dilute matter due to the high density, band structure, and periodicity of the crystal. Moreover, it requires a relatively lower intensity compared to HHG in gases, which makes it well suited for high-repetition-rate (multi-megahertz) nanoscale integrated light sources [16,17]. An all solid-state HHG source would open vast applications in science, but also in industry. An interesting feature specific to the generation of high harmonics in solids is the possibility to tailor the generation medium; the solid can be patterned to control the process of generation and the emission of radiation [18–20]. In comparison to HHG in gases, this offers a significant additional degree of freedom. Moreover, the pulse properties can be shaped directly at the source of the HHG emission by changing the characteristics of the generation medium.

In this Letter, we investigate HHG beams in solids carrying OAM using two approaches as illustrated in Fig. 1. The first case considers the generation by means of a Laguerre–Gaussian laser beam in a bare crystal [Fig. 1(a)]. Similar to HHG in gases, we show that the OAM of the harmonic beams is conserved such that their topological charge l_q is a multiple of the harmonic order q following the relation $l_q = l_l \times q$, with l_l being the topological charge of the driving laser. The second case exploits the solid-state nature of the generation medium to macroscopically control the harmonic beams. By patterning the surface of the crystal, one can design either refractive or diffractive optics. For example, nanostructured surfaces can be designed and arranged spatially in such a way that the harmonics generated in the bulk diffract and build a new mode of the light.

Figure 1(b) shows a diffractive optic, specifically a spiral zone plate (SZP) [21–23], etched at the surface of the crystal. The SZP combines beam focusing, just like an ordinary Fresnel zone plate, together with the OAM mode conversion to produce focused optical vortices carrying an arbitrary topological charge.

The first experiment was performed with an optical parametric chirped pulse amplification laser system emitting at 1550 nm [24]. It provides pulses with a duration of ≈80 fs and energy of ≈2 μJ at the repetition rate of 125 kHz. The laser beam is converted from a Gaussian to a Laguerre–Gaussian mode, with a unitary topological charge, using a q-plate combined with a quarter-wave plate (QWP) [25]. The linear polarization recommended for HHG in the crystal is induced by the second QWP. The laser is focused by a 5 cm focal length off-axis parabola ($f/15$) in a 500 μm thick zinc oxide (ZnO) crystal (laser propagation along the optical axis of the crystal) reaching intensities ranging from 0.2 to 1.5 TW/cm^2. An aspheric lens (numerical aperture NA = 0.63) and a CCD camera are used to image the harmonic beams at the exit of the crystal (see Fig. 2). Figure 2(a) displays the modes at the exit of the crystal for the fundamental and the generated harmonics h3 (517 nm), h5 (310 nm), and h7 (221 nm). The modes show the expected ring-shaped distribution with a radius of about 15 μm. The thickness of the rings decreases with an increase of the harmonic order, as a consequence of the nonlinear response to the annular fundamental intensity distribution in the sample. The imperfections in the fundamental mode are enhanced for high harmonics and suggest a decrease of the Laguerre–Gaussian mode purity. To determine the topological charge of each mode we performed self-referenced spatial interferometric measurements [26]. The principle is illustrated in Fig. 2(b). A rectangular slit (15 × 1 μm size) patterned on the crystal front surface diffracts a part of the harmonic beam generated in the crystal. At a distance of about 100 μm from the crystal, the diffraction spreads over the harmonic beam (not affected by the slit) that propagates outside the crystal. The slit is small enough with respect to the OAM mode such that the diffracted wavefront does not contain any phase singularity and can be approximated by a spherical wavefront. The interference of the latter with the helical wavefront of the main beam gives a characteristic fork grating pattern, as depicted Fig. 2(c). The topological charge of the mode is deduced directly from the number of bifurcations. Figures 2(d) and 2(e) display the experimental results for the third and fifth harmonics, respectively. In Fig. 2(d), one fringe splits into four fringes which gives a topological charge of 3. For the 5th harmonic, one fringe splits into six fringes, corresponding to a topological charge of 5. These results validate the *multiplicative* rule for the OAM transfer from the generation laser to the harmonics.

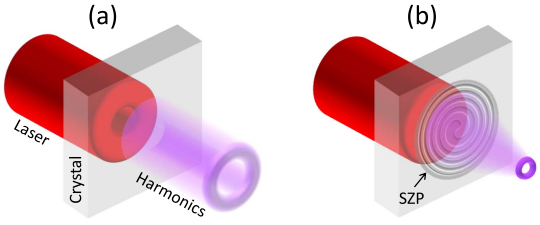

Fig. 1. Sketch of two approaches to create HHG beams carrying an OAM in semiconductor crystals: (a) transfer of the OAM from the driving laser to the harmonics; (b) diffraction of the harmonics by a SZP patterned at the surface of the generation crystal.

They have been obtained with laser peak intensity estimated (in vacuum) to 0.8 TW/cm^2 which corresponds to a Keldysh parameter near the tunneling limit of strong-field ionization [14]. We conclude that in this highly nonlinear regime, the mechanisms related to HHG in semiconductors do not affect the conservation rules of OAMs for harmonics having photon energies below and above the ZnO bandgap (3.3 eV).

The second experiment was performed with a commercial all-fiber (oscillator and amplifier) femtosecond mode-locked laser emitting at 2100 nm [27]. It provides pulses with a duration of ≈85 fs and energy of ≈8 nJ at a repetition rate of 18.66 MHz. The laser beam is directly focused at the rear side of the sample by a 2.5 cm focal length off-axis parabola ($f/6$) at a peak intensity of 0.3 TW/cm^2. The sample is a ZnO crystal with various SZPs etched at its surface using a nano-focused ion beam. The image of the beam diffracted by the SZP is obtained with an objective

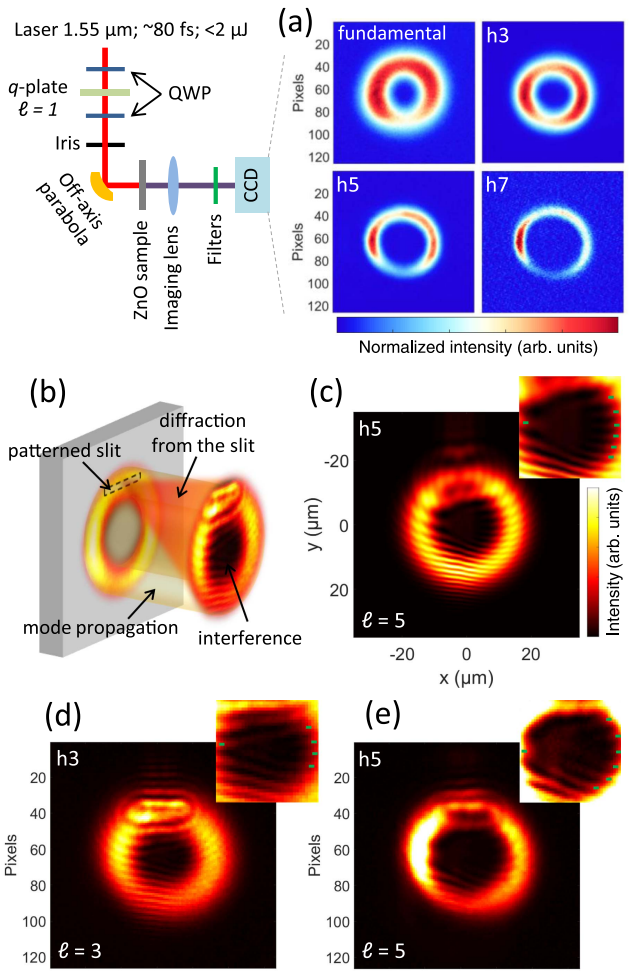

Fig. 2. OAM conservation of HHG in semiconductor crystals. Sketch of the experimental setup; a q-plate between two QWPs imparts an OAM with a topological charge $l = 1$ on the laser. The beam is then focused by a parabolic mirror in a ZnO crystal. The generated harmonics are collected by a lens to image the mode at the exit of the crystal (a). Each harmonic order is selected using bandpass filters. (b) Topological charge of the modes is defined using self-referenced interferences. (c) Simulation result with the experimental parameters of the self-referenced interferogram for harmonic h5. (d) and (e) Experimental results for harmonics h3 and h5. The insets show the detail of the fork pattern. The green dots highlight the extremity of each fringe.

lens (numerical aperture NA = 0.65) coupled to a CCD camera (see Fig. 3). The desired SZPs are pure phase objects computed numerically by combining the phase profiles of a helical and spherical waves following the relation $P = \exp(-il\phi)\exp(i2\pi\sqrt{R^2 + r^2}/\lambda)$, where λ is the wavelength of the spherical wave of the radius of curvature R (determining the focal length of the SZP), and r is the radial coordinate. All the SZPs have been designed to generate optical vortices with a topological charge $l = 1$. From the computed phase P, two types of etching profile have been defined: the *non-binary* SZP directly corresponds to the wrapping of P within $0 - 2\pi$, and the *binary* SZP is the binarization of the latter at 0 and π. For below bandgap energies, the harmonic radiation is generated in the bulk, and the etching depth d in the crystal can be defined as $d = \lambda P/2\pi(n - 1)$, where n is the index of refraction of the ZnO material at the relevant wavelength. For the data in Figs. 3 and 4 showing harmonic h5 (420 nm), $n \approx 2.1$.

Figure 3(a) shows the binary SZP and the intensity distribution measured at the focal plane of the first diffraction order located at 6 μm from the sample. Although imperfect, the mode shows the characteristic donut-shaped profile. The main cause of the imperfection is the restricted number of illuminated zones (grooves) of the SZP that limit an efficient build-up of the diffracted wave. Indeed, only the central part of the structure is actually illuminated by the 3 μm diameter (FWHM) harmonic beam generated in the bulk. Increasing the number of illuminated zones would imply either increasing the size of the laser beam or decreasing the zone periodicity. In the first case, one has to ensure that the laser intensity stays large enough for HHG, while the latter would result in decreasing the focal length of the SZP, leading to a tighter focus. However, the design of the SZP was a tradeoff between the laser energy available and the image resolution allowed with our objective lens. Another source of imperfection is coming from the fabrication defaults; the etched depth is about 205 nm, inducing a phase step about 7% larger than requested. Moreover, the gallium ions contamination and the ruggedness induced by the etching process with the focused ion beam might have modified the transmittance of the optics. The last source of imperfection is coming from residual aberrations in the generating laser and misalignments. Figure 3(b) shows the design of the non-binary version of the previous SZP and the resulting mode. This non-binary SZP is not rigorously a diffractive optics, because it is based on the principle of a Fresnel lens. For this reason, it does not suffer from the problem of the limited number of illuminated zones, and the donut-shaped profile, with a radius of 380 nm, is better defined. However, due to small errors in the etching depth, it also shows a diffractive behavior with presence of diffraction orders, which explains the parasitic signal surrounding the main mode similar to the binary SZP.

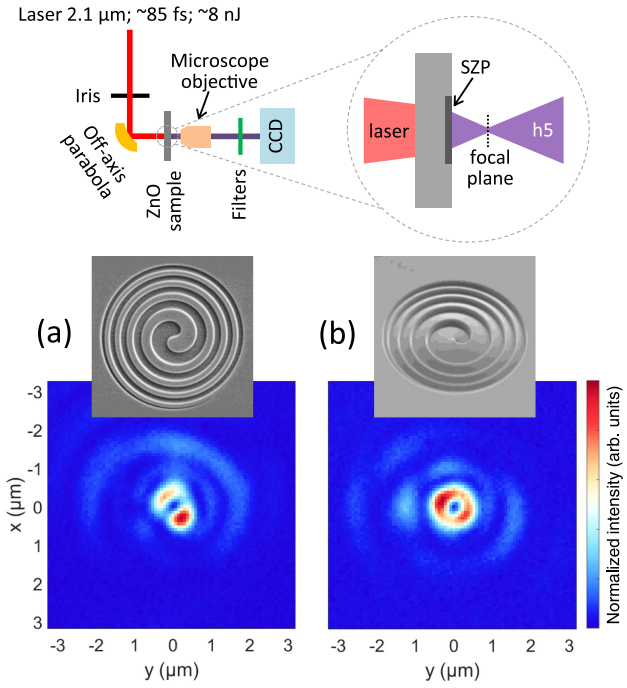

Fig. 3. Spatial beam shaping using a SZP that combines beam focusing and OAM manipulation. Sketch of the experimental setup; a microscope objective is used to image the focal plane of the SZP. Experimental results for (a) a binary and (b) a non-binary SZP etched at the surface of a ZnO crystal. Scanning electron microscope images of each diffractive structure (diameter = 10 μm; (a) normal incidence and (b) perspective view) and resulting intensity distributions at the focal plane for harmonic h5.

Figure 4 displays the results obtained with a binary and a non-binary off-axis SZP. The computed pattern of off-axis SZPs is achieved by a transversal shift between the centers of the spherical and helical waves. The shift is of 6 μm for a radius of curvature of 10 μm. Consequently, the first order of diffraction is tilted from the main optical axis by an angle of 31 deg (see sketch in Fig. 4). Figure 4(a) shows the etched binary off-axis SZP and the intensity distribution in the focal plane of the first order of diffraction. Compared to the previous binary on-axis SZP, the mode quality is significantly improved, because the off-axis design leads to a larger density of zones illuminated in the center of the optics. Off-axis SZPs have other advantages: the diffraction orders are spatially separated, so there is no parasitic signal surrounding the main mode; for properly chosen parameters, beams from different harmonic orders can be split as well. The latter is particularly interesting for fully integrated and compact sources of optical vortices. Notice that OAM beams from adjacent harmonic orders are generated from the same SZP and share the same topological charge. However, the efficiency is rather low, because the etching is not optimized for a broad wavelength range. For the non-binary off-axis SZP [Fig. 4(b)], the blazed grating profile optimizes the flux diffracted in the first order, which contains 76% of the detected photons, when this number is only of 9% for the binary case. Finally, we performed interferometric measurements in order to verify the topological charge of the beam shaped by the SZP. In this case, the reference beam is provided by the zero order that spreads over the first order by means of a knife edge, as depicted in Fig. 4(c). We find a fork grating pattern with one bifurcation, which confirms the unitary topological charge of the OAM beam.

In conclusion, we reviewed and demonstrated two different methods to generate high-harmonic photons carrying an OAM from a semiconductor crystal. First, the conservation rule of OAM beam is verified for below and above bandgap harmonics in the strong-field regime of interaction. Then, we show that the integration of a SZP to the generation medium can produce focused optical vortices with sub-micrometric size. Structured surfaces have been established for below bandgap harmonics. Shaping the crystal surface can change the intensity distribution of the driving laser with the appearance of local field confinements that modify the properties of the generated harmonics

and possibly enhance the emission [20]. This is particularly relevant for above bandgap harmonics that are not efficiently generated in the bulk crystal due to absorption. Therefore, structured surfaces for above bandgap harmonic generation have to consider together the action on the generating laser and on the harmonics. The resulting 2-in-1 design can combine enhancement and spatial shaping of the harmonic emission. Pushing the idea of integrated devices can also merge with other nano-technologies such as nano-plasmonics [28]. For example, the generating medium could be arranged as a metamaterial. Planar devices based on metasurfaces enable various manipulations beyond the simple light diffraction, including the control of the polarization (spin) and orbital angular momentum of light [29]. HHG in solids would take advantage of the numerous possibilities offered by the metasurfaces for the control of the light.

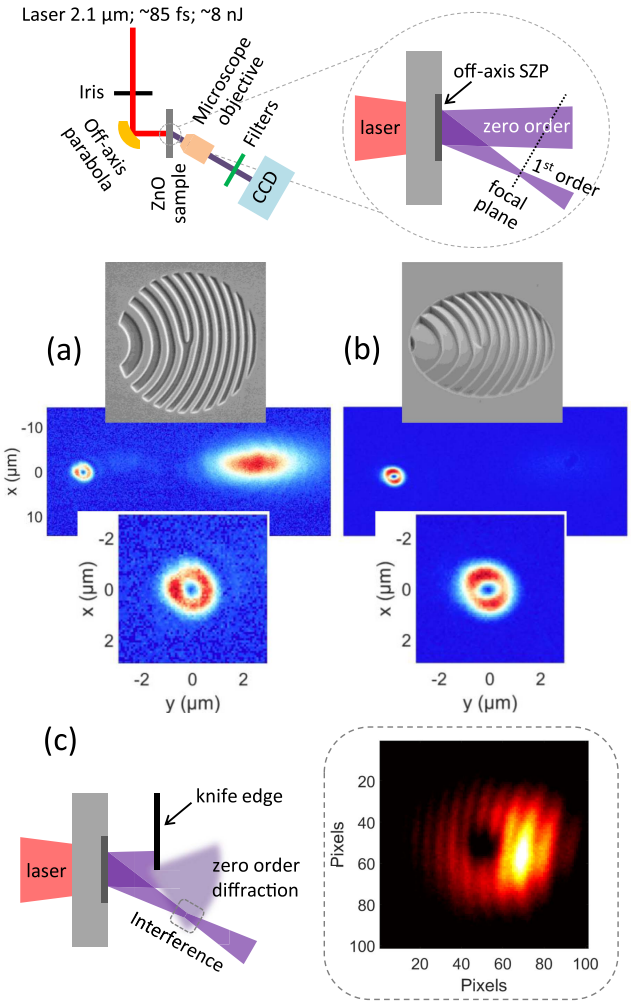

Fig. 4. Off-axis SZP. Sketch of the experimental setup; the microscope objective is tilted by an angle of 31 deg to be aligned along the optical axis of the first diffraction order. Experimental results for (a) a binary and (b) a non-binary off-axis SZP. Scanning electron microscope images of each diffractive structure (diameter = 10 μm) with the resulting intensity distributions at the focal plane of the first order, showing the zeroth and first orders of diffraction. The first order is magnified in the inset. The zeroth order shows strong aberrations due to the coupling with the microscope objective. (c) Sketch of the procedure used to measure the topological charge by the interference of the first order with the zeroth order and the resulting fork grating.

Funding. Agence Nationale de la Recherche (ANR) (2014 IPEX, 2016 BISCOT, 2017 PACHA, ANR-10-LABX-0039-PALM); French ASTRE program (NanoLight grant); Direction Générale de l'Armement (DGA) (2017 SWIM LASER grant); Laserlab-Europe (EU-H2020 654148).

REFERENCES

1. J. P. Torres and L. Torner, *Twisted Photons* (Wiley, 2011).
2. M. Padgett, J. Courtial, and L. Allen, Phys. Today **57**(5), 35 (2004).
3. L. Allen, M. W. Beijersbergen, R. J. C. Spreeuw, and J. P. Woerdman, Phys. Rev. A **45**, 8185 (1992).
4. C. Hernandez-Garcia, J. Vieira, T. J. Mendonça, L. Rego, J. San Roman, L. Plaja, P. R. Ribic, D. Gauthier, and A. Picon, Photonics **4**, 28 (2017).
5. D. Gauthier, P. R. Ribič, G. Adhikary, A. Camper, C. Chappuis, R. Cucini, L. F. DiMauro, G. Dovillaire, F. Frassetto, R. Géneaux, P. Miotti, L. Poletto, B. Ressel, C. Spezzani, M. Stupar, T. Ruchon, and G. De Ninno, Nat. Commun. **8**, 14971 (2017).
6. P. R. Ribič, B. Rösner, D. Gauthier, E. Allaria, F. Döring, L. Foglia, L. Giannessi, N. Mahne, M. Manfredda, C. Masciovecchio, R. Mincigrucci, N. Mirian, E. Principi, E. Roussel, A. Simoncig, S. Spampinati, C. David, and G. De Ninno, Phys. Rev. X **7**, 031036 (2017).
7. J. Vieira, R. M. G. M. Trines, E. P. Alves, R. A. Fonseca, J. T. Mendonça, R. Bingham, P. Norreys, and L. O. Silva, Phys. Rev. Lett. **117**, 265001 (2016).
8. V. Petrillo, G. Dattoli, I. Drebot, and F. Nguyenal, Phys. Rev. Lett. **117**, 123903 (2016).
9. T. Brabec and F. Krausz, Rev. Mod. Phys. **72**, 545 (2000).
10. G. Gariepy, J. Leach, K. T. Kim, T. J. Hammond, E. Frumker, R. W. Boyd, and P. B. Corkum, Phys. Rev. Lett. **113**, 153901 (2014).
11. R. Geneaux, A. Camper, T. Auguste, O. Gobert, J. Caillat, R. Taeïb, and T. Ruchon, Nat. Commun. **7**, 12583 (2016).
12. A. Denoeud, L. Chopineau, A. Leblanc, and F. Quéré, Phys. Rev. Lett. **118**, 033902 (2017).
13. S. Ghimire, A. D. DiChiara, E. Sistrunk, P. Agostini, L. F. DiMauro, and D. A. Reis, Nat. Phys. **7**, 138 (2011).
14. S. Ghimire, G. Ndabashimiye, A. D. DiChiara, E. Sistrunk, M. I. Stockman, P. Agostini, L. F. DiMauro, and D. A. Reis, J. Phys. B **47**, 204030 (2014).
15. G. Vampa and T. Brabec, J. Phys. B **50**, 083001 (2017).
16. K. F. Lee, X. Ding, T. J. Hammond, M. E. Fermann, G. Vampa, and P. B. Corkum, Opt. Lett. **42**, 1113 (2017).
17. T. T. Luu, V. Scagnoli, S. Saha, L. J. Heyderman, and H. J. Wörner, Opt. Lett. **43**, 1790 (2018).
18. S. Han, H. Kim, Y. W. Kim, Y.-J. Kim, S. Kim, I.-Y. Park, and S.-W. Kim, Nat. Commun. **7**, 13105 (2016).
19. H. Kim, S. Han, Y. W. Kim, S. Kim, and S.-W. Kim, ACS Photonics **4**, 1627 (2017).
20. M. Sivis, M. Taucer, G. Vampa, K. Johnston, A. Staudte, A. Y. Naumov, D. M. Villeneuve, C. Ropers, and P. B. Corkum, Science **357**, 303 (2017).
21. N. R. Heckenberg, R. McDuff, C. P. Smith, and A. G. White, Opt. Lett. **17**, 221 (1992).
22. V. Y. Bazhenov, M. S. Soskin, and M. V. Vasnetsov, J. Mod. Opt. **39**, 985 (1992).
23. A. Sakdinawat and Y. Liu, Opt. Lett. **32**, 2635 (2007).
24. P. Rigaud, A. Van de Walle, M. Hanna, N. Forget, F. Guichard, Y. Zaouter, K. Guesmi, F. Druon, and P. Georges, Opt. Express **24**, 26494 (2016).
25. L. Marrucci, C. Manzo, and D. Paparo, Phys. Rev. Lett. **96**, 163905 (2006).
26. D. G. Lee, J. J. Park, J. H. Sung, and C. H. Nam, Opt. Lett. **28**, 480 (2003).
27. https://www.novae-laser.com/brevity/.
28. G. Vampa, B. G. Ghamsari, S. S. Mousavi, T. J. Hammond, A. Olivieri, E. Lisicka-Skrek, A. Y. Naumov, D. M. Villeneuve, A. Staudte, P. Berini, and P. B. Corkum, Nat. Phys. **13**, 659 (2017).
29. N. Yu and F. Capasso, Nat. Mater. **13**, 139 (2014).

université PARIS-SACLAY

ÉCOLE DOCTORALE
Ondes et matière
(EDOM)

Titre: Spectroscopie de Polarisation de la Génération d'Harmoniques d'Ordre Elevé dans les Semi-conducteurs

Mots clés: Génération d'harmoniques d'ordre élevé, semi-conducteur, polarisation, anisotropie, effets non linéaires

Résumé: Depuis sa première observation, la génération d'harmonique d'ordre élevé (HHG) dans les cristaux s'est avérée être une source efficace, contrôlable et compacte de rayonnement XUV cohérent. Dans cette thèse, nous étudions la génération d'harmonique d'ordre élevé (HHG) dans le graphène, et dans différents semi-conducteurs principalement oxyde de zinc, silicium, arséniure de gallium et oxyde de magnésium. Nous observons que les propriétés du laser, notamment l'intensité, polarisation et ellipticité ainsi que les propriétés du cristal impactent de manière corrélée le processus de génération d'harmonique. De plus, nous surlignons le rôle important des effets de propagation linéaire et non linéaire, surtout l'effet Kerr, qui peut modifier l'efficacité de génération d'harmonique. Bien que ceux-ci induisent des limitations, dans certains conditions ils présentent un avantage. Finalement, nous démontrons la possibilité d'augmenter localement l'intensité du laser par confinement dans un cone nanostructuré et ainsi d'accroître le flux harmonique généré. Enfin, nous démontrons une application en imagerie par diffraction cohérente de la source hamonique nanostructurée.

Title: Polarization Spectroscopy of High Order Harmonic Generation in Semiconductors

Keywords: high harmonic generation, semiconductors, polarization, anisotropy, nonlinear effects

Abstract: Since its first observation, a decade ago, high harmonic generation (HHG) in crystals has proved to be an efficient, controllable and compact source of coherent XUV radiation. In this thesis, we investigate HHG in 2D materials, particularly graphene, and in different semiconductor crystals mainly zinc oxide, silicon, gallium arsenide and magnesium oxide. We find that the laser properties, such as its intensity, polarization and ellipticity, and the crystal properties are correlated. Moreover, we shed the light on the role of the linear and nonlinear propagation effects mainly the Kerr effect, upon laser interaction with the crystal, which can significantly influence the high harmonic generation efficiency. Although this presents major limitations, we show that in some cases it turns out to be an advantage. Finally, we demonstrate the manipulation of the harmonic radiation at the source of the emission by patterning nanostructures to confine and enhance nanojoule laser pulses, and generate harmonic beams carrying orbital angular momentum. Lastly, we successfully image a micrometer-sized sample by the coherent diffractive imaging (CDI) technique based on solid-state harmonics.

Université Paris-Saclay
Espace Technologique / Immeuble Discovery
Route de l'Orme aux Merisiers RD 128 / 91190 Saint-Aubin, France